CWP-488

— Project Review —

Consortium Project on
Seismic Inverse Methods for Complex Structures

Estes Park, Colorado, May 10-13, 2004

CWP Students and Research Leaders:

Ramzy Al-Zayer
Jyoti Behura
Norm Bleistein
Maarten de Hoop
Pawan Dewangan
Huub Douma
Rodrigo Fuck
Alexandre Grêt
Matthew Haney
Ken Larner
Alison Malcolm
Kurang Mehta
Carlos Pacheco
Matt Reynolds
Roel Snieder
John Stockwell
Ilya Tsvankin
Ivan Vasconcelos
Greg Wimpey
Xiaoxia (Ellen) Xu
Brian Zadler
Yaping Zhu

Visitors:

David Eckert
Mark Vrijlandt

CWP Staff:

Michelle Szobody
Program Assistant

Barbara McLenon
Publications Specialist

Center for Wave Phenomena
Colorado School of Mines
Golden, Colorado 80401
(303) 273-3557 fax: (303) 273-3478
email: cwpcsm@dix.mines.edu http://www.cwp.mines.edu

Contents

Velocity Analysis

Migration & Imaging

Multicomponent Seismology

Acknowledgments

This project review book is prepared for the sponsors of the Consortium Project at the Center for Wave Phenomena. The Consortium Project provides substantial funding for the overall research and educational program at the Center. The Center has also received funds from the following agencies:

- National Science Foundation
- Chemical Sciences, Geosciences and Biosciences Division, Office of Basic Energy Sciences, U.S. Department of Energy
- U.S. Civilian Research and Development Foundation (CRDF)

We are extremely grateful for the support of these agencies during the past year and for that of the Consortium sponsors who are listed here.

Amerada Hess Corporation
Anadarko Petroleum Corp.
Aramco
BHP Billiton Petroleum
BP America Inc.
Bureau of Geophysical Prospecting
ChevronTexaco
ConocoPhillips
Encana
ENI-AGIP E & P Division
ExxonMobil Upstream Research Co.
GMG/AXIS, Inc.
GX Technology
Instituto Mexicano del Petroleo
Kerr-McGee Oil & Gas Corporation
Landmark Graphics Corporation
Norsk Hydro A.S.
Petrobras America Inc.
Shell International E & P
Spinnaker Exploration Co.
Statoil Research Centre
Talisman Energy Inc.
Total E & P Services
Union Oil Company of CA
Veritas DGC, Ltd.
WesternGeco L.L.C.

In addition, the Seismic Un*x (SU) project is partially funded by the Society of Exploration Geophysicists.

CWP Policy on Proprietary Printed Material

New printed material that is produced at the Center for Wave Phenomena under Consortium support is presented to Sponsors before it is released to the general public. We delay general publication by 60 days so that Sponsors may benefit directly from their support of the Center for Wave Phenomena.

During this delay, Sponsors may make whatever use of the material inside their organization that they deem proper. However, we expect that all Sponsors will respect the rights of other Sponsors, and of CWP, by not publishing these results externally and independently, in advance of this 60-day delay (even with attribution to CWP). Please refer to your Consortium Membership Agreement under the paragraph entitled "Sponsor Confidentiality Obligation."

Those reports in this book that were produced primarily under consortium support and have not been previously distributed or submitted for publication, will be available for general distribution after July 10, 2004. If you have independently generated results that duplicate or overlap these, and plan to submit them for publication under your own name before this date, please notify us immediately, so that misunderstandings do not arise.

INTRODUCTION

This, the 20th anniversary edition of the report on the Consortium Project at the Center for Wave Phenomena, summarizes much of the research conducted within CWP, as it enters its twenty-first year. As in past years, the papers in this report and those that will be presented orally during the Annual Project Review Meeting, May 10-13, 2004, only partially overlap. Also, in addition to these papers, a number of last-minute manuscripts will be distributed during the Meeting and mailed to representatives of sponsor companies.

Papers in This Report

The 20 papers contained herein span a range of research areas grouped into the following six categories: velocity analysis, migration and imaging, multicomponent seismology, data processing and interpretation, scattering, and multiple suppression. These categories show both similarities to and differences from those of the past few years, indicative of the continuity with research of the recent past and the expanding breadth of our research. Readily, many of the papers could have been placed in any of several of these categories, and the categorization could have been different from that selected.

The two papers on *velocity analysis* extend beyond historic assessment of hyperbolic moveout, using the nonhyperbolic behavior at long offset to estimate anisotropy parameters. Where the subsurface is anisotropic, conventional flattening of events in velocity analysis does not yield the velocity information necessary for proper conversion from time to depth or for accurate positioning in migration. One of the papers shows application of an approach to anisotropic migration velocity analysis of P-wave data, described last year, to field data from West Africa. The second paper is a study of the feasibility of estimating fracture direction and parameters of an orthorhombic layer from inversion of the azimuthal variation in nonhyperbolic moveout of P-wave data.

The *migration and imaging* section includes three papers. Two of them provide theoretical bases for problems of imaging, multiple suppression, and inversion. The first one develops an amplitude-preserving approach to modeling and inverse scattering based on downward continuation with the double-square-root equation that uses the Kirchhoff, rather than Born, approximation, thus overcoming the limitation to the small-angle approximation for reflection coefficients. Despite the predominance of 3D seismic today, the principles of 2.5D remain of importance in the imaging of data from 2D surveys conducted in the direction perpendicular to dominant strike, in particular of widely separated ocean-bottom seismic lines. The second paper in this category extends the 2.5D principle to treatment of data in anisotropic elastic media in the presence of caustics. The third paper uses spectral-element modeling in an analysis of the sensitivity in imaging of fault-plane reflections to errors in stacking and migration.

Five papers are included under the category of *multicomponent seismology*. A sequence of two papers exploits the asymmetry of PS-wave moveout for parameter estimation in transversely isotropic (TI) media with tilted axis of symmetry. The third paper assesses the possibility of using offset data in common-image gathers of migrated SV-wave data to estimate the parameters of TI media with vertical symmetry axis, and thus the velocity needed to obtain correct imaged depth. Following on the methodology for analysis of P-wave data last year, this study finds strikingly different behavior for imaging of SV-wave data. The fourth paper in this category is a modeling study of radiation patterns of waves in mdeia that exhibit transverse isotropy in both elastic and inelastic properties, in particular in media that have TI attenuation. The final paper in this section combines differential semblance in scattering angle with a *co-depthing* approach to address the difficult problem of co-registration of PP- and PS-data for joint P- and S-wave reflection tomography.

The broad category of *data processing and interpretation* contains three papers of differing character. Approximate reconstitution of missing data can be done using any of a variety of interpolation approaches. In the presence of caustics, numerically-based approaches fail. The first paper shows a wave-based methodology for continuing data in the presence of caustics, and shows successful application for model data with large gaps of missing traces. The second paper addresses the large departure constraints on corporate budgets for research and support of university research projects. We thank the representatives of our sponsor companies for their continued support. A full list of sponsors over the term of the past year appears on the acknowledgment page at the beginning of this volume.

We benefit from approximately the same level of government support as last year. A list of those sponsor agencies also appears in the acknowledgment page.

Our industrial and government support for both research and education complement one another; each gains from, and strengthens, the other. As a net result, for the present annual fee of $45,000, a company participates in a research project whose total funding level is about $1.5M — giving a slight increase in the leverage factor to about 35.

In addition, the SEG Foundation has continued to provide support for Seismic Unix (SU) that is under John Stockwell's leadership.

Joint Projects with Shell International E&P and Total

Roel Snieder and CWP student, Matt Haney, are continuing their collaboration with Jon Sheiman at Shell International E&P in Houston on a project to relate physical properties of fault zones to the seismic response from these structures. Though this research is not strictly part of the Consortium Project, Shell is willing for CWP to share results with Consortium sponsors, within constraints of Shell's research agreement.

Henri Calandra, of Total in Houston, has been working with and providing support for the research that Alison Malcolm and Martijn de Hoop have been doing in data continuation and modeling and inversion of internal multiples. Total, also, has agreed that their research results and code be available to CWP sponsors.

We encourage similar types of directly sponsored research with other companies that could lead to prospective sharing of results with the Consortium.

Papers at SEG and EAGE

Once again, CWP students and faculty presented a large number of papers at the SEG Annual Meeting. During the 2003 Annual Meeting in Dallas, they presented a total of 27 oral presentations, poster papers, and workshop presentations. A number of these presentations result from the CSM Department of Geophysics requirement that Ph.D. students must complete research papers in two different areas with two separate faculty members. The two goals of this policy are to broaden students' educational background in geophysics and to encourage students to embark on research early in their Ph.D. studies.

CWP personnel also presented four papers at the EAGE Meeting in Stavanger, Norway.

Summer School on Uncertainty

Roel Snieder is co-organizer of the summer school "Mathematical Geophysics and Uncertainty in Earth Models," which will be held for two weeks, June 14-25, 2004, at Colorado School of Mines. Instructors and speakers for this school include noted individuals from the mathematics community as well as geophysicists from the global and exploration communities.

Interaction with Other Research Projects at CSM and Elsewhere

During this past year, as in previous years, faculty and students of CWP have interacted closely with CSM students and faculty members of other industry-funded research projects in the CSM Department of Geophysics. These include the Reservoir Characterization Project (RCP), led by Tom Davis; the Physical Acoustics Laboratory (PAL), led by John Scales and Kasper van Wijk; the Center for Rock Abuse, led by Mike Batzle; and the Gravity/Magnetics Project (GMP), led by Yaoguo Li. Some CWP students receive joint support from these other consortia.

Annual Project Review Meeting

This year's Annual Project Review Meeting, May 10-13, 2004, will be held for the first time in Estes Park, Colorado. During the 3.5-day meeting, students and faculty will present more than 20 papers. In addition, the program will have two guest speakers from industry: Jon Sheiman, of Shell International E&P, in Houston, and Ben White, of Exxon Corporate Strategic Research, in Annandale, New Jersey. A tradition of recent years is that, prior to the opening reception for the Meeting, we hold a tutorial for sponsors on a topic of particular interest within CWP. This year, Ilya Tsvankin will give a tutorial entitled "Seismic amplitude analysis in anisotropic media." Four years ago, Ilya and Vladimir Grechka gave a tutorial overview of CWP developments on anisotropy that expanded into a well-received two-day SEG short course.

Visitors to CWP

CWP has benefited again this year from visits by a number of scientists and friends from other universities and industry. We strongly encourage visits from our sponsor representatives, whether it be for a single day, or for an extended period. Below is a list of those who spent time at CWP:

- Adrianus T. de Hoop, Delft University of Technology; one week in October for collaboration with Martijn;
- Ivan Vasconcelos, Visiting Scholar from University of San Paulo; July through November, 2003; now a PhD student in CWP;
- Bill Dragoset, WesternGeco, two days of seminars and meetings with Roel and Ken, March, 2004;
- Mark Vrijlandt, Visiting Student from Utrecht University working with Roel, July, 2003 through February, 2004;
- David Eckert, Visiting Scholar from Total, France; January 2003 through May 2004;
- Guust Nolet, Princeton, University, April 11-13, 2004;
- Jim Gaiser, WesternGeco, Denver, numerous visits as participant in A-team, and speaker.

Travels and Activities of CWP People

Interactions and collaborations with others have taken place away from Golden and across the Net as well as in Golden. Collaborations and activities elsewhere include the following.

Norm Bleistein –

- two talks at biannual meeting of the Brazilian Geophysical Society, Rio de Janeiro, Brazil, September 14-18, 2003;
- CGS-SEG Meeting in Beijing, China, March 26-April 5, 2004; collaboration with Professor Guanquan Zhang, Academica Synica, Beijing;
- PIMS Workshop, Calgary, Canada, July 20-25, 2003;
- Alexander von Humboldt Foundation Senior Fellowship, University of Karlsruhe, Germany, August 1-November 30, 2003;
- lectured Charles University, Prague; Ecole des Mines, Paris; IFP, Paris.

Ken Larner –

- received the Petr L. Kapitsa Gold Medal of the Russian Academy of Natural Sciences during the Moscow 2003 International Conference and Exhibition of the EAGO, SEG, and EAGE, Moscow, September 1-4, 2003

Martijn de Hoop –

- co-organizer and presenter at opening workshop at IPAM (UCLA), May 18-23, 2003;
- invited presentation at 5th Intl. Congress on Industrial and Applied Mathematics, Sydney, Australia, July 5-12, 2003;
- Co-organizer and speaker at PIMS Workshop, Calgary, Canada, July 20-28, 2003;
- invited speaker at Opening Conference: Year on Inverse Problems, Helsinki, Finland, August 25-29, 2003;
- invited speaker at symposium honoring Bjorn Ursin, Trondheim, Norway, September 9-13, 2003;
- invited Core Participant at IPAM, California, November 9-21, 2003;
- Guest Professor at Innsbruck University, Innsbruck, Austria, December 2003;
- interaction with Henri Calandra of Total in Houston, January 23, 2004;
- invited research and colloquia with G. Makrakis, Crete, Greece, March, 2004;
- Plenary Speaker at RPI Opening Conference of Institute for Inverse Problems, Boston, April 4-6, 2004.

Roel Snieder –

- UNAVCO Meeting, Feb. 26-27, Boulder, CO;
- EAEG Workshop on Faults and Top Seals, September 8-11, Montpellier, France;
- AGU Meeting, December 7-10, 2003, San Francisco;
- Invited seminar at Mayo Clinic, Rochester, MN, January 16, 2004.

Ilya Tsvankin –

- Anisotropy SEG Short Course, October 25 - 31, 2003, Dallas, TX.

Our students traveled considerably as well. Alison Malcolm presented a paper at the PIMS Workshop, Calgary, Canada, July 28, 2003, and made two trips to Total US E&P Services, Houston, in Spring 2004, for collaborative research. Pawan Dewangan participated in the Indian Geophysical Conference in Iderabad, January 12-15, 2004. Alex Gret presented a paper at the AGU Meeting, December 7-15, 2003.

Matt Haney had extended visits for collaborations with Jon Sheiman at Shell Bellaire Research Centre, Houston, February 15-March 3, 2004, and again March 29-April 7, 2004. He also conducted computer experiments for the Shell Project in Princeton, NJ, July 13-20, 2003

CWP-474

Anisotropic migration velocity analysis: Application to a data set from West Africa

Debashish Sarkar and Ilya Tsvankin
Center for Wave Phenomena, Department of Geophysics, Colorado School of Mines, Golden, CO 80401-1887, USA

ABSTRACT

Although it is widely recognized that anisotropy can have a significant influence on the focusing and positioning of migrated reflection events, conventional imaging methods still operate with isotropic velocity fields. Here, we present an application of a migration velocity analysis (MVA) algorithm designed for factorized $v(x,z)$ VTI (transversely isotropic with a vertical symmetry axis) media to an offshore data set from West Africa. By approximating the subsurface with factorized VTI blocks, it is possible to decouple the spatial variations in the vertical velocity from the anisotropic parameters with minimal *a priori* information.

Since our method accounts for lateral velocity variation, it produces more accurate estimates of the anisotropic parameters than those previously obtained with time-domain techniques. The values of the anellipticity parameter η found for the massive shales exceed 0.2, which confirms that ignoring anisotropy in the study area can lead to substantial imaging distortions, such as misstacking and mispositioning of dipping events. While some of these distortions can be removed by using anisotropic time processing, further marked improvement in image quality is achieved by prestack depth migration with the estimated factorized VTI model. In particular, many fault planes, including antithetic faults in the shallow part of the section, are better focused by the depth-migration algorithm and appear more continuous. Anisotropic depth migration also facilitates structural interpretation by eliminating false dips at the bottom of the section and improving the images of a number of gently dipping features.

One of the main difficulties in anisotropic MVA is the need to use *a priori* information for constraining the vertical velocity. In this case study, we successfully reconstructed the time-depth curve from reflection data by assuming that the vertical velocity is a continuous function of depth and estimating the vertical and lateral velocity gradients in each factorized block. If the subsurface contains strong boundaries with known jumps in velocity, this information can be incorporated into our MVA algorithm.

Key words: transverse isotropy, factorized media, velocity analysis, prestack migration, field data, P-waves

1 INTRODUCTION

Since most subsurface formations are both heterogeneous and anisotropic, building physically realistic velocity models from reflection data remains a highly challenging problem. Conventional velocity-analysis methods, which range from those employing simple analytic functions (e.g., Faust, 1951, 1953; Gardner et al., 1974) to sophisticated tomographic schemes (e.g., Stork, 1988; Liu, 1997; Meng, 1999; Chauris and Noble, 2001), are designed to account for smooth spatial velocity variations but still ignore anisotropy. Their application often tion. Application of the factorized $v(x, z)$ model here yields more accurate, laterally varying anisotropic velocity fields and greatly improved imaging of several important structural features.

2 BRIEF OVERVIEW OF THE GEOLOGICAL HISTORY

The geology of the area (offshore Angola) is largely governed by tectonic rifting that occurred around the early Cretaceous. The major tectono-stratigraphic units in the order they were formed are (Brice et al., 1982):
(1) Prerift with gentle tectonism;
(2) synrift I with strong tectonism;
(3) synrift II with moderate tectonism;
(4) postrift with gentle tectonism; and
(5) regional subsidence with major tilting.
The available seismic sections contain only the subsidence and postrift phases schematically shown in Figure 1.

The regional subsidence phase, which dates back to the Oligocene and Miocene times, is characterized by a rapidly deposited regressive sequence, turbidites, shaly clastics, and high-pressure shale. Reflectors within this unit are weak and discontinuous, and show extensive cut-and-fill patterns. The ubiquitous presence of shales makes the subsidence unit strongly anisotropic, which is well documented in the literature (Ball, 1995; Alkhalifah et al., 1996). The thickness of this unit increases away from the shore, and at places can reach 6 km.

The early Tertiary postrift deposition includes marine clastics and carbonates, nonmarine red beds, and transgressive sequences. This unit is less anisotropic than the subsudence layer and increases in thickness toward the shore, where it can be up to 2-km thick. Seismic velocity within the postrift unit varies significantly and is proportional to the carbonate content in the sediments. The structural style is defined by gentle conformable folds near the top, with faulting and complex halokinesis prevalent at the base.

3 FIRST LINE

The first section includes primarily subhorizontal interfaces and is about 9 km long. The depth of the water is close to 150 m, and both the subsidence and postrift units are approximately 2-km thick. Preprocessing steps included dip filtering and muting applied to CMP gathers to remove groundroll and some near-surface low-velocity dipping events; also, amplitudes at late times were boosted by a time-variant gain.

As the first step in building the velocity model, we identified the water bottom by migrating and stacking the data with a moveout velocity of 1500 m/s. Next, we estimated the velocity field of the underwater sediments. Because this layer is too thin ($\approx$ 400 m) to allow for picking of two events sufficiently separated in depth, we were unable to apply our MVA algorithm. Instead, we assumed that the underwater layer is isotropic with the water velocity (1500 m/s) at the top and computed the vertical gradient $k_z = 0.8$ s^{-1} using NMO velocities obtained from standard semblance velocity analysis. Figure 2 shows common-image gathers after migration with the estimated velocity field in the underwater layer (block II); the bottom of the layer is defined by the deepest events with no residual moveout.

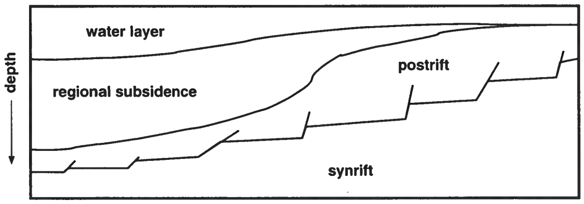

Figure 1. Cartoon of the geological history of the area depicting the subsidence, postrift, and synrift units.

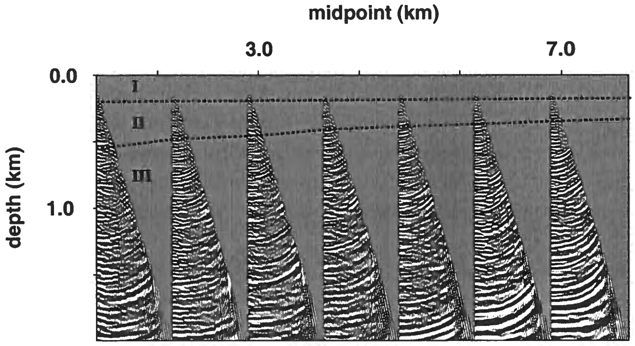

Figure 2. Common-image gathers (computed with an increment of 1 km) after Kirchhoff prestack depth migration with the velocity $V_{P0} = 1500$ m/s for the water and the parameters $V_{P0} = 1500$ m/s and $k_z = 0.8$ s^{-1} for the underwater sediments. Blocks I, II, and III used in the velocity analysis are separated by dashed lines that correspond to the deepest flat events within the first two blocks. The overcorrected events in block III indicate that the velocity field in block II is not appropriate for the deeper reflectors.

Next, we apply migration velocity analysis to image gathers in block III. To get unique estimates of the medium parameters, we assumed that the vertical velocity V_{P0} is continuous at a certain point on the boundary between the second and the third blocks (see Paper II). Since the residual moveout of events in block III shows insignificant lateral variation (Figure 2), we expect that the lateral gradient k_x in this block can be neglected, and any point at the top of block III can be picked as the point of continuity. The velocity was taken to be continuous at the point ($x = 3000\,\text{m}, z = 452\,\text{m}$), which is

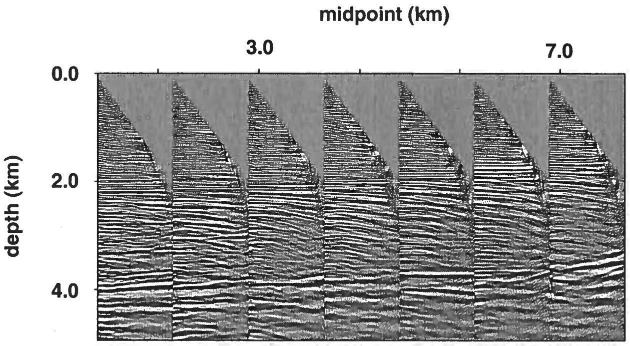

Figure 7. Common-image gathers after prestack depth migration with the estimated parameters. Most undercorrected events stack at extremely low velocities, and likely are interbed multiples.

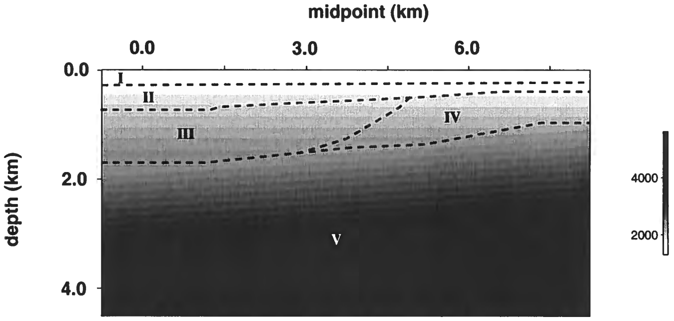

Figure 8. Depth section of the estimated vertical-velocity field. The dashed lines mark the block boundaries. The values in the legend are in m/s.

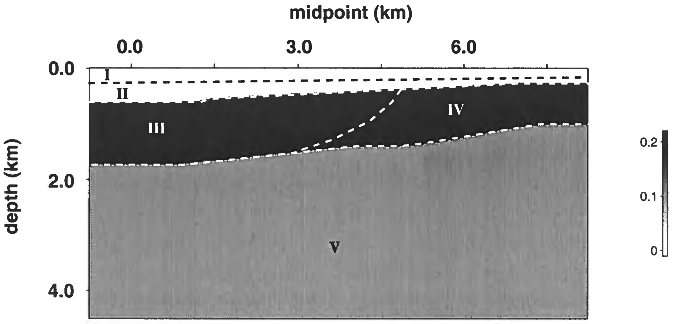

Figure 9. Depth section of the estimated anellipticity parameter η.

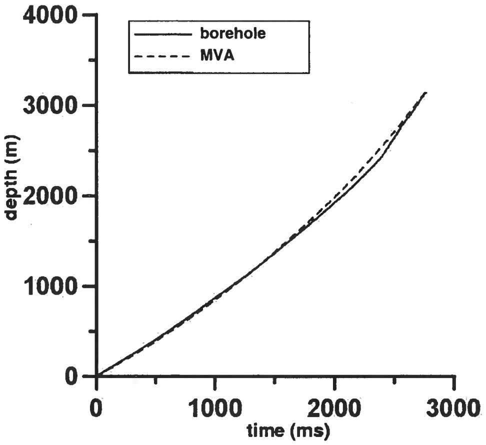

Figure 10. Comparison of the time-depth curves estimated from the MVA at midpoint 5 km (dashed) and derived from sonic logs and check-shot data in a borehole close to the seismic line (solid).

to introduce another block in the same depth interval but for midpoints to the right of the 4-km mark. Similar to the procedure described above, we selected the point of continuity between the underwater layer and the new block IV close to the midpoints where we performed the MVA ($x = 7000\,\mathrm{m}, z = 310$ m) and computed the vertical velocity at this point ($V_{P0} = 1625$ m/s). Keeping this value of V_{P0} fixed, we carried out the migration velocity analysis using the residual moveout of the two events marked in Figure 4 between midpoints 6 and 8 km. The algorithm converged to the following parameter estimates for block IV: $k_z = 0.65 \pm 0.03$ s^{-1}, $k_x = 0.0 \pm 0.01$ s^{-1}, $\epsilon = 0.35 \pm 0.03$, and $\delta = 0.1 \pm 0.02$. As illustrated by the stacked section in Figure 5, the boundary between the third and fourth blocks corresponds to a fault that stretches over a significant depth interval. While events in blocks III and IV (i.e., above the dashed line in Figure 4) are largely flat, and the shallow part of the image in Figure 5 exhibits good coherence and resolution, most deeper events remain undercorrected.

In contrast to that in the first four blocks, the residual moveout in the deeper part of the section (i.e., in block V) noticeably decreases to the right, which indicates a significant lateral velocity variation. To determine the point of velocity continuity at the top of block V in the presence of laterally varying velocity, we followed the procedure outined in Paper II. First, we performed prestack depth migration for a homogeneous isotropic medium using the vertical velocity at the bottom of block IV ($V_{P0} = 2230$ m/s). Since the minimum residual moveout in block V was observed at midpoint 7 km, the coordinates of the continuity point were found to be ($x = 7000\,\mathrm{m}, z = 1235\,\mathrm{m}$), where $V_{P0} = 2230$ m/s. Although this way of building a continuous velocity function relies on the assumption that the parameter

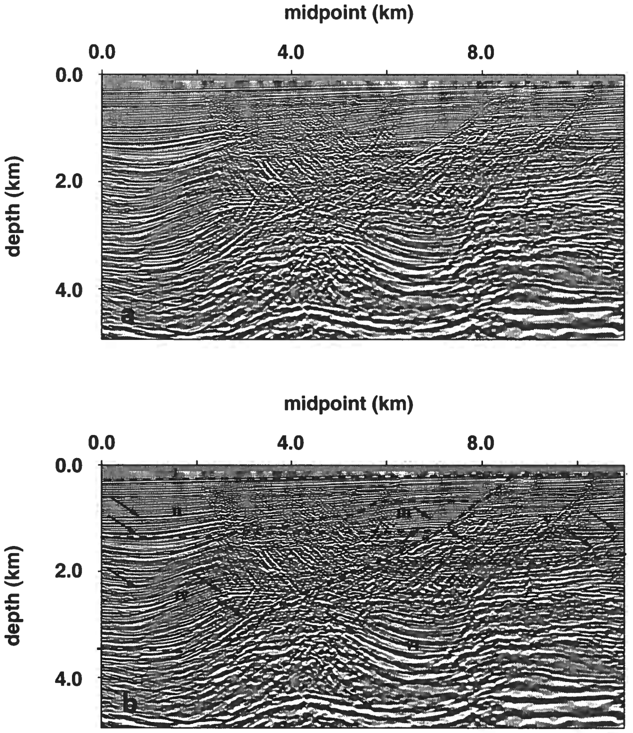

Figure 11. (a) Stacked section for the second line after prestack depth migration with the estimated parameters; (b) same section with delineated block boundaries. The arrows point to the reflectors used in the MVA. Block I is water with V_{P0} = 1500 m/s; the estimated parameters for block II are $V_{P0}(x = 4\,\text{km}, z = 240\,\text{m}) = 1500$ m/s, $k_z = 0.66 \pm 0.03\ \text{s}^{-1}$, $k_x = 0.02 \pm 0.01\ \text{s}^{-1}$, $\epsilon = 0.02 \pm 0.02$, and $\delta = -0.02 \pm 0.02$; for block III, $V_{P0}(x = 6.0\,\text{km}, z = 650\,\text{m}) = 1890$ m/s, $k_z = 0.4 \pm 0.04\ \text{s}^{-1}$, $k_x = 0.01 \pm 0.01\ \text{s}^{-1}$, $\epsilon = 0.12 \pm 0.03$, and $\delta = 0.03 \pm 0.03$; for block IV, $V_{P0}(x = 2.5\,\text{km}, z = 1400\,\text{m}) = 2200$ m/s, $k_z = 0.4 \pm 0.04\ \text{s}^{-1}$, $k_x = -0.07 \pm 0.02\ \text{s}^{-1}$, $\epsilon = 0.19 \pm 0.03$, and $\delta = 0.07 \pm 0.03$; for block V, $V_{P0}(x = 8.5\,\text{km}, z = 250\,\text{m}) = 1500$ m/s, $k_z = 0.65 \pm 0.03\ \text{s}^{-1}$, $k_x = 0.03 \pm 0.02\ \text{s}^{-1}$, $\epsilon = 0.15 \pm 0.02$, and $\delta = 0.06 \pm 0.02$; and for block VI, $V_{P0}(x = 6.5\,\text{km}, z = 1950\,\text{m}) = 2500$ m/s, $k_z = 0.65 \pm 0.03\ \text{s}^{-1}$, $k_x = 0.16 \pm 0.02\ \text{s}^{-1}$, $\epsilon = 0$, and $\delta = 0$.

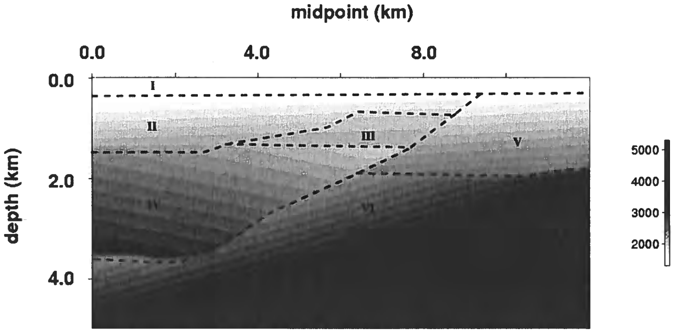

Figure 12. Depth section of the estimated vertical-velocity field. The values in the legend are in m/s.

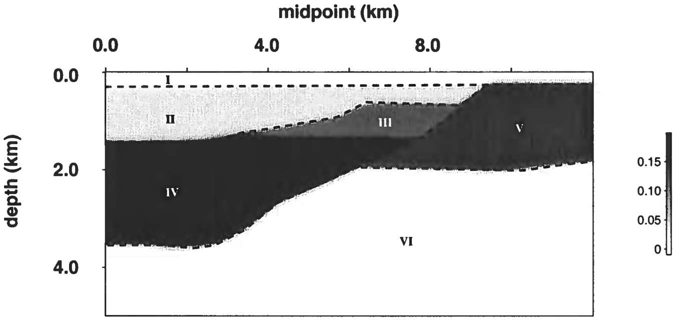

Figure 13. Depth section of the estimated parameter ϵ.

above the first prominent reflector make up the subsidence unit, while the deeper part of the section belongs to the postrift unit. Blocks IV ($k_x = -0.07\ \text{s}^{-1}$) and VI ($k_x = 0.16\ \text{s}^{-1}$) exhibit significant lateral velocity variation, which results in a decrease in V_{P0} towards the middle of the section. Since this low-velocity zone is close to the major fault plane, it may point to a zone of weakness that often accompanies major faulting.

The magnitude of the parameter η for this line ($\eta_{\max} \approx 0.12 \pm 0.04$) is smaller than that for the first line. One possible reason for the lower η values is that the shales near the second line are less consolidated, and the clay platelets responsible for the effective anisotropy are not well aligned. The weaker anisotropy on the second line can also be attributed to the influence of overpressure, which is well documented in this area (Brice et al., 1982; Alkhalifah, 1996). Overpressure may cause a reduction in the deviatoric stress, which, in turn, reduces the value of η (Sarkar et al., 2003). Although the magnitude of η is substantial only in blocks III, IV, and V, geological data indicate that the shales extend all the way to the bottom of the subsidence unit in block VI. Accurate estimation of η in block VI, however, requires larger offsets for subhorizontal events or more prominent dipping events.

Figure 17 was used by Alkhalifah (1996) and Alkhalifah et al. (1996) to illustrate the improvements in time imaging after taking anisotropy into account. For example, the anisotropic processing succeeded in imaging the fault plane at midpoint 7.5 km and depth 3 km (Figure 17b), which is absent on the isotropic image (Figure 17a). Also, the major fault plane that runs through the section between midpoints 2 and 8 km and subhorizontal reflectors near midpoint 3 km and depth 2.7 km show improved continuity on the anisotropic section.

Comparison of the prestack depth-migrated image in Figure 18b and the time-migrated image in Figure 18a

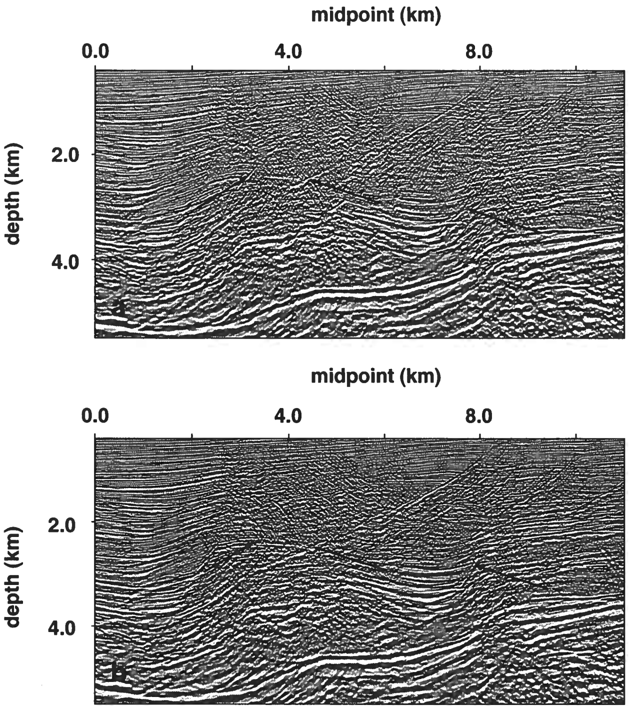

Figure 17. Second section after (a) isotropic and (b) anisotropic phase-shift time migration (from Alkhalifah et al., 1996). Both sections were filtered to match the amplitude spectrum of the depth-migrated section in Figure 11 and stretched to depth using the vertical-velocity function from Figure 12. The arrows point to the main improvements achieved by taking anisotropy into account.

the lines exceeding 0.2. The reconstructed velocity field also indicates the presence of substantial lateral heterogeneity in some of the layers, which was unaccounted for by the time-domain techniques of Alkhalifah et al. (1996) and Toldi et al. (1999). Since the piecewise factorized VTI model can handle both anisotropy and heterogeneity, our MVA algorithm produced more accurate estimates of the anisotropic coefficients than those obtained previously in the time domain by inverting dip moveout or long-spread traveltimes of horizontal events.

Anisotropic prestack depth migration with the reconstructed velocity field resulted in a number of significant improvements in image quality compared to the time sections of Alkhalifah et al. (1996). In particular, most faults on the depth-migrated image show greater continuity, the antithetic faults that are fuzzy on the time images are well focused, and subhorizontal reflectors within the anisotropic layers are better positioned and stacked. The accurate depth scale of our velocity model substantially changed the structure of the deeper part of one of the sections, where false dips seen on the time-migrated image were removed after the MVA and prestack depth migration.

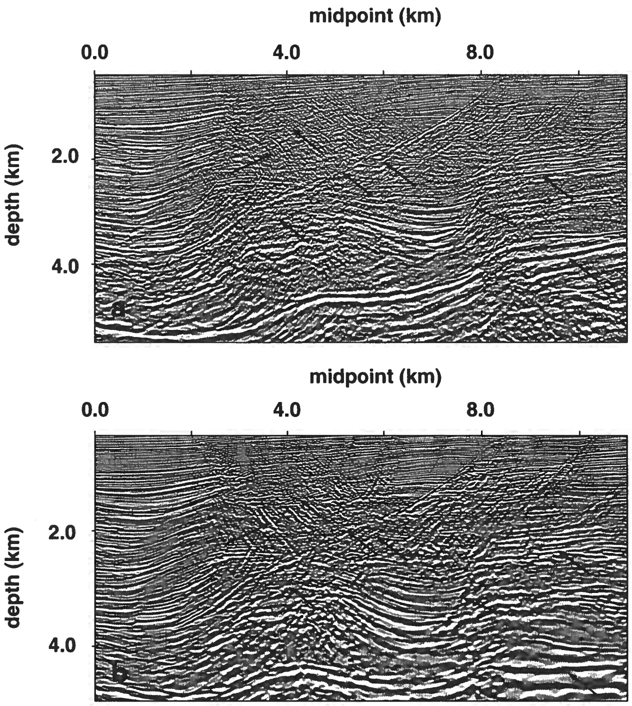

Figure 18. Second section after (a) anisotropic phase-shift time migration (Figure 17b) and (b) prestack depth migration (Figure 11). The arrows point to the main improvements achieved by applying the MVA and prestack depth migration.

Flat image gathers after the iterative maigration velocity analysis suggest that the factorized $v(x, z)$ VTI medium provides an adequate approximation for realistic, spatially varying anisotropic velocity fields. Although the vertical velocity can seldom be constrained by P-wave reflection data alone, the field-data example discussed here indicates that the assumption of a continuous vertical velocity field offers a practical way to build anisotropic models for prestack depth migration with minimal *a priori* information. Furthermore, as confirmed by this case study, in the absence of pronounced velocity jumps across medium interfaces, the time-depth curve obtained from the MVA algorithm closely matches the curve computed from borehole data.

Similar to any other MVA technique, the main cost of our method is in the repeated application of prestack migration, which makes this algorithm substantially more expensive than the time-domain parameter-estimation methods of Alkhalifah and Tsvankin (1995), Alkhalifah et al. (1996), and Grechka et al. (2002). The time-domain algorithms, however, produce inferior results in the presence of lateral velocity variation, as illustrated by the examples above.

Although migration becomes somewhat more time-consuming in the presence of anisotropy because of the

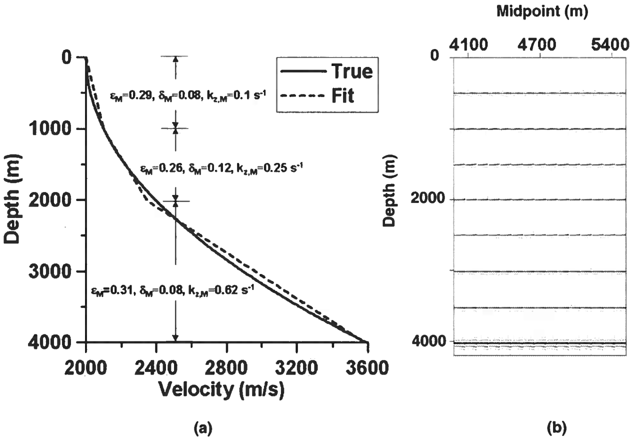

Figure A1. (a) Comparison of the true (solid line) and estimated (dashed line) vertical velocity V_{P0} for a VTI medium with $V_{P0}(z) = 2000{+}0.0001z^2$ (z is in meters, V_{P0} is in m/s), $\epsilon = 0.3$, and $\delta = 0.1$. The migration velocity analysis was performed for three factorized $v(z)$ layers with the boundaries marked on the plot. The reflectors are spaced every 500 m, and the maximum offset is equal to 4000 m. The interval parameters (subscript "M") were estimated using the moveout associated with two reflectors in each factorized layer. (b) Image gathers obtained after prestack depth migration with the estimated parameters shown on plot (a).

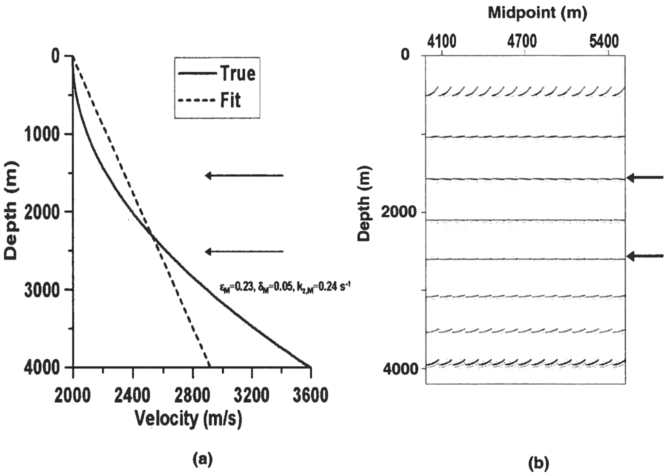

Figure A2. Same as Figure A1, but the MVA was performed for a single factorized $v(z)$ layer using the moveout associated with the reflectors at depths 1500 and 2500 m (marked by the arrows).

moveout associated with two reflectors for each factorized $v(z)$ layer, we obtained a piecewise factorized medium with the function $V_{P0}(z)$ that closely reproduces the true nonlinear vertical-velocity variation (Figure A1a). The vertical velocity at the top of the model was fixed at the correct value, while the velocities in the two deeper layers were found under the assumption that V_{P0} is a continuous function of depth. The accuracy of the estimated three-layer factorized model is confirmed by the flat image gathers in Figure A1b.

The success of the piecewise-linear velocity approximation, however, depends on whether the available reflectors sample the velocity function in sufficient detail. Consider the same true medium as that in Figure A1, but now with only two reflectors (located at depths of 1500 m and 2500 m) available for velocity analysis. In this case, our MVA algorithm can estimate the parameters of just one factorized $v(z)$ layer (Figure A2a). As illustrated by the image gathers in Figure A2b, the events associated with the reflectors used in the velocity analysis are flat. Events both above 1500 m and below 2500 m, however, are overcorrected because the NMO velocities for them are too low. Clearly, no single factorized medium can properly image reflection events for the whole range of depths.

CWP-475

Nonhyperbolic moveout inversion of P-waves in azimuthally anisotropic media: Algorithm and application to field data

Ivan Vasconcelos & Ilya Tsvankin
Center for Wave Phenomena, Department of Geophysics, Colorado School of Mines

ABSTRACT

The azimuthally varying nonhyperbolic moveout of P-waves in orthorhombic media can provide valuable information for characterization of fractured reservoirs and seismic processing. Here, we present a technique to invert long-spread, wide-azimuth P-wave data for the orientation of the vertical symmetry planes and five key moveout parameters – the symmetry-plane NMO velocities $V_{\mathrm{nmo}}^{(1)}$ and $V_{\mathrm{nmo}}^{(2)}$ and the anellipticity parameters $\eta^{(1)}$, $\eta^{(2)}$, and $\eta^{(3)}$. The inversion algorithm is based on a coherency operator that computes the semblance for the full range of offsets and azimuths using a generalized version of the Alkhalifah-Tsvankin nonhyperbolic moveout equation. To make the 3D semblance search more efficient, the starting model is obtained by estimating the NMO ellipse from the hyperbolic moveout term and applying 2D inversion of nonhyperbolic moveout for the parameters $\eta^{(1)}$ and $\eta^{(2)}$ in the symmetry-plane directions.

The moveout equation provides a close approximation to the reflection traveltimes in layered anisotropic media with a uniform orientation of the vertical symmetry planes. Numerical tests on noise-contaminated data for a single orthorhombic layer show that the inversion yields satisfactory results if the offset-to-depth ratio reaches at least 2.5. The best-constrained parameters are the azimuth φ of one of the symmetry planes and the velocities $V_{\mathrm{nmo}}^{(1)}$ and $V_{\mathrm{nmo}}^{(2)}$, while the resolution in $\eta^{(1)}$ and $\eta^{(2)}$ is somewhat compromised by the tradeoff between the quadratic and quartic moveout terms. The largest uncertainty is observed in the parameter $\eta^{(3)}$, which influences only long-spread moveout in off-symmetry directions.

The symmetry-plane orientation φ can still be estimated, albeit with a lower accuracy, if an orthorhombic layer is overlain by an azimuthally isotropic medium. For more complicated stratified models with depth-dependent symmetry-plane azimuths, the moveout equation has to be modified by allowing the orientation of the effective NMO ellipse to differ from the principal direction of the effective quartic moveout.

The inversion algorithm was successfully tested on wide-azimuth P-wave reflections recorded at Weyburn Field in Canada. Taking azimuthal anisotropy into account increased the semblance values for most long-offset reflection events in the overburden, which indicates that fracturing is not limited to the reservoir level. The estimated symmetry-plane directions are close to the azimuths of the off-trend fracture sets determined from borehole data and shear-wave splitting analysis. Estimated values of effective anellipticity parameters reach values as large as 0.25; a more detailed interpretation of the results, however, requires layer-stripping of the nonhyperbolic moveout term. The effective moveout parameters estimated by our algorithm also provide input for P-wave time imaging and geometrical-spreading correction in layered orthorhombic media.

Key words: azimuthal anisotropy, nonhyperbolic moveout, parameter estimation

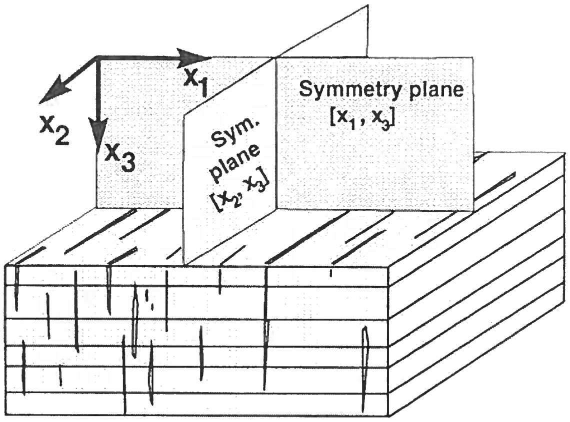

Figure 1. Orthorhombic models are characterized by three mutually orthogonal planes of mirror symmetry. Effective orthorhombic anisotropy may be caused by parallel, vertical, penny-shaped cracks embedded in a VTI matrix.

bic layer. Al-Dajani et al. (1998) demonstrated that the Tsvankin-Thomsen equation can be applied in off-symmetry directions as well by making the moveout coefficients A_2, A_4, and A azimuthally dependent:

$$T^2(x,\alpha) = A_0 + A_2(\alpha)x^2 + \frac{A_4(\alpha)\,x^4}{1 + A(\alpha)\,x^2}, \tag{1}$$

$$A_0 = T_0^2, \tag{2}$$

$$A_2(\alpha) = \left.\frac{d(T^2)}{d(x^2)}\right|_{x=0}, \tag{3}$$

$$A_4(\alpha) = \frac{1}{2}\,\frac{d}{d(x^2)}\,\left.\frac{d(T^2)}{d(x^2)}\right|_{x=0}. \tag{4}$$

Here T is the reflection traveltime, x is the source-receiver offset, α is the azimuth with respect to the $[x_1, x_3]$ symmetry plane, T_0 is the zero-offset time, $A_2 = 1/V_{\rm nmo}^2$ controls the hyperbolic portion of the moveout curve, and A_4 is the quartic moveout coefficient that accounts for nonhyperbolic moveout at long offsets. The parameter A was introduced by Tsvankin and Thomsen (1994) to make $T(x)$ convergent at $x \to \infty$:

$$A(\alpha) = \frac{A_4(\alpha)}{V_{\rm hor}^{-2}(\alpha) - V_{\rm nmo}^{-2}(\alpha)}; \tag{5}$$

$V_{\rm hor}$ is the horizontal group velocity.

The quadratic moveout coefficient A_2 depends on the azimuthally varying NMO velocity described by the equation of an ellipse (Grechka and Tsvankin, 1998a). In a single horizontal orthorhombic layer, the axes of the NMO ellipse are aligned with the vertical symmetry planes:

$$A_2(\alpha) = A_2^{(1)}\sin^2\alpha + A_2^{(2)}\cos^2\alpha, \tag{6}$$

$$A_2^{(1)} = \frac{1}{[V_{\rm nmo}^{(1)}]^2}, \quad A_2^{(2)} = \frac{1}{[V_{\rm nmo}^{(2)}]^2}, \tag{7}$$

where $V_{\rm nmo}^{(1)}$ and $V_{\rm nmo}^{(2)}$ are the NMO velocities in the symmetry planes $[x_2, x_3]$ and $[x_1, x_3]$, respectively (the superscript denotes the axis orthogonal to the plane; see Appendix A for details).

Al-Dajani et al. (1998) showed that the azimuthal dependence of the quartic moveout coefficient A_4 in an orthorhombic layer has the following form:

$$A_4(\alpha) = A_4^{(1)}\sin^4\alpha + A_4^{(2)}\cos^4\alpha + A_4^{(x)}\sin^2\alpha\cos^2\alpha. \tag{8}$$

The coefficients $A_4^{(1)}$ and $A_4^{(2)}$ control nonhyperbolic moveout in the symmetry planes, while $A_4^{(x)}$ is a cross-term that contributes to long-offset traveltimes in off-symmetry azimuthal directions. All three coefficients in equation (8) can be expressed through the symmetry-plane NMO velocities and the anellipticity parameters $\eta^{(1,2,3)}$ defined in Appendix A. Substitution of equations (8) and (6) into the moveout equation (1) yields a close approximation for P-wave reflection traveltimes up to offset-to-depth ratios of about three (Al-Dajani et al., 1998).

For moveout inversion it is more convenient to use a simplified form of the general equation (1) based on the approximate kinematic equivalence between vertical planes of orthorhombic and VTI media (Xu et al., 2003). As discussed in Tsvankin (1997, 2001), kinematic signatures and plane-wave polarizations in the vertical *symmetry* planes of orthorhombic models can be described by the corresponding VTI equations. This analogy with VTI media is no longer exact for off-symmetry directions, but it remains valid for P-wave kinematics in the weak-anisotropy approximation. P-wave phase velocity and all other 2D kinematic signatures in any vertical plane of weakly anisotropic orthorhombic media can be adapted from the VTI equations by using azimuthally-dependent Thomsen parameters ϵ and δ (Tsvankin, 1997, 2001). Therefore, the widely used nonhyperbolic moveout equation for VTI media in terms of $V_{\rm nmo}$ and η (Alkhalifah and Tsvankin, 1995; Tsvankin, 2001) can be applied to orthorhombic media by making both parameters functions of azimuth (Xu et al., 2003):

$$\begin{aligned} t^2(x) = t_0^2 &+ \frac{x^2}{V_{\rm nmo}^2(\alpha)} \\ &- \frac{2\eta(\alpha)x^4}{V_{\rm nmo}^2(\alpha)\,[t_0^2 V_{\rm nmo}^2(\alpha) + (1 + 2\eta(\alpha))x^2]}; \end{aligned} \tag{9}$$

$$V_{\rm nmo}^{-2}(\alpha) = \frac{\sin^2(\alpha - \varphi)}{[V_{\rm nmo}^{(1)}]^2} + \frac{\cos^2(\alpha - \varphi)}{[V_{\rm nmo}^{(2)}]^2}, \tag{10}$$

$$\begin{aligned} \eta(\alpha) &= \eta^{(2)}\cos^2(\alpha - \varphi) \\ &- \eta^{(3)}\cos^2(\alpha - \varphi)\sin^2(\alpha - \varphi) + \eta^{(1)}\sin^2(\alpha - \varphi), \end{aligned} \tag{11}$$

blance and thus invert for all six parameters using the full range of offsets and azimuths. Since the search does not start far from the maximum of the objective function, the algorithm usually converges in less than 20 iterations. If the model includes layers with depth-varying azimuths of the symmetry planes, the only change in the inversion methodology described above is that the 3D semblance search is carried out using equation (12) for $\eta(\alpha)$ instead of equation (11). During this semblance search, we estimate the azimuth φ_1, while holding the orientation of the NMO ellipse (i.e., the azimuth φ) constant.

4 TESTS ON SYNTHETIC DATA

The main purposes of the synthetic examples below are to assess if the inversion is sufficiently robust in the presence of random noise and can provide an accurate estimate of the medium parameters starting from different initial solutions in the model space. It is also important to evaluate the performance of the algorithm for layered media that do not conform to the model assumptions that underlie equation (9), derived for a homogeneous orthorhombic layer.

4.1 Single orthorhombic layer

The first test is performed for a single horizontal orthorhombic layer using synthetic data generated by anisotropic ray tracing (Gajewski and Pšenčík, 1987). Following the methodolody described above, we start by estimating the NMO ellipse using source-receiver pairs with offset-to-depth ratios less than one, which gives initial values for the symmetry-plane azimuth $\varphi = 130°$ and the velocities $V_{\rm nmo}^{(1)} = 2345$ m/s and $V_{\rm nmo}^{(2)} = 2715$ m/s (the model parameters are listed in the caption of Figure 2). The high semblance value (0.97) and the accurate estimate of φ confirm that the reconstructed NMO ellipse provides a good fit to conventional-spread data. The deviations of the symmetry-plane NMO velocities from the actual values are caused by the small influence of nonhyperbolic moveout unaccounted for at this stage of the inversion.

Next, we form two azimuthal sectors 10° wide around the identified symmetry-plane directions and carry out 2D nonhyperbolic moveout analysis in these sectors to obtain approximate values of $\eta^{(1)}$ and $\eta^{(2)}$. The results are displayed in Figure 2 as functions of $V_{\rm nmo}$ and the horizontal velocity $V_{\rm hor} = V_{\rm nmo}\sqrt{1+2\eta}$ related to the corresponding η coefficient. The errors in both η parameters are largely caused by the azimuthal variations in traveltimes within both azimuthal sectors. Using these initial values, we carry out the 3D nonhyperbolic moveout inversion for the whole data set and obtain the following estimates of the model parameters: $\varphi = 130°$, $V_{\rm nmo}^{(1)} = 2277$ m/s, $V_{\rm nmo}^{(2)} = 2703$ m/s, $\eta^{(1)} = 0.19$, $\eta^{(2)} = 0.06$, and $\eta^{(3)} = 0.12$; the semblance for the best-fit model is 0.885.

Although the algorithm in this noise-free test was able to converge toward the correct model, it is important to identify possible tradeoffs among the medium parameters by studying the shape of the objective function. To quantify such tradeoffs, we hold four model parameters at the correct values and compute the objective function near the actual solution as a function of the remaining two parameters. Figure 3 shows the semblance scan over the parameters $V_{\rm nmo}^{(2)}$ and $\eta^{(2)}$ computed from equation (9) using the correct values of φ, $V_{\rm nmo}^{(1)}$, $\eta^{(1)}$, and $\eta^{(3)}$. Clearly, there exists a family of models with a relatively wide range of $\eta^{(2)}$ values that fit the data, whereas the velocity $V_{\rm nmo}^{(2)}$ is constrained much more tightly.

This tradeoff between $V_{\rm nmo}^{(2)}$ and $\eta^{(2)}$ has the same character as the interplay between the NMO velocity and η in VTI media (Grechka and Tsvankin, 1998b; Tsvankin, 2001). Relatively small percentage errors in $V_{\rm nmo}^{(2)}$ can be compensated by larger absolute errors in $\eta^{(2)}$ in such a way that the reflection traveltime stays almost the same. The ambiguity in $\eta^{(2)}$ can be substantially reduced by increasing the offset-to-depth ratio x/z from two to three, as illustrated in Figure 3.

Large offset-to-depth ratios are also necessary to estimate the other two anellipticity coefficients, $\eta^{(1)}$ and $\eta^{(3)}$, which contribute only to nonhyperbolic moveout on long spreads. Still, since the parameter $\eta^{(3)}$ has no influence on reflection traveltimes near both symmetry planes, it is not well constrained even for $x/z = 3$ (Figure 4a). In contrast, the inversion algorithm yields a highly accurate estimate of the azimuth φ (Figure 4b) because the orientation of the symmetry planes can be inferred from both the NMO ellipse and azimuthally varying nonhyperbolic moveout.

Figure 5 confirms that the inversion results for $\eta^{(3)}$, as well as for the other parameters (not shown), are not sensitive to random (Gaussian) noise. The signal-to-noise ratio (S/N) in this test is defined as the ratio of the maximum absolute values of the signal and noise amplitude on each trace. The stability of the parameter estimation in the presence of random noise is not surprising because our algorithm is based on the semblance (coherency) operator (13).

4.2 Layered anisotropic media

Although equation (9) is designed for a single orthorhombic layer, we expect it to remain adequate for layered media with a uniform orientation of the vertical symmetry planes. If the medium above the reflector is multilayered, the moveout coefficients become effective quantities that incorporate the influence of both anisotropy and vertical heterogeneity. For example, the effective NMO ellipse can be found from the Dix-type averaging of the interval ellipses described by Grechka et

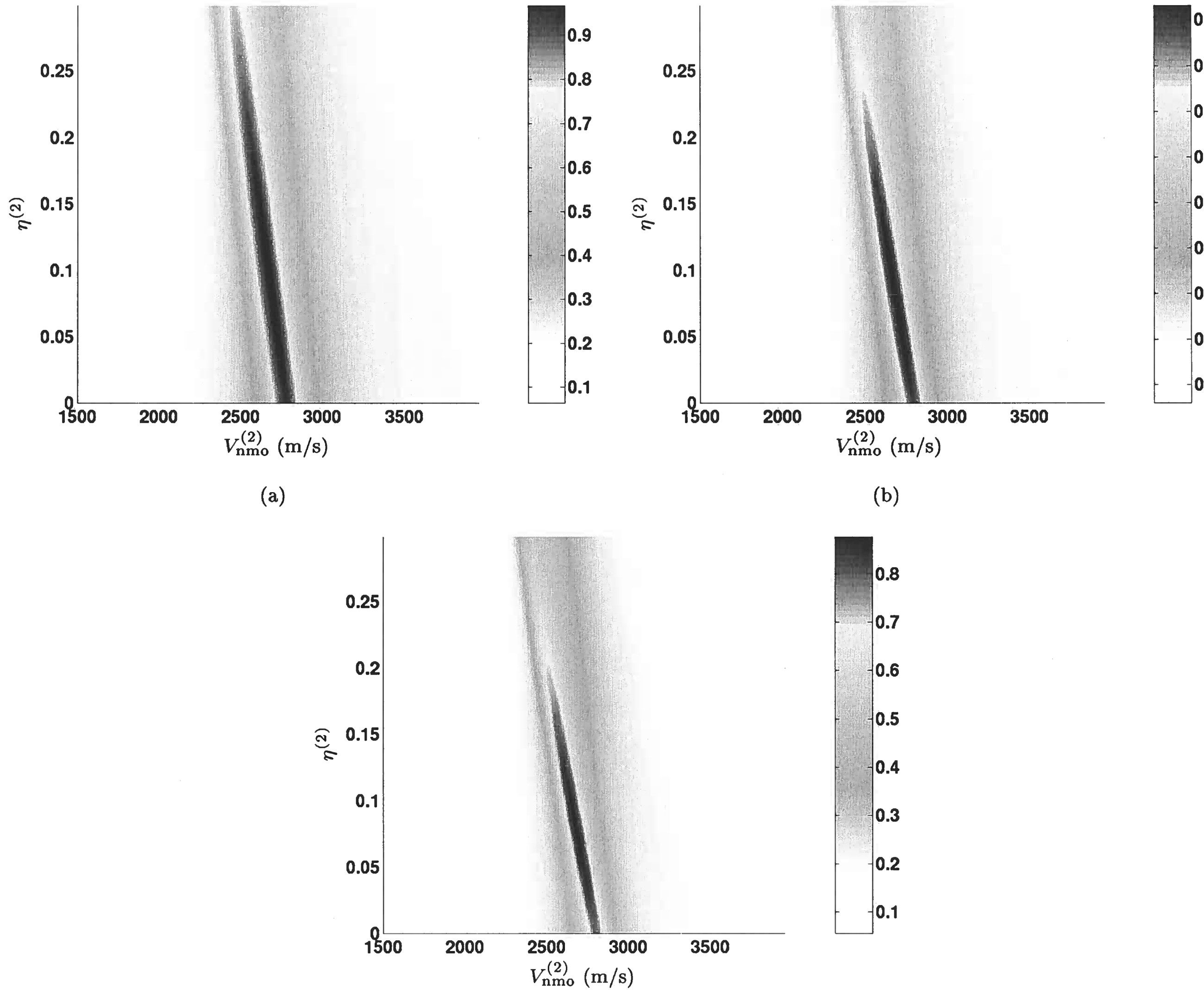

(a)

(b)

(c)

Figure 3. Semblance scans over $V_{\rm nmo}^{(2)}$ and $\eta^{(2)}$ computed from equation (9) for the following offset-to-depth ratios: (a) x/z=2; (b) x/z=2.5; (c) x/z=3. The model is the same as that in Figure 2; the parameters φ, $V_{\rm nmo}^{(1)}$, $\eta^{(1)}$, and $\eta^{(3)}$ are fixed at the correct values.

5 FIELD-DATA EXAMPLE

We applied the moveout inversion algorithm to wide-azimuth data acquired at Weyburn Field located in the Williston basin in Canada. This multicomponent data set was processed and interpreted by the Reservoir Characterization Project at the Colorado School of Mines with the main goal of dynamic monitoring of the CO_2 flood in the fractured reservoir. Jenner (2001) identified the presence of laterally varying azimuthal anisotropy at the reservoir level by computing the interval P-wave NMO ellipses and performing azimuthal AVO (amplitude variation with offset) analysis. The azimuthal dependence of the P-wave signatures in the overburden was found to be much less pronounced (Jenner, 2001).

The most reliable indicator of azimuthal anisotropy is shear-wave splitting at near-vertical incidence, which was studied at Weyburn Field by Cardona (2002). Comparison of the S-wave polarization directions with the orientation of the NMO ellipse allowed him to discriminate between different anisotropic symmetries at the

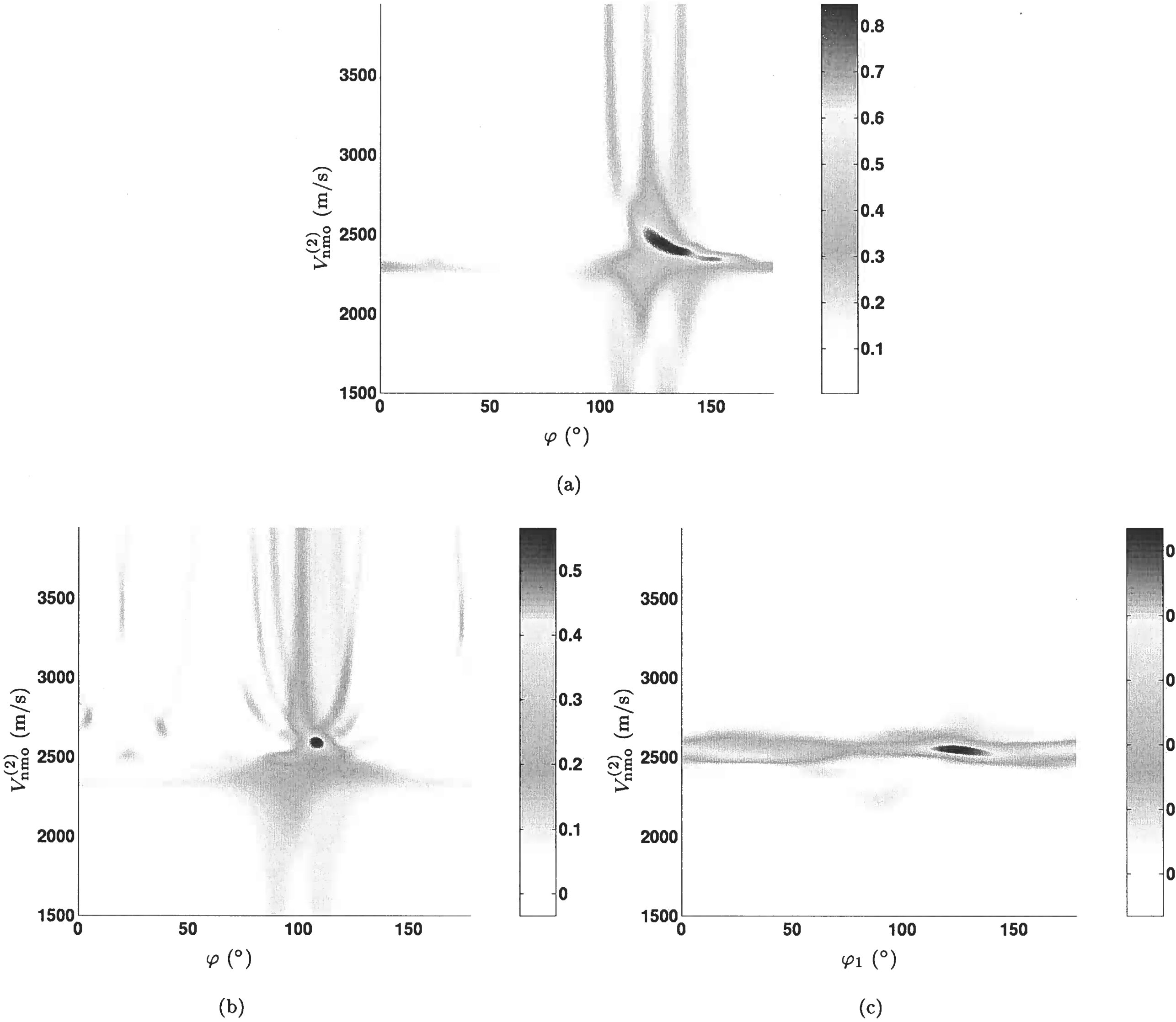

(a)

(b)

(c)

Figure 6. Semblance scans for the reflection from the bottom of a model composed of two layers with equal thickness. The orthorhombic layer from Figure 2 is overlain by (a) VTI layer with $V_{\text{nmo}} = 2158$ m/s and $\eta = 0.196$; (b), (c) orthorhombic layer with a different orientation of the symmetry planes ($\varphi = 90°$) and the parameters $V_{\text{nmo}}^{(1)} = 2156$ m/s, $V_{\text{nmo}}^{(2)} = 2534$ m/s, $\eta^{(1)} = 0.398$, $\eta^{(2)} = 0.211$ and $\eta^{(3)} = 0.193$. The parameter estimation was performed using equation (11) for plot (b) and equation (12) for plot (c).

ner than half the dominant wavelength, which is below the vertical resolution of any traveltime method. In his estimation of the interval NMO ellipses, Jenner (2001) had to combine the reservoir with some underlying beds into a single coarse layer.

Still, our methodology can be used to improve the velocity model of the overburden, which consists of the four main horizons marked in Figure 8. Adam et al. (2002) carried out anisotropic inversion of 3D walkaway VSP (vertical seismic profiling) data acquired above the reservoir and concluded that the results can be largely explained by a VTI model. The shear-wave splitting observed by Cardona (2002) above the Lower Vanguard, however, is indicative of azimuthal anisotropy in the upper part of the overburden.

The 3D nonhyperbolic moveout inversion [using equation (11) for $\eta(\alpha)$] was applied to P-waves collected into two 9x9 superbins, one of which is centered at CMP 10103 and the other at CMP 10829. (Figure 8). Clearly, anisotropy is quite substantial through most of the overburden, with η values reaching 0.25 for the reflection from the deepest interface (the Mississippian unconformity). The semblance scans in Figure 9 demonstrate that the resolution in $\eta^{(2)}$ (and the other anellip-

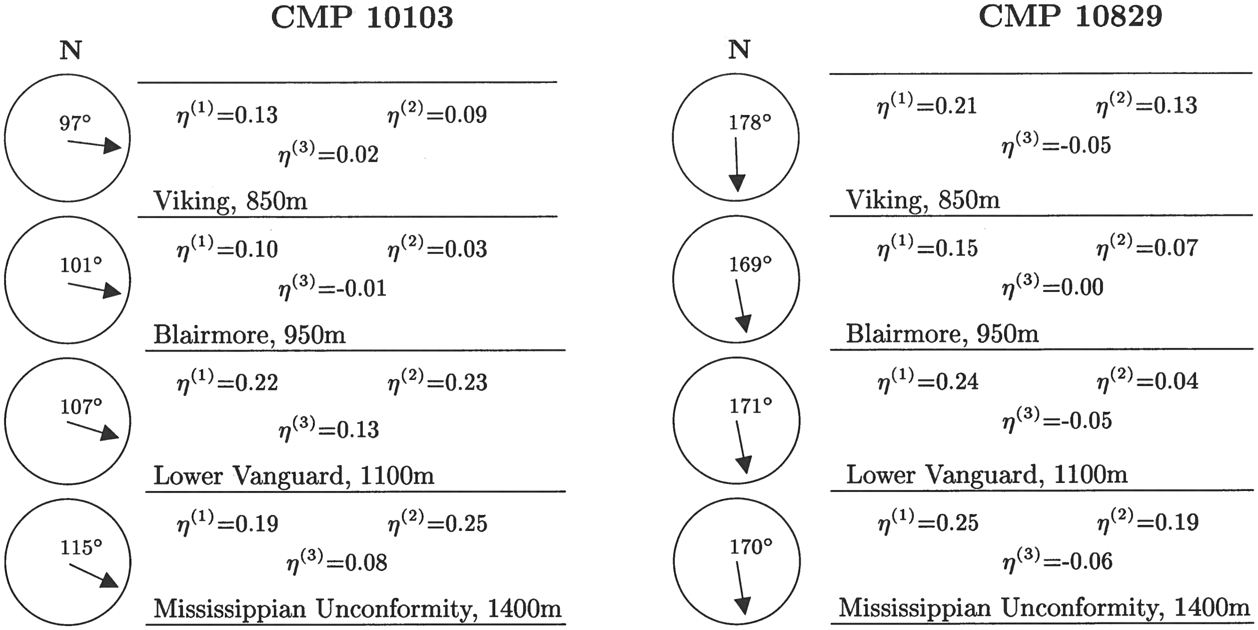

Figure 8. Final inversion results for the reflections from (a) the Viking horizon, the maximum offset-to-depth ratio $x/z = 2.5$; (b) the Blairmore, $x/z = 2.0$; (c) the Lower Vanguard, $x/z = 1.9$; and (d) the Mississippian Unconformity, $x/z = 1.8$. The arrows mark the estimated direction of the semi-major axis of the NMO ellipse; the number by each arrow is the azimuth of the axis with respect to the north.

the Lower Vanguard contributes to the nonhyperbolic moveout of the Mississippian Unconformity event, but the symmetry within this interval may be close to VTI, which agrees with the results of Cardona (2002).

6 DISCUSSION AND CONCLUSIONS

Long-spread moveout of P-waves in orthorhombic media with a horizontal symmetry plane is governed by the azimuth φ of one of the vertical symmetry planes, the symmetry-plane NMO velocities $V_{\rm nmo}^{(1)}$ and $V_{\rm nmo}^{(2)}$, and the anellipticity parameters $\eta^{(1)}$, $\eta^{(2)}$, and $\eta^{(3)}$. Here, we apply a modified version of the nonhyperbolic moveout equation of Alkhalifah and Tsvankin (1995) to invert for these six parameters from wide-azimuth, long-offset data. The inversion algorithm is organized as a three-step procedure that starts with estimation of the NMO ellipse on conventional-length spreads using the method of Grechka and Tsvankin (1999a). After evaluating the azimuths of the symmetry planes and the velocities $V_{\rm nmo}^{(1)}$ and $V_{\rm nmo}^{(2)}$ from the NMO ellipse, we perform 2D inversion for the parameters $\eta^{(1)}$ and $\eta^{(2)}$ in the symmetry-plane directions. Then the obtained initial values of the moveout parameters are used in a global semblance search that operates with data for all available offsets and azimuths.

Although our moveout equation is based on the analogy with VTI media, which is not strictly valid in off-symmetry directions, the inversion provides sufficiently accurate results for a single horizontal layer of orthorhombic symmetry. Since the azimuth φ and the velocities $V_{\rm nmo}^{(1)}$ and $V_{\rm nmo}^{(2)}$ define the NMO ellipse, they are constrained better than are the parameters $\eta^{(1)}$, $\eta^{(2)}$, and $\eta^{(3)}$, which make a significant contribution to the traveltimes only for large offset-to-depth ratios (e.g., x/z exceeding two). As is the case for VTI media, estimation of the anellipticity parameters is hampered by the tradeoffs between $V_{\rm nmo}^{(1)}$ and $\eta^{(1)}$, and between $V_{\rm nmo}^{(2)}$ and $\eta^{(2)}$ (Grechka and Tsvankin, 1998b). These tradeoffs can cause substantial uncertainties in $\eta^{(1)}$ and $\eta^{(2)}$ if the data are contaminated by correlated noise and the maximum ratio x/z is smaller than 2.5. The least-constrained model parameter is $\eta^{(3)}$ because it influences only long-spread moveout in off-symmetry directions.

Although the moveout equation used here was originally designed for homogeneous media, it provides a close approximation for P-wave nonhyperbolic moveout in layered azimuthally anisotropic models with a uniform direction of the vertical symmetry planes. The accuracy of estimating the symmetry-plane azimuth φ, however, is reduced if an orthorhombic layer is overlaid by a relatively thick azimuthally isotropic (e.g., VTI) overburden.

If the orientation of the symmetry planes varies with depth, our moveout equation is less accurate, and the semblance values become smaller. Still, the time residuals after the inversion may be relatively small (less than 1% of the zero-offset time in the example given

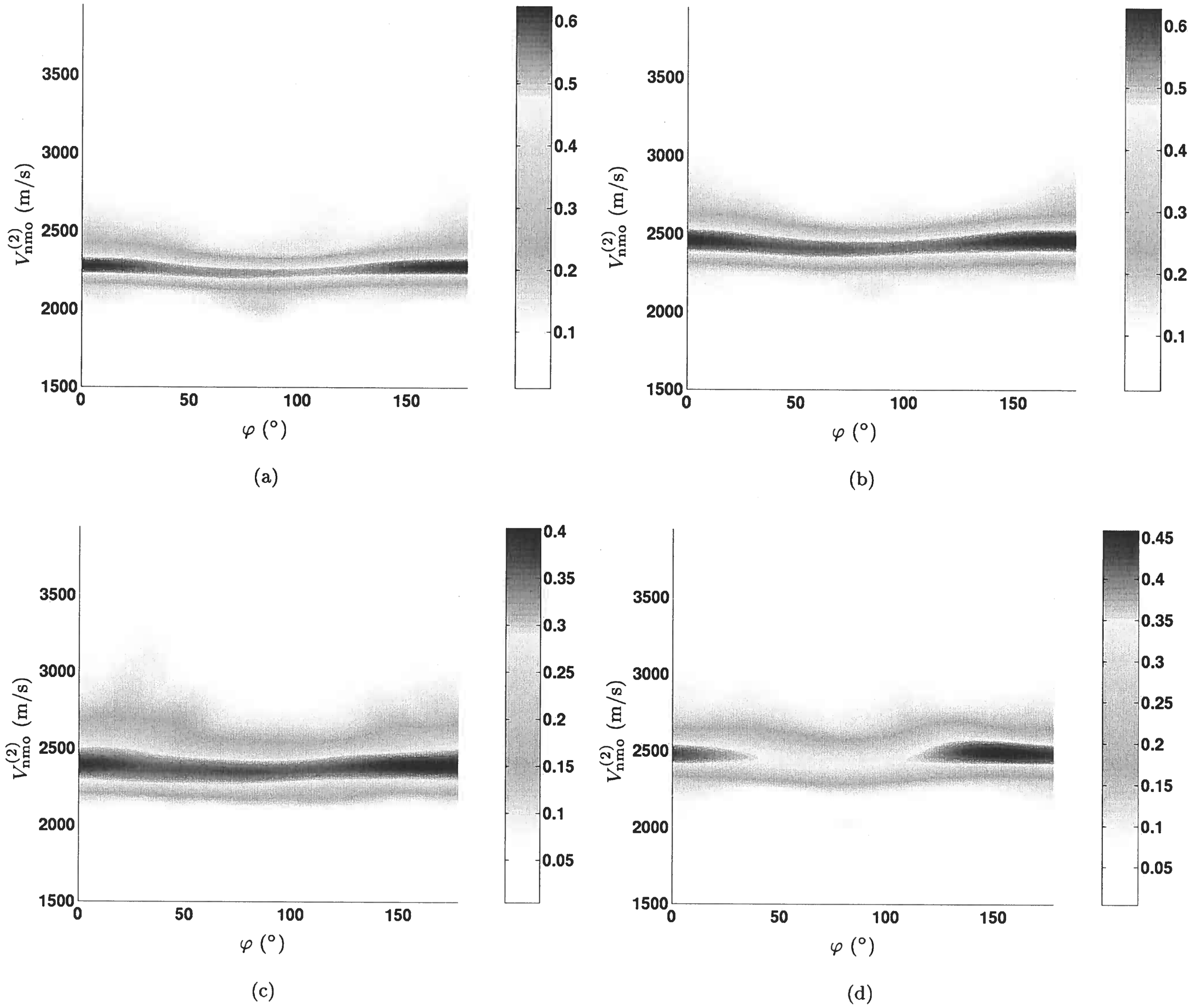

Figure 10. Semblance scans over $V_{\mathrm{nmo}}^{(2)}$ and φ at CMP 10103 for the reflections from (a) the Viking horizon; (b) the Blairmore; (c) the Lower Vanguard; and (d) the Mississipian Uncoformity. The azimuth φ is measured counterclockwise from the survey's x-axis, which points eastward.

imuths of the off-trend fracture sets in the area. Also, our conclusion that the magnitude of azimuthal anisotropy is significant mostly in the shallow part of the section (above the Lower Vanguard horizon) is in agreement with the shear-wave splitting analysis of Cardona (2002). A more detailed interpretation of the inversion results is impossible without layer-stripping the effective values of the anellipticity parameters obtained from nonhyperbolic moveout. The interval parameter estimation, which is currently under development, should allow us to not only remove the influence of vertical heterogeneity on nonhyperbolic moveout, but also treat layered models with depth-varying orientation of the symmetry planes.

It should be emphasized that while fracture characterization and lithology discrimination require the interval anellipticity parameters in the horizon of interest, the effective values of $\eta^{(1,2,3)}$ and $V_{\mathrm{nmo}}^{(1,2)}$ are sufficient for several important applications in seismic processing. For example, Xu and Tsvankin (2004) develop a correction for geometrical spreading in layered orthorhombic media based on equation (9) with the effective move-

velocity variation: Theory and a case study: Geophysics, **64**, 1202–1218.

Grechka, V., and Tsvankin, I., 1999b, 3-D moveout velocity analysis and parameter estimation for orthorhombic media: Geophysics, **64**, 820–837.

Grechka, V., Pech, A., and Tsvankin, I., 2002, Multicomponent stacking-velocity tomography for transversely isotropic media: Geophysics, **67**, 1564–1574.

Grechka, V., Tsvankin, I., and Cohen, J. K., 1999, Generalized Dix equation and analytic treatment of normal-moveout velocity for anisotropic media: Geophys. Prosp., **47**, 117–148.

Jenner, E., 2001, Azimuthal anisotropy of 3-D compressional wave seismic data, Weyburn field, Saskachewan, Canada: PhD thesis, Colorado School of Mines.

Pech, A., and Tsvankin, I., 2004, Quartic moveout coefficient for a dipping azimuthally anisotropic layer: Geophysics, in print.

Pech, A., Tsvankin, I., and Grechka, V., 2003, Quartic moveout coefficient: 3D description and application to tilted TI media: Geophysics, **68**, 1600–1610.

Sayers, C. M., and Ebrom, D. A., 1997, Seismic traveltime analysis for azimuthally anisotropic media: Theory and experiment: Geophysics, **36**, 1570–1582.

Thomsen, L., 1986, Weak elastic anisotropy: Geophysics, **51**, 1954–1966.

Toldi, J., Alkhalifah, T., Berthet, P., Arnaud, J., Williamson, P., and Conche, B., 1999, Case study of estimation of anisotropy: The Leading Edge, **18**, no. 5, 588–594.

Tsvankin, I., 1997, Anisotropic parameters and P-wave velocity for orthorhombic media: Geophysics, **62**, 1292–1309.

Tsvankin, I., 2001, Seismic signatures and analysis of reflection data in anisotropic media: Elsevier Science Publ. Co., Inc.

Tsvankin, I., and Thomsen, L., 1994, Nonhyperbolic reflection moveout in anisotropic media: Geophysics, **59**, 1290–1304.

Xu, X., and Tsvankin, I., 2004, Geometrical spreading correction for P-waves in azimuthally anisotropic media: CWP Project Review.

Xu, X., Tsvankin, I., and Pech, A., 2003, Analytic description of geometrical spreading in azimuthally anisotropic media: CWP Project Review, 40–47.

APPENDIX A: NOTATION FOR ORTHORHOMBIC MEDIA

Seismic inversion and processing for orthorhombic media (see Figure 1) can be facilitated by combining the stiffness coefficients in a way that simplifies analytic description of seismic signatures. The identical form of the Christoffel equation in the symmetry planes of orthorhombic and TI media allowed Tsvankin (1997) to introduce a notation based on the same principle as Thomsen (1986) parameters for vertical transverse isotropy. This notation contains two reference velocities (the vertical velocities of the P-wave and one of the split S-waves) and seven dimensionless anisotropic parameters defined in the symmetry planes by analogy with the VTI coefficients ϵ, δ, and γ:

- V_{P0} – the P-wave vertical velocity:

$$V_{P0} \equiv \sqrt{\frac{c_{33}}{\rho}} \quad (\rho \text{ is the density}). \tag{A1}$$

- V_{S0} – the vertical velocity of the S-wave polarized in the x_1-direction:

$$V_{S0} \equiv \sqrt{\frac{c_{55}}{\rho}}. \tag{A2}$$

- $\epsilon^{(2)}$ – the VTI parameter ϵ in the $[x_1, x_3]$ symmetry plane (the superscript "2" refers to the orthogonal axis x_2):

$$\epsilon^{(2)} \equiv \frac{c_{11} - c_{33}}{2\, c_{33}}. \tag{A3}$$

- $\delta^{(2)}$ – the VTI parameter δ in the $[x_1, x_3]$ plane:

$$\delta^{(2)} \equiv \frac{(c_{13} + c_{55})^2 - (c_{33} - c_{55})^2}{2\, c_{33}\,(c_{33} - c_{55})}. \tag{A4}$$

- $\gamma^{(2)}$ – the VTI parameter γ in the $[x_1, x_3]$ plane :

$$\gamma^{(2)} \equiv \frac{c_{66} - c_{44}}{2\, c_{44}}. \tag{A5}$$

- $\epsilon^{(1)}$ – the VTI parameter ϵ in the $[x_2, x_3]$ symmetry plane:

$$\epsilon^{(1)} \equiv \frac{c_{22} - c_{33}}{2\, c_{33}}. \tag{A6}$$

- $\delta^{(1)}$ – the VTI parameter δ in the $[x_2, x_3]$ plane:

$$\delta^{(1)} \equiv \frac{(c_{23} + c_{44})^2 - (c_{33} - c_{44})^2}{2\, c_{33}\,(c_{33} - c_{44})}. \tag{A7}$$

- $\gamma^{(1)}$ – the VTI parameter γ in the $[x_2, x_3]$ plane:

$$\gamma^{(1)} \equiv \frac{c_{66} - c_{55}}{2\, c_{55}}. \tag{A8}$$

- $\delta^{(3)}$ – the VTI parameter δ in the $[x_1, x_2]$ plane (x_1 plays the role of the symmetry axis):

$$\delta^{(3)} \equiv \frac{(c_{12} + c_{66})^2 - (c_{11} - c_{66})^2}{2\, c_{11}\,(c_{11} - c_{66})}. \tag{A9}$$

Tsvankin (1997, 2001) shows that this notation provides a convenient description of phase and NMO velocities, reflection coefficients, and other signatures both within and outside the symmetry planes. Also, P-wave velocities and traveltimes (including reflection moveout) depend on just six parameters (V_{P0}, $\epsilon^{(1)}$, $\delta^{(1)}$, $\epsilon^{(2)}$, $\delta^{(2)}$, and $\delta^{(3)}$) and the orientation of the symmetry planes, rather than on nine coefficients in the conventional (c_{ij}) notation.

CWP-472P

The downward continuation approach to modeling and inverse scattering of seismic data in the Kirchhoff approximation

Maarten V. de Hoop

Center for Wave Phenomena, Colorado School of Mines, Golden CO 80401-1887 USA

ABSTRACT

In this paper we use methods from microlocal analysis and the theory of Fourier integral operators, to study the downward continuation approach to seismic inverse scattering in the Kirchhoff approximation. Furthermore, we explain, analyze and connect different notions and processing procedures that appear in seismic imaging-inversion. These are 'downward continuation' with the 'double-square-root equation', 'controlled illumination', 'common-focus-point technology', (wave-equation) 'angle transform', and the 'Bremmer coupling series'.

Key words: seismic inversion, Kirchhoff approximation, downward continuation, microlocal analysis

1 INTRODUCTION

In reflection seismology one places point sources and point receivers on the earth's surface. The source generates acoustic waves in the subsurface, that are reflected where the medium properties vary discontinuously. The recorded reflections that can be observed in the data are used to reconstruct these discontinuities. This reconstruction is called seismic imaging-inversion.

The *first* key objective of this paper is to explain, analyze and connect different notions and processing procedures that occur in seismic imaging-inversion, in the framework of microlocal analysis. These are 'downward continuation' (Clay, 1978; Claerbout, 1985; Popvici, 1996), 'controlled illumination' (Rietveld, Berkhout and Wapenaar, 1992), 'common-focus-point technology' (Thorbecke, 1997), '(wave-equation) angle transform' (De Bruin et al. 1990; De Haas, 1992; Prucha, Biondi and Symes, 1999; Fomel and Prucha, 1999), 'Bremmer coupling series' (Mendel et al. 1981; De Hoop, 1996), and 'Kirchhoff approximation' (Bleistein et al. 2001). From a mathematical perspective this paper is a follow-up and an application of the work by Stolk and De Hoop (2001) on the downward continuation approach to seismic inverse scattering in the Born approximation.

Seismic data are commonly modeled by a high-frequency single scattering approximation. In what follows, we distinguish the vertical coordinate $z \in \mathbb{R}$ from the horizontal coordinates $x \in \mathbb{R}^{n-1}$ and write $(x, z) \in \mathbb{R}^n$. In these coordinates the scalar acoustic wave equation is given by

$$Pu = f\,, \qquad P = c(x,z)^{-2}\frac{\partial}{\partial t}^{2} + \sum_{j=1}^{n-1} D_{x_j}^2 + D_z^2\,, \quad (1)$$

where $D_x = -\mathrm{i}\frac{\partial}{\partial x}, D_z = -\mathrm{i}\frac{\partial}{\partial z}$. The equation is considered for $(x, z) \in \mathbb{R}^n$, and t in an open time interval $(0, T)$.

By Duhamel's principle, a causal solution operator for the inhomogeneous equation (1) is given by

$$u(x,z,t) = \int_0^t \int G(x,z,t-t_0,x_0,z_0) f(x_0,z_0,t_0)\, \mathrm{d}x_0 \mathrm{d}z_0 \mathrm{d}t_0, \quad (2)$$

where (when the coefficient c is in C^∞) G defines a Fourier integral operator with canonical relation that is essentially a union of bicharacteristics. The source f is a distribution in $\mathcal{E}'(X_0 \times (0,T))$ where X_0 is a bounded open subset of $\mathbb{R}^n$. The kernel of the Fourier integral operator can be written as a sum of contributions

$$G(x,z,t,x_0,z_0) = \sum_{j \in J} \int_{\mathbb{R}^{N(i)}} a^{(j)}(x,z,t,x_0,z_0,\theta) \exp[\mathrm{i}\phi^{(j)}(x,z,x_0,z_0,t,\theta)]\, \mathrm{d}\theta, \quad (3)$$

where the $\phi^{(j)}$ are non-degenerate phase functions and the $a^{(j)}$ are suitable symbols, see section 4.2.1 and chapter 5 in Duistermaat (1996); J is a finite set. Away from endpoint caustics, the only phase variable is frequency, $\theta = \tau$, and the phase function takes the form $\phi^{(m)} = \tau(T^{(m)}(x,z,x_0,z_0) - t)$, singularities. The perturbation in G is given by (see e.g. Beylkin (1985))

$$\delta G(z_r, r, t, z_s, s) = \int_{\mathbb{R}_+ \times \mathbb{R}^{n-1}} \int_0^t G(z_r, r, t - t_0, z_0, x_0)\, 2c_0^{-3}(z_0, x_0)\delta c(z_0, x_0) \times \partial_{t_0}^2 G(z_0, x_0, t_0, z_s, s)\, \mathrm{d}t_0 \mathrm{d}z_0 \mathrm{d}x_0, \tag{7}$$

where both $s, r \in \mathbb{R}^{n-1}$. The Born modeling map F is then defined through (7) as the map from δc to δG evaluated at the *acquisition surface*, here $z_r = z_s = z = 0$. We assume that the acquisition manifold Y, which contains the set of points (s, r, t) used in the acquisition, is a bounded open subset of $\mathbb{R}^{2n-2} \times \mathbb{R}_+$. Since Y is bounded and the waves propagate with finite speed we may assume that δc is supported in a bounded open subset X of $\mathbb{R}_+ \times \mathbb{R}^{n-1}$. Furthermore, we assume that $\overline{X} \cap \{z = 0\} = \emptyset$.

To ensure that δG defines a continuous map from $\mathcal{E}'(X)$ to $\mathcal{D}'(\mathbb{R}^n \times \mathbb{R}^n \times (0, T))$, and that the restriction of δG to Y is a Fourier integral, operator we make the following assumption on c_0

Assumption 1. There are no rays from $(0, s)$ to $(0, r)$ with travel time t such that $(s, r, t) \in Y$. For all ray pairs connecting $(0, r)$ via some $(z, x) \in X$ to $(0, s)$ with total time t such that $(s, r, t) \in Y$, the rays intersect the plane $z = 0$ transversally at r and s.

We also assume that rays from such a point $(z, x) \in X$ intersect the surface $z = 0$ only once, because all reflections must come from the subsurface $z > 0$. The first part of the assumption excludes rays that scatter over π; the second part of the assumption excludes rays grazing the plane $z = 0$. Concerning the second part, strictly only caustics grazing the plane $z = 0$ have to be excluded. We have

Theorem 2.1. (Rakesh, 1988; ten Kroode, 1998) With Assumption 1 the map F is a Fourier integral operator $\mathcal{D}'(X) \to \mathcal{D}'(Y)$ with canonical relation

$$\begin{aligned} &\{(\eta_x(t_\mathrm{s}, z, x, \beta, \tau), \eta_x(t_\mathrm{r}, z, x, \alpha, \tau), t_\mathrm{s} + t_\mathrm{r}, \eta_\xi(t_\mathrm{s}, z, x, \beta, \tau), \eta_\xi(t_\mathrm{r}, z, x, \alpha, \tau), \tau; z, x, \zeta, \xi) \mid \\ &\qquad t_\mathrm{s}, t_\mathrm{r} > 0,\ \eta_z(t_\mathrm{s}, z, x, \beta, \tau) = \eta_z(t_\mathrm{r}, z, x, \alpha, \tau) = 0,\ (\zeta, \xi) = -\tau c_0(z, x)^{-1}(\alpha + \beta), \\ &\qquad\qquad (z, x, \alpha, \beta, \tau) \in \text{ subset of } X \times (S^{n-1})^2 \times \mathbb{R}\backslash 0\} \subset T^*\mathbb{R}^{2n-1}_{(s,r,t)} \times T^*\mathbb{R}^n_{(z,x)}. \end{aligned} \tag{8}$$

Assumption 1 is microlocal. One can identify the set of points $(s, r, t, \sigma, \rho, \tau) \in T^*Y\backslash 0$ where this assumption is violated. If the symbol $\psi = \psi(s, r, t, \sigma, \rho, \tau)$ vanishes on a neighborhood of this set, then the composition ψF of the pseudodifferential cutoff $\psi = \psi(s, r, t, D_s, D_r, D_t)$ with F is a Fourier integral operator as in the theorem.

Kirchhoff approximation

We make use of the above insights in the development, here, of the theory for seismic modeling and inverse scattering in the downward continuation approach (Claerbout, 1985) rather than the reverse time approach, and in the Kirchhoff approximation (Bleistein et al. 2001) rather than in the Born approximation. We discuss the Kirchhoff approximation in this section and integrate it in the downward continuation approach to modeling seismic data in the next two sections.

Typically, in the Kirchhoff approximation we assume δc to be a conormal distribution representative of interfaces reflecting waves off sedimentary layers, faults and so on. Let

$$\kappa :\ (z, x) \mapsto (\underbrace{z'(z, x)}_{\kappa_1(z,x)}, \underbrace{x'(z, x)}_{\kappa_2(z,x)}), \tag{9}$$

be a coordinate transformation such that a reflecting interface, Σ say, is given by the zero level set, $z'(z, x) = 0$; thus (z', x') are 'interface normal' coordinates. The acoustic Kirchhoff approximation (Bleistein et al. 2001, E.6.13, E.8.17, 5.1.45-5.1.46), (Stolk and De Hoop, 2002, Thm. 3.6.1) can be written in the form

$$\begin{aligned} \delta G(z_r, r, t, z_s, s) = \int_0^t \int & G(z_r, r, t - t_0, z(z', x'), x(z', x'))\, 2\partial_{t_0} R(z', x', D_{x'}, D_{t_0}) \\ & G(z(z', x'), x(z', x'), t_0, z_s, s) \underbrace{\left|\det \frac{\partial(z, x)}{\partial(z', x')}\right| \left\|\frac{\partial z'}{\partial(z, x)}\right\| \delta(z')\mathrm{d}z'\mathrm{d}x'}_{\left\|\frac{\partial z'}{\partial(z, x)}\right\| \delta(z'(z, x))\, \mathrm{d}z\mathrm{d}x}\, \mathrm{d}t_0. \end{aligned} \tag{10}$$

Here, we assume the presence of a single interface but the extension to multiple interfaces is straightforward. In expression (10), R is a pseudodifferential operator. Its principal symbol, $r = r(z', x', \xi', \tau)$ say, is given by the product of the reflection coefficient

$$r_0(0, x', \xi', \tau) = \frac{\sqrt{\frac{1}{c_1^2} - \tau^{-2}\|\xi'\|^2} - \sqrt{\frac{1}{c_2^2} - \tau^{-2}\|\xi'\|^2}}{\sqrt{\frac{1}{c_1^2} - \tau^{-2}\|\xi'\|^2} + \sqrt{\frac{1}{c_2^2} - \tau^{-2}\|\xi'\|^2}}, \tag{11}$$

Changing variables of integration, i.e. $t_0 \mapsto t_0' = t_0 - \bar{t}_0$, (14) can be written in the form of an integral operator acting on a distribution,

$$\delta G(0,r,t,0,s) = \int_{\mathbb{R}_+}\int_{\mathbb{R}_+}\left\{\int_{\mathbb{R}}\int_{\mathbb{R}^{n-1}}\int_{\mathbb{R}^{n-1}}\left(\int_{\mathbb{R}_+} G(0,r,t-t_0'-\bar{t}_0,z,x) \times G(\bar{z},\bar{x},\bar{t}_0,0,s)\,\mathrm{d}\bar{t}_0\right)\right.$$
$$\left. \times\, 2\partial_{t_0} R_1(z,x,t_0',\bar{z},\bar{x}) \left\| \frac{\partial z'}{\partial(z,x)} \right\| \delta(z'(z,x))\,\mathrm{d}\bar{x}\,\mathrm{d}x\,\mathrm{d}t_0' \right\}\mathrm{d}\bar{z}\mathrm{d}z. \tag{15}$$

Using the reciprocity relation of the time-convolution type for the Green's function, we arrive at the integral representation

$$\delta G(0,r,t,0,s) = 2\partial_t \int_{\mathbb{R}_+}\int_{\mathbb{R}_+}\left\{\int_{\mathbb{R}^{n-1}}\int_{\mathbb{R}^{n-1}}\int_{\mathbb{R}}\left(\int_0^{t-t_0} G(0,r,t-t_0-\bar{t}_0,z,x) \times G(0,s,\bar{t}_0,\bar{z},\bar{x})\,\mathrm{d}\bar{t}_0\right)\right.$$
$$\left. \times\, R_1(z,x,t_0,\bar{z},\bar{x}) \left\| \frac{\partial z'}{\partial(z,x)} \right\| \delta(z'(z,x))\,\mathrm{d}\bar{x}\,\mathrm{d}x\,\mathrm{d}t_0 \right\}\mathrm{d}\bar{z}\mathrm{d}z. \tag{16}$$

The associated operator kernel appears to propagate singularities from two different scattering points, $(\bar{z},\bar{x})$ and (z,x) to the surface at $z = 0$.

Microlocally, the extension $\widetilde{R}$ with kernel $\widetilde{R}(z',x',t_0-\bar{t}_0,\bar{z}',\bar{x}')$ of the reflection operator R with kernel $R = R(z',x',t_0-\bar{t}_0,\bar{x}')$ can be thought of as

$$\widetilde{R}(z',x',t_0-\bar{t}_0,\bar{z}',\bar{x}') \sim (2\pi)^{-(n+1)} \int r(z',x',\xi',\tau) \times \exp[\mathrm{i}((z'-\bar{z}')\zeta' + \langle (x'-\bar{x}'),\xi'\rangle + (t_0-\bar{t}_0)\tau)]\,\mathrm{d}(\zeta',\xi',\tau)$$
$$= \delta(z'-\bar{z}')R(z',x',t_0-\bar{t}_0,\bar{x}'). \tag{17}$$

This implies that

$$\widetilde{R}(z',x',t_0-\bar{t}_0,\bar{z}',\bar{x}')\,\delta(z') \sim R(0,x',t_0-\bar{t}_0,\bar{x}')\,\delta(z')\delta(\bar{z}'),$$

where the product of δ's is to be interpreted as a tensor product. Subject to the assumption that $\frac{\partial\kappa_1}{\partial z} \neq 0$ (cf. (9)), we now write the solution to $z'(z,x) = 0$ as $z = \boldsymbol{z}(x)$. Then

$$\delta(\kappa_1(z,x)) = \left|\frac{\partial\kappa_1}{\partial z}\right|^{-1}_{z=\boldsymbol{z}(x)} \delta(z - \boldsymbol{z}(x)),$$

and similarly for $\delta(\kappa_1(\bar{z},\bar{x}))$.

Substituting the change of coordinates (9), yields

$$R_1(z,x,t_0-\bar{t}_0,\bar{z},\bar{x})\delta(z'(z,x))$$
$$\sim (2\pi)^{-n} \int r(0,\kappa_2(z,x),\xi',\tau)\exp[\mathrm{i}(\langle\kappa_2(z,x)-\kappa_2(\bar{z},\bar{x}),\xi'\rangle + (t_0-\bar{t}_0)\tau)]\,\mathrm{d}(\xi',\tau)$$
$$\times\,(2\pi)^{-1}\int \exp[\mathrm{i}(-\kappa_1(\bar{z},\bar{x}))\zeta']\,\mathrm{d}\zeta'\;\delta(\kappa_1(z,x))$$
$$= (2\pi)^{-n}\int r(0,\kappa_2(\boldsymbol{z}(x),x),\xi',\tau)\left|\frac{\partial\kappa_1}{\partial z}\right|^{-1}_{z=\boldsymbol{z}(x)}\left|\frac{\partial\kappa_1}{\partial z}\right|^{-1}_{z=\boldsymbol{z}(\bar{x})}$$
$$\times\,\exp[\mathrm{i}(\langle\kappa_2(\boldsymbol{z}(x),x)-\kappa_2(\boldsymbol{z}(\bar{x}),\bar{x}),\xi'\rangle + (t_0-\bar{t}_0)\tau)]\,\mathrm{d}(\xi',\tau)\;\delta(z-\boldsymbol{z}(x))\delta(\bar{z}-\boldsymbol{z}(\bar{x})). \tag{18}$$

Let us analyze the contribution to the phase function,

$$\langle\underbrace{\kappa_2(\boldsymbol{z}(x),x)-\kappa_2(\boldsymbol{z}(\bar{x}),\bar{x})}_{\Phi(x,\bar{x})},\xi'\rangle,$$

that has the property that

$$\forall_{\xi'\neq 0}\;\exists_{k\in\{1,\ldots,n-1\}}\;\left\langle \left.\frac{\partial\Phi}{\partial x_k}\right|_{x=\bar{x}},\xi'\right\rangle \neq 0,$$

where

$$\frac{\partial\Phi}{\partial x_k} = \frac{\partial\kappa_2}{\partial x_k} + \frac{\partial\kappa_2}{\partial z}\frac{\partial z}{\partial x_k}, \quad \frac{\partial z}{\partial x_k} = -\left(\frac{\partial\kappa_1}{\partial z}\right)^{-1}\frac{\partial\kappa_1}{\partial x_k}.$$

Thus, (16) reduces to

$$\delta G(0,r,t,0,s) = 2\partial_t \int_{\mathbb{R}_+} \Big\{ \int_{\mathbb{R}^{n-1}} \int_{\mathbb{R}^{n-1}} \int_{\mathbb{R}} \Big(\int_0^{t-t_0} G(0,r,t-t_0-\bar{t}_0,z,x) \times G(0,s,\bar{t}_0,z,\bar{x})\,\mathrm{d}\bar{t}_0 \Big) \times R(z,x,t_0-\bar{t}_0,\bar{x})\delta(z-z_\Sigma)\,\mathrm{d}\bar{x}\,\mathrm{d}x\,\mathrm{d}t_0 \Big\} \mathrm{d}z \tag{23}$$

if the interface is at depth $z_\Sigma > 0$; see Figure 1 for an illustration of the kernel action.

Remark 2.4. In the flat interface case, we can invoke the Weyl calculus for symbols defined on $T^*\mathbb{R}^n_{(z,x)}$. Let r denote the principal part of the Weyl symbol associated with reflection operator R in (23); r is homogeneous of degree zero in (ξ,τ). Upon substituting $\xi = \tau p$ in $r = r(z,x,\xi,\tau)$, it follows that the dependence on τ drops out: $r = r(z,x,p,1)$. The kernel representation attains the form

$$R(z,x,t_0-\bar{t}_0,\bar{x}) = (2\pi)^{-n} \int \Big[r\Big(z, \frac{x+\bar{x}}{2}, p, 1\Big) + \text{l.o.t.}\Big] \times \exp[\mathrm{i}\langle (x-\bar{x}), p\rangle \tau] \exp[\mathrm{i}(t_0-\bar{t}_0)\tau]\, |\tau|^{n-1} \mathrm{d}(p,\tau), \tag{24}$$

which can be written as

$$R = \Lambda \mathrm{E} r + \text{l.o.t.}, \tag{25}$$

where Λ is a convolutional operator with symbol $|\tau|^{n-1}$, and E is the transform defined by

$$(\mathrm{E}r)(z,x,t,\bar{x}) = (2\pi)^{-(n-1)} \int \delta(t - \langle (x-\bar{x}), p\rangle)\, r\Big(z, \frac{x+\bar{x}}{2}, p, 1\Big)\, \mathrm{d}p. \tag{26}$$

In (24) or (26), inside the p-integral, we observe a separation of *midpoint*, $\frac{x+\bar{x}}{2}$, and *offset*, $x - \bar{x}$, variables. This representation is closely related to Gel'fand's plane-wave expansion. In fact, ΛE maps the Weyl reflection symbol to fictituous reflection data.

3 THE ONE-WAY WAVE EQUATIONS

In this section, we discuss the solution of the wave equation (1) in the background model ($c(z,x) = c_0(z,x)$) by evolution in one of the space variables (wave field extrapolation). This evolution problem is in general not well posed, but the propagation of the singularities of the solution can be obtained microlocally, when the propagation direction of the corresponding rays stays somewhat away from horizontal.

Singularities of solutions to the wave equation, that propagate with non-zero vertical velocity are described by a first order evolution equation in z. This follows from a well known factorization argument, see e.g. Taylor (1975) and is at the basis of the generalized Bremmer coupling series. In Stolk (in press) the approximation of solutions to the wave equation, by solutions to an evolution equation in z is discussed, for the acoustic case. Such an equation is called a one-way wave equation. We summarize the results we need for the upward/downward continuation approach to modeling seismic data.

To determine whether the velocity vector at some point of the ray is close to horizontal we use the angle with the vertical, defined to be in $[0,\pi/2]$ and given by $\tan(\theta) = \frac{\|\xi\|}{|\zeta|}$. Recall that the propagating singularities are microlocally in the characteristic set given by (4). Given a point (z,x,ξ,τ) with $\|\xi\| < c(z,x)^{-1}|\tau|$, there are two solutions ζ to (4), given by $\zeta = \pm b$, where $b = b(z,x,\xi,\tau)$ is defined by

$$b(z,x,\xi,\tau) = -\tau\sqrt{c(z,x)^{-2} - \tau^{-2}\xi^2}; \tag{27}$$

in seismology, b/τ is known as the *vertical slowness*. The sign is chosen such that $\zeta = \pm b$ corresponds to propagation with $\pm\frac{\mathrm{d}\eta_z}{\mathrm{d}t} > 0$. There is an angle (phase angle) associated with (z,x,ξ,τ), given by the solution $\theta \in [0,\pi/2]$ of the equation

$$\sin(\theta) = c(z,x)\|\tau^{-1}\xi\|. \tag{28}$$

When this angle is strictly smaller than $\pi/2$ along a ray segment, then the vertical velocity $\frac{\mathrm{d}\eta_z}{\mathrm{d}t}$ does not change sign, and the ray segment can be parameterized by z rather than time. The maximal z-interval such that $\arcsin(c(z,x)\|\tau^{-1}\xi\|) < \theta$ for given θ along the bicharacteristic (cf. (6)) determined by the initial values $(z,x,\pm b,\xi,\tau)$, with $(\pm b,\xi) = -\tau c(z,x)^{-1}\alpha$, will be denoted by

$$(z_{\min,\pm}(z,x,\xi,\tau,\theta), z_{\max,\pm}(z,x,\xi,\tau,\theta)). \tag{29}$$

We also define a subset

$$I_\theta = \{(z,x,t,\zeta,\xi,\tau) \mid \arcsin(c(z,x)\|\tau^{-1}\xi\|) < \theta, |\tau^{-1}\zeta| < C\} \subset T^*(\mathbb{R}^n \times \mathbb{R}_+), \tag{30}$$

where $c(z,x)^{-1} < C$.

[h]

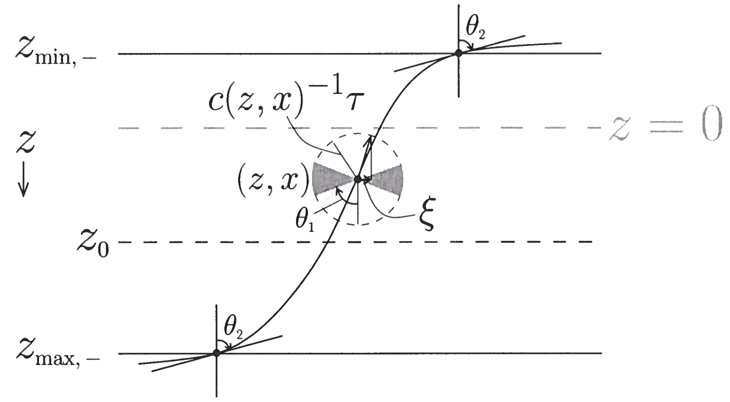

Figure 2. Illustration of θ_1, θ_2, the ψ_1 operator, and propagation of singularities.

The solution operator can also be written as a pseudodifferential cutoff, $\psi_1(z_0, z)$, applied prior to $G_{0,-}$ *,

$$G_-(z, z_0) = G_{0,-}(z, z_0)\psi_1(z_0, z). \tag{45}$$

We use the notation $\gamma(z, z_0, x_0, t_0, \xi_0, \tau)$ for the bicharacteristics of $P_{0,-}$ parameterized by z. In components, we write

$$\gamma(z, z_0, x_0, t_0, \xi_0, \tau) \quad = \quad (z, \gamma_x(z, z_0, x_0, \xi_0, \tau), \gamma_t(z, z_0, x_0, \xi_0, \tau) \; + \; t_0, -b(z, \gamma_x, \gamma_\xi, \tau), \gamma_\xi(z, z_0, x_0, \xi_0, \tau), \tau). \tag{46}$$

Remark 3.1. The operators $B_\pm$ are selfadjoint. It follows that $G_{0,-}(z, z_0)$ is unitary. We have that

$$G_-(z, z_0)^* G_-(z, z_0) = \psi_1(z_0, z)^* \psi_1(z_0, z), \tag{47}$$

and $G_-(z, z_0)^* G_-(z, z_0)$ is one microlocally where $\psi_1(z_0, z)$ is one.

Let the singularities in f be such that $\tau^{-1}\zeta > 0$ (corresponding to propagation direction $\frac{\partial \eta_z}{\partial t} < 0$). Consider u_- defined by (Duhamel's principle)

$$u_-(z, \cdot) = \int_z^\infty G_-(z, z_0)(-\tfrac{1}{2}\mathrm{i}Q_-(z_0))f(z_0, \cdot)\,\mathrm{d}z_0, \tag{48}$$

assuming also that $f = 0$ on a neighborhood of the plane given by z. We have that $Q_-^* u_-(z, \cdot) \equiv u(z, \cdot)$, where u is the solution to (1) with f replaced by $Q_-^{-1}\psi_1(z_0, z)Q_- f$. The contribution to the original Green's function $G(z, x, t - t_0, z_0, x_0)$ from upgoing propagating singularities thus follows to be (compare (2))

$$-\frac{1}{2}\mathrm{i}Q_-^*(z, x, D_x, D_t)G_- Q_-(z_0, x_0, D_{x_0}, D_{t_0}). \tag{49}$$

This is precisely the substitution to be made in (16) and (23).

4 MODELING IN THE KIRCHHOFF APPROXIMATION WITH THE DOWNWARD CONTINUATION APPROACH

We show that the Kirchhoff modeling operator can be written, modulo smoothing terms, in terms of solution operators to a one-way wave equation; in case of *horizontal* reflectors, this modeling operator can be written, modulo smoothing terms, in terms of downward/upward data continuation.

---

*The operator $\psi_1(z_0, z)$ is a (z_0, z)-family of pseudodifferential operators with symbol in $S^0_{\rho,1-\rho}(\mathbb{R}^n \times \mathbb{R}^n)$, such that the derivatives $\frac{\partial^{j+k}\psi_1}{\partial z_0^j \partial_z^k}$ are in $S^{(j+k)(1-\rho)}_{\rho,1-\rho}(\mathbb{R}^n \times \mathbb{R}^n)$ for $z \neq z_0$, where ρ can be any number satisfying $\frac{1}{2} < \rho < 1$ ((Stolk, in press; Stolk and De Hoop, 2003a)). For the theory of such operators, see Taylor (1981) and Hörmander (1985a).

Lemma 4.1. (Stolk and De Hoop, 2003a) $H(z, z_0)$ is a Fourier integral operator with canonical relation

$$\{(\Gamma(z, z_0, s, r, t, \sigma, \rho, \tau); s, r, t, \sigma, \rho, \tau) \,|(s, r, t, \sigma, \rho, \tau) \in T^*\mathbb{R}^{2n-1}_{(s,r,t)}\backslash 0, Z_{\min}(z, s, r, t, \sigma, \rho, \tau, \theta_2) < 0\}. \tag{60}$$

The operator L is a Fourier integral operator with canonical relation (56). The kernel of $H(0, z)$ admits microlocally an oscillatory integral representation with phase variables η_{0J} given by

$$(H(0, z))(s_0, r_0, t_0, s, r, t) = \\ (2\pi)^{-(2n-1+|I|)/2} \int A(z, y_0, \eta_{0J}, s, r, t) \exp[\mathrm{i}(S(z, y_{0I}, \eta_{0J}, s, r, t) + \langle \eta_{0J}, y_{0J}\rangle)]\, \mathrm{d}\eta_{0J}, \tag{61}$$

such that the principal part a of the amplitude A satisfies

$$|a(z, y_0, \eta_{0J}, s, r, t)| = \left| \frac{\partial(\sigma, \rho, \tau)}{\partial(y_{0I}, \eta_{0J})} \right|^{1/2} \tag{62}$$

with

$$(\sigma(z, y_{0I}, \eta_{0J}, s, r, t), \rho(z, y_{0I}, \eta_{0J}, s, r, t), \tau(z, y_{0I}, \eta_{0J}, s, r, t)) = -\frac{\partial S}{\partial(s, r, t)}(z, y_{0I}, \eta_{0J}, s, r, t) \tag{63}$$

in accordance with (59).

Scattering

We return to scattering problem described by (16) and (66) and Theorem 2.1. We will assume that the tangent vectors to the rays that connect source and receiver to a scattering point in X stay away some finite distance from horizontal. We make this precise by using some angle θ, $0 < \theta < \pi/2$, an angle with the vertical, in

Assumption 3. (DSR assumption (Stolk and De Hoop, 2001; Stolk and De Hoop, 2003a)) If $(z, x) \in X$ and $\alpha, \beta \in S^{n-1}$, $t_{\mathrm{s}}, t_{\mathrm{r}} > 0$ depending on (z, x, α, β) are such that $\eta_z(t_{\mathrm{s}}, z, x, \beta, \tau) = \eta_z(t_{\mathrm{r}}, z, x, \alpha, \tau) = 0$, then

$$c(z, x)^{-1} \frac{\partial \eta_z}{\partial t}(t, z, x, \beta, \tau) < -\cos(\theta), t \in [0, t_{\mathrm{s}}], \tag{64}$$

$$c(z, x)^{-1} \frac{\partial \eta_z}{\partial t}(t, z, x, \alpha, \tau) < -\cos(\theta), t \in [0, t_{\mathrm{r}}]. \tag{65}$$

The assumption is microlocal (and restricts to a *common* scattering point (z, x), see Figure 3(left)); given the background medium, a pseudodifferential cutoff can be applied to the data to remove microlocally the part of the data where Assumption 3 is violated.

Under Assumption 3 and the assumption that the medium perturbation (a conormal distribution) is supported outside a neighborhood of $z = 0$, the singular part of the modeled data is unchanged when G in (16) or (23) is replaced by (49).

Modeling operator in terms of the reflection operator kernel

Using (50) and (52) together with (49) in (23) yields the operator F_{K} defined by

$$F_{\mathrm{K}} = -\tfrac{1}{2}\partial_t LR \,:\, \delta(\cdot - z_\Sigma) \to -\tfrac{1}{2}\partial_t L(R\delta(\cdot - z_\Sigma)). \tag{66}$$

Modeling operator in terms of the Weyl symbol

Upon substituting (24) or (25) into (66), we obtain the equivalent map

$$F_{\mathrm{K}} = -\tfrac{1}{2}\partial_t \Lambda L \mathrm{E} r \,:\, \delta(\cdot - z_\Sigma) \to -\tfrac{1}{2}\partial_t \Lambda \int L\Big(\delta(\overset{t}{\cdot} - \langle(\overset{r}{\cdot} - \overset{s}{\cdot}), p\rangle)\, r\Big(\overset{z}{\cdot}, \frac{\overset{s}{\cdot} + \overset{r}{\cdot}}{2}, p, 1\Big) \delta(\overset{z}{\cdot} - z_\Sigma)\Big)\, \mathrm{d}p. \tag{67}$$

In the later analysis we consider the operator $-\frac{1}{2}\partial_t \Lambda L \mathrm{E}$ that maps functions of (z, x, p) to functions of (s, r, t).

Remark 4.2. In the Born approximation, essentially, r is p-independent, viz.,

$$r = \frac{c'}{c_0^3}$$

(cf. (22)). Then

$$\Lambda \mathrm{E} r = E_2 E_1 r,$$

5 RECONSTRUCTION

The inverse problem can be split into an imaging problem and an inverse scattering problem. For example, the depth z_Σ of an interface could be established by imaging (using, for example,the Born approximation). Once z_Σ is known (and, hence, the modeling no longer contains an integration over z), the operator $H(0, z_\Sigma)^*$ could be applied to the data, and as a consequence of Remark 3.1, the kernel of the reflection operator is obtained.

As mentioned below (67) we consider the operator $-\frac{1}{2}\partial_t \Lambda L E$ as the point of departure for developing an inverse scattering formula. The reconstruction of the symbol r given the background (c_0) is essentially done by applying the adjoint of this operator to the data d. We make use of the results for reconstruction in the Born approximation (Stolk and De Hoop, 2001; Stolk and De Hoop, 2003b).

Definition 5.1. Let L be as defined in (52), and let R denote the adjoint of E, given by

$$\mathrm{R} \;:\; g(z,s,r,t) \mapsto (\mathrm{R}g)(z,x,p) = \int_{\mathbb{R}^{n-1}} g(z, x - \tfrac{h}{2}, x + \tfrac{h}{2}, ph)\chi(z,x,h)\,\mathrm{d}h. \tag{71}$$

Here, $h \mapsto \chi(z,x,h)$ is a compactly supported cutoff function the support of which contains $h = 0$. We define the (wave-equation) angle transform, denoted by A_{WE}, as the composition of adjoints

$$A_{\mathrm{WE}} = \mathrm{R}L^*. \tag{72}$$

In the above, R is closely related to what seismologists call *beamforming*. In (Stolk and De Hoop, 2003b) the properties of A_{WE} (up to a time derivative) were analyzed; they are summarized in the following theorem. A map similar to A_{WE} was introduced in (De Bruin et al. 1990) for the purpose of imaging angle dependent reflection coefficients, see also (Prucha, Biondi and Symes, 1999). For each x, $(A_{\mathrm{WE}}d)(z,x,p)$ is a so-called *common-image-point gather.*

Theorem 5.2. (Stolk and De Hoop, 2003b) Suppose Assumption 3 holds. Let C_0 be an upper bound for c_0. Assume that

$$\|p\| < p_{\max} < \tfrac{1}{2}C_0^{-1}. \tag{73}$$

Then A_{WE} is a Fourier integral operator. Let C_1 be an upper bound for $\frac{\partial c_0^{-2}}{\partial x}$, C_2 an upper bound for c_0^{-1}. If in addition the function $h \mapsto \chi(z,x,h)$, contained in R_3, is supported in $B(0,d)$, where d depends on θ_2, C_0, C_1, C_2, then the canonical relation of A_{WE} corresponds to an invertible map from a subset of $T^*\mathbb{R}^{2n-1}_{(s,r,t)}$ to a subset of $T^*\mathbb{R}^{2n-1}_{(z,x,p)}$ that has nonempty intersection with the set $\vartheta = 0$ (where ϑ denotes the p-covector).

In L, the operator $H(0,z)$ contains an operator $\psi_2(0,z)$. To account for limited acquisition aperture, we introduced a smooth cutoff function $\psi_Y = \psi_Y(s,r,t)$ on Y that is zero near the boundary of Y. The key component operator in L^* is $H(0,z)^*$.

Remark 5.3. Through the convolution in (50), $H(0,z)^*$ represents the so-called
'double-focusing operator' (Thorbecke, 1997): It retrofocuses the data in source and receiver arrays. The reference to 'double' arises from the following observation: While replacing F in Theorem 2.1 by an operator (66) or (67) containing $H(0,z)$, we have 'uncoupled' (except in time) the source and receiver bicharacteristics in the canonical relation of L (cf. (56)) at the scattering point (z,x), see also Figure 3.

Remark 5.4. Data are modeled as $\delta G(0,r,t,0,s)$. Viewing the data as a function of r and t for fixed s yields what seismologists call a *shot record.* Shot records can be 'synthesized' to yield what seismologists call an areal shot record: Each shot record is convolved in time with a single time trace (fixed source location) out of the synthesis distribution, and subsequently the shot records are stacked (integrated) per common receiver location. The synthesis can be formulated as an operator acting on the data $\delta G(0,r,t,0,s)$ and is at the basis of *controlled illumination*, see Rietveld *et al.* (1992). (An example of controlled illumination is beamforming.) A particularly interesting choice of synthesis is obtained by requiring focus point (delta) illumination at the reflector depth. For a focus point at $(z,\bar{s})$, say this is achieved when the 'synthesis operator' is given by $G_{-,s}(0,z)^* Q^*_{-,s}(0)^{-1}$; indeed, the kernel of the composition $G_{-,s}(0,z)^* H(0,z)$ follows to be

$$\begin{aligned}
&\iint (G_-(0,z))^*(\bar{s},\bar{t}-t,s)(H(0,z))(s,r,t,s_0,r_0,t_0)\,\mathrm{d}s\mathrm{d}t = \\
&\qquad \iiint (G_-(0,z))^*(\bar{s},\bar{t}-t,s)(G_-(0,z))(s,t-t_0-\bar{t}_0,s_0)\,\mathrm{d}s\mathrm{d}t\,(G_-(0,z))(r,\bar{t}_0,r_0)\,\mathrm{d}\bar{t}_0 \\
&\qquad\qquad = \int \delta(\bar{s}-s_0)\delta(\bar{t}-t_0-\bar{t}_0)(G_-(0,z))(r,\bar{t}_0,r_0)\,\mathrm{d}\bar{t}_0 = \delta(\bar{s}-s_0)\,(G_-(0,z))(r,\bar{t}-t_0,r_0),
\end{aligned} \tag{74}$$

which should be modified to include the cutoffs $\psi_1(z,0)^*\psi_1(z,0)$ of Remark 3.1.

we define

$$\varXi := \left|\frac{\partial(\zeta,\sigma,\rho)}{\partial(y_{0I},\eta_{0J})}\right|^{-1}\cdot\left|\frac{\partial(\sigma,\rho,\tau)}{\partial(y_{0I},\eta_{0J})}\right|_{t=\langle h,p\rangle} \quad \text{at } (z,s,r)=(z,x-\tfrac{1}{2}h,x+\tfrac{1}{2}h);$$

note that $\varXi = \left|\frac{\partial \Upsilon}{\partial\zeta}\right|$.

Upon changing integration variables, again, $\sigma = \frac{1}{2}\xi - \theta$, $\rho = \frac{1}{2}\xi + \theta$, the linearized phase attains the form

$$\zeta(\tilde{z}-z)+\langle\xi,\tilde{x}-x\rangle+\langle\theta,h'-h\rangle+\tau\,(\langle h',\tilde{p}\rangle-\langle h,p\rangle)=\zeta(\tilde{z}-z)+\langle\xi,\tilde{x}-x\rangle+\langle\theta+\tau p,h'-h\rangle+\tau\,\langle h',\tilde{p}-p\rangle,$$
$$\tau=\Upsilon(z,x,h,p,\zeta,\tfrac{1}{2}\xi-\theta,\tfrac{1}{2}\xi+\theta). \quad (81)$$

The leading order contribution to the oscillatory integral of the kernel associated with the map $\mathrm{R}\bar{L}^{*}\Lambda\bar{L}\mathrm{E}$ as in (75) then becomes, microlocally (cf. (76))

$$\begin{aligned}(2\pi)^{-(2n-1)}\int \varXi\exp[\mathrm{i}(\zeta(\tilde{z}-z)+\langle\xi,\tilde{x}-x\rangle+\langle\theta,h'-h\rangle+\tau\,(\langle h',\tilde{p}\rangle-\langle h,p\rangle))]|\tau|^{n-1}\,\mathrm{d}\zeta\mathrm{d}\xi\,\mathrm{d}\theta\mathrm{d}h\mathrm{d}h'\\
=(2\pi)^{-n}\int\exp[\mathrm{i}(\zeta(\tilde{z}-z)+\langle\xi,\tilde{x}-x\rangle)]\\
\times\left\{(2\pi)^{-(n-1)}\int\varXi\exp[\mathrm{i}(\langle\theta+\tau p,h'-h\rangle+\tau\,\langle h',\tilde{p}-p\rangle)]|\tau|^{n-1}\,\mathrm{d}h'\mathrm{d}\theta\mathrm{d}h\right\}\mathrm{d}\zeta\mathrm{d}\xi,\\
\tau=\Upsilon(z,x,h,p,\zeta,\tfrac{1}{2}\xi-\theta,\tfrac{1}{2}\xi+\theta). \quad (82)\end{aligned}$$

Upon substituting Υ for τ, omitting the symbol $\varXi$, and changing the integration variable h' by $\widehat{h}' = \Upsilon(z,x,h,p,\zeta,\frac{1}{2}\xi-\theta,\frac{1}{2}\xi+\theta)\,h'$, the integral in between the braces becomes

$$\begin{aligned}(2\pi)^{-(n-1)}\int\left\{\int\exp[\mathrm{i}(\langle\Upsilon(z,x,h,p,\zeta,\tfrac{1}{2}\xi-\theta,\tfrac{1}{2}\xi+\theta)^{-1}\theta+p,\widehat{h}'-\Upsilon(z,x,h,p,\zeta,\tfrac{1}{2}\xi-\theta,\tfrac{1}{2}\xi+\theta)\,h\rangle)]\,\mathrm{d}\theta\mathrm{d}h\right\}\\
\times\exp[\mathrm{i}\langle\widehat{h}',\tilde{p}-p\rangle]\,\mathrm{d}\widehat{h}'. \quad (83)\end{aligned}$$

The integral in between braces defines a symbol in $(z,x,p,\zeta,\xi,\widehat{h}')$. The principal part, $\varPi$ say, of this symbol can be found by changing variables of integration, $(h,\theta)\mapsto(\widehat{h},\widehat{\theta})$ with $\widehat{h}=\Upsilon(z,x,h,p,\zeta,\frac{1}{2}\xi-\theta,\frac{1}{2}\xi+\theta)h$ and $\widehat{\theta}=\Upsilon(z,x,h,p,\zeta,\frac{1}{2}\xi-\theta,\frac{1}{2}\xi+\theta)^{-1}\theta$ for given (z,x,ζ,ξ), and applying the method of stationary phase.

The projection of (56), the canonical relation of L, on the τ variable is non-degenerate; we can always choose τ_0 to be a component of η_{0J}, while $\tau=\tau_0$. But then $\tau=\frac{\partial S}{\partial t}$ is t independent. This implies that Υ becomes p independent.

We summarize these results in the following theorem. The canonical relation of A_{WE} defines a map $(s,r,t,\sigma,\rho,\tau)\mapsto(z,x,p,\zeta,\xi,\vartheta)$ (where ϑ is the p-covector); there is also an associated value of $h=r-s$. By pull back with the inverse of the mentioned map, we map the symbols ψ_Y,ψ_{D} to symbols in the variables $(z,x,p,\zeta,\xi,\vartheta)$. By the evaluation of h one obtains by pull back the cutoff χ in these variables also. We define $\varPsi$ as the product of these symbols and cutoff.

Theorem 5.5. Let the modified angle transform be given by

$$\begin{aligned}(\widehat{A}'_{\mathrm{WE}}\,\psi_Y d)(x,z,p)=\int(\varXi^{-1}Q_{-,s}(z)^{-1}Q_{-,r}(z)^{-1}H(0,z)^{*}\\
Q^{*}_{-,s}(0)^{-1}Q^{*}_{-,r}(0)^{-1}\psi_Y(-2\partial_t^{-1})d)(x-\tfrac{1}{2}h,x+\tfrac{1}{2}h,\langle p,h\rangle)\,\chi(x,z,h)\,\mathrm{d}h;\end{aligned}$$

then

$$(\varPsi(z,x,p,D_z,D_x,D_p)+\text{l.o.t.})\,(r\delta(\tbinom{z}{\cdot}))=(\varPi^{-1}\widehat{A}'_{\mathrm{WE}}d)(z,x,p) \quad (84)$$

if $d=F_{\mathrm{K}}\delta(\binom{z}{\cdot})$ is the Kirchhoff modeled data in accordance with (67).

Acknowledgments

The author thanks The Pan-American Advanced Studies Institute, and in particular Gunther Uhlmann, for providing a very stimulating environment during the workshop on Partial Differential Equations, Inverse Problems and Non-linear Analysis in January 2003. The author also thanks Günther Hörmann for many helpful discussions.

CWP-431P

Linearized 2.5-D parameter imaging-inversion in anisotropic elastic media

Stig-Kyrre Foss[1], Maarten V. de Hoop[2] and Bjørn Ursin[3]

[1] *Institute of Mathematics, NTNU, Trondheim, Norway.*
[2] *Center for Wave Phenomena, Colorado School of Mines, Golden CO 80401-1887, USA*
[3] *Institute of Petroleum Technology, NTNU, Trondheim, Norway.*

ABSTRACT

In this paper we derive 2.5-D high frequency modelling and imaging-inversion formulas of seismic reflection data in the Born approximation in anisotropic elastic media. The 2.5-D approach encompasses 3-D wave scattering measured in a common azimuth acquisition geometry subject to 2-D dimensional computations under appropriate assumptions. The lowest possible symmetry of the medium in this approach, in principle, is monoclinic, while the medium must be translationally invariant in the normal direction to the associated symmetry plane. In the presence of caustics, artifacts may be generated by the imaging-inversion procedures. We show that in the 2.5-D approach the analysis of artifacts in the 2-D symmetry plane implies the corresponding analysis in 3-D in the framework of the common azimuth acquisition geometry. An interesting aspect of our results is the occurrence of out-of-plane geometrical spreading in the least-squares removal of the contrast source radiation patterns on the data. We finally introduce the 2.5-D transform that generates common image-point gathers. This transform yields an efficient, though in general, approximate tool for migration velocity analysis in anisotropic media. A real ocean bottom seismic data example from the North Sea, using the derived formulas, is given.

Key words: Reflection seismology, seismic modelling, inversion, ray theory, anisotropy.

SYMBOLS AND NOTATION

Symbols	**Description**
t	time
ω	angular frequency
$\boldsymbol{x} = (x_1, x_3)(= (x_1, x_2, x_3))$	position vector (before redefinition in main text)
$G_{in}(\boldsymbol{x}^r, \omega, \boldsymbol{x}^s)$	Green's function in the frequency domain
$\boldsymbol{x}^s, \boldsymbol{x}^r$	source and receiver positions
$A(\boldsymbol{x}, \boldsymbol{x}^s)$	amplitude for a ray at $\boldsymbol{x}^s$ from $\boldsymbol{x}$
$\mathbf{h} = (h_1, h_2, h_3)$	polarization vector
$T(\boldsymbol{x}, \boldsymbol{x}^s)$	traveltime for a ray between $\boldsymbol{x}$ and $\boldsymbol{x}^s$
$\kappa(\boldsymbol{x}, \boldsymbol{x}^s)$	KMAH index for a ray between $\boldsymbol{x}$ and $\boldsymbol{x}^s$
$v(\boldsymbol{x})$	phase velocity
$\rho(\boldsymbol{x}) = \rho^{(0)}(\boldsymbol{x}) + \rho^{(1)}(\boldsymbol{x})$	density as a sum of a smoothly varying term and a perturbation
$c_{ijkl}(\boldsymbol{x}) = c_{ijkl}^{(0)}(\boldsymbol{x}) + c_{ijkl}^{(1)}(\boldsymbol{x})$	elastic stiffness tensor as a sum of smooth background parameters and a perturbation
$\det \mathbf{Q}_2(\boldsymbol{x}, \boldsymbol{x}^s)$	relative geometrical spreading in local surface coordinates on the wavefront
$Q_2^{\parallel}(\boldsymbol{x}, \boldsymbol{x}^s)$	in-plane relative geometrical spreading
$Q_2^{\perp}(\boldsymbol{x}, \boldsymbol{x}^s)$	out-of-plane relative geometrical spreading
(q_1, q_2)	local wavefront coordinates
$\mathbf{p} = (p_1, p_2, p_3)$	slowness vector

migration in transversely isotropic media with a vertical symmetry axis.

The imaging-inversion results in this paper are derived using the inverse generalized Radon transform (GRT) (Miller, Oristaglio and Beylkin 1987) and using natural coordinates at each subsurface point to be imaged, namely scattering angle and migration dip. Sollid and Ursin (2003) derived a 2.5-D migration formula, using the GRT, in transversely isotropic media. A review of 2-D and 2.5-D inversion and migration is found in (Foss and Ursin 2003). Using the aforementioned choice of coordinates removes the use of a Beylkin determinant (de Hoop, Spencer and Burridge 1999). Additionally, this choice unravels caustics that may occur in an inhomogeneous medium giving rise to multivalued travel time functions. In the presence of caustics, strictly speaking, the GRT should be developed with Maslov Green's functions. However, de Hoop and Brandsberg-Dahl (2000) carried out an analysis that showed that as long as there are no caustics occurring at the source or receiver positions, through a stationary phase argument, the Maslov formulation reduces to a GRT based upon the geometrical ray approximation (GRA) for the Green's functions. Following this observation, we employ the GRA Green's function in our development. The formulas derived in this paper are applicable in the presence of multipathing and caustics under assumptions that will be clarified.

The high frequency linearized inversion, given a smooth background medium, yields the most singular part of the unknown medium contrast and is developed in the framework of pseudodifferential and Fourier integral operators (FIOs), see e.g. Duistermaat (1996). This was done in the acoustic case by Rakesh (1988), Hansen (1991) and in the anisotropic elastic.

In the presence of caustics, in the CA geometry, imaging artifacts may occur; for the acoustic case, see Nolan and Symes (1997). An artifact is defined as a false event in the image that is not contained in the medium contrast, i.e. an image reflectorthat is not there. The inversion is artifact-free under the so-called *Bolker condition* (Guillemin 1985). When this condition is violated, the image resulting from the inversion procedure will contain artifacts we have coined *artifacts of type 1*. The transformation of seismic data into common-image point gathers, based upon the GRT, can be viewed as introducing a restriction to a fixed scattering angle in the inversion formula (Brandsberg-Dahl *et al.* 2003b). This restriction in the presence of caustics will give rise to *artifacts of type 2* (for an exhaustive analysis of these artifacts, see Stolk (2002)). Brandsberg-Dahl *et al* (2003b) suppressed such artifacts by a procedure called focusing in dip by selecting contributions to the imaging-inversion integral from isochrones by an isochrone filter.

The outline of the paper is as follows. In section 2, we introduce the notation and the fundamental assumptions pertaining to 2.5-D. We also show by an example that, due to the anisotropy, an additional assumption is required to restrict the rays to travel in-plane, compared to Bleistein (1986). A detailed description of all aspects of the 2.5-D Born single scattering modelling formula is given. The derivation of this formula can be found in the Appendix A; it is based on approximating the out-of-plane integral of the 3-D Born modelling formula by the method of stationary phase (Bleistein 1986) given that there are no out-of-plane caustics. We give a description of which elastic parameters can be determined in the 2.5-D framework of CA data. A more detailed description of the parametrization and resolution of the smooth and perturbed parts of the medium in this context is given by Foss and Ursin (2003). Additionally, we give the precise assumptions subject to which our 2.5-D modelling is well defined and show how it pertains to the CA acquisition geometry. Section 3 contains the detailed guide through our inversion procedure, which is an analogue to least squares inversion. The inversion follows closely that of de Hoop and Brandsberg-Dahl (2000). We show that the 2-D Bolker condition pertaining to the symmetry plane implies the likewise condition in 3-D subject to the restriction to CA. First, we construct the adjoint (imaging) operator of the 2.5-D modelling operator. Second, we evaluate the normal operator and identify its 'inverse' up to leading order. Third, we compose this 'inverse' with mentioned adjoint to find the 2.5-D inversion operator. (For 'inverse', one should read parametrix, which is the inverse modulo smoothing operators.) The actual inversion result, for the most singular part of the medium contrast, is given in subsection 3.2 as an inverse by GRT in natural coordinates. In section 4 we present the 2.5-D transformation of the data to common-image point gathers. Section 5 shows results using the formulas derived in this paper applied to real ocean bottom cable (OBC) seismic data from the North Sea. We conclude with a discussion on future applications.

2 MODELLING

2.1 Green's functions in a smoothly varying medium

The geometrical ray approximation (GRA) to the Green's functions is a causal, short period approximate solution to the elastic wave equation, in the frequency domain given by

$$\rho(\boldsymbol{x})\omega^2 G_{in} + \partial_j(c_{ijkl}(\boldsymbol{x})\partial_l G_{kn}) = -\delta_{in}\delta(\boldsymbol{x}-\boldsymbol{x}^s) \qquad i,j,k,l,n = 1,2,3, \quad (1)$$

where ω is angular frequency and the position vector is denoted by $\boldsymbol{x} = (x_1, x_2, x_3)$, $\rho(\boldsymbol{x})$ and $c_{ijkl}(\boldsymbol{x})$ are density and the stiffness tensor, respectively. The Kronecker delta, δ_{in}, gives the source term on the right-hand side in the canonical directions, operative at the source point, $\boldsymbol{x}^s$, through the delta function δ. The summation convention applies here and in the following. The Green's function is a sum over the different wave modes, where each term is of the form

$$G_{ip}(\boldsymbol{x},\omega,\boldsymbol{x}^s) = A(\boldsymbol{x},\boldsymbol{x}^s)h_i^s(\boldsymbol{x})h_p(\boldsymbol{x}^s)e^{\mathrm{i}\omega T(\boldsymbol{x},\boldsymbol{x}^s)}, \quad (2)$$

in which $T(\boldsymbol{x},\boldsymbol{x}^s)$ is the travel time along the ray connecting $\boldsymbol{x}$ with $\boldsymbol{x}^s$. (We do not explicitly indicate the mode of propagation; we treat the modes of propagation separately.) h_i^s and h_p are components of the unit polarization vectors at the endpoints of the ray, where the superscript s indicates that this polarization vector is associated with the ray originating at $\boldsymbol{x}^s$.

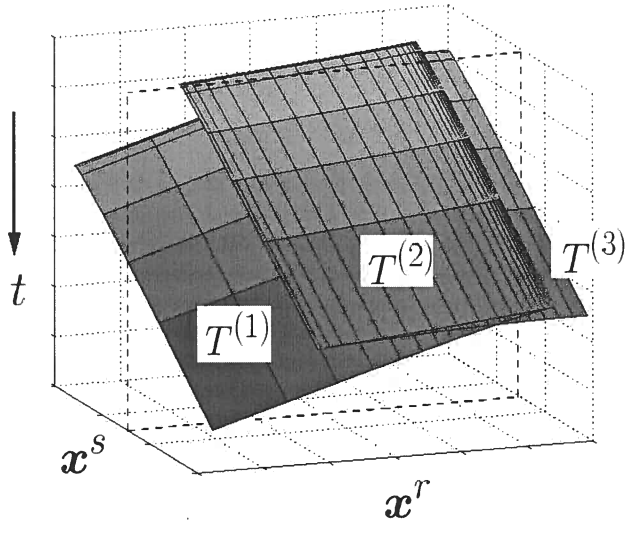

Figure 3. Triplication of the recorded wave field with travel time functions per branch denoted $T^{(1)}$, $T^{(2)}$ and $T^{(3)}$. Dotted plane indicates a common shot gather.

smoothly as shown on the right of the figure for three different depths in the model used in the ray tracing on the left. All axes are given in meters. The group velocity vector, $\mathbf{V}$, is perpendicular to the slowness surface and governs the direction of the ray. This is indicated with the surface normal to the slowness surface, $\hat{n}$. As suggested in the figure, we may change smoothly the direction of the energy velocity, sending the rays out of the plane and back again while keeping p_2 fixed (implication of assumption 1 a)). Two rays are shot at a small positive and negative angle with the x_3-axis in the out-of-plane direction ($p_1^s = p_1^r = 0$) from $(x_1, x_2, x_3) = (0, 0, 200)$. They travel in the (x_2, x_3)-plane and intersect at the point $(0, 0, 2800)$ with incoming angles following Snell's law and satisfying equation (7). We note that the anisotropy in this example allows triplications on the symmetry axis, which is unusual in a sedimentary sequence setting.

We admit in-plane scattering events only, by imposing:

Assumption 2. (Seismic phase restriction) *Only seismic events with at least one ray, or leg, associated with a wave type that pertains to a convex slowness surface are considered.*

If one of the ray legs is associated with a convex slowness surface, the only solution to equation (7) is $p_2^r = p_2^s = 0$. Due to the symmetry in assumption 1 b) this also means that $V_2^s = V_2^r = 0$. This follows because $p_2^r = -p_2^s \neq 0$ on a convex slowness surface will induce group velocity vectors pointing out of the plane (the middle slowness surface on the right of Figure 4 illustrates this). The group vectors send seismic energy away from the plane never to return. In particular, P waves always have a convex slowness surface (Musgrave 1970); hence, qP-qP and qP-qSV scattering events always satisfy assumption 2.

The medium parameters are represented by a sum of a smooth part, $\rho^{(0)}$ and $c_{ijkl}^{(0)}$, and a singular perturbation, $\rho^{(1)}$ and $c_{ijkl}^{(1)}$:

$$\rho(\boldsymbol{x}) = \rho^{(0)}(\boldsymbol{x}) + \rho^{(1)}(\boldsymbol{x}), \quad c_{ijkl}(\boldsymbol{x}) = c_{ijkl}^{(0)}(\boldsymbol{x}) + c_{ijkl}^{(1)}(\boldsymbol{x}). \tag{8}$$

Note that both the smooth part and the perturbation are restricted in accordance with assumption 1a) and b) making the reflectors parts of the cylindrical surfaces (see Figure 1). In the Born approximation, the waves travel in the smooth part of the medium and are scattered off the perturbation once. In the imaging-inversion problem the smooth medium is assumed to be known. It is the medium perturbation we will invert for. The multicomponent data collected in a seismic experiment, u_{mn}, under the condition of a smooth background, will be, in this approximation, the asymptotic part of the modelling formula. The subscripts indicate that u_{mn} is the m-component of the recorded wave field due to a body force in the n-direction. The data (scattered wave field) can be modelled by an operator $\mathbf{L}$ acting on the medium perturbation (see Appendix A for a detailed derivation, where U_{mn} is the time-Fourier transform of the data u_{mn})

$$\begin{aligned} u_{mn}(\boldsymbol{x}^s, \boldsymbol{x}^r, t) &= \mathbf{L}\mathbf{c}^{(1)}(\boldsymbol{x}^s, \boldsymbol{x}^r, t) \\ &\approx \sum_{i \in I} \sqrt{\frac{\mathrm{i}}{2\pi}} \int_X \int_{\mathbb{R}} h_m(\boldsymbol{x}^r) \omega^{3/2} \rho^{(0)}(\boldsymbol{x}) \frac{A^{||}(\boldsymbol{x}^s, \boldsymbol{x}) A^{||}(\boldsymbol{x}, \boldsymbol{x}^r)}{\mathcal{L}^{\perp}(\boldsymbol{x}^r, \boldsymbol{x}, \boldsymbol{x}^s)} \\ &\qquad \cdot \mathbf{w}^T(\boldsymbol{x}^r, \boldsymbol{x}, \boldsymbol{x}^s) \mathbf{c}^{(1)}(\boldsymbol{x}) e^{\mathrm{i}\omega(T^{(i)}(\boldsymbol{x}^r, \boldsymbol{x}, \boldsymbol{x}^s) - t)} h_n(\boldsymbol{x}^s) \mathrm{d}\omega \mathrm{d}\boldsymbol{x}. \end{aligned} \tag{9}$$

both V_2, p_2 tend to zero (in accordance with the 2.5-D approach, where $p_2 = 0$, $V_2 = 0$). Closed form expressions for the integrand for isotropic, transversely isotropic and orthorhombic media can be found in Ettrich *et al.* (2002), equations (15), (19) and (22), respectively. The medium perturbations are collected in the matrix $\mathbf{c}^{(1)}(\boldsymbol{x})$ and the radiation patterns equivalently in $\mathbf{w}(\boldsymbol{x}^r, \boldsymbol{x}, \boldsymbol{x}^s)$. They will be defined in the next subsection.

Remark 1. *We restrict our analysis to the part of phase space where out-of-plane caustics do not occur. Thus we mute events associated with rays forming out-of-plane caustics (see Remark 4 in the appendix).*

2.2.1 *Medium perturbations and radiation patterns*

Since by assumption 1, the medium is restricted to monoclinic or higher symmetry, there are at most 13 stiffness parameters plus density as independent unknown distributions. The stiffness tensor is given by (if the (x_1, x_3)-plane is the symmetry plane):

$$[c_{ijkl}] = \begin{bmatrix} c_{1111} & c_{1122} & c_{1133} & 0 & c_{1113} & 0 \\ c_{1122} & c_{2222} & c_{2233} & 0 & c_{2213} & 0 \\ c_{1133} & c_{2233} & c_{3333} & 0 & c_{3313} & 0 \\ 0 & 0 & 0 & c_{2323} & 0 & c_{2312} \\ c_{1113} & c_{2213} & c_{3313} & 0 & c_{1313} & 0 \\ 0 & 0 & 0 & c_{1223} & 0 & c_{1212} \end{bmatrix} . \tag{14}$$

The medium perturbations are collected in the 14 × 1 matrix for monoclinic anisotropy (Burridge *et al.* 1998)

$$\mathbf{c}^{(1)}(\boldsymbol{x}) = \left\{ \frac{\rho^{(1)}(\boldsymbol{x})}{\rho^{(0)}(\boldsymbol{x})}, \frac{c^{(1)}_{ijkl}(\boldsymbol{x})}{\rho^{(0)}(\boldsymbol{x}) v^s_\circ(\boldsymbol{x}) v^r_\circ(\boldsymbol{x})} \right\}, \tag{15}$$

where $v^s_\circ$ and $v^r_\circ$ are local phase velocities averaged over all phase angles. These are introduced for computational purposes so that the matrix has components of similar magnitude (Burridge *et al.* 1998). We restrict the indices of $c^{(1)}_{ijkl}$ to the 13 independent components of the stiffness tensor (cf. (12)). With higher symmetry, such as isotropy, the matrix reduces accordingly (Beylkin and Burridge 1990). The radiation pattern matrix is defined similarly as the 14 × 1 matrix (Burridge *et al.* 1998)

$$\mathbf{w}(\boldsymbol{x}^r, \boldsymbol{x}, \boldsymbol{x}^s) = \left\{ h^s_m(\boldsymbol{x}) h^r_m(\boldsymbol{x}), [h^s_i(\boldsymbol{x}) p^s_j(\boldsymbol{x}) h^r_k(\boldsymbol{x}) p^r_l(\boldsymbol{x})] v^s_\circ(\boldsymbol{x}) v^r_\circ(\boldsymbol{x}) \right\}, \tag{16}$$

where the indices follow those of the stiffness matrix in the ordering defined by the matrix or inner product $\mathbf{w}^T(\boldsymbol{x}^r, \boldsymbol{x}, \boldsymbol{x}^s)\mathbf{c}^{(1)}(\boldsymbol{x})$ in the modelling equation (9). Since the out-of-plane slowness will be zero, $p^s_2 = p^r_2 = 0$, we see from equation (16) that the contribution vanishes if $j, l = 2$ in $c^{(1)}_{ijkl}$. In view of assumptions 1 and 2, having $p^s_2 = p^r_2 = 0$, the polarizations of qP and qSV waves satisfy $h_2 = 0$. Thus the parameters we can invert for from qP-qP and qP-qSV scattering are the 7 parameters out of the 14 independent ones in a monoclinic medium, $c^{(1)}_{1111}, c^{(1)}_{1133}, c^{(1)}_{3333}, c^{(1)}_{1113}, c^{(1)}_{3313}, c^{(1)}_{1313}$ and density $\rho^{(1)}$ ($h_2 = 0$, and hence the contributions for $i, k = 2$ in $c^{(1)}_{ijkl}$ are zero). The kinematic aspects for a monoclinic background medium are governed by the same partitioning of parameters (Chapman and Pratt 1992; Foss and Ursin 2003).

Remark 2. *In imaging, the smooth background medium is given, and hence the relevant amplitudes can be computed in the lowest possible symmetry admitted by the 2.5-D framework: monoclinic. However, for inversion and reflection tomography, having observations restricted to the plane under consideration, only parameters associated with this plane can be estimated. Hence the lowest possible symmetry is transversely isotropic with a symmetry axis in the plane. Due to the rotational symmetry of the medium, parameters needed in out-of-plane amplitude calculations are found from in-plane propagation (Ettrich et al 2002; equation (19)).*

2.3 The modelling operator in common azimuth

The 3-D Born modelling operator has been shown to be a Fourier integral operator (FIO) under the mild conditions that there are no direct rays between the source and the receiver reaching the medium perturbation (i.e. rays that have scattered off a subsurface point over an angle π) and no grazing rays (i.e. rays that reach the acquisition surface tangentially to the surface) (Rakesh 1988; Hansen 1991). The 3-D modelling operator with common azimuth (CA) acquisition geometry (Biondi and Palacharla 1996) is also an FIO under similar conditions (Nolan and Symes 1997; de Hoop *et al* 2003). 2.5-D implies CA (but not the other way) aligning our symmetry plane with the acquisition geometry, i.e. $x^s_2 = x^r_2$. We conclude that the 2.5-D modelling operator (9) has the properties of a FIO, and has the following canonical relation (superscript S indicates that this is a canonical relation in two space dimensions coinciding with the symmetry plane)

$$\begin{aligned} \Lambda^S_L = \{ & (\boldsymbol{x}^s(\boldsymbol{x}, \boldsymbol{\alpha}^s), \boldsymbol{x}^r(\boldsymbol{x}, \boldsymbol{\alpha}^r), T(\boldsymbol{x}^s(\boldsymbol{x}, \boldsymbol{\alpha}^s), \boldsymbol{x}, \boldsymbol{x}^r(\boldsymbol{x}, \boldsymbol{\alpha}^r)), \boldsymbol{k}^s(\boldsymbol{x}, \boldsymbol{\alpha}^s, \omega), \boldsymbol{k}^r(\boldsymbol{x}, \boldsymbol{\alpha}^r, \omega), \omega; \\ & \boldsymbol{x}, -\boldsymbol{k}(\boldsymbol{x}^s(\boldsymbol{x}, \boldsymbol{\alpha}^s), \boldsymbol{x}, \boldsymbol{x}^r(\boldsymbol{x}, \boldsymbol{\alpha}^r), \omega)) | (\boldsymbol{x}, \boldsymbol{\alpha}^s, \boldsymbol{\alpha}^r) \in K, \omega \in \mathbb{R} \setminus 0 \} . \end{aligned} \tag{17}$$

Assumption 3. *The projection of the canonical relation Λ_L^S of the 2.5-D modelling operator on the acquisition variables $(\boldsymbol{x}^s, \boldsymbol{x}^r, t, \boldsymbol{k}^s, \boldsymbol{k}^r, \omega)$ is one-to-one.*

This assumption is consistent with a 2-D Bolker condition (Guillemin 1985), for the acoustic case see Ten Kroode *et al.* (1998). It means that $(\boldsymbol{x}^s, \boldsymbol{x}^r, t, \boldsymbol{k}^s, \boldsymbol{k}^r, \omega)$ determine a scattering point $\boldsymbol{x} \in X$ and associated wave vector $\boldsymbol{k}$, uniquely and smoothly. This condition ensures that the normal operator is an elliptic pseudodifferential operator. Hence the procedure of imaging the modelled data, equation (20), does not generate reflectorsthat were not there to begin with, i.e. that are not present in $\mathbf{c}^{(1)}$.

Since $\mathbf{N}$ is elliptic and pseudodifferential we can construct its parametrix, denoted by $\langle \mathbf{N}^{-1} \rangle$. The brackets indicate that this is a pseudo inverse. Following the analogue of least-squares inversion, an estimate of the medium perturbation in equation (15) can be recovered from the composition

$$\hat{\mathbf{c}}^{(1)} \approx \langle \mathbf{N}^{-1} \rangle \mathbf{L}^\star u, \tag{21}$$

where u is the data. If assumption 3 is violated we generate artifacts (discussed in the introduction). A less restrictive condition and a discussion of the implied artifacts can be found in de Hoop and Brandsberg-Dahl (2000) and Stolk (2000).

In view of Remark 3, assumption 3 (or the 2-D Bolker condition) in the symmetry plane implies the 3-D CA Bolker condition. This condition encompasses that for any point in Λ_L^{CA}, i.e., for an intersecting pair of source and receiver rays, given $(x_1^s, x_2^s, x_1^r, x_2^r, t, k_1^s, k_2^s + k_2^r, k_1^r, \omega)$, there is only one (t, k_2^s) that explains the reflection.

3.1 The adjoint scattering (imaging) and the normal operators

In this subsection, we evaluate the adjoint $\mathbf{L}^\star$ of the modelling operator $\mathbf{L}$ and deduce the leading order contribution to the normal operator $\mathbf{N}$ for which we can derive a parametrix. We will write the action of the normal operator as a pseudodifferential operator, i.e. as integrals over $\boldsymbol{x}$ and its Fourier dual $\boldsymbol{k}$, the wave vector. The inverse of the integrand thus obtained (the integrand yields the so-called *symbol* of the normal operator) generates the 'inverse' of the normal operator up to leading order.

We let the acquisition coordinates be defined on the two acquisition lines in the symmetry plane, ∂S and ∂R for sources and receivers, respectively. By the reciprocity theorem of the time-correlation type found in de Hoop and de Hoop (2000) the adjoint or imaging operator $\mathbf{L}^\star$ can be written

$$\mathbf{L}^\star u(\boldsymbol{x}') \approx \frac{1}{\sqrt{2\pi \mathrm{i}}} \int_{\partial S \times \partial R} \int_{\mathbb{R}} \int_{\mathbb{R} \geq 0} \omega'^{3/2} \rho^{(0)}(\boldsymbol{x}') \frac{(A^{||}(\boldsymbol{x}^s, \boldsymbol{x}') A^{||}(\boldsymbol{x}', \boldsymbol{x}^r))^\star}{\mathcal{L}^\perp(\boldsymbol{x}^r, \boldsymbol{x}', \boldsymbol{x}^s)^\star} \\ \cdot \mathbf{w}(\boldsymbol{x}^r, \boldsymbol{x}', \boldsymbol{x}^s) h_m(\boldsymbol{x}^r; \boldsymbol{x}') u_{mn}(\boldsymbol{x}^s, \boldsymbol{x}^r, t) h_n(\boldsymbol{x}^s; \boldsymbol{x}') e^{-\mathrm{i}\omega'(T(\boldsymbol{x}^r, \boldsymbol{x}', \boldsymbol{x}^s) - t)} \mathrm{d}t \mathrm{d}\omega' \mathrm{d}\boldsymbol{x}^s \mathrm{d}\boldsymbol{x}^r, \tag{22}$$

where ω' is the frequency and * indicates the adjoint as well as complex conjugation. The polarization vectors associated with the scattering off the point $\boldsymbol{x}'$ are denoted by $h_m(\boldsymbol{x}^r; \boldsymbol{x}')$ and $h_n(\boldsymbol{x}^s; \boldsymbol{x}')$ to distinguish them from the polarization vectors due to the scattering off $\boldsymbol{x}$ as in equation (9). Note that there is a summation over the different indices of the data u_{mn} in the integrand of the adjoint, following the summation convention. Hence the notation of $\mathbf{L}^\star$ acting on all the data denoted by u. Note also that $\mathbf{w} = (\mathbf{w}^T)^\star$.

Composing the imaging operator with the modelling operator (having used a pseudodifferential cutoff for when it fails to satisfy assumption 3) gives us the normal operator. The u_{mn} from the modelling equation (9) is inserted into the above expression to yield

$$\mathbf{L}^\star \psi \mathbf{L} \mathbf{c}^{(1)}(\boldsymbol{x}') \approx \\ \frac{1}{2\pi} \int_{\partial S \times \partial R} \int_X \int_{\mathbb{R}} \int_{\mathbb{R}} \int_{\mathbb{R} \geq 0} \omega'^{3/2} \omega^{3/2} \rho^{(0)}(\boldsymbol{x}') \rho^{(0)}(\boldsymbol{x}) \frac{(A^{||}(\boldsymbol{x}^s, \boldsymbol{x}') A^{||}(\boldsymbol{x}', \boldsymbol{x}^r))^\star}{\mathcal{L}^\perp(\boldsymbol{x}^r, \boldsymbol{x}', \boldsymbol{x}^s)^\star} \frac{A^{||}(\boldsymbol{x}^s, \boldsymbol{x}) A^{||}(\boldsymbol{x}, \boldsymbol{x}^r)}{\mathcal{L}^\perp(\boldsymbol{x}^r, \boldsymbol{x}', \boldsymbol{x}^s)} \\ \cdot e^{\mathrm{i}\omega(T(\boldsymbol{x}^r, \boldsymbol{x}, \boldsymbol{x}^s) - t) - \mathrm{i}\omega'(T(\boldsymbol{x}^r, \boldsymbol{x}', \boldsymbol{x}^s) - t)} \mathrm{d}t \mathrm{d}\omega \mathrm{d}\omega' \mathrm{d}\boldsymbol{x} \mathrm{d}\boldsymbol{x}^s \mathrm{d}\boldsymbol{x}^r. \tag{23}$$

If assumption 3 is satisfied it is indeed an elliptic pseudodifferential operator. The integral over t yields a delta function $\delta(\omega - \omega')$ so we can collapse the integral over ω' and set $\omega = \omega'$. Invoking a Taylor expansion about $\boldsymbol{x}'$ for the two-way travel time $T(\boldsymbol{x}^r, \boldsymbol{x}, \boldsymbol{x}^s)$ yields, due to the fact that higher order derivatives give smoother contributions to the amplitude (Hörmander 1985a) through expansion of the exponential,

$$\omega[T(\boldsymbol{x}^r, \boldsymbol{x}, \boldsymbol{x}^s) - T(\boldsymbol{x}^r, \boldsymbol{x}', \boldsymbol{x}^s)] = \omega[(\nabla_{\boldsymbol{x}'} T)(\boldsymbol{x}^r, \boldsymbol{x}', \boldsymbol{x}^s) \cdot (\boldsymbol{x} - \boldsymbol{x}')] + \dots. \tag{24}$$

results in the simplified expression

$$\mathbf{N}\mathbf{c}^{(1)}(\boldsymbol{x}') \approx \int_{S^s \times S^r} \int_X \int_{\mathbb{R}} \bar{\omega}^3 \frac{\mu_{LS}(\boldsymbol{\alpha}^r, \boldsymbol{x}', \boldsymbol{\alpha}^s)}{|\mathcal{L}^{\perp}(\boldsymbol{\alpha}^r, \boldsymbol{x}', \boldsymbol{\alpha}^s)|^2} \mathbf{w}(\boldsymbol{\alpha}^r, \boldsymbol{x}', \boldsymbol{\alpha}^s) \mathbf{w}^T(\boldsymbol{\alpha}^r, \boldsymbol{x}', \boldsymbol{\alpha}^s) \cdot \mathbf{c}^{(1)}(\boldsymbol{x}) e^{\mathrm{i}\bar{\omega}\boldsymbol{\nu}^m(\boldsymbol{\alpha}^r, \boldsymbol{x}', \boldsymbol{\alpha}^s)\cdot(\boldsymbol{x}-\boldsymbol{x}')} \mathrm{d}\bar{\omega}\,\mathrm{d}\boldsymbol{x}\,\mathrm{d}\boldsymbol{\alpha}^s\,\mathrm{d}\boldsymbol{\alpha}^r. \quad (33)$$

3.1.2 Migration dip, scattering angle and the leading order contribution

We change variables again, from the phase angles to scattering angle θ, which is the angle between $\boldsymbol{\alpha}^s$ and $\boldsymbol{\alpha}^r$, and the migration dip $\boldsymbol{\nu}^m$ (see Figure 5). The scattering angle follows to be

$$\theta = \theta(\boldsymbol{\alpha}^r, \boldsymbol{x}', \boldsymbol{\alpha}^s) = \arccos(\boldsymbol{\alpha}^s \cdot \boldsymbol{\alpha}^r). \quad (34)$$

To be able to integrate over the migration dip, there is assumed to be no scattering over $\theta = \pi$ so that $\nabla_{\boldsymbol{x}'} T \neq 0$ and $\boldsymbol{\nu}^m$ is defined. We have

$$(\boldsymbol{x}', \boldsymbol{\alpha}^s, \boldsymbol{\alpha}^r) \leftrightarrows (\boldsymbol{x}', \boldsymbol{\nu}^m, \theta). \quad (35)$$

In 2.5-D this mapping exists both ways; there is no integration over the azimuth (de Hoop and Brandsberg-Dahl 2000). The domains of integration can now be written as

$$S^s \times S^r \longrightarrow E_{\boldsymbol{\nu}^m} \times E_\theta \text{ for given } \boldsymbol{x}'. \quad (36)$$

Changing all relevant coordinates under the mapping in equation (35) and collecting the integration over the scattering angle θ yields

$$\mathbf{N}\mathbf{c}^{(1)}(\boldsymbol{x}') \approx \int_{E_{\boldsymbol{\nu}^m}} \int_{\mathbb{R}} \int_X \bar{\omega}^3 \left\{ \int_{E_\theta} \frac{\mu_{LS}(\boldsymbol{x}', \boldsymbol{\nu}^m, \theta)}{|\mathcal{L}^{\perp}(\boldsymbol{x}', \boldsymbol{\nu}^m, \theta)|^2} \cdot \mathbf{w}(\boldsymbol{x}', \boldsymbol{\nu}^m, \theta) \mathbf{w}^T(\boldsymbol{x}', \boldsymbol{\nu}^m, \theta) \frac{\partial(\boldsymbol{\alpha}^s, \boldsymbol{\alpha}^r)}{\partial(\boldsymbol{\nu}^m, \theta)} \mathrm{d}\theta \right\} \mathbf{c}^{(1)}(\boldsymbol{x}) e^{\mathrm{i}\bar{\omega}\boldsymbol{\nu}^m \cdot(\boldsymbol{x}-\boldsymbol{x}')} \mathrm{d}\boldsymbol{x}\,\mathrm{d}\bar{\omega}\,\mathrm{d}\boldsymbol{\nu}^m. \quad (37)$$

We introduce the square matrix (of the dimensionality of $\mathbf{w}$)

$$\Gamma(\boldsymbol{x}', \boldsymbol{\nu}^m) = \frac{1}{2} \int_{E_\theta} \frac{\mu_{LS}(\boldsymbol{x}', \boldsymbol{\nu}^m, \theta)}{|\mathcal{L}^{\perp}(\boldsymbol{x}', \boldsymbol{\nu}^m, \theta)|^2} \mathbf{w}(\boldsymbol{x}', \boldsymbol{\nu}^m, \theta) \mathbf{w}^T(\boldsymbol{x}', \boldsymbol{\nu}^m, \theta) \frac{\partial(\boldsymbol{\alpha}^s, \boldsymbol{\alpha}^r)}{\partial(\boldsymbol{\nu}^m, \theta)} \mathrm{d}\theta + (\ldots)(\boldsymbol{x}', -\boldsymbol{\nu}^m), \quad (38)$$

where the second term is the same as the first but with $\boldsymbol{\nu}^m$ replaced by $-\boldsymbol{\nu}^m$. This enables us to rewrite equation (37) with positive $\bar{\omega}$ only as

$$\mathbf{N}\mathbf{c}^{(1)}(\boldsymbol{x}') \approx \frac{1}{(2\pi)^2} \int_{E_{\boldsymbol{\nu}^m}} \int_{\mathbb{R}\geq 0} \int_X \bar{\omega}^2 8\pi^2 \Gamma(\boldsymbol{x}', \boldsymbol{\nu}^m) \mathbf{c}^{(1)}(\boldsymbol{x}) e^{\mathrm{i}\bar{\omega}\boldsymbol{\nu}^m \cdot(\boldsymbol{x}-\boldsymbol{x}')} \bar{\omega}\,\mathrm{d}\boldsymbol{x}\,\mathrm{d}\bar{\omega}\,\mathrm{d}\boldsymbol{\nu}^m. \quad (39)$$

This has now explicitly the form of a pseudodifferential operator with integration over $\boldsymbol{x}$ and its dual $\boldsymbol{k}$ through the identification $\boldsymbol{k} = \bar{\omega}\boldsymbol{\nu}^m$. We recognize here the leading order symbol, $\bar{\omega}^2 8\pi^2 \Gamma(\boldsymbol{x}', \boldsymbol{\nu}^m)$, of $\mathbf{N}$. Note the differences when compared with the 3-D case found in de Hoop and Brandsberg-Dahl (2000): the out-of-plane geometrical spreading $\mathcal{L}^{\perp}$ naturally appears in the leading order symbol of the normal operator in equation (38) combined with the radiation patterns. Also the power of (2π) has been modified in accordance with the stationary phase calculation in 2.5-D.

3.2 Least-Squares Inversion

To leading order, the inverse normal operator composed with the normal operator from the last subsection should yield the identity. The departure from the identitity is due to taking the generalized inverse of and smoother contributions to the normal operator. We denote the generalized inverse of $\mathbf{N}$ by $\langle \mathbf{N}^{-1} \rangle$. The resolution is controlled by $\langle \mathbf{N}^{-1} \rangle \mathbf{N}$. General analysis of the resolution is given by de Hoop *et al* (1999) and for the 2.5-D case by Foss and Ursin (2003).

Note that

$$\frac{1}{(2\pi)^2} \int_{\mathbb{R}\geq 0} \int_{S^1} e^{\mathrm{i}\bar{\omega}\boldsymbol{\nu}^m \cdot(\boldsymbol{x}-\boldsymbol{x}')} \bar{\omega}\,\mathrm{d}\boldsymbol{\nu}^m \mathrm{d}\bar{\omega} = \delta(\boldsymbol{x}-\boldsymbol{x}'). \quad (40)$$

(Equation (47) is in fact a direct manifestation of the composition of a pseudodifferential operator with a FIO (Treves 1980, Section 6.1. Chapter VIII)). The surface coordinates $\boldsymbol{x}^r$ and $\boldsymbol{x}^s$ are changed to the phase directions at the scattering point as in relation (27). Using equation (29) and (32), the appropriate Jacobian can be expressed as

$$\frac{\partial(\boldsymbol{x}^s,\boldsymbol{x}^r)}{\partial(\boldsymbol{\alpha}^s,\boldsymbol{\alpha}^r)}=\frac{\mu_{LS}(\boldsymbol{\alpha}^r,\boldsymbol{x}',\boldsymbol{\alpha}^s)|\nabla_{\boldsymbol{x}'}\,T(\boldsymbol{x}^r,\boldsymbol{x}',\boldsymbol{x}^s)|^4}{|\rho^{(0)}(\boldsymbol{x}')A^{||}(\boldsymbol{x}^s,\boldsymbol{x}')A^{||}(\boldsymbol{x}',\boldsymbol{x}^r)|^2}. \tag{48}$$

Inserting the result in equation (47) yields the estimate of the medium perturbation

$$\begin{aligned}\hat{\mathrm{c}}^{(1)}(\boldsymbol{x}')\approx\frac{1}{(2\pi)^{5/2}}\mathrm{Re}\Big\{\int_{S^s\times S^r}&\mathrm{d}\boldsymbol{\alpha}^s\mathrm{d}\boldsymbol{\alpha}^r\int_{\mathbb{R}\geq 0}\frac{\mathrm{d}\omega'}{(\omega'\mathrm{i})^{1/2}}\mu_{LS}(\boldsymbol{\alpha}^r,\boldsymbol{x}',\boldsymbol{\alpha}^s)\langle\Gamma(\boldsymbol{x}',\boldsymbol{\nu}^m)\rangle^{-1}\\ &\cdot\frac{|\nabla_{\boldsymbol{x}'}\,T(\boldsymbol{\alpha}^r,\boldsymbol{x}',\boldsymbol{\alpha}^s)|^2\mathrm{w}(\boldsymbol{\alpha}^r,\boldsymbol{x}',\boldsymbol{\alpha}^s)h_m(\boldsymbol{x}^r;\boldsymbol{x}')U_{mn}(\boldsymbol{x}^s,\boldsymbol{x}^r,\omega')h_n(\boldsymbol{x}^s;\boldsymbol{x}')}{\rho^{(0)}(\boldsymbol{x}')A^{||}(\boldsymbol{\alpha}^s,\boldsymbol{x}')A^{||}(\boldsymbol{x}',\boldsymbol{\alpha}^r)\mathcal{L}^{\perp}(\boldsymbol{\alpha}^r,\boldsymbol{x}',\boldsymbol{\alpha}^s)^{\star}}e^{-\mathrm{i}\omega' T(\boldsymbol{\alpha}^r,\boldsymbol{x}',\boldsymbol{\alpha}^s)}\Big\}.\end{aligned} \tag{49}$$

We observe in the denominator the out-of-plane geometrical spreading, which also exists in the expression for Γ (equation (38)). Changing the variables from phase angles to scattering angle θ and migration dip $\boldsymbol{\nu}^m$ as in (35) yields

$$\begin{aligned}\hat{\mathrm{c}}^{(1)}(\boldsymbol{x}')\approx\frac{1}{(2\pi)^{5/2}}\mathrm{Re}\Big\{\int_{E_{\boldsymbol{\nu}^m}\times E_\theta}&\mathrm{d}\theta\mathrm{d}\boldsymbol{\nu}^m\frac{\partial(\boldsymbol{\alpha}^s,\boldsymbol{\alpha}^r)}{\partial(\boldsymbol{\nu}^m,\theta)}\int_{\mathbb{R}\geq 0}\frac{\mathrm{d}\omega'}{(\omega'\mathrm{i})^{1/2}}\mu_{LS}(\boldsymbol{x}',\boldsymbol{\nu}^m,\theta)\langle\Gamma(\boldsymbol{x}',\boldsymbol{\nu}^m)\rangle^{-1}\\ &\cdot\frac{|\nabla_{\boldsymbol{x}'}\,T(\boldsymbol{x}',\boldsymbol{\nu}^m,\theta)|^2\mathrm{w}(\boldsymbol{x}',\boldsymbol{\nu}^m,\theta)h_m(\boldsymbol{x}^r;\boldsymbol{x}')U_{mn}(\boldsymbol{x}^s,\boldsymbol{x}^r,\omega')h_n(\boldsymbol{x}^s;\boldsymbol{x}')}{\rho^{(0)}(\boldsymbol{x}')A^{||}(\boldsymbol{\alpha}^s,\boldsymbol{x}')A^{||}(\boldsymbol{x}',\boldsymbol{\alpha}^r)\mathcal{L}^{\perp}(\boldsymbol{x}',\boldsymbol{\nu}^m,\theta)^{\star}}e^{-\mathrm{i}\omega' T(\boldsymbol{x}',\boldsymbol{\nu}^m,\theta)}\Big\},\end{aligned} \tag{50}$$

where we have left the phase directions in the argument of the in-plane amplitudes to distinguish them. The Jacobian inside the integral can be found in (Burridge *et al.* 1998). The integral over migration dip makes this an inverse by generalized Radon transform (GRT).

4 TRANSFORMATION INTO ANGLE GATHERS

When constructing angle gathers we fix the scattering angle, θ, and integrate over the migration dip, $\boldsymbol{\nu}^m$. The restriction can introduce artifacts in the angle gathers when the medium is inhomogeneous (i.e. in the presence of caustics) due to multipathing in the recorded wave-field. These artifacts are different from the artifacts due to the failure of assumption 3. These artifacts are not present in the inversion by equation (50) since they stack destructively (Stolk and de Hoop 2002).

Since the restriction to a fixed scattering angle means that we no longer stack over all the data, but rather over subsets of the data that change with image point and scattering angle, we reintroduce $\boldsymbol{x}^s$ and $\boldsymbol{x}^r$ as the variables of integration. This requires the notion of branches of the two-way travel time (see equation (10)). We define $\theta^{(i)}$ as $\theta(\boldsymbol{\alpha}^r,\boldsymbol{x}',\boldsymbol{\alpha}^s)$ (cf. (34)-(35)) composed with the inverse of map (27), associating the scattering angle with the acquisition coordinates $\boldsymbol{x}^s,\boldsymbol{x}^r$. We define the 'angle' transform $\mathbf{K}$ (the GRT) via a restriction of the imaging operator $\mathbf{L}^\star$ in equation (22) to fixed angle $\theta^{(i)}=\theta'$, where $i\in I$ indexes the travel time branch. We reintroduce the sum over the different travel time branches suppressed since equation (9). Thus we multiply the kernel of $\mathbf{L}^\star$ in equation (22) by a delta function, $\delta(\theta^{(i)}-\theta')$. The kernel of $\mathbf{K}$, denoted by $\mathcal{K}_{mn}$, can be written as an oscillatory integral (after a change of $\boldsymbol{x}'$ to $\boldsymbol{x}$)

$$\begin{aligned}\mathcal{K}_{mn}(\boldsymbol{x},\theta',\boldsymbol{x}^s,\boldsymbol{x}^r,t)=\sum_{i\in I}&(2\pi\sqrt{\mathrm{i}})^{-1}\int\omega'^{3/2}\rho^{(0)}(\boldsymbol{x})\\ &\cdot\frac{(A^{||}(\boldsymbol{x}^s,\boldsymbol{x})A^{||}(\boldsymbol{x},\boldsymbol{x}^r))^\star}{\mathcal{L}^{\perp}(\boldsymbol{x}^r,\boldsymbol{x},\boldsymbol{x}^s)^\star}\mathrm{w}(\boldsymbol{x}^r,\boldsymbol{x},\boldsymbol{x}^s)h_m(\boldsymbol{x}^r;\boldsymbol{x})h_n(\boldsymbol{x}^s;\boldsymbol{x})e^{-\mathrm{i}\Phi^{(i)}(\boldsymbol{x},\boldsymbol{x}^r,\boldsymbol{x}^s,t,\theta',\omega',\varepsilon)}\mathrm{d}\omega'\mathrm{d}\varepsilon.\end{aligned} \tag{51}$$

Here ε is the Fourier dual of the scattering angle θ (Stolk and de Hoop 2002) and

$$\Phi^{(i)}(\boldsymbol{x},\boldsymbol{x}^r,\boldsymbol{x}^s,t,\theta',\omega',\varepsilon)=\omega'[T^{(i)}(\boldsymbol{x}^r,\boldsymbol{x},\boldsymbol{x}^s)-t]+\varepsilon[\theta'-\theta^{(i)}(\boldsymbol{x}^r,\boldsymbol{x},\boldsymbol{x}^s)]. \tag{52}$$

The artifacts of the restriction can be evaluated by considering the composition $\mathbf{KL}$, a θ'-family of operators each member of which resembles the normal operator. The artifacts in the angle gathers can be recognized by their 'move-out' in angle. A multi-dimensional filter in the Fourier domain (see equation (51)) can be applied to remove the artifacts associated with $|\varepsilon|\geq\varepsilon_0>0$. Brandsberg-Dahl *et al.* (2003b) suppressed the artifacts by so-called *focusing in dip*.

By proceeding as suggested above using the appropriate changes of variables leading up to equation (50), the angle depen-

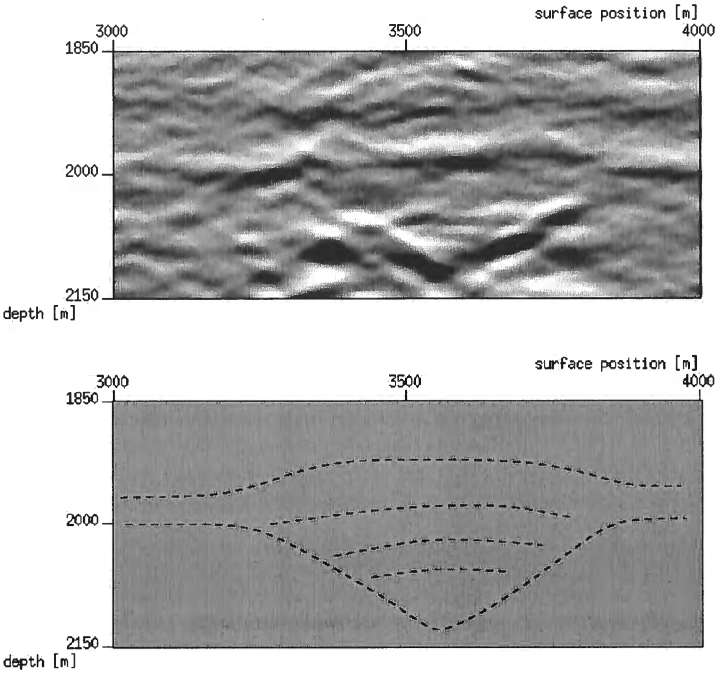

Figure 7. Top figure is a high resolution image of detail from Figure 6. The image shows a possible slump fault or erosive channel deposit. Their dominant features are captured in this 2-D slice. The bottom figure is a schematic drawing of the image as an erosive channel deposit.

the horizontal layer and new material has deposited later leaving a slight curve in the layer, the V-shape. Both of these geological features have a slowly varying behavior in one direction. Given that our computational plane is intersecting at the right angle, the main features are described by this slice and the smoothly varying behavior are in the out-of-plane direction. Hence the 2.5-D framework applies with decent accuracy.

Figure 8 shows LS-AVA-compensated common-image point gathers for PP- and PS-scattering events, respectively, created as a combination of the parameters from equation (53) at surface position $x_1 = 1500\,m$. The combinations are chosen as the appropriate acoustic impedances; i.e. P-wave impedance for the PP-gather and S-wave impedance for the PS-gather. The vertical scale is from $800\,m$ to $3200\,m$ in depth. Following convention, both common-image point gathers are plotted as functions of incoming P-wave angle, ranging from 0 to 35 degrees. Note that the zero angle contribution of the PS-gather is set to zero as this is not defined. Only a subset of the reflectorsare comparable in depth between PP- and PS-gathers, yet with very different strength in amplitudes. As mentioned, the imaging is done in an isotropic smooth background medium, yet the medium is anisotropic. The anisotropy has a strong effect on the travel times and thus the depths. This can explain why certain reflectors,when comparing the two common-image point gathers, seem to be at different depths. Note that the amplitude behavior is close to constant with angle. Hence, for this range of scattering angles, the LS-AVA-compensation in equation (53) suppresses the amplitude behavior. This is important in angle tomography through the use of 'differential semblance' (Brandsberg-Dahl *et al.* 2003a). It is clear from this example, that a joint treatment of (q)P and (q)S velocities becomes necessary in reflectiontomography.

6 DISCUSSION

This paper presents the general form of 2.5-D modeling, imaging-inversion and AVA-compensated angle transform formulas in anisotropic elastic media under necessary and sufficient assumptions. The results extend those of Bleistein (1986) to the cases of multipathing and anisotropic elasticity. Assumption 1 restricts us to a monoclinic medium as the lowest possible symmetry. However, under the addition of assumption 2, the wave propagation is restricted to the plane. Any symmetries lower than a transversely isotropic medium with the symmetry axis contained in the plane of consideration have to be excluded for the purpose of inversion and reflectiontomography.

In the presence of caustics, artifacts may be generated by the imaging-inversion procedures. Subject to the Bolker condition such artifacts are avoided. We have made the observation that the 2-D Bolker condition in the symmetry plane implies the Bolker condition in three dimensions in the framework of the common azimuth acquisition geometry. Artifacts in the common image-point applying the appropriate out-of-plane 'annihilator' as a Tikhonov regularizer to the misfit functional

$$J[\underline{\mathbf{m}}] = \frac{1}{2} \int \Big\{ \int\int \Big| \big[\partial_\theta - (\partial_\theta \Xi(\boldsymbol{x},\theta,x_2))\Xi(\boldsymbol{x},\theta,x_2)^{-1}\big] \hat{\mathbf{c}}^{(1)}[\underline{\mathbf{m}}](\boldsymbol{x};\theta,x_2) \Big|^2 \,\mathrm{d}\boldsymbol{x}\mathrm{d}\theta \\ + \lambda \int \Big| \partial^2_{x_2} \mathbf{c}^{(0)}[\underline{\mathbf{m}}](\boldsymbol{x},x_2) \Big|^2 \,\mathrm{d}\boldsymbol{x} \Big\} \,\mathrm{d}x_2, \qquad (54)$$

where (cf. equation (38))

$$\Xi(\boldsymbol{x},\theta,x_2) = \frac{\mu_{LS}(\boldsymbol{x},\boldsymbol{\nu}^m,\theta)}{|\mathcal{L}^\perp(\boldsymbol{x},\boldsymbol{\nu}^m,\theta)|^2} \frac{\partial(\boldsymbol{\alpha}^s,\boldsymbol{\alpha}^r)}{\partial(\boldsymbol{\nu}^m,\theta)} \langle \Gamma(\boldsymbol{x},\boldsymbol{\nu}^m)\rangle^{-1} \mathbf{w}(\boldsymbol{x},\boldsymbol{\nu}^m,\theta)\mathbf{w}^T(\boldsymbol{x},\boldsymbol{\nu}^m,\theta). \qquad (55)$$

All relevant parameters of equation (55) are calculated for $\boldsymbol{\nu}^m$ in the wavefront set of $\hat{\mathbf{c}}^{(1)}$. $\mathbf{c}^{(0)}[\underline{\mathbf{m}}](\boldsymbol{x},x_2)$ is a vector of the parameters of the background medium given the current parametrization $\underline{\mathbf{m}}$. λ in equation (54) is a statistical quantity controlling the trade-off between in-plane and out-of-plane fit (Tenorio 2001) and $\boldsymbol{x} = (x_1,x_3)$. ∂_θ and ∂_{x_2} are the partial derivatives with respect to the scattering angle and out-of-plane coordinate, respectively. The LS-AVA-compensated inversion result from equation (53) is denoted $\hat{\mathbf{c}}^{(1)}[\underline{\mathbf{m}}](\boldsymbol{x};\theta,x_2)$ to emphasize that it is generated using the current parametrization of the smooth background model, $\underline{\mathbf{m}}$, for the slice at out-of-plane coordinate x_2. The minimum of this function indicates a smooth background model such that the data are in the range of the 2.5-D modelling operator. In this way the 2.5-D framework provides a fast computational tool for 3-D tomography and an increased ability to monitor the regularization of the search for a fitting model.

APPENDIX A: THE 2.5-D BORN MODELLING FORMULA

The 3-D Born formula is a high frequency approximation to the field scattered off the medium perturbation at $\boldsymbol{x} \in \mathbb{R}^3$, collected at the receiver position $\boldsymbol{x}^r$ generated by a source at $\boldsymbol{x}^s$. This field is calculated by substituting the appropriate GRA Green's functions (2) in the Born approximation. It gives that, under assumption 1 on the medium, the m-direction of the scattered field at the receiver position $\boldsymbol{x}^r$ due to a n-component source at $\boldsymbol{x}^s$ written as a Fourier integral operator is

$$
\begin{aligned}
&U_{mn}(\boldsymbol{x}^r, \boldsymbol{x}^s, \omega) \approx \\
&\qquad \int_X \left\{ \int_{\mathbb{R}} \omega^2 h_m(\boldsymbol{x}^r) \rho^{(0)}(\boldsymbol{x}) A(\boldsymbol{x}^s, \boldsymbol{x}) A(\boldsymbol{x}, \boldsymbol{x}^r) \mathbf{w}^T(\boldsymbol{x}^r, \boldsymbol{x}, \boldsymbol{x}^s) e^{\mathrm{i}\omega T(\boldsymbol{x}^r, \boldsymbol{x}, \boldsymbol{x}^s)} h_n(\boldsymbol{x}^s) \mathrm{d}x_2 \right\} \\
&\qquad\qquad \cdot \mathbf{c}^{(1)}(x_1, x_3) \mathrm{d}x_1 \mathrm{d}x_3. \qquad \text{(A1)}
\end{aligned}
$$

The medium perturbation $\mathbf{c}^{(1)}$ and the radiation patterns $\mathbf{w}$ are, for the lowest possible symmetry (triclinic), 22 × 1-matrices of the form as in equations (15) and (16), respectively. The domain of integration of the (x_1, x_3)-coordinates, X, is defined in subsection 2.2.

Upon scaling, $x_2 = \tilde{x}_2/|\omega|$, we recognize the phase variables $(\tilde{x}_2, \omega)$. We proceed as in Bleistein (1986) and use the method of stationary phase to integrate out the out-of-plane variable x_2 in (A1). The one-dimensional stationary phase formula approximates integrals of the type

$$
\int f(\sigma) e^{\mathrm{i}\omega T(\sigma)} \mathrm{d}\sigma \approx \sqrt{\frac{2\pi}{|\omega| |\partial_\sigma^2 T(\sigma_0)|}} f(\sigma_0) e^{\mathrm{i}\omega T(\sigma_0) + \mathrm{i}(\pi/4)\mathrm{sgn}(\omega)\mathrm{sgn}(\partial_\sigma^2 \mathrm{T}(\sigma_0))}, \qquad \text{(A2)}
$$

for sufficiently large $|\omega|$ and $\partial_\sigma^2 T(\sigma_0) \neq 0$, where σ_0 is the stationary point, such that $\partial_\sigma T(\sigma)|_{\sigma=\sigma_0} = 0$. In the mentioned integral, the stationary point is given by

$$
\partial_{x_2} T(\boldsymbol{x}^r, \boldsymbol{x}, \boldsymbol{x}^s) = p_2^s + p_2^r = 0. \qquad \text{(A3)}
$$

Due to assumptions 1 and 2, the only solution to (A3) is $p_2^s = p_2^r = 0$ which implies that the stationary point is $x_2 = 0$. A discussion on this is given in the main text. Observe that the sum of the slownesses in equation (A3) also occurs in the common azimuth case, equation (18). The second derivative of the phase function at the stationary point is

$$
\partial_{x_2}^2 T(\boldsymbol{x}^r, \boldsymbol{x}, \boldsymbol{x}^s)\big|_{x_2=0, p_2=0} = (\partial_{x_2} p_2^s + \partial_{x_2} p_2^r)|_{x_2=0, p_2=0} = \frac{1}{Q_2^{\perp}(\boldsymbol{x}, \boldsymbol{x}^s)} + \frac{1}{Q_2^{\perp}(\boldsymbol{x}, \boldsymbol{x}^r)}, \qquad \text{(A4)}
$$

where $Q_2^{\perp}(\boldsymbol{x}, \boldsymbol{x}^s)$ and $Q_2^{\perp}(\boldsymbol{x}, \boldsymbol{x}^r)$ are the out-of-plane geometrical spreading factors defined in equation (5) for the rays connecting the imaging point $\boldsymbol{x}$ with the source $\boldsymbol{x}^s$ and receiver $\boldsymbol{x}^r$, respectively.

Remark 4.
In points, in phase space, where either $Q_2^{\perp}(\boldsymbol{x}, \boldsymbol{x}^s)$ or $Q_2^{\perp}(\boldsymbol{x}, \boldsymbol{x}^r)$ tends to zero the travel time function is not smooth. We observe this in equation (A4) where the Hessian of the travel time function will tend towards infinity and will not be defined. This essentially means that the stationary phase argument does not hold. The integral over x_2 in equation (A1) remains. Out-of-plane caustics are thus not allowed for the stationary phase formula to be applicable. We restrict the analysis in the following to rays with no out-of-plane caustics.

From this it follows that $\mathrm{sgn}(\partial_{x_2}^2 T(\boldsymbol{x}^r, \boldsymbol{x}, \boldsymbol{x}^s)|_{x_2=0}) = 1$ since the out-of-plane geometrical spreading is positive. The stationary phase formula (A2) then yields for the x_2 integral (in view of Remark 4)

$$
\begin{aligned}
&\int_X \left[\omega^2 \int_{\mathbb{R}} h_m(\boldsymbol{x}^r) \rho^{(0)}(\boldsymbol{x}) A(\boldsymbol{x}^s, \boldsymbol{x}) A(\boldsymbol{x}, \boldsymbol{x}^r) \mathbf{w}^T(\boldsymbol{x}^r, \boldsymbol{x}, \boldsymbol{x}^s) \mathbf{c}^{(1)}(\boldsymbol{x}) e^{\mathrm{i}\omega T(\boldsymbol{x}^r, \boldsymbol{x}, \boldsymbol{x}^s)} h_n(\boldsymbol{x}^s) \mathrm{d}x_2 \right] \mathrm{d}x_1 \mathrm{d}x_3 \\
&\qquad \approx \sqrt{2\pi\mathrm{i}}\,\omega^{3/2} \int_X h_m(\boldsymbol{x}^r) \frac{(Q_2^{\perp}(\boldsymbol{x}, \boldsymbol{x}^s) Q_2^{\perp}(\boldsymbol{x}, \boldsymbol{x}^r))^{1/2}}{(Q_2^{\perp}(\boldsymbol{x}, \boldsymbol{x}^s) + Q_2^{\perp}(\boldsymbol{x}, \boldsymbol{x}^r))^{1/2}} \rho^{(0)}(\boldsymbol{x}) A(\boldsymbol{x}^s, \boldsymbol{x}) A(\boldsymbol{x}, \boldsymbol{x}^r) \\
&\qquad\qquad \cdot \mathbf{w}^T(\boldsymbol{x}^r, \boldsymbol{x}, \boldsymbol{x}^s) \mathbf{c}^{(1)}(\boldsymbol{x}) e^{\mathrm{i}\omega T(\boldsymbol{x}^r, \boldsymbol{x}, \boldsymbol{x}^s)} h_n(\boldsymbol{x}^s) \Big|_{x_2=0, p_2=0} \mathrm{d}x_1 \mathrm{d}x_3. \qquad \text{(A5)}
\end{aligned}
$$

Using equation (6) this equation reduces to the 2.5-D modelling formula (9) in the main text (here in the frequency domain),

$$
\begin{aligned}
&U_{mn}(\boldsymbol{x}^s, \boldsymbol{x}^r, \omega) \\
&\qquad = \sqrt{2\pi\mathrm{i}}\,\omega^{3/2} \int_X h_m(\boldsymbol{x}^r) \rho^{(0)}(\boldsymbol{x}) \frac{A^{||}(\boldsymbol{x}^s, \boldsymbol{x}) A^{||}(\boldsymbol{x}, \boldsymbol{x}^r)}{\mathcal{L}^{\perp}(\boldsymbol{x}^r, \boldsymbol{x}, \boldsymbol{x}^s)} \mathbf{w}^T(\boldsymbol{x}^r, \boldsymbol{x}, \boldsymbol{x}^s) \mathbf{c}^{(1)}(\boldsymbol{x}) e^{\mathrm{i}\omega T(\boldsymbol{x}^r, \boldsymbol{x}, \boldsymbol{x}^s)} h_n(\boldsymbol{x}^s) \mathrm{d}\boldsymbol{x}. \qquad \text{(A6)}
\end{aligned}
$$

Spectral element modeling of fault-plane reflections and their sensitivity to stacking and migration errors

Matthew Haney[1], Roel Snieder[1] and Jean-Paul Ampuero[2]
[1] *Center for Wave Phenomena, Colorado School of Mines, Golden, CO 80401*
[2] *Geosciences Department, Princeton University, Princeton, NJ 08544*

ABSTRACT

Simulating the 2D elastic wave equation via the spectral element method (SEM) has advantages over other modeling techniques for studying seismic reflectivity associated with faults. For instance, irregular geometries can be easily accommodated and slip boundary conditions are naturally implemented. We run through a complete modeling exercise incorporating both SEM forward modeling of shot gathers over a realistically-sized numerical model containing a normal fault and processing of the simulated data to reconstruct post-stack time-migrated images of the kind that are routinely interpreted. To gain insight into the pitfalls involved in interpreting, for instance, amplitudes on post-stack time-migrated data, we develop a simple theory for gauging the amplitude and phase errors resulting from stacking and migration velocity errors. We utilize our modeling capabilities to test the theoretical results pertaining to stacking velocity errors. We find that the character of fault-plane reflections are relatively more robust to stacking and migration errors than the reflections from flat-lying layers and conclude that, in order to gauge stacking and migration errors, information on the acquisition geometry is critical. Though the robust nature of the fault-plane reflections we model may be a special case for post-stack migration, the claim that fault-plane reflections are less sensitive to stacking errors should hold more generally for pre-stack migration.

Key words: weak formulation, stack response, fault reflectivity

INTRODUCTION

Seismic data acquisition and processing have evolved to the point that fault-plane reflections are often imaged under favorable conditions, such as above-salt in the Gulf of Mexico (Liner, 1999). Reflections originating from fault-zones may hold important information about fluid movement along faults or the capacity of a fault to act as a seal (Haney *et al.*, 2004a). Faults have long stumped interpreters by virtue of their split-personality as effective hydrocarbon traps and pathways for hydrocarbons to move from deep kitchens into shallower, economically producible reservoirs. Any light that seismic data can shed on the situation would be useful.

To gain a stronger grasp on the factors at play in causing fault-plane reflectivity and errors that can deteriorate their imaging, we have pursued a complete numerical study of wave interaction with fault models. By complete, we mean that we do not simply model the entire measured (elastic) wavefield with high fidelity, but process the data back into its time-migrated image, which is at what point many geoscientists in the oil industry gain access to and begin examining seismic data. We model the wavefield with an implementation of the spectral element method (SEM) written by Dimitri Komatitsch and Jean-Pierre Vilotte at the Institut de Physique du Globe in Paris, France. Further improvements have been made to original code by the third author of this paper in the course of his graduate work (Ampuero, 2002). Processing of the wavefield output by the SEM code has been accomplished in Seismic Unix (Stockwell, 1997).

SEM forward modeling has been run in serial (one node for each shot) on a 32 processor pentium IV xeon (3.0 GHz) cluster. All of the processing has been performed on a workstation using the Seismic Unix package (Stockwell, 1997). Fig. 1 depicts the geometry of the model and Table I shows the material properties of the various layers. The normal fault we model has a vertical throw of 20 m, a typical value for a small growth fault in the Gulf of Mexico (Rowan *et al.*, 1998). The model we present here, called Model A, has been introduced by Townsend *et al.* (1998) to study changes in seismic attributes due to faults disrupting the lateral continuity of events.

We mesh the interior of the computational grid shown in Fig. 1 using a freely available mesh program developed by INRIA called EMC2. The program can be downloaded at:

http://www-rocq.inria.fr/gamma/cdrom/www/emc2/eng.htm

For this example and others in this paper, we used a semi-structured mesh since the geometries are not overly complex. Though the mesh has some structure, it honors the sharp edges at the fault. After initial construction of the mesh, the quadrangle elements are regularized so that their shapes mimic squares as closely as possible.

Layer	Thickness (m)	V_P (m/s)	ρ (kg/m^3)
1	900	2000	2000
2	50	2350	2080
3	30	2400	2150
4	50	2500	2130
5	30	2600	2200
6	90	2750	2180
7	850	2800	2250

Table I. Model A for our SEM examples. $V_S = V_P/\sqrt{3}$

We show a typical shot record in the left panel of Fig. 2. Since the SEM code is elastic, both primary and converted waves show up on the vertical component of the displacement seismograms. It should be noted that, if we had introduced a physically realistic vertical velocity gradient in the uppermost layer, ray bending would have served to separate the P- and S-waves more effectively into the vertical and horizontal components. We relied on model-specific muting of the converted waves in order to proceed with conventional P-wave time-processing. We first subtracted the direct waves by running a homogeneous subsurface simulation with the elastic properties of layer 1 (see Fig. 1 and Table I). After this step, we performed the geometrical spreading correction, NMO, constant-velocity DMO, and stacked to simulate zero-offset data. The stacked section is shown in the middle panel of Fig. 2. Note the significant diffracted energy coming from the sharp cor-

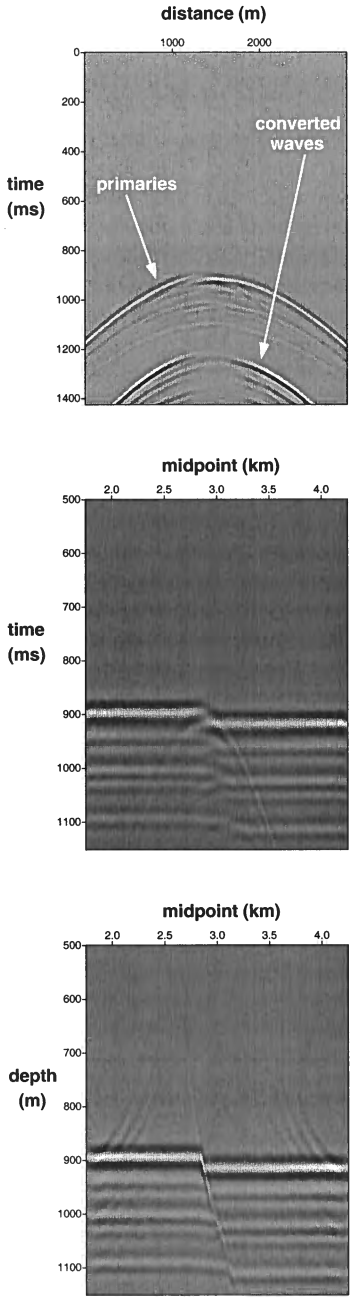

Figure 2. Three stages of data processing. On the top is a shot record from the SEM code after subtracting off the direct waves, leaving the purely up-going wavefield. The middle panel depicts the data in the midpoint domain after geometric-spreading, NMO, DMO, and stack. Note the diffractions from the bed terminations at the fault plane. Finally, the migrated image is shown on the bottom, with the fault plane clearly illuminated. The migration, though constant velocity, was depth converted.

integral over offset. Formally taking the limit of continuous sources/receivers, $n \to \infty$ and $h \to 0$, and allowing the discrete variable kh to become the continuous variable x results in

$$K(\omega) = \frac{1}{L_s} \times \int_{-\frac{L_s}{2}}^{\frac{L_s}{2}} \exp\left[i\omega\left(\sqrt{T_0^2 + \frac{x^2}{v_{tr}^2}} - \sqrt{T_0^2 + \frac{x^2}{v_{st}^2}}\right)\right] dx. \quad (7)$$

We simplify the evaluation of the integral in equation (7) by letting the spreadlength go to infinity, $L_s \to \infty$. This simplification avoids accounting for Cornu's spiral in the Fresnel integral (Born & Wolf, 1980). Denoting $I(\omega) = K(\omega)L_s$ as a scaled version of the transfer function gives

$$I(\omega) = \int_{-\infty}^{\infty} \exp\left[i\omega\left(\sqrt{T_0^2 + \frac{x^2}{v_{tr}^2}} - \sqrt{T_0^2 + \frac{x^2}{v_{st}^2}}\right)\right] dx. \quad (8)$$

This type of integral can be approximately evaluated by the method of stationary phase (Born & Wolf, 1980). In this limit, $I(\omega)$ is given by

$$I(\omega) = \sqrt{2\pi}e^{i\pi/4}\left[\frac{\partial^2\phi}{\partial x^2}\right]_{x_{st}}^{-1/2} e^{i\phi(x_{st})}, \quad (9)$$

where x_{st} is the stationary point of the phase function $\phi(x)$ of equation (8) that is given by

$$\phi(x) = \omega\left(\sqrt{T_0^2 + \frac{x^2}{v_{tr}^2}} - \sqrt{T_0^2 + \frac{x^2}{v_{st}^2}}\right). \quad (10)$$

In equation (9), the subscript x_{st} indicates the quantity is to be evaluated at the stationary point. To find the stationary point, we set the x-derivative of the phase function to zero

$$\frac{\partial\phi}{\partial x} = \omega x\left[\frac{1}{v_{tr}^2\sqrt{T_0^2 + \frac{x^2}{v_{tr}^2}}} - \frac{1}{v_{st}^2\sqrt{T_0^2 + \frac{x^2}{v_{st}^2}}}\right] = 0. \quad (11)$$

From equation (11), we identify the stationary point $x_{st} = 0$.

After calculating the second x-derivative of the phase function and evaluating it at the stationary point, the scaled transfer function $I(\omega)$ can be expressed, in the stationary phase approximation, as

$$I(\omega) = \sqrt{\frac{2\pi T_0}{|\omega|}}\frac{\exp(i \ \mathrm{sgn}(v_{st} - v_{tr})\pi/4)}{|\ (v_{tr}^{-2} - v_{st}^{-2})^{-1/2}\ |}. \quad (12)$$

Equation (12) states that, when an event is stacked with a velocity that is not the true velocity, a phase shift of $\pm 45^\circ$ results. The phase shift is positive or negative depending on whether the stacking velocity is higher or lower than the true velocity. The amplitude of $I(\omega)$ scales with $\sqrt{T_0}$ and as a quasi-hyperbola as a function of stacking velocity, $|\ (v_{tr}^{-2} - v_{st}^{-2})^{-1/2}\ |^{-1}$. The amplitude response is also inversely proportional to $\sqrt{\omega}$. Hence, stacking errors cause the stacked waveform to be lower in frequency than it should be - an effect identical to stacking NMO-stretched waveforms. Note that the factor of $1/\sqrt{\omega}$ does not apply at $v_{st} = v_{tr}$. From our construction of the series in equation (4), the phase delays Δt_k are all zero for $v_{st} = v_{tr}$ and stacking does not change the frequency content of the waveform. We venture that, for finite frequencies, the frequency filtering aspect of mis-stacking vanishes gradually as $v_{st} \to v_{tr}$.

As a result of the $\pm 45^\circ$ phase shifts introduced by stacking errors, incorrectly stacked events acquire a time advance or delay (Gausland, 2004). Such a property suggests a complimentary method of performing velocity analysis. Traditional semblance-based velocity analysis exploits the fact that the amplitude of the stack maximizes at the true velocity. This is evident from equation (12) since the amplitude of $I(\omega) \to \infty$ when $v_{st} = v_{tr}$. Alternately, the time advance/delay caused by the phase shift vanishes for the correct stacking velocity. Cross-correlation of waveforms with different stacking velocities could provide the time-lag as a function of stacking velocity. Instead of picking "bullseyes" on the semblance contour plot, zero-crossings would be picked on a time-advance/delay plot.

survey parameter	value
offset spacing, h	400 m
fold, $2n + 1$	5
true NMO velocity, v_{tr}	2000 m/s
erroneous stacking velocity, v_{st}	1800 m/s
zero-offset two-way-traveltime, T_0	0.9 s
dominant frequency	20 Hz

Table II. Parameters for studying stacking errors

NUMERICAL TEST OF MIS-STACKING

We illustrate the impact of stacking velocity errors on a post-stack migrated image with a numerical example, using the SEM code. Our example does not satisfy the approximations we made above to obtain analytic results for the stack response - there is finite spreadlength, discrete receivers, and finite frequency. To evaluate the stack response, we numerically calculate the exact transfer function $K(\omega)$ - the finite series appearing in equation (4). Table II summarizes the parameters from our numerical survey that are necessary to evaluate the exact transfer function. Note that our offset spacing is two times the shot spacing (see Fig. 1) and that the velocity of layer 1 serves as the true NMO velocity. We generate two tests for the stacking velocity - one with the true NMO velocity (2000 m/s) and another with a -10% error (1800 m/s). The material properties for the model

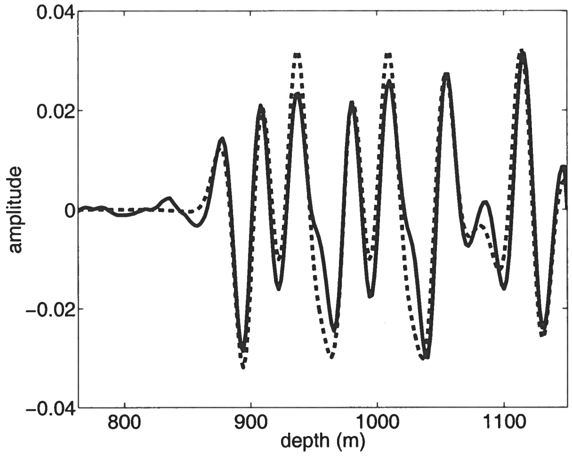

Figure 5. An overlap of the correct stacking velocity migration (solid) and the convolutional model (dashed) along the white, dashed line of Fig. 4.

relative to the amplitude at the correct stacking velocity and have acquired a phase shift of ~ 60°. For our survey parameters, it is evident that we are far from the geometrical optics limit, when the phase shifts away from the true stacking velocity should be ± 45°. This demonstrates that, away from the geometrical optics limit, the error due to stacking velocity errors are mostly determined by the survey and acquisition geometry.

To test the array-based *f*-*x* domain theory for stacking errors, we ran through the complete sequence of SEM and processing with Model B and formed migrated images both with and without stacking velocity errors. Note that a stacking velocity error implies that both the NMO and constant-velocity DMO steps had erroneous (-10%) velocities. The migration velocity for the following examples is kept as the correct migration velocity. Two migrated images are displayed in Fig. 4. In comparing the migration without stacking errors to the migration with, the degradation of the image with errors is noticeable.

To quantify the error in the images, we first took a slice from the migrated image shown by the white dashed lines in Fig. 4. This slice of the migrated image is shown as a solid line in Fig. 5. Also plotted in Fig. 5 is the convolutional model obtained from our far-field wavelet and the known reflectivity series. Good agreement exists between the zero-offset migration and the convolutional model, as there should be.

In the top panel of Fig. 6, we plot the same convolutional model as in Fig. 5, but now show the slice of the migration with incorrect stacking velocity in the solid line. As discussed before, amplitude degradation and phase shift is evident between the convolutional model and the migration with erroneous stacking velocity. As a further check if the array-based theory for stacking errors accurately describes the migrated waveform in the top panel of Fig. 6, we multiplied the far-field wavelet by 0.6, phase-shifted it by 60°, and recomputed the convolutional model. These factors come from the circles at -10% error in Fig. 3 for the flat reflector. The damped and shifted version of the convolutional model is plotted in the bottom panel of Fig. 6 together with the migration with the erroneous stacking velocities. Indeed, by virtue of the excellent match of the two curves in the bottom plot of Fig. 6, incorrect stacking velocities have caused the amplitude and phase response of the migrated waveform to be as that predicted by the exact array-based theory (not in the geometrical optics limit).

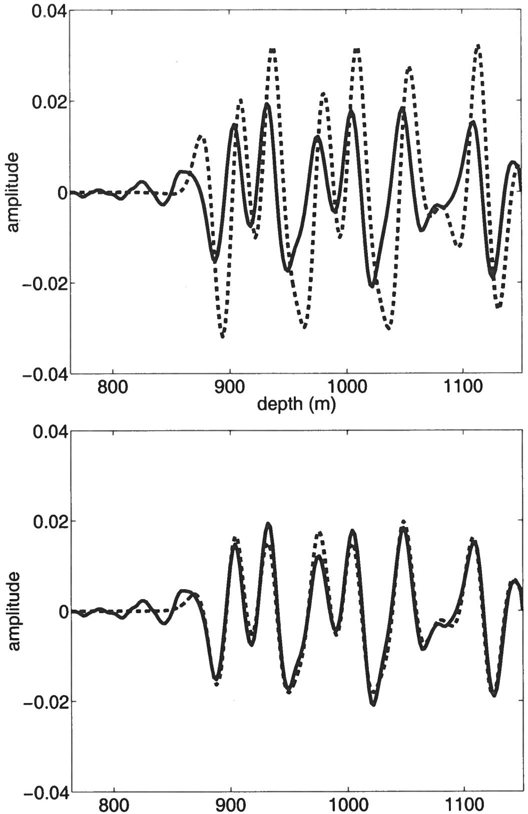

Figure 6. On the top: an overlap of the incorrect stacking velocity migration (solid) and the correct convolutional model (dashed) along the white, dashed line of Fig. 4. Note the disparity in the amplitudes and phases of the two plots. On the bottom: an overlap of the incorrect stacking velocity migration (solid) and the incorrect convolutional model (dashed) calculated by dampening and phase shifting the source wavelet by the factors predicted in Fig. 3.

We now turn our attention to the impact of the stacking velocity errors on the fault-plane reflections instead of the flat layers. Shown in Fig. 7 are dip-filtered versions of the migrations both with and without the errors in stacking velocity. We dip-filter the images in order to isolate the reflectivity from the fault plane, as in Haney *et al.* (2004a). The main difference here is that the dip-filter is in the *f*-*k* domain and not the *t*-*x* do-acquisition geometries (strike-line instead of dip-line), but once their reflection has been captured, their reconstructed finite-frequency waveform is relatively robust in shape and amplitude. Particularly if velocity analysis is performed on the reflections from flat layers (since there are more of these than fault-plane reflections), the associated error in the velocity picks is reduced when considering the reflections from the fault-plane.

THE MIGRATION RESPONSE

We have already touched on the filtering action of migration in our discussion on the stack response, specifically with equation (12). The connection with the migration response exists for $v_{tr} \rightarrow \infty$. When an event has a true stacking velocity that is infinite and it is stacked in the offset domain with a hyperbolic trajectory described by a finite velocity, an analogy exists with diffraction summation of a flat reflector in the midpoint domain. To pursue this further, in the case of $v_{tr} \rightarrow \infty$, equation (12) becomes

$$I(\omega) = v_{st}\sqrt{\frac{2\pi T_0}{\omega}}\exp(-i\pi/4). \tag{13}$$

Two of the three corrections made to simple diffraction summation for Kirchhoff migration are shown in equation (13). The factor $v_{st}\sqrt{T_0}$ in the transfer function requires multiplying the result of diffraction summation by $1/v_{st}\sqrt{T_0}$ to recover the true waveform. Yilmaz (1987) calls this the 2D geometrical spreading factor. Furthermore, to recover the true waveform after diffraction summation requires multiplying by $\exp(i\pi/4)\sqrt{\omega}$ (a half-derivative). This correction is called the wavelet shaping factor (Yilmaz, 1987). The obliquity factor does not appear in equation (13) - this is a result of the reflector being flat for infinite moveout velocity.

In the rest of this section, we briefly generalize the above connection with migration for the case of a dipping reflector and recover the obliquity factor, which was not present for a flat reflector. Moreover, we are able to confirm the well-known fact that the amplitudes and phases of post-stack time-migrated waveforms from planar features are virtually insensitive to migration velocity errors. The same cannot be said for diffractions, which can contain errors due to incorrect migration velocities just as stacked waveforms contained errors due to mis-stacking.

We want to study the phase and amplitude distortion of a waveform at x_{in}, t_{in} (in the zero-offset section) after it is migrated to an output point x_{out}, t_{out}. Since we are primarily interested in fault-plane reflections, we assume a single dipping event in the zero-offset section with a time dip

$$p = 2\ \sin\theta/v_{tr}, \tag{14}$$

where θ is the dip angle and v_{tr} is the true migration velocity. When the zero-offset section is migrated with a velocity v_m not necessarily equal to v_{tr}, the hyperbola that is tangent to the reflector at x_{in}, t_{in} is described by

$$t_{hyp}(x) = \sqrt{t_{in}^2(1 - p^2v_m^2/4) + \frac{4(x - x_{in} + pv_m^2t_{in}/4)^2}{v_m^2}}, \tag{15}$$

where the output points are

$$t_{out} = t_{in}\sqrt{1 - p^2v_m^2/4}, \tag{16}$$

$$x_{out} = x_{in} - pv_m^2t_{in}/4. \tag{17}$$

The equation describing the dipping reflector in the zero-offset section is

$$t_{ref}(x) = px + t_{in} - px_{in}. \tag{18}$$

From equations (15) through (18), the diffraction summation transfer function can be written

$$K(\omega) = \frac{1}{2n+1}\sum_{k=-n}^{n} e^{i\omega\Delta t_k}, \tag{19}$$

where now $2n + 1$ is the number of midpoints in the migration aperture and Δt_k are the time shifts given by

$$\Delta t_k = t_{ref}(kh) - t_{hyp}(kh), \tag{20}$$

with h representing the spacing between midpoints.

Moving from the finite series to an integral expression as we did earlier for stacking, the diffraction summation response is given, for the case of infinite aperture and continuous midpoints, by

$$I(\omega) = \int_{-\infty}^{\infty} \exp\left[i\omega(t_{ref}(x) - t_{hyp}(x))\right] dx, \tag{21}$$

where $t_{ref}(x)$ and $t_{hyp}(x)$ are defined above. We note that, just as we ignored NMO-stretch for the stack response, we neglect the analogous stretch due to migration. The stretch caused by migration is manifested through rotation and steepening of a reflector in the migrated image. Its origins are the same as NMO-stretch.

Applying the method of stationary phase to the integral in equation (21) yields a stationary point at x_{in}. The resulting expression for the scaled transfer function $I(\omega)$ in the infinite frequency limit is

$$I(\omega) = \frac{\sqrt{2\pi}}{2}\frac{\exp(-i\pi/4)}{\sqrt{\omega}}\frac{t_{in}}{t_{out}}v_m\sqrt{t_{in}}. \tag{22}$$

From equation (22), it is evident that the waveform coming out of the diffraction stack must be filtered by the half-derivative $\exp(i\pi/4)\sqrt{\omega}$ and divided by $v_m\sqrt{t_{in}}$ to give the original waveform. In addition, for a dipping reflector, the factor of t_{in}/t_{out} appearing in equation (22) must be taken into account. This is the obliquity factor, whose effect is to dampen the amplitude of dipping reflectors, such as fault-plane reflections. Note that nowhere in equation (22) does the time dip, p, and therefore the true migration velocity, v_{tr} appear. This demonstrates the insensitivity of the amplitude and phase of

the South Eugene Island Basin, Gulf of Mexico. *Earth and Planetary Science Letters*, **202**, 321–335.

Rowan, M. G., Hart, B. S., Nelson, S., Flemings, P. B., & Trudgill, B. D. 1998. Three-dimensional geometry and evolution of a salt-related growth-fault array: Eugene Island 330 field, offshore Louisiana, Gulf of Mexico. *Marine and Petroleum Geology*, **15**, 309–328.

Schoenberg, M. 1980. Elastic wave behavior across linear slip interfaces. *J. Acoust. Soc. Am.*, **68**, 1516–1521.

Seriani, G., & Priolo, E. 1994. Spectral element method for acoustic wave simulation in hetrogeneous media. *Finite Elements in Analysis and Design*, **16**, 337–348.

Snieder, R. 2004. Extracting the Green's function from the correlation of coda waves: A derivation based on stationary phase. *in press Phys. Rev. E.*

Stockwell, Jr., J. W. 1997. Free software in education; a case study of CWP7SU: Seismic Unix. *The Leading Edge*, **16**, 1045–1049.

Townsend, C., Firth, I. R., Westerman, R., Kirkevollen, L., Harde, M., & Anderson, T. 1998. Small seismic-scale fault identification and mapping. *in: Faulting, Fault Sealing and Fluid Flow in Hydrocarbon Resrvoirs, eds. G. Jones, Q. J. Fisher, and R. J. Knipe, Geological Society Special Publication No. 147.*

Yilmaz, Ö. 1987. *Seismic Data Processing.* Tulsa: Society of Exploration Geophysicists.

APPENDIX A: MODELING OF A LINEAR-SLIP INTERFACE

We chose SEM to simulate fault reflectivity for its ability to allow a free-form mesh and in order to include the possibility of slip at interfaces in our numerical models. As evidence of SEM's ability to handle challenging boundary conditions, it has recently been applied to wave propagation near a fluid-solid interface (Komatitsch *et al.*, 2000). However, interfacial slip had not yet, to our knowledge, been implemented in SEM. In fact, Komatitsch and Tromp (2003) claimed in the description of their SEM code that "at every internal boundary, both the displacement and the traction need to be continuous", in clear contradiction to slip.

For a normally incident P-wave, the linear-slip boundary condition can be expressed as (Schoenberg, 1980)

$$u_z^+ - u_z^- = \eta_N \sigma_{zz} \tag{A1}$$

$$\sigma_{zz}^+ = \sigma_{zz}^- \tag{A2}$$

where the superscript (-) refers to the side of the interface on which the wave is incident, (+) the other side of the interface, u_z is the displacement in the direction of propagation, and σ_{zz} is the normal stress. The parameter η_N is called the normal compliance and quantifies the degree of slip along the interface. For $\eta_N = 0$,the interface is welded, and for $\eta_N = \infty$, it is a free surface. The boundary condition described by equations (A1) and (A2) can be obtained in the limit of a thin, weak layer in welded contact with its surrounding rock. Linear-slip has been suggested as a good model for scattering from faults and fractures (Coates & Schoenberg, 1995). With this in mind, it is important not to confuse the slip model in equations (A1) and (A2) with slip that occurs along a fault during an earthquake. The linear-slip model entails some slipping at the interface that is the order of particle displacements during the passage of a seismic wave ($\sim 10^{-6}$ m). Active, earthquake-generating faults typically slip on a length scale 3 to 4 orders of magnitude larger ($\sim 10^{-3}$ - 10^{-2} m). Earthquake slip is also hysteretic, whereas interfaces undergoing linear-slip return to their equilibrium state after the seismic wave has moved on.

To implement the linear-slip model in SEM, the weak form of the equation of motion is needed

$$\int\int \rho\, \ddot{u}\, \phi + \int\int \nabla\phi : c : \nabla u - \int \tau\, \phi = 0, \tag{A3}$$

where u is the displacement, ρ is the density, τ is the traction on the boundary of the computational domain, c is the elastic stiffness tensor, and ϕ is the test function. The semi-colons in equation (A3) represent tensor multiplication. After discretizing the displacement, equation (A3) can be written as a matrix equation

$$M\ddot{u} = -Ku + B\tau, \tag{A4}$$

with M and K the mass and stiffness matrices, respectively. The last term is non-zero only on the part of the boundary where slip occurs; this is described by the matrix B. The essence of this implementation is that two separate meshes on either side of the slip discontinuity (let's call them mesh 1 and mesh 2) are put into communication via the last term in equation (A4). To get linear-slip between the two meshes along a direction normal to their contact, we substitute equation (A1) for the traction into equation (A4) for meshes 1 and 2 to get two matrix equations

$$\begin{aligned} M_1\ddot{u}_1 &= -K_1u_1 + \eta_N^{-1}B_1(u_1^z - u_2^z) \\ M_2\ddot{u}_2 &= -K_2u_2 - \eta_N^{-1}B_2(u_1^z - u_2^z), \end{aligned} \tag{A5}$$

where the asymmetry of the ±-signs between the two last terms is in accordance with Newton's third law and the superscript z means the normal component of the displacement. In the formulation we have outlined here, the slip law, equation (A1), enters into the equation of motion by a substitution of the slip for the traction at the fault. A weak formulation of the first-order velocity-stress equations, instead of the second-order wave equation, results in the opposite substitution: the slip emerges from the equations by applying the weak form, and substitution for the traction is necessary to impose the slip (Haney & Snieder, 2003).

The SEM implementation of equation (A5) utilizes an explicit Newmark scheme whose algorithm consists of a predictor, a solver, and a corrector:

CWP-465P

Application of PS-wave moveout asymmetry in parameter estimation for tilted TI media – Part I: Horizontal TTI layer

Pawan Dewangan† and Ilya Tsvankin†
† *Center for Wave Phenomena, Department of Geophysics, Colorado School of Mines, Golden, CO 80401-1887*

ABSTRACT

One of the distinctive features of mode-converted waves is their asymmetric moveout (i.e., PS-wave traveltime may not stay the same if the source and receiver are interchanged) caused by lateral heterogeneity or elastic anisotropy. If the medium is anisotropic, the moveout asymmetry contains valuable information for parameter estimation that cannot be obtained from pure reflection modes.

Here, we generalize the so-called "PP+PS=SS" method, which is designed to replace reflected PS modes in velocity analysis with pure (non-converted) SS-waves, by supplementing the output SS traces with the moveout asymmetry attributes of PS-waves. The moveout asymmetry factor Δt_{PS} is computed in the slowness domain as the difference between the traveltimes of the PS arrivals with opposite signs of the ray parameter (horizontal slowness). Another useful asymmetry attribute is the offset $x_{\min}(\alpha)$ of the PS-wave moveout minimum on a common-midpoint (CMP) gather with azimuth α. The computation of both Δt_{PS} and $x_{\min}$ is integrated in a straightforward way into the processing flow of the PP+PS=SS method.

The effectiveness of the developed algorithm and the importance of including the asymmetry attributes of PS-waves in anisotropic velocity analysis are demonstrated for transversely isotropic models with a tilted symmetry axis (TTI media). Simple analytic expressions for the moveout asymmetry of the PSV-wave in a horizontal TTI layer are derived in the weak-anisotropy approximation and verified by anisotropic ray tracing. The asymmetry attributes reach their maximum in the vertical plane that contains the symmetry axis and vanish in the orthogonal direction. The factor Δt_{PS} is proportional to the anellipticity parameter η and rapidly varies with the tilt ν of the symmetry axis. The largest values of Δt_{PS} are found for the symmetry axis that deviates by 20-30° from the vertical or horizontal directions.

All relevant parameters of a TTI layer can be estimated by a nonlinear inversion of the normal-moveout (NMO) velocities and zero-offset traveltimes of PP- and SS(actually, SVSV)-waves combined with the moveout asymmetry attributes of the PSV-wave. It should be emphasized that the inversion of pure-mode (PP and SS) moveout alone is ambiguous, while the addition of the attributes Δt_{PS} and $x_{\min}$ yields stable parameter estimates for noise-contaminated input data. Although the algorithm generally requires a wide range of azimuths, the parameters of most TTI models (except those with near-horizontal axis orientations) can be obtained from 2-D data acquired in the vertical symmetry-axis plane. If the TTI model is formed by obliquely dipping fractures, the estimated anisotropic parameters can be inverted further for the fracture orientation and compliances.

Key words: converted waves, dipping fracture, moveout asymmetry

2 MODIFICATION OF THE PP+PS=SS METHOD

The PP+PS=SS method introduced by Grechka and Tsvankin (2002a) is designed for seismic surveys in which shear waves are not excited (e.g., ocean-bottom cable, or OBC) but may be recorded by multicomponent receivers. In this case, the shear wavefield is formed by mode-converted PS-waves, with the conversion often happening at the reflector. Although PS arrivals carry valuable information about the shear-wave velocities, inversion and processing of mode conversions is hindered by their large reflection-point dispersal, polarity reversals, and moveout asymmetry. The idea of the PP+PS=SS method is to recompute the recorded PP and PS wavefields into the corresponding pure SS reflections, which are not physically generated in the survey.

The construction of SS-waves with the correct kinematics (but not amplitudes) does not require explicit information about the velocity field, but it is necessary to correlate PP and PS arrivals and identify the events reflected from the same interface. The original version of the PP+PS=SS method described by Grechka and Tsvankin (2002a) operates with PP and PS traveltimes picked on prestack data. As illustrated in Figure 1, matching the reflection slopes on common-receiver gathers makes it possible to find two PS rays (recorded at points $x^{(3)}$ and $x^{(4)}$) with the same reflection point as the PP reflection $x^{(1)}Rx^{(2)}$. Then the traveltime of the SS-wave is determined from

$$\begin{aligned}\tau_{SS}(x^{(3)},x^{(4)}) &= t_{PS}(x^{(1)},x^{(3)}) + t_{PS}(x^{(2)},x^{(4)}) \quad (1)\\ &- t_{PP}(x^{(1)},x^{(2)}) .\end{aligned}$$

Application of equation (1) produces reflection SS data with the correct kinematics but generally distorted amplitudes. Clearly, the SS traveltime $\tau_{SS}(x^{(3)},x^{(4)})$ will remain the same if we interchange the source ($x^{(3)}$) and receiver ($x^{(4)}$). Therefore, the moveout of the constructed SS-waves in common-midpoint (CMP) geometry is always symmetric, as is the case for any pure reflection mode. Conventional-spread SS traveltimes are described by the NMO velocity (in 2-D) and NMO ellipse (in 3-D), which can be obtained using algorithms developed for PP-wave data. The NMO velocities or ellipses of the PP- and SS-waves can then be combined in velocity analysis using, for example, stacking-velocity tomography, which proved to be particularly efficient for anisotropic media (Grechka et al., 2002a).

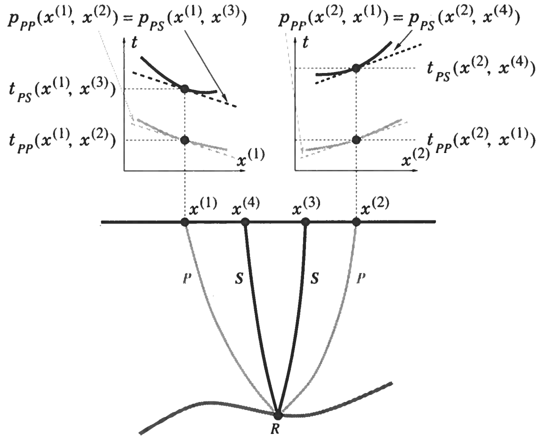

Figure 1. 2-D ray diagram of the PP+PS=SS method (after Grechka and Tsvankin, 2002a). The reflected PP ray from $x^{(1)}$ to $x^{(2)}$ and the PS rays from $x^{(1)}$ to $x^{(3)}$ and $x^{(2)}$ to $x^{(4)}$ have the same reflection point R. The rays with the common reflection point are identified by matching the slopes on common-receiver gathers (i.e., the ray parameters) of the PP- and PS-waves.

Still, for many anisotropic models including a horizontal TTI layer, pure reflection modes are not sufficient for estimating the vertical velocities and anisotropic coefficients (Grechka and Tsvankin, 2000; Grechka et al., 2002a). In such a case, an important question is whether or not including some attributes of the recorded PS-waves in the inversion algorithm can help in recovering the medium parameters. It is clear from equation (1) that the information about the moveout asymmetry of PS arrivals is not preserved in the computed SS traveltime, which depends on only the *sum* of the traveltimes of the PS-waves converted at point R (Figure 1). Below, we add certain measures of the PS-wave moveout asymmetry to the traveltimes of the PP-waves and the reconstructed SS-waves in the inversion for the parameters of TTI media.

A generalized version of the PP+PS=SS method based on equation (1) was developed by Grechka and Dewangan (2003). Instead of operating with prestack PP and PS traveltimes, they apply a particular convolution of PP and PS traces to produce seismograms of the corresponding SS-waves. The convolution operator in the frequency domain is given by

$$W_{SS}(\omega,x^{(3)},x^{(4)}) = \iint \Big[\; W_{PS}(\omega,x^{(1)},x^{(3)}) \times W^{\star}_{PP}(\omega,x^{(1)},x^{(2)}) \times W_{PS}(\omega,x^{(2)},x^{(4)})\Big] dx^{(1)}dx^{(2)}, \quad (2)$$

where ω is the radial frequency, W_{PP} are W_{PS} are the spectra of PP and PS traces, W_{SS} is the spectrum of the constructed SS trace for the source and receiver located at points $x^{(3)}$ and $x^{(4)}$, and the star denotes complex conjugate. The integration is performed over the P-wave source and receiver coordinates $x^{(1)}$ and $x^{(2)}$ (Figure 1). The main contribution to the integral comes from the stationary point that yields the traveltime of the measure of asymmetry for $\boldsymbol{x}$ can be defined in the following way:

$$\Delta \boldsymbol{x}_{PS} = \boldsymbol{x}_{PS}(p_1, p_2) + \boldsymbol{x}_{PS}(-p_1, -p_2) \,. \tag{12}$$

The main advantage of treating the asymmetry in the slowness domain is that, for a laterally homogeneous medium, both Δt_{PS} and $\Delta \boldsymbol{x}_{PS}$ can be obtained directly from the PP+PS=SS method [see equation (4) and Figure 1]. Equations (7), (11), (8), and (12) give an exact representation of the moveout asymmetry of PS-waves for any horizontal anisotropic layer. Next, we apply this formulation to study the dependence of Δt_{PS} on the parameters of TI media with an arbitrary tilt of the symmetry axis. The factor $\Delta \boldsymbol{x}_{PS}$ is discussed later on, after the introduction of the offset $x_{\min}$ of the PS-wave moveout minimum in CMP geometry.

Since the contributions of the symmetry-axis orientation and anisotropic parameters to the time asymmetry factor Δt_{PS} are hidden in the components of the slowness vector, in Appendix A we linearize equation (11) with respect to ϵ and δ under the assumption of weak anisotropy ($|\epsilon| \ll 1$ and $|\delta| \ll 1$). The derivation is carried out for the PS mode that is polarized in the plane formed by the slowness vector and the symmetry axis. Note that although we will denote this wave "PSV," its polarization vector lies in the vertical incidence plane only if that plane contains the symmetry axis.

The coordinate system is chosen in such a way that the symmetry axis is confined to the $[x_1, x_3]$-plane, which represents the only vertical symmetry plane of the model and will be called here the *symmetry-axis plane* (Figure A1). The sign of the time difference in equation (11) is specified by assuming that the symmetry axis is dipping in the positive x_1-direction.

Substituting equations (A5) and (A6) into equation (11), we obtain a linearized expression for the moveout asymmetry factor of the PSV-wave:

$$\Delta t_{PS} = -8 \, \eta \, z \, V_{P0}^2 \; p_1 \, [p_2^2 + (2p_1^2 + p_2^2) \cos 2\nu] \, \sin 2\nu \,, \tag{13}$$

where $\eta \equiv (\epsilon - \delta)/(1 + 2\delta) \approx \epsilon - \delta$ is the "anellipticity" coefficient responsible for time processing of P-wave data in VTI media (Alkhalifah and Tsvankin, 1995). In the symmetry-axis plane $[x_1, x_3]$, the slowness component p_2 vanishes that and equation (13) simplifies to

$$\Delta t_{PS}(p_2 = x_2 = 0) = -8 \, \eta \, z \, V_{P0}^2 \; p_1^3 \, \sin 4\nu \,. \tag{14}$$

Equations (13) and (14) give a concise description of the azimuthally-varying factor Δt_{PS}. The main properties of the PSV-wave moveout asymmetry in the slowness domain can be summarized as follows:

- The asymmetry factor vanishes for VTI ($\nu = 0°$) and HTI ($\nu = 90°$) media because these two models have a horizontal symmetry plane. In the symmetry-axis plane, the linearized factor Δt_{PS} [equation (14)] also goes to zero for $\nu = 45°$. In this case, however, the higher-order terms in ϵ and δ do not vanish, which makes the moveout weakly asymmetric.
- The contributions to the asymmetry factor from the P-leg [equation (A5)] and S-leg [equation (A6)] of the converted wave are identical. Although this result was proved here in the weak-anisotropy approximation, numerical tests show that it remains valid for arbitrary strength of the anisotropy.
- The asymmetry in the slowness domain depends only on the *difference* $\eta = \epsilon - \delta$ and vanishes if the anisotropy is elliptical ($\epsilon = \delta$). Since for elliptical media with any magnitude of $\epsilon = \delta$ there is no SV-wave velocity anisotropy, the S-leg of the converted wave does not produce any moveout asymmetry. This means that the P-leg cannot cause the asymmetry either (see above).
- The magnitude of the asymmetry factor in the symmetry-axis plane [equation (14)] reaches its maximum for the tilts $\nu = 22.5°$ and $\nu = 67.5°$. Therefore, Δt_{PS} is quite sensitive to the deviation of the symmetry axis from the vertical and horizontal directions.

The azimuthally-varying asymmetry factor Δt_{PS} computed for a typical TTI model from the exact equations (7) and (11) is displayed in Figure 2. There is a substantial variation of Δt_{PS} with the slowness component p_1 (e.g., in the x_1-direction where $p_2 = 0$), while the influence of p_2 is much weaker. Therefore, Figure 2 indicates that most of the 3-D (wide-azimuth) moveout asymmetry information can be obtained in the symmetry-axis plane $[x_1, x_3]$.

Note that the line $p_1 = 0$ in Figure 2 where $\Delta t_{PS} = 0$ *does not* correspond to acquisition in the $[x_2, x_3]$-plane. Since $[x_2, x_3]$ is not a symmetry plane, downgoing P rays with $p_1 = 0$ deviate from the vertical incidence plane $[x_2, x_3]$, and the source-receiver direction of the reflected PS-wave is not parallel to the x_2-axis.

Figure 3 shows the function $\Delta t_{PS}(p_1)$ in the symmetry-axis plane in more detail. Both the PP+PS=SS method and parametric equation (11) are supposed to produce exact values of Δt_{PS}, which is confirmed by our numerical results. The magnitude of the asymmetry factor is quite substantial – it exceeds 40% of the zero-offset time before rapidly decreasing for large values of p_1.

The accuracy of the weak-anisotropy approximation (14) in Figure 3 is quite satisfactory considering that it incorporates the contribution of the S-leg of the converted wave. Typically, the weak-anisotropy approximation is much less accurate for SV-waves than it is for P-waves because of the large magnitude of the anisotropic parameter $\sigma \equiv (V_{P0}^2/V_{S0}^2)\,(\epsilon - \delta)$ (Tsvankin and Thomsen, 1994; Tsvankin, 2001). In our case, however, the anisotropy-related asymmetry factors for the P- and S-legs are equal to each other (see above), and the error of the weak-anisotropy approximation is the same for both P- and S-waves.

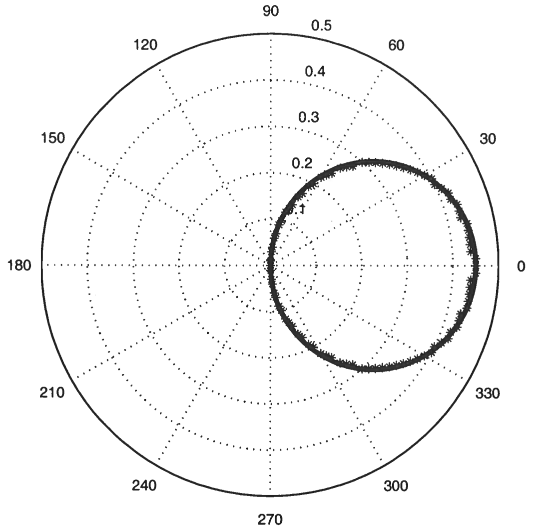

Figure 4. Polar plot of the offset $x_{\min}(\alpha)$ for the model from Figure 2. The stars mark values obtained from anisotropic ray tracing of PS-waves and the solid line is computed from equation (16) with the exact value of x_0.

$$\boldsymbol{\Delta x}_{PS} = \boldsymbol{x}_{PS}(p_1, 0) + \boldsymbol{x}_{PS}(-p_1, 0). \qquad (18)$$

Linearizing equation (18) in the anisotropic coefficients using equation (8) yields the projection of the vector $\boldsymbol{\Delta x}_{PS}$ onto the x_1-axis in the form

$$(\Delta x_{PS})_{x_1} = 2\,x_0 + 12\,\eta\,z\,V_{P0}^2\,p_1^2\,\sin 4\nu\,, \qquad (19)$$

where x_0 is given by equation (17). According to equation (19), the factor $|\boldsymbol{\Delta x}_{PS}|$ can be approximated by a hyperbolic function of the slowness p_1 with the value at the apex determined by $2\,x_0$. Indeed, when $p_1 = 0$, the PS-rays corresponding to both p_1 and $-p_1$ coincide and have the same offset x_0 (Figure 5). If the PS moveout were symmetric, the offsets for p_1 and $-p_1$ (circles and diamonds, respectively, in Figure 5) would have identical absolute values but *opposite* signs, and the zero-offset PS-ray would have the slowness $p_1 = 0$. Figure 5 also confirms that the linearized equation (19) is sufficiently accurate for weak and moderate anisotropy.

Therefore, an alternative way of estimating x_0 is to fit a hyperbolic function to the slowness-dependent factor $|\boldsymbol{\Delta x}_{PS}|$ and find its intercept for $p_1 = 0$. It is interesting that the coefficient of the quadratic term of the hyperbola (19) is formed by the same combination of the medium parameters that governs the traveltime asymmetry factor (14).

3.3.2 Asymmetry factor in the offset domain

To give an analytic description of the factor Δt_{PS} [equation (15)] in the offset domain, we expanded the traveltime in a double Taylor series around the offset $x_{\min}$ (see Appendix C). The result is convenient to represent in terms of the offset x and the azimuth α of the source-receiver line. The linearized expression (C13) for Δt_{PS} contains linear and cubic terms in the offset x and is sufficiently accurate for relatively small offsets.

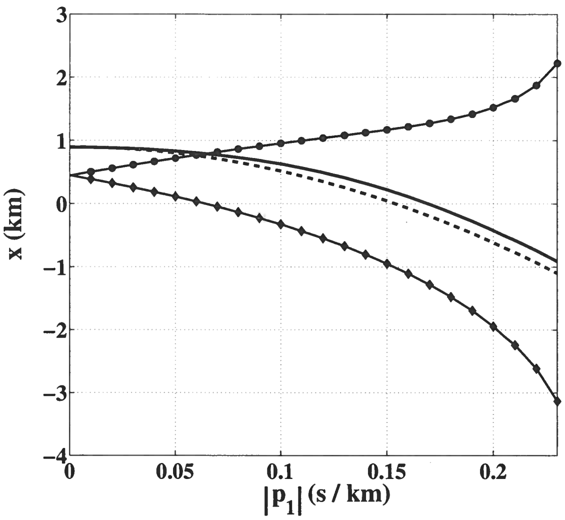

Figure 5. Slowness-domain factor $|\boldsymbol{\Delta x}_{PS}|$ in the symmetry-axis plane of a TTI layer with the same parameters as those in Figure 2. The solid line marks exact values of $|\boldsymbol{\Delta x}_{PS}|$ from equation (18), and the dashed line is the weak-anisotropy approximation (19). Exact PS-wave offsets for positive slownesses p_1 are marked by circles, offsets for negative slownesses by diamonds; the offset is considered positive if the vector $\boldsymbol{x}_{PS}$ points in the x_1-direction.

This approximation can be extended to larger offsets by adapting the approach of Tsvankin and Thomsen (1994) who developed a highly accurate nonhyperbolic moveout equation for P-waves by modifying the $t^2(x^2)$ Taylor series in such a way that it became convergent at $x \to \infty$. For long-offset converted PS-waves, the incident P-wave travels almost horizontally and accounts for most of the total reflection traveltime. The contribution of the S-leg then becomes negligible, and the asymmetry factor at infinite offset goes to zero. To ensure that Δt_{PS} vanishes for $x \to \infty$, we add a denominator $(1 + Cx^2)$ to the cubic term in equation (C13):

$$\Delta t_{PS} = A\,x + \frac{B\,x^3}{1 + C\,x^2}\,; \qquad (20)$$

$$A = -\frac{2x_0 \cos\alpha}{z(V_{P0} + V_{S0})}\,,$$

$$B = -\frac{4\eta V_{P0}^2 \sin 2\nu \cos\alpha}{z^2(V_{P0} + V_{S0})^3}\left(2\cos 2\nu \cos^2\alpha + \sin^2\alpha\right)\,,$$

$$C = -\frac{B}{A}\,.$$

In the symmetry-axis plane ($\alpha = 0°$) the coefficients A and B in equation (20) become

$$A = -\frac{2\,x_0}{z\,(V_{P0} + V_{S0})}\,, \qquad (21)$$

$$B = -\frac{4\,\eta\,V_{P0}^2\,\sin 4\nu}{z^2\,(V_{P0} + V_{S0})^3}\,. \qquad (22)$$

ically excited in the survey. If the data have a wide range of source-receiver azimuths, azimuthal velocity analysis can be applied to obtain the NMO ellipses of the PP- and SS-waves (Grechka and Tsvankin, 1998; Grechka et al., 2002a).

The above methodology, described in detail by Grechka et al. (2002a), is designed to avoid complications associated with the processing of mode-converted waves. For some anisotropic models, the combination of PP- and SS-waves is sufficient to estimate the medium parameters without additional information. For TTI media, however, the inversion of PP- and SS-waves is feasible only for substantial reflector dips or near-horizontal orientations of the symmetry axis (Grechka et al., 2002a).

Here, we supplement the moveouts of the PP-waves and constructed SS-waves in parameter estimation with the PS-wave asymmetry attributes obtained from the PP+PS=SS method. For laterally homogeneous media, the traveltime asymmetry $\Delta t_{PS}(x^{(3)}, x^{(4)})$ produced by the PP+PS=SS method [equation (4)] coincides the asymmetry factor defined in the slowness domain [equation (11)]. Another reason to work with the asymmetry attributes in the slowness domain is the relative simplicity of the corresponding analytic expressions.

The offset $x_{\min}(\alpha = 0)$ of the PS-wave traveltime minimum in the symmetry-axis plane $[x_1, x_3]$ can also be obtained from the PP+PS=SS method. As shown by Tsvankin and Grechka (2000) and Tsvankin (2001, Appendix 5B), the traveltime minimum of any reflected wave in CMP geometry corresponds to the ray with equal projections of the slowness vector onto the CMP line at the source and receiver locations (both legs of the ray have to be treated as upgoing waves). Applying this result to the symmetry-axis plane of a horizontal TTI layer where the slowness vector cannot have out-of-plane components, we find that the horizontal slowness at the traveltime minimum has to go to zero. Then, for both PP-waves and the constructed SS-waves the horizontal slowness has to vanish at zero offset (an obvious result for pure modes), while for PS-waves it vanishes at the offset $x_{\min}(0) = x_0$. Since the PS- and PP-waves with the same reflection point have identical absolute values of the horizontal slowness (Figure 1), the PS ray at the offset x_0 is generated by the zero-offset P-wave that corresponds to the stationary point $x_1 = x_2$.

Another way to estimate x_0 is to pick the offsets (along with the traveltimes) of the two PS-waves corresponding to the same reflection point for a range of the slownesses p_1 and build the function $|\boldsymbol{\Delta x}_{PS}(p_1)|$ [equation (18)]. This function can then be approximated with a hyperbola whose apex yields the value of x_0 [equation (19)]. The main advantage of this approach is in using multiple data points, which may help to obtain more stable estimates of x_0 for noisy data.

4.2 Inversion algorithm

We assume that the azimuth of the symmetry-axis plane was established, for example, from azimuthally varying moveout of pure modes. The general expression of the NMO ellipse has the following form (Grechka and Tsvankin, 1998):

$$V_{\text{nmo}}^{-2}(\alpha) = W_{11} \cos^2 \alpha + 2\, W_{12} \sin\alpha \cos\alpha + W_{22} \sin^2 \alpha, \quad (23)$$

where $W_{ij} \equiv \tau_0\, \partial p_i / \partial x_j$ $(i, j = 1, 2)$, $\tau_0 \equiv t_0/2$ is the one-way zero-offset traveltime, and p_1 and p_2 are the horizontal slowness components for one-way rays from the zero-offset reflection point to the surface; all derivatives are evaluated at the CMP location. For a homogeneous horizontal layer, the matrix $\boldsymbol{W}$ can be represented as (Grechka et al., 1999)

$$\boldsymbol{W} = \frac{-q}{q_{,11}\, q_{,22} - q_{,12}^2} \begin{pmatrix} q_{,22} & q_{,12} \\ -q_{,12} & q_{,11} \end{pmatrix}, \quad (24)$$

where $q \equiv q(p_1, p_2)$ is the vertical slowness and $q_{,ij} \equiv \partial^2 q / (\partial p_i\, \partial p_j)$. As mentioned above, the slowness vector of the zero-offset ray for a horizontal layer is vertical, so the derivatives are computed for $p_1 = p_2 = 0$.

If the medium has a vertical symmetry plane, one of the axes of the NMO ellipse is parallel to the symmetry-plane direction (Grechka and Tsvankin, 1998). For a TTI layer with the symmetry axis confined to the $[x_1, x_3]$-plane, the terms $q_{,12}$ and W_{12} [equation (24)] vanish, while W_{11} and W_{22} define the semiaxes of the NMO ellipse (23). Therefore, the orientation of the NMO ellipse of the recorded PP-waves or the constructed SS-waves can be used to find the azimuth of the symmetry-axis plane $[x_1, x_3]$.

Then, as described above, the processing of 2-D multicomponent data in the symmetry-axis plane produces the following data vector $\boldsymbol{d}$:

$$\boldsymbol{d} \equiv \Big\{ V_{\text{nmo,P}}\,,\ t_{P0}\,,\ V_{\text{nmo,S}}\,,\ t_{S0}\,, \quad (25)$$
$$\Delta t_{PS}(p_1, 0)\,,\ x_{\min}(\alpha = 0^\circ) \Big\}.$$

Although $\Delta t_{PS}(p_1, 0)$ denotes multiple measurements of the asymmetry factor for the available range of the horizontal slownesses p_1, equation (14) indicates that the moveout asymmetry in the $[x_1, x_3]$-plane may constrain only one combination of the layer parameters.

Analytic expressions for $\Delta t_{PS}(p_1, 0)$ and $x_0 = x_{\min}(\alpha = 0^\circ)$ needed to model these quantities in the inversion algorithm were introduced in the previous section. The NMO velocities $V_{\text{nmo,P}}$ and $V_{\text{nmo,S}}$ in the x_1-direction ($\alpha = 0^\circ$) can be computed from equation (24) with $q_{,12} = 0$:

$$V_{\text{nmo}} = \frac{1}{\sqrt{W_{11}}} = -\frac{q}{q_{,11}}\,. \quad (26)$$

The model vector $\boldsymbol{m}$ includes the following parameters of the TTI layer:

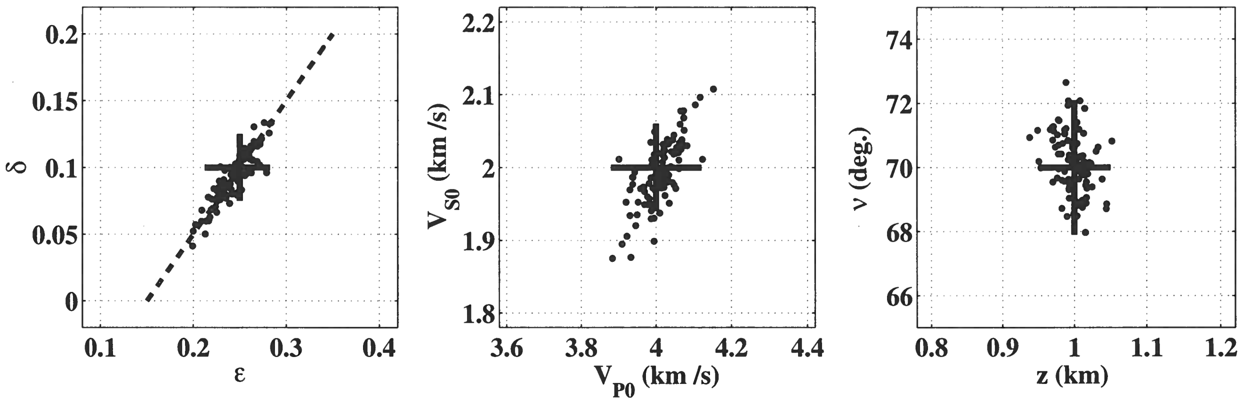

Figure 8. Inverted parameters (dots) of a horizontal TTI layer obtained from 2-D PP and PS data in the symmetry-axis plane. The correct model parameters ($V_{P0} = 4$ km/s, $V_{S0} = 2$ km/s, $\epsilon = 0.25$, $\delta = 0.1$, $\nu = 70°$, $z = 1$ km) are marked by the crosses. The dashed line on the [ϵ, δ] plot corresponds to the correct value of the difference ($\epsilon - \delta$). The input data were contaminated by Gaussian noise with the standard deviations of 2% for the NMO velocities, 0.5% for the zero-offset traveltimes, and 2% for the PS-wave asymmetry attributes.

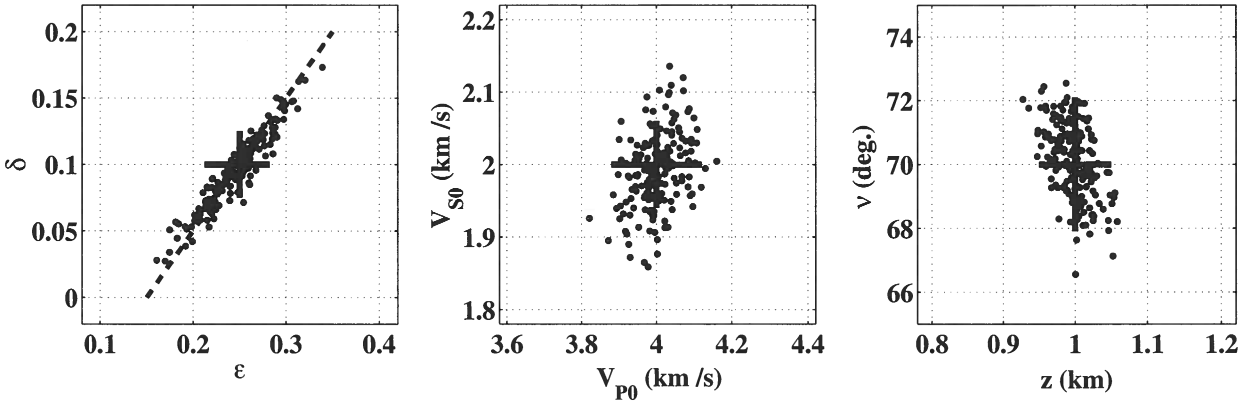

Figure 9. Same as Figure 8, but the standard deviations of the Gaussian noise are increased to 1% for the zero-offset traveltimes and 4% for the asymmetry attributes of PS-waves (the standard deviations for the NMO velocities remain unchanged at 2%).

the standard deviations of the noise were fixed at the values used in Figure 8.

For HTI media ($\nu = 90°$) the PS-wave moveout is symmetric, and the 2-D inversion in the symmetry-axis plane cannot constrain the medium parameters. However, as illustrated by Figure 10, even a small (5°) deviation of the symmetry axis from the horizontal plane creates a measurable moveout asymmetry. For the model from Figure 10, the offset $x_{\min}$ is close to 11% of the depth z, and the factor Δt_{PS} reaches about 4% of the zero-offset PS traveltime for $x = 2z$. Although the magnitude of the asymmetry attributes is not large, it proved to be sufficient for stable 2-D parameter estimation. The standard deviations do not exceed 0.02 for ϵ and δ, 2% for V_{P0}, V_{S0}, and z, and 1° for ν.

4.3.2 Models with intermediate tilt

The moveout asymmetry factor in the slowness domain is small not only for near-vertical and near-horizontal orientations of the symmetry axis, but also for tilts ν close to 45° [equation (14)]. The model of a horizontal TTI layer with $35° < \nu < 55°$ can be used to describe reflections from a horizontal interface beneath dipping shale layers in fold-and-thrust belts, such as the Canadian Foothills (e.g., Isaac and Lawton, 1999).

Figure 11 helps to assess the feasibility of the inversion for a tilt of 50°. Although the asymmetry in the offset domain for intermediate tilts is substantial (x_0 is about 34% of z), the inverted parameters are biased and exhibit significant scatter. Analysis of the inversion results shows that many estimated models correspond to local minima of the objective (misfit) function and do not fit the input data within the noise level.

The problem with local minima was addressed by

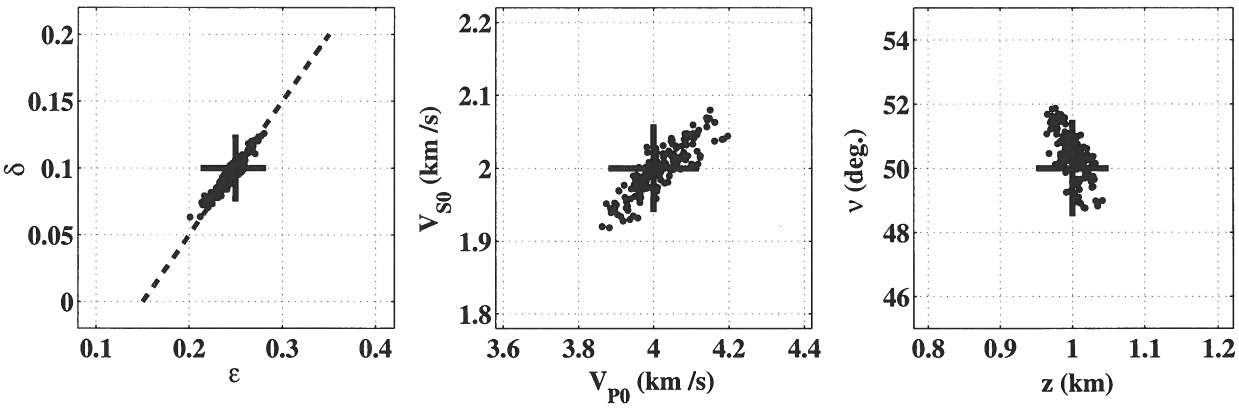

Figure 12. Same as Figure 11, but the inversion algorithm is modified to avoid local minima.

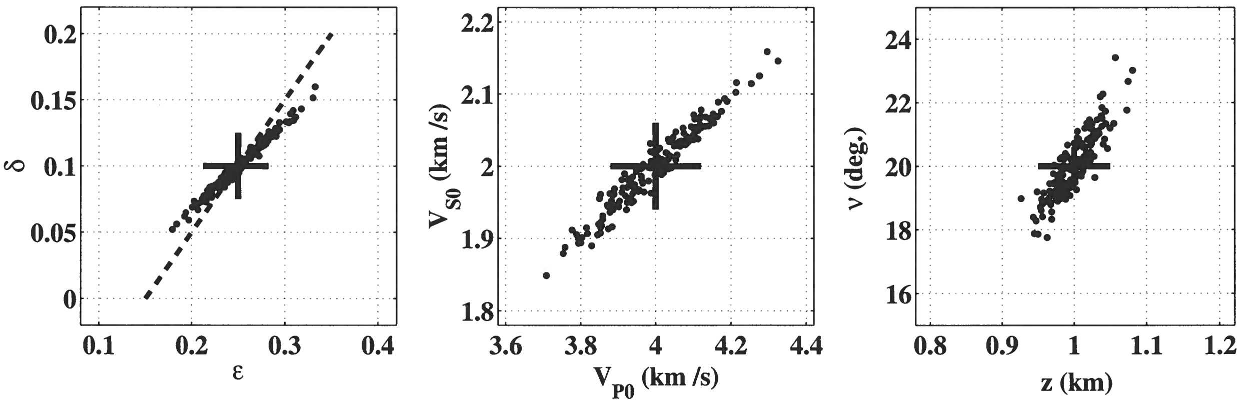

Figure 13. Inversion results for a model with the same parameters as those in Figure 8 except for the tilt $\nu = 20°$.

TTI models from VTI and HTI, for which PS moveout is symmetric in any domain. As illustrated by Figure 15, all parameters of an elliptically anisotropic layer except for the tilt are well constrained, and the standard deviations are less than 0.03 for $\epsilon = \delta$ and less than 2% for V_{P0}, V_{S0}, and z. The points on the $[\epsilon, \delta]$ plot are almost perfectly aligned along the $\epsilon = \delta$ line, which indicates that the algorithm is able to identify elliptical anisotropy. The estimates of ν, however, are more scattered (the standard deviation reaches 5°) than those for anelliptical models with the same tilt, and the average ν is biased by about 2°.

5 DISCUSSION AND CONCLUSIONS

The moveout asymmetry of mode-converted waves causes complications in seismic processing and can be removed by applying the PP+PS=SS method introduced by Grechka and Tsvankin (2002a) and Grechka and Dewangan (2003). This method makes it possible to compute the reflection traveltimes of SS-waves (if they are not excited in the survey) from PP and PS data prior to anisotropic velocity analysis. However, while the replacement of converted waves with pure-mode SS reflections is convenient for processing purposes, it results in the loss of the PS-wave moveout asymmetry information that can play a critical role in estimating the anisotropic parameters.

Here, we presented a modification of the PP+PS=SS method designed to supplement the computed SS data with such asymmetry attributes of the converted waves as the difference Δt_{PS} between the "reciprocal" traveltimes in the slowness domain and the offset $x_{\min}$ of the traveltime minimum in CMP geometry. The new algorithm was applied to the inversion of multicomponent data for a horizontal TTI (transversely isotropic with a tilted symmetry axis) layer – the model used to describe the effective anisotropy caused by parallel dipping penny-shaped cracks, dipping shale beds, or progradational sequences.

The weak-anisotropy approximation helped to obtain concise expressions for the azimuthally varying asymmetry attributes of PSV-waves in terms of the tilt ν of the symmetry axis and the anisotropic coefficients ϵ and δ. The moveout asymmetry in a TTI layer is caused by the oblique orientation of the symmetry axis; for VTI

The inversion algorithm developed here can be used for characterizing a system of obliquely dipping penny-shaped cracks embedded in a layer-cake isotropic medium (Angerer et al., 2002). Grechka and Tsvankin (2003b) demonstrate that wide-azimuth seismic data can be inverted for the parameters of the more complicated model that includes penny-shaped cracks in a VTI background. Their method operates with only pure-mode reflections but the vertical velocities are assumed to be known. It is possible that the addition of the asymmetry attributes of PS-waves to the signatures of pure PP and SS reflections can make *a priori* information for their model unnecessary. Note that according to the feasibility study by Grechka and Tsvankin (2003a), seismic data can constrain the parameters of up to four dipping systems of penny-shaped cracks embedded in either isotropic or VTI host rock.

Tilted transverse isotropy is also used to describe dipping shale layers in fold-and-thrust belts (such as the Canadian Foothills) and the effective anisotropy of progradational sequences. Joint inversion of PP- and PS-waves reflected from dipping interfaces overlaid by TTI media will be the subject of a sequel paper.

6 ACKNOWLEDGMENTS

We are grateful to Vladimir Grechka (Shell) and members of the A(nisotropy)-Team of the Center for Wave Phenomena (CWP), Colorado School of Mines, for helpful discussions and to Ken Larner (CSM) for his careful review of the manuscript. The support for this work was provided by the Consortium Project on Seismic Inverse Methods for Complex Structures at CWP and by the Chemical Sciences, Geosciences and Biosciences Division, Office of Basic Energy Sciences, U.S. Department of Energy.

7 REFERENCES

Alkhalifah, T., and Tsvankin, I., 1995, Velocity analysis for transversely isotropic media: Geophysics, **60**, 1550–1566.

Angerer, E., Horne, S. A., Gaiser, J. E., Walters, R., Bagala, S. and Vetri, L., 2002, Characterization of dipping fractures using PS mode-converted data: 72th Ann. Internat. Mtg., Soc. of Expl. Geophys., Expanded Abstracts, 1010–1013.

Bakulin, A., Grechka, V., and Tsvankin, I., 2000, Estimation of fracture parameters from reflection seismic data – Part I: HTI model due to a single fracture set: Geophysics, **65**, 1788–1802.

Grechka, V., and Dewangan, P., 2003, Generation and processing of pseudo shear-wave data:
Theory and case study: Geophysics, in print.

Grechka, V., and Tsvankin, I., 1998, 3-D description of normal moveout in anisotropic inhomogeneous media: Geophysics, **63**, 1079–1092.

Grechka, V., and Tsvankin, I., 2000, Inversion of azimuthally dependent NMO velocity in transversely isotropic media with a tilted axis of symmetry: Geophysics, **65**, 232–246.

Grechka, V., and Tsvankin, I., 2002a, PP+PS=SS: Geophysics, **67**, 1961–1971.

Grechka, V., and Tsvankin, I., 2002b, The joint nonhyperbolic moveout inversion of PP and PS data in VTI media: Geophysics, **67**, 1929–1932.

Grechka, V., and Tsvankin, I., 2003a, Feasibility of seismic characterization of multiple fracture sets: Geophysics, **68**, 1399–1407.

Grechka, V., and Tsvankin, I., 2003b, Characterization of dipping fractures in transversely isotropic background: Geophys. Prosp., in print.

Grechka, V., Pech, A., and Tsvankin, I., 2002a, Multicomponent stacking-velocity tomography for transversely isotropic media: Geophysics, **67**, 1564–1574.

Grechka, V., Tsvankin, I., and Cohen, J. K., 1999, Generalized Dix equation and analytic treatment of normal-moveout velocity for anisotropic media: Geophys. Prosp., **47**, 117–148.

Grechka, V., Tsvankin, I., Bakulin, A., Hansen, J.O., and Signer, C., 2002b, Joint inversion of PP and PS reflection data for VTI media: A North Sea case study: Geophysics, **67**, 1382–1395.

Isaac, J.H., and Lawton, D.C., 1999, Image mispositioning due to dipping TI media: A physical seismic modeling study: Geophysics, **64**, 1230–1238.

Pelissier, M. A., Thomas-Betts, A., and Vestergaard, P. D., 1991, Azimuthal variations in scattering amplitudes induced by transverse isotropy: Geophysics, **56**, 1584–1595.

Sarg, J. F., and Schuelke, J. S., 2003, Integrated seismic analysis of carbonate reservoirs: From the framework to the volume attributes: The Leading Edge, **22**, 640–645.

Thomsen, L., 1986, Weak elastic anisotropy: Geophysics, **51**, 1954–1966.

Thomsen, L., 1999, Converted-wave reflection seismology over inhomogeneous, anisotropic media: Geophysics, **64**, 678–690.

Tsvankin, I., 1997, Reflection moveout and parameter estimation for horizontal transverse isotropy: Geophysics, **62**, 614–629.

Tsvankin, I., 2001, Seismic signatures and analysis of reflection data in anisotropic media: Elsevier Science Publ. Co., Inc.

Tsvankin, I., and Grechka, V., 2000, Dip moveout of converted waves and parameter estimation in transversely isotropic media: Geophys. Prosp., **48**, 257–292.

Tsvankin, I., and Grechka, V., 2002, 3D description and inversion of reflection moveout of PS-waves in anisotropic media: Geophys. Prosp., **50**, 301–316.

Tsvankin, I., and Thomsen, L., 1994, Nonhyperbolic reflection moveout in anisotropic media: Geophysics, **59**, 1290–1304.

Taking into account that the asymmetry for the S-leg of a given PS-ray has to be computed for the opposite sign of the horizontal slowness [so p_1 in equation (A5) has to be replaced with $-p_1$, and p_2 with $-p_2$], we find

$$\Delta t_S = -4\,z\,(\epsilon-\delta)\,p_1 V_{P0}^2 \sin 2\nu\,[p_2^2 + (2p_1^2+p_2^2)\cos 2\nu] = \Delta t_P\,. \tag{A6}$$

APPENDIX B: AZIMUTHAL VARIATION OF THE OFFSET X_{MIN}

The slope dt/dx of the CMP moveout curve for any pure or converted reflection mode is determined by the difference between the projections onto the CMP line of the slowness vectors at the source and receiver locations[†] (Tsvankin and Grechka, 2000; Tsvankin, 2001, Appendix 5B). This general result, which is valid for any heterogeneous, anisotropic medium, can be used to find the offset $x_{\min}$ of the PS-wave traveltime minimum where the moveout slope goes to zero. For a horizontal, laterally homogeneous layer, the horizontal slowness has the same absolute value for both legs of the reflected ray, and the slope can vanish only for a ray with the slowness vector orthogonal to the CMP line.

Suppose p_α is the projection of the slowness vector onto the CMP line that makes the angle α with the x_1-axis, and p_t is the slowness projection onto the orthogonal $(\alpha + 90°)$ direction. The offset $x_{\min}(\alpha)$ then corresponds to the PS ray for which $p_\alpha = 0$. Rotating the slowness vector by the angle α in the horizontal plane yields

$$p_1 = p_\alpha \cos\alpha - p_t \sin\alpha\,, \tag{B1}$$

$$p_2 = p_\alpha \sin\alpha + p_t \cos\alpha\,. \tag{B2}$$

The offset x can be parametrically represented as [equations (8) and (9)]

$$x = z\,\sqrt{(q_{,1P} - q_{,1S})^2 + (q_{,2P} - q_{,2S})^2}\,. \tag{B3}$$

To find $x_{\min}$ from equation (B3), the derivatives $q_{,i} \equiv \partial q/\partial p_i$ $(i = 1, 2)$, which are derived for weakly anisotropic TTI media in Appendix A, have to be evaluated for $p_\alpha = 0$.

Substituting $q_{,i}$ from Appendix A into equation (B3) and further linearizing the result in ϵ and δ produces x as a function of p_1 and p_2, which can be replaced by p_α and p_t using equations (B1) and (B2). The component p_α is then set to zero, while p_t can be found from equation (10) for the azimuth α. Linearizing equation (10) and using equations (B1) and (B2) with $p_\alpha = 0$ allows us to obtain p_t:

$$p_t = \frac{x_0 \sin\alpha}{V_{S0} - V_{P0}}\,, \tag{B4}$$

where $x_0 = x_{\min}(\alpha = 0°)$ is the value of $x_{\min}$ in the symmetry-axis plane.

Since the slowness vectors of reflected rays propagating in the symmetry-axis plane cannot have out-of-plane components, the offset x_0 corresponds to the ray with the vertical slowness vector $(p_\alpha = p_t = p_1 = p_2 = 0)$. Evaluating x from equation (B3) with $p_1 = p_2 = 0$ gives

$$x_0 = z\left[\epsilon \sin 2\nu - \frac{1}{2}(\epsilon - \delta)\left(1 + \frac{V_{P0}^2}{V_{S0}^2}\right)\sin 4\nu\right]. \tag{B5}$$

Finally, we substitute $p_\alpha = 0$ and p_t from equations (B4) and (B5) into equation (B3) to obtain the following expression for the azimuthally varying offset of the moveout minimum:

$$x_{\min}(\alpha) = x_0 \cos\alpha\,. \tag{B6}$$

APPENDIX C: APPROXIMATE MOVEOUT ASYMMETRY FACTOR IN THE OFFSET DOMAIN

To describe the moveout asymmetry in the offset domain defined in equation (15), we express the PS traveltime through the components x_1 and x_2 of the PS-wave offset vector $\mathbf{x}_{PS}$ [equation (8)]. An approximation for the asymmetry factor in a horizontal TTI layer can be found by expanding the traveltime $t(x_1, x_2)$ in a double Taylor series in the vicinity of the offset $(x_0, 0)$ of the moveout minimum [equation (B5)]:

$$t(x_1, x_2) = t(x_0, 0) + \frac{\partial t}{\partial x_1}(x_1 - x_0) + \frac{\partial t}{\partial x_2}x_2 + \frac{1}{2}\frac{\partial^2 t}{\partial x_1^2}(x_1 - x_0)^2 + \frac{1}{2}\frac{\partial^2 t}{\partial x_2^2}x_2^2 + \frac{\partial^2 t}{\partial x_1 \partial x_2}(x_1 - x_0)\,x_2$$

[†] In this formulation both legs of the reflected ray are treated as upgoing waves.

metry factor as

$$\Delta t_{_{PS}} = -\frac{2\,x_1\,x_0}{z\,(V_{P0}+V_{S0})} - \frac{4(\epsilon-\delta)\,V_{P0}^2\,\sin 4\nu}{z^2\,(V_{P0}+V_{S0})^3}\,x_1^3 - \frac{4(\epsilon-\delta)\,V_{P0}^2\,\sin 2\nu}{z^2\,(V_{P0}+V_{S0})^3}\,x_1\,x_2^2\,. \tag{C12}$$

Finally, equation (C12) can be rewritten in terms of the offset x and the azimuth α of the source-receiver line ($x_1 = x\cos\alpha$, $x_2 = x\sin\alpha$):

$$\Delta t_{_{PS}}(x,\alpha) = -\frac{2\,x\,x_0\,\cos\alpha}{z\,(V_{P0}+V_{S0})} - \frac{4(\epsilon-\delta)\,V_{P0}^2\,\sin 4\nu}{z^2\,(V_{P0}+V_{S0})^3}\,x^3\cos^3\alpha - \frac{4(\epsilon-\delta)\,V_{P0}^2\,\sin 2\nu}{z^2\,(V_{P0}+V_{S0})^3}\,x^3\cos\alpha\,\sin^2\alpha\,,$$

or

$$\Delta t_{_{PS}}(x,\alpha) = -\frac{2\,x\,x_0\,\cos\alpha}{z\,(V_{P0}+V_{S0})} - \frac{4\,x^3\,(\epsilon-\delta)\,V_{P0}^2\,\sin 2\nu\,\cos\alpha}{z^2\,(V_{P0}+V_{S0})^3}\left(2\cos 2\nu\,\cos^2\alpha + \sin^2\alpha\right). \tag{C13}$$

CWP-477

Application of PS-wave moveout asymmetry in parameter estimation for tilted TI media – Part II: Dipping TTI layer

Pawan Dewangan[†] and Ilya Tsvankin[†]
[†] *Center for Wave Phenomena, Department of Geophysics, Colorado School of Mines, Golden, CO 80401-1887*

ABSTRACT

Dipping transversely isotropic layers with a tilted symmetry axis (TTI media) cause serious imaging problems in fold-and-thrust belts and near salt domes. Here, we apply the modified PP+PS=SS method introduced in Part I to the inversion of long-spread PP and PS reflection data for the parameters of a TTI layer with the symmetry axis orthogonal to the bedding. The inversion algorithm combines the asymmetry attributes of the PSV-wave with the hyperbolic moveout of the pure PP- and SS-waves in the symmetry-axis plane (i.e., the vertical plane that contains the symmetry axis).

Analysis of the asymmetry attributes for a dipping layer is complicated by the fact that the PS-waves with the same conversion point do not have identical ray parameters (horizontal slownesses). The weak-anisotropy, small-offset approximations for the time and offset asymmetry factors show that the leading terms in offset do not contain independent information for the inversion. Therefore, the parameter-estimation algorithm has to rely on long-offset PS data (with maximum offset-to-depth ratios of at least two), which makes the results generally less stable than those for a horizontal TTI layer in Part I.

Still, the contribution of the PS-wave asymmetry factors helps to constrain the TTI parameters for large tilts ν of the symmetry axis ($\nu > 40°$). The least resolved parameter is Thomsen's coefficient ϵ because it that does not directly influence the moveout signatures of either pure or converted modes. The accuracy in ϵ and other parameters for large tilts can be improved by using wide-azimuth PP and PS reflections. With high-quality PS data, the inversion remains feasible for moderate tilts ($25° < \nu < 40°$), but it breaks down for models with smaller values of ν in which the moveout asymmetry is too weak. However, the tilt itself and several combinations of the medium parameters (e.g., the ratio of the symmetry-direction P-and S-wave velocities and the anisotropic parameter χ) are well-constrained for all symmetry-axis orientations.

The inversion results prove that 2D measurements of the PS-wave asymmetry attributes can be effectively used in velocity analysis for dipping TTI layers. In addition to providing an improved velocity model for imaging beneath TTI beds, our algorithm can yield valuable information for lithology discrimination and structural interpretation.

Key words: converted waves, dipping shale, moveout asymmetry

1 INTRODUCTION

Estimation of the parameters of tilted transversely isotropic (TTI) media is essential for anisotropic imaging beneath TTI formations and characterization of dipping fracture systems. Mode-converted PS-waves can make an important contribution to building TTI ve-

We consider a homogeneous TTI layer with the axis of symmetry orthogonal to the layer's bottom (reflector) that may have an arbitrary dip. Hence, the symmetry axis is confined to the reflector's dip plane that represents the only vertical symmetry plane of the model (we call it the symmetry-axis plane). The x_1-axis of the Cartesian coordinate system points in the updip direction of the reflector (Figure A1).

According to Snell's law, the projection of the slowness vector onto the reflector should be the same for all reflected waves. If we denote the slowness components in the dip and strike directions of the reflector by p_{int1} and p_{int2} (both p_{int1} and p_{int2} are confined to the reflector plane), the difference between the traveltimes of the two PS-waves with the same conversion point can be represented as

$$\begin{aligned}\Delta t_{PS} &= t_{PS}(p_{\text{int1}}, p_{\text{int2}}) - t_{PS}(-p_{\text{int1}}, -p_{\text{int2}}) \qquad (1)\\ &= \Delta t_P + \Delta t_S,\end{aligned}$$

where Δt_P and Δt_S are the contributions to Δt_{PS} from the P- and S-legs of the PS ray, respectively. Equation (1) has the same form as the expression for Δt_{PS} in Paper I, where the slowness components have to be computed for a *horizontal* interface.

Following Paper I, we also define the measure of asymmetry in the offset $\boldsymbol{x}$ [equation (A4)] using the two PS-waves with the opposite signs of the slowness projection onto the reflector:

$$\boldsymbol{\Delta x}_{PS} = \boldsymbol{x}_{PS}(p_{\text{int1}}, p_{\text{int2}}) + \boldsymbol{x}_{PS}(-p_{\text{int1}}, -p_{\text{int2}})\,. \qquad (2)$$

To gain insight into the influence of the model parameters on the time and offset asymmetry factors, we analyze approximate expressions for Δt_{PS} and $\boldsymbol{\Delta x}_{PS}$ obtained in Appendices A and B under the assumption of weak anisotropy ($|\epsilon| \ll 1$ and $|\delta| \ll 1$) and small offset-to-depth ratio ($|p_{\text{int1}}\, V_{P0}| \ll 1$ and $|p_{\text{int2}}\, V_{P0}| \ll 1$). As shown in Appendix A, the approximate moveout asymmetry factor Δt_{PS} for the PSV-wave in the symmetry-axis plane (i.e., for the azimuth $\alpha = 0$) is given by

$$\begin{aligned}\Delta t_{PS} &= \frac{-2\sin\nu}{V_{S0}}\,\chi\, x_{SS} \qquad (3)\\ &+ \frac{(1+4\epsilon)\,V_{P0}^2\,\sin\nu\,\cos^2\nu}{4\,(1+2\sigma)^3\,V_{S0}^3\,z_d^2}\, x_{SS}^3\,,\end{aligned}$$

where $\chi \equiv (\sigma - \delta)/(1 + 2\sigma)$ is the anisotropic parameter that can be obtained from the zero-offset traveltimes and NMO velocities of P- and SV-waves in layer-cake VTI media (Grechka and Dewangan, 2003), and z_d is the normal distance from the common midpoint (CMP) to the reflector. As expected, the asymmetry factor Δt_{PS} vanishes for zero tilt and dip ($\nu = 0$) when the medium becomes VTI. The linear term in offset is proportional to the anisotropic parameter χ that can be estimated from the moveout of pure PP and SS reflections (see below), so it does not carry independent information for velocity analysis. Note that PS moveout is asymmetric even in a dipping isotropic layer, where the cubic [equation (3)] and higher-order terms in x_{SS} do not go to zero. Figure 1 shows the asymmetry factor Δt_{PS} computed for a typical dipping TTI model from the exact equations (1) and (A1), as well as from approximation (3). While the initial slope of Δt_{PS} is well-described by the linear term in equation (3), the cubic and higher-order terms make a significant contribution at far offsets that correspond to offset-to-depth ratios of about two for the original PP and PS data. The linear term provides a good approximation for Δt_{PS} at near offsets even for larger absolute values of δ and σ when equation (3) as a whole becomes inaccurate.

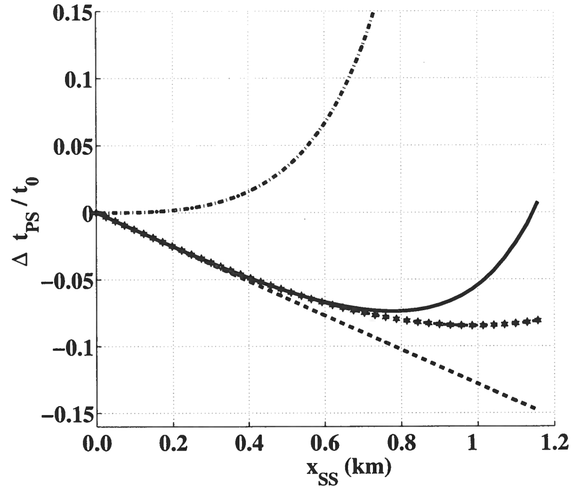

Figure 1. Time asymmetry factor Δt_{PS} for the PSV-wave in the symmetry-axis plane of a dipping TTI layer. The exact asymmetry factor is marked by the solid line, the weak-anisotropy approximation (3) by the dashed line with stars, the linear term in equation (3) by the dashed line, and Δt_{PS} in the reference isotropic model by the dash-dotted line. Δt_{PS} is normalized by the zero-offset traveltime of the PS-wave. The medium parameters are $V_{P0} = 4$ km/s, $V_{S0} = 2$ km/s, $\epsilon = 0.25$, $\delta = 0.1$, $\nu = 25°$, and $z_d = 1$ km. The maximum offset-to-depth ratio of the PP and PS data is close to two.

The weak-anisotropy approximation for the azimuthally varying offset asymmetry factor [equation (2)] is derived in Appendix B. In the symmetry-axis plane ($\alpha = 0$), the approximate Δx_{PS} takes the following form:

$$\Delta x_{PS} = \frac{\sin\nu}{2\,z_d}\left[\frac{(1+4\delta)\,V_{P0}^2}{(1+4\sigma)\,V_{S0}^2} - 1\right] x_{SS}^2\,. \qquad (4)$$

Equation (4) indicates that for typical TI models with $\sigma \gg \delta$, the influence of anisotropy *reduces* the offset asymmetry factor, which is confirmed by the numerical results in Figure 2. The weak-anisotropy approximation (4) deteriorates with increasing offset because the exact solution is influenced by the quartic term in x_{SS} even for offset-to-depth ratios of the PS-wave close to two. For the moderately anisotropic model in Fig-

$$t_{S0} = \frac{z_d}{V_{S0}}, \tag{10}$$

$$p_{S0} = \frac{\sin\nu}{V_{S0}}. \tag{11}$$

The model vector for the TTI layer includes the following components:

$$\boldsymbol{m} \equiv \left\{ V_{P0}\,,\, V_{S0}\,,\, \epsilon\,,\, \delta\,,\, \nu = \phi,\, z_d \right\}, \tag{12}$$

where the tilt ν of the symmetry axis is taken to be equal to the reflector dip ϕ. For noise-free data, all six model parameters can be recovered uniquely using the NMO velocities, zero-offset traveltimes and zero-offset slopes of the PP- and SS-waves. Indeed, the tilt ν can be found from the ratio of the NMO velocities of either wave in the dip and strike directions, which allows us to obtain the vertical velocities V_{P0} and V_{S0} from the ray parameters p_{P0} and p_{S0}. Finally, the distance z_d and parameters ϵ and δ can be inferred from the zero-offset times and NMO ellipses. However, in the presence of noise, the estimation of tilt from the ratio of the NMO velocities is highly unstable for small and moderate tilts.

This instability can be illustrated by computing the range of possible tilt values for the NMO velocities contaminated by Gaussian noise with a standard deviation of 2% (Figure 3). Although the estimation of tilt is unbiased, with the distribution centered at the correct value ($\nu = 25°$), the standard deviation of ν is about 3.5°. According to the sensitivity plots in Figure 4, such a scatter in ν is sufficient to cause unacceptably large errors in the parameters ϵ and V_{P0} reaching 0.3 and 15%, respectively. Thus, a realistic distortion of 1–2% in the NMO velocities propagates with a significant amplification into the other parameters. This conclusion is also supported by the results of Grechka et al. (2002) who found the inversion of the PP and SS (SVSV) NMO ellipses, zero-offset times and reflection slopes in a dipping TTI layer to be nonunique for tilts and dips smaller than 30–40°.

It is equally important for practical applications to study the inverse problem for the common case when only 2D data in the symmetry-axis plane are available. The data vector in this case has six elements ($V^{\text{dip}}_{\text{nmo,P}}$, t_{P0}, p_{P0}, $V^{\text{dip}}_{\text{nmo,S}}$, t_{S0}, and p_{S0}) but only five of them are independent because of the constraint,

$$\frac{p_{S0}}{p_{P0}} = \frac{t_{S0}}{t_{P0}}. \tag{13}$$

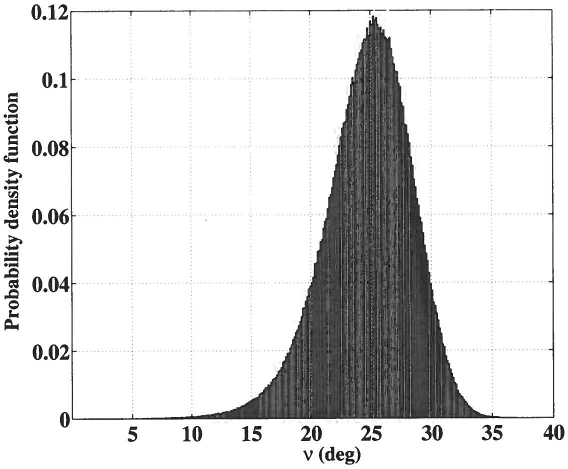

Figure 3. Probability density function of the tilt ν assuming a 2% error in the NMO velocities. The model parameters are the same as those in Figure 1.

Since the model vector (12) includes six parameters, 2D inversion cannot be carried out without additional information, such as the asymmetry attributes of the PS-wave. The results of the previous section, however, indicate that the leading terms in the expressions for asymmetry attributes depend just on the moveout parameters of the pure (PP and SS) modes. Indeed, rewriting equations (3), (4), and (5) in terms of NMO velocities, zero-offset times and reflection slopes of the PP- and SS-waves, we find [only the linear term in equation (3) is included]

$$\Delta t_{PS} = p_{S0} \left(\frac{V^2_{\text{nmo,P}}\, t^2_{P0}}{V^2_{\text{nmo,S}}\, t^2_{S0}} - 1 \right) x_{SS}\,, \tag{14}$$

$$\Delta x_{PS} = \frac{p_{S0}}{2\, t_{S0}} \left(\frac{V^4_{\text{nmo,P}}\, t^2_{P0}}{V^4_{\text{nmo,S}}\, t^2_{S0}} - 1 \right) x^2_{SS}\,, \tag{15}$$

$$x_{\min} = \frac{t_{S0}}{2 p_{S0}} \left(p_{P0} - p_{S0}\right) \left(V^2_{\text{nmo,P}}\, p_{P0} + V^2_{\text{nmo,S}}\, p_{S0}\right). \tag{16}$$

All NMO velocities in equations (14)–(16) are the dip components of the NMO ellipses measured in the symmetry-axis plane.

Clearly, only the *deviations* of the exact asymmetry attributes from the approximations (14)–(16) can provide independent information for the parameter estimation. As illustrated by Figures 1 and 2, such deviations do become substantial at large offsets x_{SS} for both the time and offset asymmetry factors.

We propose the following algorithm to invert the 2D multicomponent data in the symmetry-axis plane for the model vector (12):

- For each value of the tilt ν from 0° to 90°, find the model vector using equations (6)–(11). Restrict the range of plausible tilts by putting reasonable constraints on the parameter ϵ ($0 \le \epsilon \le 1$; see Figure 4 below).
- Taking into account errors in the measured quantities, compute the range of models that fit the data within the noise level for each plausible tilt.
- For each model found in the previous step, compute the asymmetry attributes from the exact equations (1) and (2).
- Calculate the following misfit function for the asymmetry attributes over the full range of offsets (the maximum offset-to-depth ratio of the PP and PS data

the offset asymmetry. The asymmetry information becomes useless for the inversion purposes if errors reach 20% in Δt_{PS} and 40% in Δx_{PS}.

3.3 Numerical examples

To evaluate the stability of the parameter estimation, we present a series of numerical tests in which the input data were computed from the exact equations for a representative range of TTI models and contaminated by Gaussian noise. For each model, the parameter vector m [equation (12)] is obtained for 200 realizations of the input data using the inversion algorithm described above.

In the previous section, we showed that the leading terms in x_{SS} in the equations for the asymmetry attributes do not provide independent information for the parameter estimation. Therefore, to assess the accuracy of the inversion, it is convenient to define the "quality factor" for the time asymmetry Δt_{PS} as

$$Q = \max \left\{ \frac{|\Delta t_{PS}^{\text{lin}} - \Delta t_{PS}^{\text{exact}}|}{|\Delta t_{PS}^{\text{lin}}|} \right\}, \tag{18}$$

where $\Delta t_{PS}^{\text{exact}}$ is the exact value and $\Delta t_{PS}^{\text{lin}}$ is the linear term in x_{SS} [equation (3)]; Q is computed for the maximum offset-to-depth ratio of two for the PS-waves. Since the sensitivity of the offset asymmetry factor to the model parameters is similar to that for the time asymmetry (see Figure 5), we do not include Δx_{PS} in equation (18). If the quality factor is large (close to or greater than unity, according to our estimates), we expect the asymmetry attributes to make a substantial contribution to the inversion for the tilt ν and other parameters.

First, we consider TTI media with large tilts of the symmetry axis ($\nu > 40°$), which also implies steep reflector dips. Such models are typical for the Rocky Mountain Foothills in Western Canada and other fold-and-thrust belts that contain steeply dipping TI shale layers (e.g., Isaac and Lawton, 1999). The inversion for $\nu = 60°$ produces unbiased results, with the mean of each model parameter being close to the correct value (Figure 6). Although the quality factor for the model in Figure 6 is smaller than unity ($Q = 0.6$), the moveout asymmetry is quite pronounced, with the maximum of Δt_{PS} reaching 20% of the zero-offset PS traveltime, and Δx_{PS} at far offsets reaching 70% of z_d. In comparison, for the reference isotropic medium with $\epsilon = \delta = 0$, the quality factor is infinite, the maximum of Δt_{PS} is also 20% of the zero-offset time, and Δx_{PS} is up to 110% of z_d. Since the magnitude of the asymmetry attributes is relatively large, it should be possible to estimate both Δt_{PS} and Δx_{PS} with high accuracy.

If we assume that the error in the asymmetry attributes is 2%, the parameters V_{P0}, V_{S0}, and z_d are well constrained (the standard deviation is less than 1%), and the standard deviation in ν is only 1°(Figure 6). However, in agreement with the relatively small value of the quality factor, the inverted anisotropic parameters ϵ and δ exhibit more scatter, with the standard deviation reaching 0.06 and 0.04, respectively. Also, the estimates of ϵ and δ degrade rapidly as the error in the asymmetry attributes increases, while the deviations in V_{P0}, V_{S0}, and z_d remain small. It is clear from Figure 6 that the best-constrained parameter combinations are $\chi \equiv (\sigma - \delta)/(1 + 2\sigma)$, $\sin \nu / z_d$, and V_{P0}/V_{S0}. In principle, ϵ and δ for large tilts can be obtained with sufficient accuracy from wide-azimuth PP and SS data, as demonstrated by Grechka et. al. (2002).

If the tilt for the model from Figure 6 is reduced from 60° to 25° (Figure 7), the quality factor Q increases to 1.1, which indicates that for the same errors in the input data the inversion should become more stable (i.e., the model parameters should be better resolved). The magnitude of Δt_{PS} for $\nu = 25°$, however, decreases to just 8% of zero-offset time (the corresponding value for the reference isotropic medium is 14%). Therefore, it is reasonable to assume that the uncertainty in the Δt_{PS} and Δx_{PS} becomes larger for mild tilts.

If the error in the asymmetry attributes is set to 6%, the standard deviation of the tilt ν is almost the same (1°) as that in Figure 6. Despite the high resolution in ν, Figure 7 shows that the standard deviations in V_{P0}, V_{S0}, and z_d increase to about 4%; the deviations in ϵ and δ are also substantial (0.08 and 0.05, respectively). Although the accuracy in all model parameters becomes acceptable if the error in the asymmetry attributes is limited to 2%, the small magnitude of Δt_{PS} and Δx_{PS} makes such low error levels unrealistic.

An interesting special case is that of an elliptically anisotropic medium ($\epsilon = \delta$). For the same tilt $\nu = 25°$ as that in Figure 7, but with $\epsilon = \delta = 0.2$, the qualify factor $Q = 2.1$, which indicates significant higher-order terms in offset in the equations for Δt_{PS} and Δx_{PS}. The magnitude of the time asymmetry factor is also substantial (about 20% of zero-offset time), so the inversion is expected to be stable. It turns out, however, that the parameter estimation is feasible only if the elliptical condition is assumed in advance (i.e., the inversion is performed with $\epsilon = \delta$). If the inversion is carried out without any assumption about ϵ and δ, then the inversion for several model parameters is unstable, even though the tilt is well-constrained.

To understand the influence of the asymmetry error on the inverted parameters, we repeated the inversion for a wide range of the standard deviations in Δt_{PS} and Δx_{PS} (Figures 8 and 9). Figure 8 shows that for the same errors in the input data, the velocity V_{P0} becomes better constrained for models with larger tilt, whereas for ν the opposite is true. The results for V_{P0} are explained by the much lower sensitivity of this parameter to distortions in the tilt for models with large values of ν (Figure 4b). The standard deviations in the shear-wave

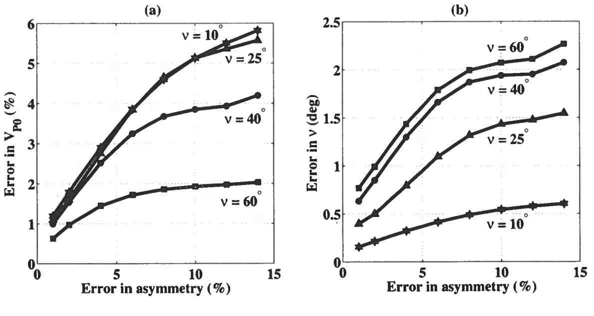

Figure 8. Error (the standard deviation) in the velocity V_{P0} (a) and the tilt ν (b) as a function of the standard deviation in the asymmetry attributes. The tilts are 10° (the line with stars), 25° (triangles), 40° (circles), and 60° (squares). The parameters V_{P0}, V_{S0}, ϵ, δ, and z_d and the standard deviations in the NMO velocities, zero-offset times, and time slopes are the same as those in Figure 6.

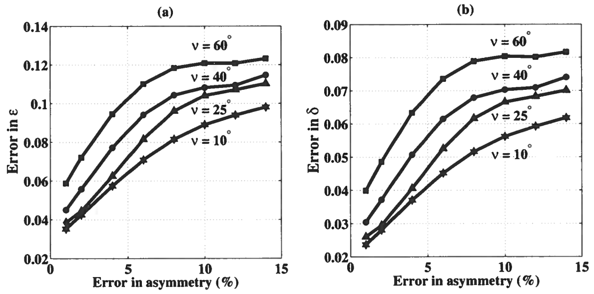

Figure 9. Same as Figure 8, but for the parameters ϵ (a) and δ (b).

tions (A26) and (B8) for small tilts ν shows, however, that the azimuthal variation of the asymmetry attributes can be predicted from their dip components ($\alpha = 0$):

$$\Delta t_{PS}(\alpha) = \Delta t_{PS}(0)\,\cos\alpha, \tag{19}$$

$$\Delta x_{PS}(\alpha) = \Delta x_{PS}(0)\,\cos\alpha. \tag{20}$$

Also, the magnitude of the asymmetry attributes decreases away from the dip direction and goes to zero in the $[x_2, x_3]$-plane. The relatively weak moveout asymmetry for intermediate azimuths means that including the azimuthal variation of Δt_{PS} and Δx_{PS} may not increase the signal-to-noise ratio. A better option for enhancing the signal may be to stack the dip components of the asymmetry attributes for adjacent CMP locations under the assumption of weak lateral heterogeneity. As discussed above [see Figure 3], the pure-mode attributes for small and moderate tilts are too sensitive to noise to help in constraining the model parameters.

For large tilts ($\nu > 40°$), the azimuthal variation of the moveout attributes becomes more complicated and cannot be described by equations (19) and (20). Numerical examples (not shown here) indicate that if $\nu > 40°$, the factors $\Delta t_{PS}(\alpha)$ and $\Delta x_{PS}(\alpha)$ measured in wide-azimuth surveys provide useful constraints on the model parameters. The asymmetry attributes, however, are redundant for large tilts because the inversion can be carried out using wide-azimuth PP and SS data alone (Grechka et al., 2002).

4 DISCUSSION AND CONCLUSIONS

The modified PP+PS=SS method introduced in Part I (Dewangan and Tsvankin, 2003) is applied here to the inversion of multicomponent (PP and PS) data acquired over a dipping TTI layer with the symmetry axis orthogonal to the layer's bottom. As was the case in Part I, the moveout asymmetry attributes of the PSV-wave play a crucial role in the parameter-estimation procedure.

To analyze the moveout asymmetry in the vertical plane that contains the symmetry axis (the symmetry-axis plane), we developed the weak-anisotropy, small-offset approximation for the time (Δt_{PS}) and offset (Δx_{PS}) asymmetry factors. Although the anisotropy has a strong influence on both Δt_{PS} and Δx_{PS} even at small offsets, the leading terms in offset depend just on the moveout parameters of the pure (PP and SS) reflection modes. Therefore, independent information for the inversion procedure is contained only in the higher-order terms that become significant when the offset-to-depth ratio for the PS-waves approaches two.

It should be emphasized that 2D moveout inversion of pure-mode (PP and SS) data in the symmetry-axis plane is nonunique, and even 3D inversion breaks down for small and moderate tilts ν of the symmetry axis. The addition of the PS-wave asymmetry attributes to the NMO velocities, zero-offset traveltimes, and reflection slopes of the recorded PP-waves and the constructed SS-waves can help to invert 2D data in the symmetry-axis plane without *a priori* information. The inversion algorithm is designed as a two-stage procedure, with the factors Δt_{PS} and Δx_{PS} computed only for the family of plausible models which fit the pure-mode data.

To predict the stability of the inversion for a given TTI model, we introduce the "quality factor" (Q) that quantifies the contribution of the cubic and higher-order terms in offset for the time asymmetry Δt_{PS}. Relatively small values of Q ($Q < 1$), which may be caused by a limited offset range of the acquired PP and PS data, typically indicate that the estimated parameters are highly sensitive to noise.

Application of the algorithm to noise-contaminated input data shows that the tilt ν of the symmetry axis is well resolved even when the model approaches VTI ($\nu = 0°$). The accuracy in the symmetry-direction velocities V_{P0} and V_{S0} and the distance z_d from the CMP to the reflector is sufficient only if the symmetry axis deviates by at least 40° from the vertical. For moderate tilts $25° < \nu < 40°$, however, the inversion for V_{P0}, V_{S0}, and z_d is possible only if the errors in the

APPENDIX A: APPROXIMATE TIME ASYMMETRY FACTOR FOR THE PSV-WAVE

To derive explicit expressions for the time and offset asymmetry factors in a TTI layer, we use the exact parametric representation of converted-wave moveout developed in Tsvankin (2001, Chapter 5) and Tsvankin and Grechka (2002). The PS-wave reflection traveltime in a homogeneous layer above a plane dipping reflector can be found in the following form:

$$t_{PS} \equiv t_P + t_S = z_r \left(q_P - p_{1P}\, q_{,1P} - p_{2P}\, q_{,2P} + q_S - p_{1S}\, q_{,1S} - p_{2S}\, q_{,2S}\right), \tag{A1}$$

where t_P and t_S are the traveltimes along the P- and S-legs, respectively, z_r is the depth of the conversion point at the reflector, p_1 and p_2 are the horizontal components of the slowness vector (the subscripts "P" and "S" indicate the wave type), $q \equiv p_3$ is the vertical slowness, and $q_{,i} \equiv \partial q/\partial p_i$ $(i = 1, 2)$. According to the convention in Grechka and Tsvankin (2000) and Paper I, the x_3-axis points down, and both legs of the PS ray represent upgoing waves (i.e., the slownesses are computed for group-velocity vectors that point toward the earth's surface). The depth of the conversion point can be represented in terms of the vertical distance z_{CMP} from the common midpoint (CMP) to the reflector:

$$z_r = \frac{z_{\text{CMP}}}{1 + \Delta z}, \tag{A2}$$

$$\Delta z = \frac{\tan\phi}{2}\left[(q_{,1P} + q_{,1S})\zeta_1 + (q_{,2P} + q_{,2S})\zeta_2\right]. \tag{A3}$$

Here $\{\zeta_1, \zeta_2\}$ is a horizontal unit vector in the updip direction and ϕ is the reflector dip.

The source-receiver offset x_{PS} of the PS-wave and the azimuth α of the source-receiver line with respect to the x_1-axis can be written as

$$x_{PS} = |\boldsymbol{x}_{PS}| = \sqrt{x_1^2 + x_2^2}, \tag{A4}$$

$$\alpha = \tan^{-1}\left(\frac{x_2}{x_1}\right), \tag{A5}$$

where x_1 and x_2 are the components of the source-receiver vector $\boldsymbol{x}_{PS}$:

$$x_1 = z_r\left(q_{,1P} - q_{,1S}\right), \tag{A6}$$

$$x_2 = z_r\left(q_{,2P} - q_{,2S}\right). \tag{A7}$$

A detailed derivation of equations (A1)–(A7) can be found in Tsvankin (2001, Appendix 5E).

For a weakly anisotropic TTI layer ($|\epsilon| \ll 1$ and $|\delta| \ll 1$), the asymmetry factor Δt_{PS} obtained from the PP+PS=SS method [equations (1) and (2)] can be linearized in the anisotropic coefficients ϵ and δ under the additional assumption of small offset x_{PS}. Here, we consider a TTI layer with the tilt of the symmetry axis equal to the reflector dip (Figure A1). Since the PP+PS=SS method operates with the PP and PS arrivals that have the same reflection point, the projection of the slowness vector onto the reflector is identical (by absolute value) for all reflected waves according to Snell's law.

Using simple trigonometric relationships, the slowness components for the incident and reflected P-waves can be written as

$$p_{\text{i}1} = p_{\text{int}1}\cos\nu + q^{\text{VTI}}\sin\nu, \tag{A8}$$

$$p_{\text{r}1} = -p_{\text{int}1}\cos\nu + q^{\text{VTI}}\sin\nu, \tag{A9}$$

$$p_{\text{i}2} = p_{\text{int}2} = -p_{\text{r}2}, \tag{A10}$$

where $p_{\text{int}1}$ and $p_{\text{int}2}$ are the slowness components of the incident and reflected waves along the interface in the dip and strike directions, respectively, q^{VTI} is the slowness component in the symmetry-axis direction, $p_{\text{i}1}$ and $p_{\text{r}1}$ are the horizontal slownesses the incidence and the reflected waves in the symmetry-axis (dip) plane (Figure A1), and $p_{\text{i}2}$ and $p_{\text{r}2}$ are the slowness components of the incidence and reflected waves in the strike direction. The above relationships between the slownesses remain valid for the S-wave with the same reflection point.

In the weak-anisotropy approximation, q^{VTI} can be expressed for P-waves in terms of $p_{\text{int}1}$ and $p_{\text{int}2}$ using the VTI equations (Tsvankin and Grechka, 2000):

$$q^{\text{VTI}} = q_{P0}\left\{1 - \frac{(p_{\text{int}1}^2 + p_{\text{int}2}^2)}{q_{P0}^2}\left[\delta + (\epsilon - \delta)\,(p_{\text{int}1}^2 + p_{\text{int}2}^2)\,V_{P0}^2\right]\right\}, \tag{A11}$$

$$q_{P0} = \sqrt{\frac{1}{V_{P0}^2} - \left(p_{\text{int}1}^2 + p_{\text{int}2}^2\right)}. \tag{A12}$$

It is convenient to expand Δt_P in a Taylor series in x_{PP} around zero offset:

$$\Delta t_P = \frac{\partial \Delta t_P}{\partial x_{PP}}\, x_{PP} + \frac{1}{6}\, \frac{\partial^3 \Delta t_P}{\partial x^3_{PP}}\, x^3_{PP} + \dots \tag{A19}$$

Equation (A19) contains only odd powers of offset because the terms even in x_{PP} do not contribute to the moveout asymmetry. Evaluating the partial derivatives in equation (A19) using the chain rule applied to equations (A17) and (A18), we arrive at

$$\Delta t_P = \frac{\sin\nu\, \cos\alpha}{V_{P0}}\, x_{PP} + \frac{(1-2\delta)\, \sin\nu\, \cos^3\alpha}{8\, V_{P0}\, z^2_{\mathrm{CMP}}} \left(1 + \frac{\tan^2\alpha}{\cos^2\nu}\right) x^3_{PP}\,. \tag{A20}$$

The linearized contribution of the S-leg to the time asymmetry factor can be found from the P-wave equation (A20) using the general transformation rule valid in the limit of weak anisotropy (Tsvankin, 2001, p. 26):

$$V_{P0} \to V_{S0}, \quad \epsilon \to 0, \quad \delta \to \sigma\,;$$

$$\sigma \equiv \frac{V^2_{P0}}{V^2_{S0}}\, (\epsilon - \delta)\,.$$

The above substitutions give the following expression for the corresponding S-wave asymmetry component Δt_S:

$$\Delta t_S = \frac{\sin\nu\, \cos\alpha}{V_{S0}}\, x_{SS} + \frac{(1-2\sigma)\, \sin\nu\, \cos^3\alpha}{8\, V_{S0}\, z^2_{\mathrm{CMP}}} \left(1 + \frac{\tan^2\alpha}{\cos^2\nu}\right) x^3_{SS}\,. \tag{A21}$$

Although the common midpoints for the PP- and SS-waves processed by the PP+PS=SS method are not exactly the same, the difference between the values of z_{CMP} for Δt_P and Δt_S can be ignored if the offsets are sufficiently small. Because of the typically large velocity ratios V_{P0}/V_{S0}, the offsets of the constructed SS-wave seldom exceed the reflector depth, so the term x^3_{SS} in equation (A21) can be neglected.

The total time asymmetry factor of the PS-wave can be found by substituting equations (A20) and (A21) into equation (A1) and taking into account that the contributions of the P-and S-legs should have opposite signs (Paper I):

$$\Delta t_{PS} = \sin\nu\, \cos\alpha \left(\frac{x_{PP}}{V_{P0}} - \frac{x_{SS}}{V_{S0}}\right) + \frac{(1-2\delta)\sin\nu \cos^3\alpha}{8\, V_{P0}\, z^2_{CMP}} \left(1 + \frac{\tan^2\alpha}{\cos^2\nu}\right) x^3_{PP}. \tag{A22}$$

Since the offsets x_{PP} and x_{SS} are related to each other, equation (A22) can be further simplified by expressing x_{PP} through x_{SS}. Applying the transformation P-to-S rule to equation (A18) yields the offset x_{SS} as a function of p_{int1} and azimuth α:

$$x_{SS} = p_{\mathrm{int1}}\, V_{S0}\, z_{\mathrm{CMP}}\, \sec\alpha \left[2 + 4\sigma + (1-4\sigma)\, p^2_{\mathrm{int1}} V^2_{S0} \left(1 + \frac{\tan^2\alpha}{\cos^2\nu}\right)\right]. \tag{A23}$$

Expanding x_{PP} in a Taylor series in x_{SS} around zero offset leads to

$$x_{PP} = \frac{\partial x_{PP}}{\partial x_{SS}}\, x_{SS} + \frac{1}{2}\, \frac{\partial^2 x_{PP}}{\partial x^2_{SS}}\, x^2_{SS} + \frac{1}{6}\, \frac{\partial^3 x_{PP}}{\partial x^3_{SS}}\, x^3_{SS}\,. \tag{A24}$$

The derivatives in equation (A24) can be determined from equations (A18) and (A23), which gives the following expression for the PP-wave offset:

$$x_{PP} = \frac{V_{P0}\,(1+2\delta)}{V_{S0}\,(1+2\sigma)}\, x_{SS} + \frac{(1-4\delta+8\epsilon)\, V^3_{P0}\, \cos^2\alpha}{8\,(1+2\sigma)^3\, V^3_{S0}\, z^2_{\mathrm{CMP}}} \left(1 + \frac{\tan^2\alpha}{\cos^2\nu}\right) x^3_{SS}\,. \tag{A25}$$

Substituting equation (A25) into equation (A22), we obtain the final expression for the time asymmetry factor in terms of the offset x_{SS}:

$$\Delta t_{PS} = \frac{-2\,(\sigma-\delta)\, \sin\nu\, \cos\alpha}{(1+2\sigma)\, V_{S0}}\, x_{SS} + \frac{(1+4\epsilon)\, V^2_{P0}\, \sin\nu\, \cos^3\alpha}{4\,(1+2\sigma)^3\, V^3_{S0}\, z^2_{\mathrm{CMP}}} \left(1 + \frac{\tan^2\alpha}{\cos^2\nu}\right) x^3_{SS}\,. \tag{A26}$$

APPENDIX B: APPROXIMATE OFFSET ASYMMETRY FACTOR

Here, we use the approach described in Appendix A to obtain an approximation for the offset asymmetry factor of the PSV-wave in a TTI layer. Using equations (2) and (A6) , the exact parametric equation for the projection of the offset asymmetry vector $\boldsymbol{\Delta x}_{PS}$ onto the x_1-axis can be written as

Image gathers of SV-waves in homogeneous and factorized VTI media

Ramzy Al-Zayer and Ilya Tsvankin
Center for Wave Phenomena, Department of Geophysics, Colorado School of Mines, Golden, CO-80401.

ABSTRACT

One of the main problems in the velocity analysis of P-wave data for VTI (transversely isotropic with a vertical symmetry axis) media is the need for *a priori* information in building a model for depth imaging. Including SV-wave moveout in the parameter-estimation procedure, either alone or in combination with P-waves, can help in positioning the reflectors at the correct depth using only reflection traveltimes. Here, in order to develop a foundation for shear-wave migration velocity analysis (MVA) in VTI media, we study SV-wave image gathers obtained after prestack depth migration. The numerical implementation is based on the modeling and migration algorithms of Alkhalifah and Liu for P-waves, which we modified to handle SV data.

For purposes of the moveout inversion of SV-waves, it is convenient to parameterize the model in terms of the NMO velocity $V_{\rm nmo}$ of horizontal SV events, the anisotropic parameter σ, which largely controls SV-wave velocity, and Thomsen parameters ϵ and δ. The moveout of horizontal events on image gathers is close to hyperbolic and depends just on $V_{\rm nmo}$ out to large offset-to-depth ratios of about 1.7. Because $V_{\rm nmo}$ differs from the vertical S-wave velocity, flattening moderate-spread gathers of SV-waves does not ensure the correct depth of the migrated events.

The influence of the parameter σ on the migrated depth of horizontal events rapidly increases as the offset-to-depth ratio approaches two. Estimation of σ, however, is hampered by the dependence of long-spread SV-wave moveout on another anisotropic parameter, ϵ (the contribution of δ to SV-wave kinematics is small). Therefore, although $V_{\rm nmo}$ and σ are sufficient to constrain the vertical S-wave velocity V_{S0} and reflector depth, the tradeoff between σ and ϵ on long-spread gathers introduces non-negligible errors in V_{S0}.

The parameters $V_{\rm nmo}$, σ, and ϵ also control the moveout of dipping SV events, but in the presence of dip both σ and ϵ influence migrated depths even at small offsets. For factorized $v(z)$ VTI media with a constant SV-wave vertical-velocity gradient k_{zs}, flattening of two or more horizontal events requires the correct NMO velocity at the surface, the gradient k_{zs} and, for large offsets, the parameters σ and ϵ. On the whole, the ambiguity in the estimation of σ and reflector depth from SV-wave moveout highlights the need to combine P- and SV-wave data in migration velocity analysis for VTI media.

Key words: SV-waves, anisotropy, VTI, velocity analysis, MVA

1 INTRODUCTION

Velocity model-building for seismic imaging is usually implemented as an iterative process that includes migration followed by velocity analysis and model updating. Most existing migration velocity analysis algorithms are designed for P-waves in heterogeneous isotropic media (e.g., Al-Yahya, 1987; Liu, 1997). The improved qual-

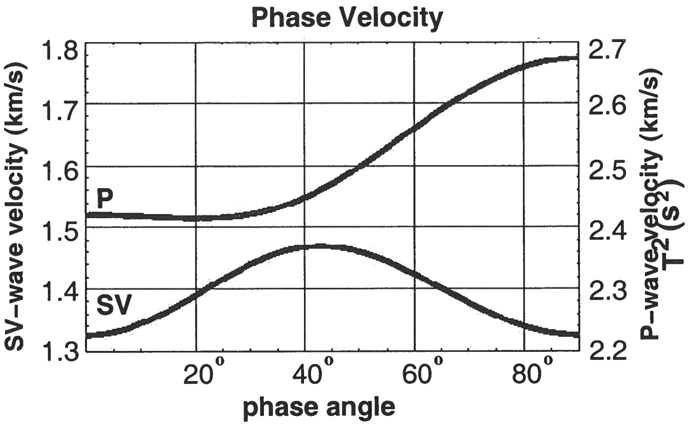

Figure 1. Phase velocity of P- and SV-waves as a function of the phase angle from the vertical in Taylor sandstone. The model parameters are $V_{P0} = 2.420\,\mathrm{km/s}$, $V_{S0} = 1.325\,\mathrm{km/s}$, $\epsilon = 0.11$, and $\delta = -0.035$.

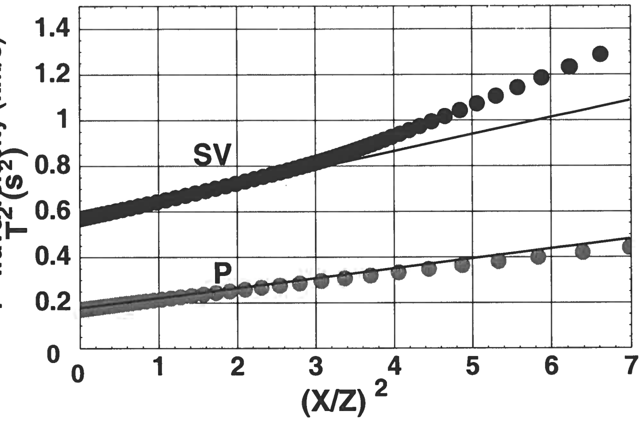

Figure 2. Squared traveltime (dots) as a function of the squared offset-to-depth ratio for P- and SV-waves in Taylor sandstone (computed at equal phase-angle increments). The solid lines mark the hyperbolic moveout curves parameterized by the NMO velocity.

the SV-wave curve stays hyperbolic out to large offsets ($x/z \approx 1.7$) and then sharply diverges from the hyperbola.

As discussed in Tsvankin and Thomsen (1994) and Tsvankin (2001), P-wave moveout becomes nonhyperbolic at smaller offsets because the magnitude of the quartic moveout coefficient is usually much larger for P-waves than for SV-waves (if $\sigma > 0$). The abrupt departure of the SV-wave moveout from the hyperbola at $x/z > 1.7$ is caused by the rapid velocity variation near the velocity maximum (notice the high density of points for $1.7 < x/z > 2$). Such a behavior of SV-wave moveout, which is not well-described by the quartic Taylor series or the Tsvankin-Thomsen (1994) nonhyperbolic equation, has serious implications for migration velocity analysis on long-spread image gathers (see below). While deviation from hyperbolic moveout for both P- and SV-waves is related to the anellipticity of the model (i.e., to the difference $\epsilon - \delta$), the parameter combinations that control the magnitude of nonhyperbolic moveout are different: η for P-waves and σ for SV-waves.

3 ANALYSIS OF SV-WAVE IMAGE GATHERS

3.1 Modeling and migration algorithms

The image gathers used for the numerical analysis below were computed by migrating 2-D synthetic data generated for homogeneous and vertically heterogeneous [factorized $v(z)$] VTI media. The traveltime table needed to build the migration operator was produced by anisotropic ray tracing.

For computing synthetic seismograms and performing ray tracing, we adapted for SV-waves the Seismic Unix (SU) codes *susynlvfti* and *rayt2dan* originally written by Alkhalifah (1995a,b) for P-waves in factorized VTI media. Prestack migration was performed using the Kirchhoff SU code *sukdmig2d* developed by Liu (1997) for isotropic media; the only change required to migrate SV data in VTI media was in using the appropriate traveltime table. Note that the work of Sarkar and Tsvankin (2003, 2004) on P-wave data was based on the same three SU codes employed here.

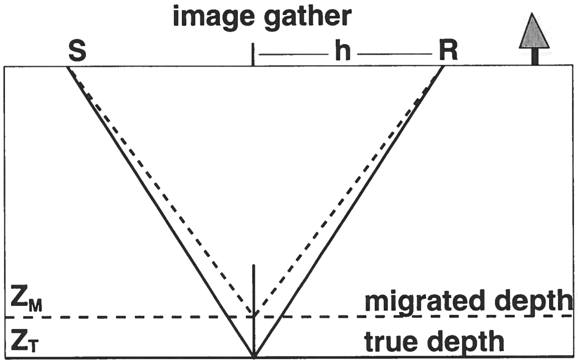

Figure 3. True and migrated positions of a horizontal reflector.

3.2 Homogeneous VTI medium

SV-wave propagation in VTI media is controlled by four Thomsen parameters: V_{P0}, V_{S0}, ϵ, and δ. For purposes of SV-wave moveout analysis, however, it is convenient to replace the two vertical velocities by the SV-wave NMO velocity V_{nmo} for horizontal interfaces [equation (2)] and the parameter σ [equation (1)]. Therefore, the parame-

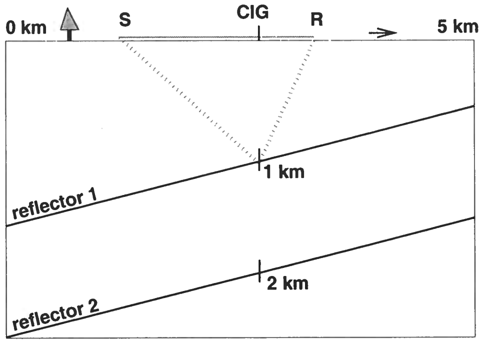

Figure 5. Geometry of the model used in the numerical modeling. Two parallel plane reflectors are embedded in a VTI medium, with the dip varying for different models between 0° and 40°. The common-image gathers (CIG) in all subsequent tests are displayed at the location where the depths of the two reflectors are 1 km and 2 km; the maximum offset is 3 km.

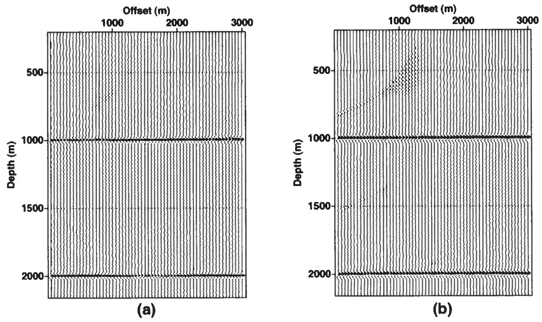

Figure 6. Common-image gathers of SV events in a homogeneous VTI medium after prestack depth migration. The reflectors are horizontal in section (a) and dipping at 40° in section (b). Migration was performed with the correct model parameters: $V_{P0,T} = 2.420\,\mathrm{km/s}$, $V_{S0,T} = 1.875\,\mathrm{km/s}$, $\epsilon_T = 0.1$, and $\delta_T = -0.1$ ($V_{\mathrm{nmo,T}} = 2.421\,\mathrm{km/s}$, $\sigma_T = 0.333$).

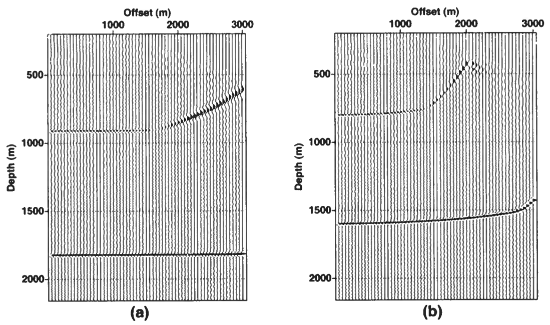

Figure 7. Influence of errors in V_{nmo} and σ on common-image gathers of horizontal SV events. In section (a), V_{nmo} is correct but σ is erroneous ($\sigma_M = 0.5$); in section (b), σ is correct but V_{nmo} is erroneous ($V_{\mathrm{nmo},M} = 1.936\,\mathrm{m/s}$). The correct parameters are $V_{\mathrm{nmo,T}} = 2.42\,\mathrm{km/s}$ and $\sigma_T = 0.333$.

is imaged at the correct depth (1 km and 2 km) because r in equation (3) is not equal to unity.

These results are similar to those obtained by Sarkar and Tsvankin (2003) for P-wave image gathers migrated using erroneous V_{nmo} or η, but differ in two important ways. First, for migration with erroneous σ but the correct NMO velocity (Figure 7a), horizontal SV events stay flat out to a large offset, $x/z \approx 1.7$. The second difference is the abrupt change and rapid increase in the residual moveout of the SV events beyond this offset. Compare Figure 7a with Figure 2a in Sarkar and Tsvankin (2003), where the residual moveout caused by an error in η increases gradually starting at an offset-to-depth ratio of about one.

The test in Figure 4 above indicates that the parameter ϵ (and possibly δ) may contribute to the migrated depth at large offsets. The influence of ϵ and δ on the residual moveout of horizontal SV events is illustrated further by Figures 8 and 9. Although the residual moveout at $x/z > 1.7$ increases almost linearly with errors in both ϵ and δ, the sensitivity of SV-wave image gathers to δ is comparatively weaker (Figure 8). Erroneous values of ϵ, however, lead to non-negligible residual moveout (Figure 9), which may complicate the estimation of σ from long-spread SV data; this issue is discussed in more detail below.

Figures 8 and 9 also illustrate one of the key differences between P- and SV-wave image gathers in VTI media: when both the correct V_{nmo} and σ (but maybe erroneous ϵ and δ) are used in the migration, the horizontal SV events are placed at the true depth. For P-waves, using the correct values of V_{nmo} and η does not ensure that the vertical velocity and, therefore, reflector depth are correct.

Hence, the long-spread moveout of horizontal SV events in image gathers depends not just on V_{nmo} and σ, but also on ϵ. Although the influence of ϵ implies that this parameter potentially may be constrained by SV-wave traveltimes, it is much more important to estimate the parameter σ. Since V_{nmo} can be obtained with high accuracy from conventional-spread SV data, reliable evaluation of σ would make it possible to determine the vertical velocity V_{S0} and reflector depth [see equation (2)]. Therefore, we next examine more closely the variation of SV-wave residual moveout with both σ and ϵ.

Suppose our goal is to estimate σ by flattening long-spread SV-wave moveout in image gathers. Unless we have *a priori* information, the value of ϵ used in the migration would be erroneous. Suppose, as in Figure 10, ϵ_M is erroneous: $\epsilon_M - \epsilon_T = 0.2$. Note the substantial residual moveout on the panel with the correct $\sigma = 0.6$; consequently, the processor would likely try changing σ to flatten the event. In Figure 10, the smallest residual moveout is observed for distorted values of σ between

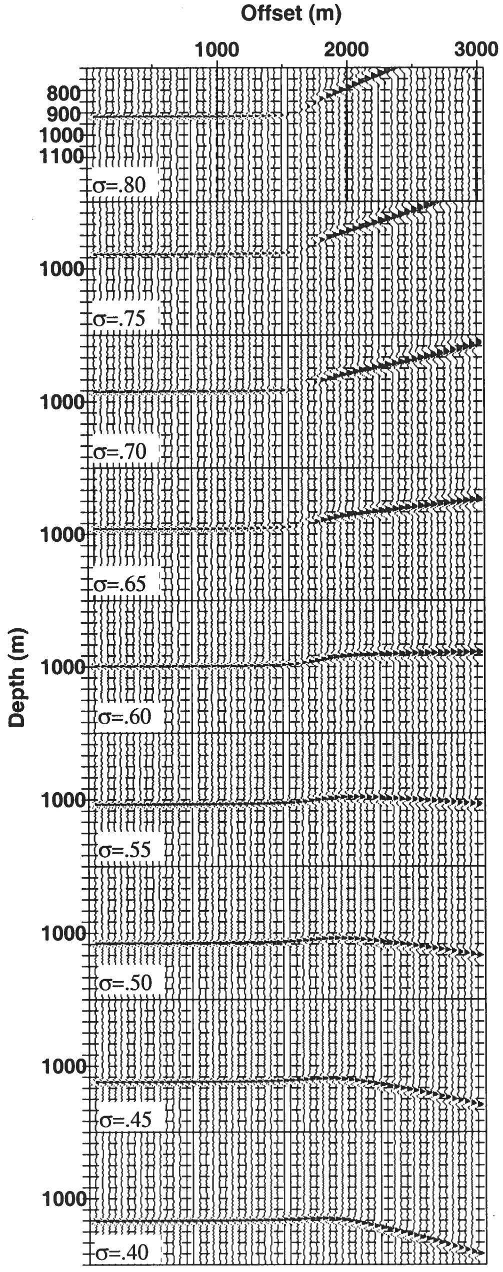

Figure 10. Tradeoff between the parameters σ and ϵ for long-spread horizontal events. The image gathers are computed for a range of σ values (σ_T = 0.6) with erroneous $\epsilon_M = 0.36$ ($\epsilon_T = 0.16$). The NMO velocity was fixed at the correct value, $V_{\mathrm{nmo,T}} = 2.420\,\mathrm{km/s}$; $\delta_M = 0.26$ ($\delta_T = 0.1$).

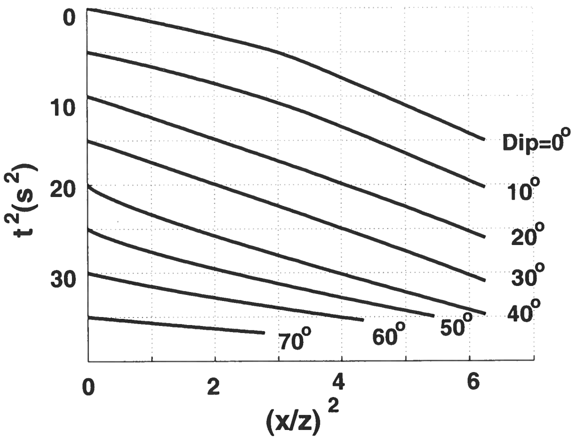

Figure 11. Exact long-spread SV-wave moveout from dipping reflectors for the model of Dog Creek shale (V_{P0} = 1.875 km/s, V_{S0} = 0.826 km/s, ϵ = 0.225, δ = 0.1; σ = 0.644). The curves are computed in the dip plane of the reflector for the dips marked on the plot and shifted vertically to avoid crossings. The offset x is normalized by the distance z from the CMP to the reflector.

series, and the series as a whole essentially breaks down. For horizontal reflectors, when $\sigma = -0.5$ [equation (2)], $V_{\mathrm{nmo}}(\phi = 0)$ goes to zero and the SV-wave moveout curve has a shape similar to that for $\phi = 40°$ (compare Figure 11 with Figure 4.11 in Tsvankin, 2001).

This dip dependence of the SV-wave moveout is completely different from that for P-waves. As shown by Tsvankin (2001) and Pech et al. (2003), the magnitude of the P-wave nonhyperbolic moveout initially decreases with dip and goes to zero for a dip close to 30°. The weak-anisotropy approximation for the quartic moveout coefficient A_4 derived by Pech et al. (2003) [their equation (19)] , which can be adapted for SV-waves by replacing η with $(-\sigma)$, predicts the same variation with dip for the moveout of SV-waves. These analytic results, however, do not apply to SV-waves for dips between 25° and 50° because the Taylor series for traveltime becomes inaccurate, and nonhyperbolic moveout is no longer described by the approximate coefficient A_4.

The increase in the magnitude of nonhyperbolic moveout for a wide range dips indicates that flattening dipping SV events may require more than one parameter (the dip-dependent NMO velocity) even for moderate offset-to-depth ratios. Since the NMO velocity of dipping events depends not only on the zero-dip value (V_{nmo}) but also on the anisotropic parameters, errors in σ lead to residual moveout even at small offsets (Figure 13). As was the case for horizontal events, the velocity V_{nmo} influences the moveout from dipping reflectors for the entire offset range (Figure 14).

It is noteworthy that the residual moveout of dipping events gradually increases with offset [sections (b-c) in Figures 13 and 14], while for horizontal events this increase is abrupt [section (a)]. Figures 13 and 14 also

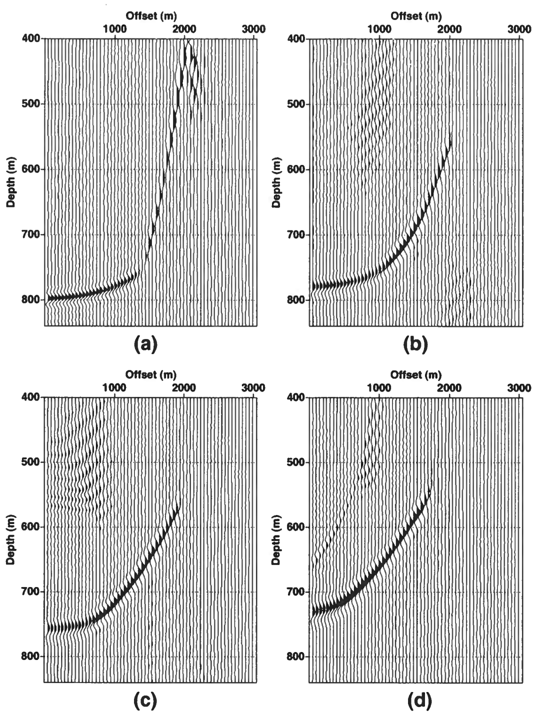

Figure 14. Influence of errors in the zero-dip NMO velocity on the residual moveout of a dipping event. The test in Figure 7b is repeated here for the shallow reflector, this time dipping at (a) 0°; (b) 20°; (c) 30°; and (d) 40°. The velocity $V_{\text{nmo,M}} = 1.936\,\text{km/s}$, while the actual value $V_{\text{nmo,T}} = 2.421\,\text{km/s}$); the rest of the model parameters are correct ($\sigma_T = 0.333$, $\epsilon_T = 0.1$, and $\delta_T = -0.1$).

3.3 Factorized vertically heterogeneous VTI medium

In factorized anisotropic media the stiffness coefficients vary in space but their ratios are held constant (e.g., Červený, 1989). Factorized models provide an efficient framework for simultaneous study of the influence of heterogeneity and anisotropy on seismic signatures and help to speed up application of such modeling tools as anisotropic ray tracing (Sarkar and Tsvankin, 2003, 2004). Since the Thomsen parameters ϵ, δ, and γ are defined through the ratios of the stiffnesses, they remain spatially invariant in factorized VTI media. The vertical velocities V_{P0} and V_{S0}, however, may change arbitrarily in space, as long as the ratio V_{P0}/V_{S0} is constant.

We consider a special type of factorized VTI media in which V_{P0} and V_{S0} are linear functions of depth z:

$$V_{P0}(z) = V_{P0}(0) + k_{zp}\, z\,; \tag{4}$$

$$V_{S0}(z) = V_{S0}(0) + k_{zs}\, z\,, \tag{5}$$

where $V_{P0}(0)$ and $V_{S0}(0)$ are the velocities at the surface ($z = 0$), and k_{zp} and k_{zs} are the vertical-velocity gradients for P-and SV-waves, respectively. According to equations (4) and (5), for the ratio $V_{P0}(z)/V_{S0}(z)$ to

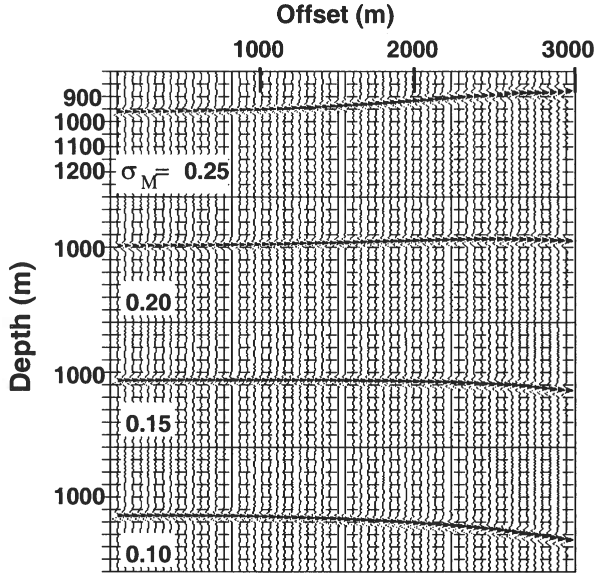

Figure 15. Image gathers of a dipping event ($\phi = 20°$) obtained using erroneous values of $V_{\text{nmo,M}} = 2.0\,\text{km/s}$ and σ_M (marked on the plot); the parameters ϵ and δ are correct. The true model parameters are $V_{\text{nmo,T}} = 2.420\,\text{km/s}$, $\sigma_T = 0.6$, $\epsilon_T = 0.16$, and $\delta_T = 0.1$. The gather for $\sigma_M = 0.15$ is practically flat.

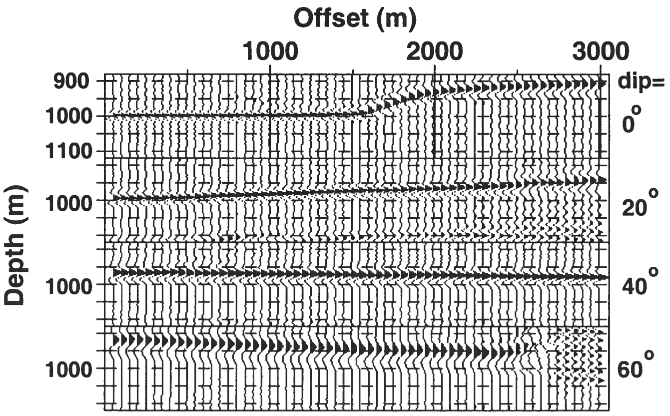

Figure 16. Influence of errors in ϵ on the residual moveout of dipping events (the dips are marked on the plot). The migration was performed with $\epsilon_M = 0.36$, while $\epsilon_T = 0.16$. The other parameters are correct: $V_{\text{nmo,T}} = 2.420\,\text{km/s}$, $\sigma_T = 0.6$, and $\delta_T = 0.1$.

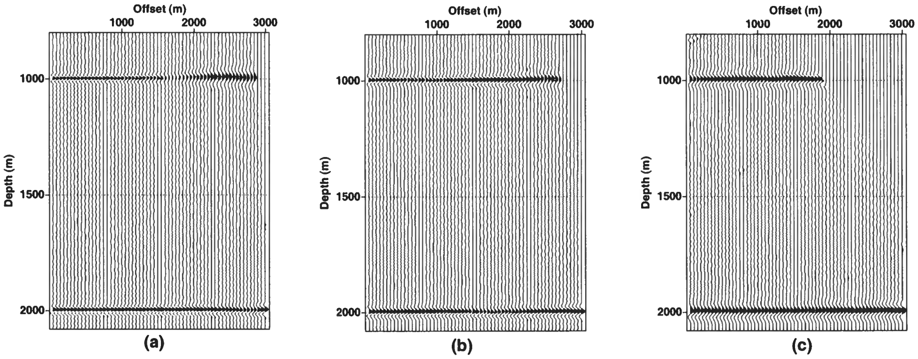

Figure 18. SV-wave image gathers for two reflectors embedded in a factorized $v(z)$ VTI medium. The reflector dips are (a) 0°; (b) 20°; and (c) 40°. The migration was performed with the actual model parameters: $V_{P0,T}(z = 0) = 2.420\,\text{km/s}$, $k_{zp,T} = 0.4\,s^{-1}$, $V_{S0,T}(z = 0) = 1.875\,\text{km/s}$, $k_{zs,T} = 0.31\,s^{-1}$, $\epsilon_T = 0.1$, and $\delta_T = -0.1$ ($V_{\text{nmo,T}}(t_0 = 0) = 2.421\,\text{km/s}$, $\sigma_T = 0.333$). The far offsets are muted to remove migration artifacts caused by the limited lateral extent of the model.

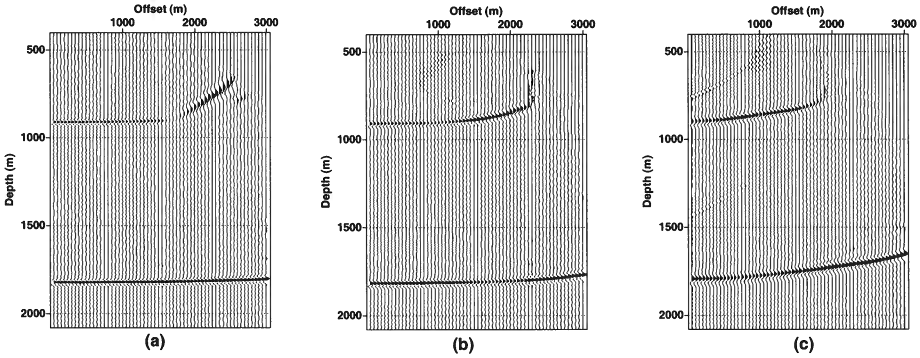

Figure 19. Influence of errors in σ on image gathers in factorized $v(z)$ VTI media. The true model is the same as that in Figure 18; the dips are (a) 0°; (b) 20°; and (c) 40°. The migration was performed with the parameters $V_{P0,M}(z = 0) = 2.707\,\text{km/s}$, $V_{S0,M}(z = 0) = 1.712\,\text{km/s}$, $k_{zp,M} = 0$, $k_{zs,M} = 0.31\,s^{-1}$, $\epsilon_M = 0.2$, and $\delta_M = 0$. The function $V_{\text{nmo}}(t_0)$ in the migration model is correct ($V_{\text{nmo,M}}(t_0 = 0) = V_{\text{nmo,T}}(t_0 = 0) = 2.421\,\text{km/s}$; $k_{zs,M} = k_{zs,T} = 0.31\,s^{-1}$), but σ_M varies from 0.5 at the surface to 0.437 at depth 3 km ($\sigma_T = 0.333$).

responsible for the quality of the migration result over a wide range of reflector dips. An analytic solution for SV-wave moveout in image gathers can be adapted from the weak-anisotropy approximation for P-waves derived by Sarkar and Tsvankin (2003). This linearized formula, however, is not sufficiently accurate for shear waves, so we developed an exact solution for the SV-wave residual moveout and also carried out prestack depth migration for a representative set of VTI models.

The moveout of both horizontal and dipping SV events in image gathers for homogeneous VTI media is mostly controlled by two main parameters: the zero-dip NMO velocity V_{nmo} and the anisotropic parameter σ. The hyperbolic portion of the moveout curve for horizontal SV events, which extends out to large offset-to-depth ratios of about 1.7, is dependent on just V_{nmo}. Therefore, small- and moderate-spread SV-wave gathers can be flattened using the correct NMO velocity without knowledge of the anisotropic parameters or the vertical S-wave velocity V_{S0}.

Erroneous values of σ lead to an abrupt increase in the residual moveout for offsets approaching twice the reflector depth, which potentially could be used to estimate both V_{nmo} and σ using SV reflections from horizontal interfaces. Since the combination of V_{nmo} and σ yields the velocity V_{S0}, it may seem that flattening of long-spread SV gathers can help to constrain reflector depth. Accurate estimation of σ, however, is hampered by the influence of the parameter ϵ on long-spread residual moveout (the contribution of δ is inconsequential). The interplay between σ and ϵ in the removal of residual moveout at large offsets can cause errors in σ of about 0.1, which is unacceptable for time-to-depth conversion.

The correct parameters V_{nmo}, σ, and ϵ are also needed to flatten SV events from dipping reflectors in homogeneous VTI media. In the presence of dip, how-

Grechka, V., Pech, A., and Tsvankin, I., 2002, Multicomponent stacking-velocity tomography for transversely isotropic media: Geophysics, **67**, 1564–1574.

Liu, Z., 1997, An analytical approach to migration velocity analysis: Geophysics, **62**, 1238–1249.

Pech, A., Tsvankin, I., and Grechka, V., 2003, Quartic moveout coefficient: 3D description and application to tilted TI media: Geophysics, **68**, 1600–1610.

Sarkar, D., and Tsvankin, I., 2003, Analysis of image gathers in factorized VTI media: Geophysics, **68**, 2016–2025.

Sarkar, D., and Tsvankin, I., 2004, Migration velocity analysis in factorized VTI media: Geophysics, in print (also CWP Research Report CWP-451).

Thomsen, L., 1986, Weak elastic anisotropy: Geophysics, **51**, 1954–1966.

Thomsen, L., 1999, Converted-wave reflection seismology over inhomogeneous, anisotropic media: Geophysics, **64**, 678–690.

Tsvankin, I., 2001, Seismic signatures and analysis of reflection data in anisotropic media: Elsevier Science Publ. Co., Inc.

Tsvankin, I. and Thomsen, L., 1994, Nonhyperbolic reflection moveout in anisotropic media: Geophysics, **59**, 1290–1304.

Tsvankin, I., and Thomsen, L., 1995, Inversion of reflection traveltimes for transverse isotropy: Geophysics, **60**, 1095–1107.

Plane-wave propagation and radiation patterns in attenuative TI media

Yaping Zhu and Ilya Tsvankin
Center for Wave Phenomena, Dept. of Geophysics, Colorado School of Mines, Golden, CO 80401

ABSTRACT

Directionally-dependent attenuation coefficient in transversely isotropic (TI) formations can have a significant influence on the amplitudes of reflected waves and distort the results of AVO (amplitude variation with offset) analysis. Here, we develop a consistent analytic treatment of plane-wave properties and point-source radiation for TI media with attenuation anisotropy.

The anisotropic quality factor can be described by matrix elements Q_{ij} defined as the ratios of the real and the imaginary parts of the corresponding stiffness coefficients. For the special "isotropic" case of $Q_{ij} = \text{const}$ the attenuation coefficient is independent of angle, even if the symmetry of the velocity anisotropy is lower than TI. To characterize TI attenuation, we follow the idea of Thomsen notation for velocity anisotropy and replace the components Q_{ij} by two reference isotropic quantities and three dimensionless anisotropic parameters ϵ_Q, δ_Q, and γ_Q. The parameters ϵ_Q and γ_Q quantify the difference between the horizontal and vertical attenuation coefficients of P- and SH-waves (respectively), while δ_Q is defined through the second derivative of the P-wave attenuation coefficient in the symmetry direction. Although the definitions of ϵ_Q, δ_Q, and γ_Q are similar to those for the corresponding Thomsen parameters, the expression for δ_Q reflects the coupling between the attenuation and velocity anisotropy.

Assuming weak attenuation as well as weak velocity and attenuation anisotropy allows us to obtain simple linearized attenuation coefficients expressed through the Thomsen-style parameters. The attenuation coefficients for both P- and SV-waves have the same form as the corresponding approximate phase-velocity functions, but the effective attenuation-anisotropy parameter for SV-waves depends on the velocity parameter σ in addition to ϵ_Q and δ_Q. The linearized approximations not only provide analytic insight into the behavior of the attenuation coefficients, they also remain accurate for the practically important range of small and moderate anisotropic coefficients, in particular for near-vertical and near-horizontal propagation directions.

We also employ the stationary-phase method to derive the far-field Green's function for arbitrarily anisotropic media with TI attenuation. The influence of the attenuation on the radiation patterns is absorbed by an exponential term that depends on the "group" attenuation coefficient along the raypath. The relationship between the group and phase (plane-wave) attenuation coefficients involves just the group and phase angles and can be used to estimate the Thomsen-style parameters from wide-angle attenuation measurements.

Key words: attenuation, attenuation anisotropy, transverse isotropy, radiation pattern, point source, seismic amplitude

where c_{ij} and c_{ij}^I are the real and the imaginary parts, respectively, of the stiffness coefficient $\tilde{c}_{ij} = c_{ij} + ic_{ij}^I$. Note that there is no summation over i and j in equation (1).

The analysis below is restricted to transversely isotropic media with either isotropic or TI attenuation. The symmetry axis is assumed to be vertical, but since all results are derived for a homogeneous medium, they can be readily adapted to TI models with any symmetry-axis orientation.

Since Q is expressed as the ratio of the real and imaginary parts of the complex stiffness coefficients, the matrix formed by the Q components inherits the structure of the stiffness matrix. For the case of VTI media with VTI attenuation, the $\mathbf{Q}$ matrix has the form

$$\mathbf{Q} = \begin{bmatrix} Q_{11} & Q_{12} & Q_{13} & 0 & 0 & 0 \\ Q_{12} & Q_{11} & Q_{13} & 0 & 0 & 0 \\ Q_{13} & Q_{13} & Q_{33} & 0 & 0 & 0 \\ 0 & 0 & 0 & Q_{55} & 0 & 0 \\ 0 & 0 & 0 & 0 & Q_{55} & 0 \\ 0 & 0 & 0 & 0 & 0 & Q_{66} \end{bmatrix}, \tag{2}$$

where $Q_{12} = Q_{11}\dfrac{c_{11} - 2c_{66}}{c_{11} - 2c_{66}\, Q_{11}/Q_{66}}$.

When both the velocity and attenuation are isotropic, the $\mathbf{Q}$ matrix includes only two independent parameters, Q_{33} and Q_{55}:

$$\mathbf{Q} = \begin{bmatrix} Q_{33} & Q_{13} & Q_{13} & 0 & 0 & 0 \\ Q_{13} & Q_{33} & Q_{13} & 0 & 0 & 0 \\ Q_{13} & Q_{13} & Q_{33} & 0 & 0 & 0 \\ 0 & 0 & 0 & Q_{55} & 0 & 0 \\ 0 & 0 & 0 & 0 & Q_{55} & 0 \\ 0 & 0 & 0 & 0 & 0 & Q_{55} \end{bmatrix}. \tag{3}$$

The component Q_{33} controls the P-wave attenuation, while Q_{55} is responsible for the SV-wave attenuation (see below). The component $Q_{13} = Q_{12}$ can be obtained from Q_{33} and Q_{55} as

$$Q_{13} = Q_{33}\frac{c_{33} - 2c_{55}}{c_{33} - 2c_{55}\, Q_{33}/Q_{55}}. \tag{4}$$

According to the attenuation measurements in sandstones by Gautam et al. (2003), the Q-factor for P-waves may be either larger or smaller than that for SV-waves, depending on the mobility of fluids in the rock. The "crossover" frequency, for which $Q_{33} = Q_{55}$, corresponds to the special case when all components of the $\mathbf{Q}$ matrix are identical:

$$Q_{ij} \equiv Q. \tag{5}$$

As discussed below, if $\mathbf{Q}$ is described by equation (5), the attenuation for both P- and S-waves is isotropic (independent of direction), even for arbitrarily anisotropic media.

The $\mathbf{Q}$ matrix can be obtained by calculating the so-called eigenstiffnesses from the stiffness matrix and applying relaxation functions to the eigenstiffnesses in order to characterize the anisotropic attenuation (Helbig, 1994; Carcione, 2001). The complex stiffness coefficients $\tilde{c}_{ij}$ and the matrix $\mathbf{Q}$ are then obtained from the eigenstiffnesses. For TI media, these operations are described in detail by Carcione (2001, Chapter 4).

The discussion here is based on the assumption of a frequency-independent Q, which is often valid in the seismic frequency band. In a more rigorous description of attenuation, the complex stiffness components and the factor Q vary with frequency, as does the velocity. Treatment of velocity dispersion, however, is outside the scope of this paper.

2.2 Christoffel equation for attenuative media

The displacement of a harmonic plane wave can be written as

$$\tilde{\mathbf{u}} = \tilde{\mathbf{U}} \exp\left[i(\omega t - \tilde{\mathbf{k}}\mathbf{x})\right], \tag{6}$$

where $\tilde{\mathbf{U}}$ denotes the polarization vector, t is the time, and ω is the angular frequency. The vector $\tilde{\mathbf{k}}$ denotes the complex wave vector, $\tilde{\mathbf{k}} = \mathbf{k} - i\mathbf{k}^I$; the imaginary part, $\mathbf{k}^I$, can be called the attenuation vector. By substituting the plane wave (6) into the wave equation, we obtain the Christoffel equation for attenuative media:

$$\left[\tilde{G}_{ik} - \rho\tilde{V}^2\delta_{ik}\right]\tilde{U}_k = 0. \tag{7}$$

Here, $\tilde{G}_{ik} = \tilde{c}_{ijkl}n_j n_l$ is the Christoffel matrix that depends on the complex stiffnesses $\tilde{c}_{ijkl}$ and the unit vector $\mathbf{n}$ in the phase direction, ρ is the density, δ_{ik} is Kronecker's symbolic δ, and $\tilde{V} = \dfrac{\omega}{\tilde{k}}$ is the complex phase velocity. The real part V of the phase velocity is given by (Carcione, 2001)

$$V = \left[\mathrm{Re}\left(\frac{1}{\tilde{V}}\right)\right]^{-1} = \frac{\omega}{k}. \tag{8}$$

2.3 SH-wave attenuation for media with isotropic Q

For waves propagating in the $[x_1, x_3]$-plane of VTI media, the Christoffel equation (7) splits into an equation for the SH-wave polarized in the x_2-direction and two coupled equations for the in-plane polarized P- and SV-waves. The equation for the wave vector of the SH-wave has the same form as that in non-attenuative media:

$$\tilde{c}_{66}\tilde{k}_1^2 + \tilde{c}_{55}\tilde{k}_3^2 - \rho\omega^2 = 0. \tag{9}$$

As shown in Appendix A2, for a medium with isotropic Q ($Q = Q_{55} = Q_{66}$), the imaginary part of equation (9) reduces to

$$\mathcal{K}_2 \equiv \frac{k^2 - (k^I)^2}{Q} - 2kk^I = 0, \tag{10}$$

where k and k^I are the real and imaginary parts (respectively) of the wave vector. Note that the assumption of isotropic Q for SH-waves does not involve the

3 TI MEDIA WITH TI ATTENUATION

Since the real and imaginary parts of the wave vector are coupled in the Christoffel equation, the directional dependence of the attenuation is influenced by the velocity anisotropy of the material. The physical reasons for the attenuation and velocity anisotropy in TI media may also be similar. For example, preferential orientation of clay platelets in shales may be responsible not just for the intrinsic velocity anisotropy (Sayers, 1994), but also for the velocity anisotropy. Therefore, it is reasonable to assume that the symmetry of the attenuation in TI media is the same as that of phase velocity. Furthermore, in the discussion below the symmetry axes of the attenuation coefficient and velocity function are taken to be parallel to each other.

3.1 SH-wave attenuation for media with TI Q

For the general TI form of the matrix $\mathbf{Q}$ in equation (2), the Christoffel equation yields the following relationship between the real and imaginary wavenumbers (Appendix A1):

$$k^2 - (k^I)^2 - 2Q_{55}\alpha k k^I = 0\,, \tag{24}$$

where

$$\alpha \equiv \frac{(1+2\gamma)\sin^2\theta + \cos^2\theta}{(1+2\gamma)\dfrac{Q_{55}}{Q_{66}}\sin^2\theta + \cos^2\theta}\,, \tag{25}$$

where γ is Thomsen's velocity-anisotropy parameter for SH-waves. Solving equation (A5) for k^I, we find the SH-wave attenuation coefficient:

$$\mathcal{A} \equiv \frac{k^I}{k} = \sqrt{1+(Q_{55}\,\alpha)^2} - Q_{55}\,\alpha\,. \tag{26}$$

In the weak-attenuation limit, equation (26) reduces to

$$\mathcal{A} = \frac{1}{2Q_{55}\,\alpha}\,. \tag{27}$$

Equation (27) shows that Q_{55} is multiplied with the parameter α to form the effective quality factor for the SH-wave, $Q_{55}^{\text{eff}} = Q_{55}\,\alpha$. At vertical incidence ($\theta = 0°$), $\alpha = 1$ and $\mathcal{A} = \dfrac{1}{2Q_{55}}$. In the horizontal direction ($\theta = 90°$), $\alpha = \dfrac{Q_{66}}{Q_{55}}$ and $\mathcal{A} = \dfrac{1}{2Q_{66}}$. For intermediate propagation directions, α reflects the coupling between the SH-wave velocity-anisotropy parameter γ and the ratio of Q_{55} and Q_{66}. The contribution of the ratio Q_{55}/Q_{66} to equation (25) is used below to define an attenuation-anisotropy parameter analogous to γ.

3.2 P-SV wave attenuation for media with TI Q

Because of the coupling between P- and SV-waves, the equations governing their velocity and attenuation are more complicated than those for SH-waves. While the complex wavenumbers for P- and SV-waves can be evaluated numerically from equations (B3)–(B4), the imaginary wavenumber k^I is difficult to obtain in closed form. Therefore, here we employ approximate solutions to study the dependence of the attenuation coefficients of P- and SV-waves on the medium parameters.

If both the attenuation anisotropy and the attenuation itself are weak, the coefficient $\mathcal{A}$ for both P- and SV-waves is given by (see Appendix C1)

$$\mathcal{A} = \frac{1}{2Q_{33}}(1+\mathcal{H})\,, \tag{28}$$

where $\mathcal{H} = \dfrac{\mathcal{H}_u}{\mathcal{H}_d}$,

$$\begin{aligned}\mathcal{H}_u = {} & \left(c_{11}n_1^2\frac{Q_{33}-Q_{11}}{Q_{11}} + c_{55}n_3^2\frac{Q_{33}-Q_{55}}{Q_{55}}\right) \\ & (c_{55}n_1^2 + c_{33}n_3^2 - \rho V^2) \\ & + c_{55}n_1^2\frac{Q_{33}-Q_{55}}{Q_{55}}(c_{11}n_1^2 + c_{55}n_3^2 - \rho V^2) \\ & - 2\left(c_{13}\frac{Q_{33}-Q_{13}}{Q_{13}} + c_{55}\frac{Q_{33}-Q_{55}}{Q_{55}}\right)(c_{13}+c_{55})n_1^2n_3^2\,,\end{aligned} \tag{29}$$

and

$$\mathcal{H}_d = \rho V^2[(c_{55}+c_{11})n_1^2 + (c_{33}+c_{55})n_3^2 - 2\rho V^2]\,. \tag{30}$$

V is the phase velocity of either the P- or SV-wave, depending on which attenuation coefficient is desired.

The parameter $\mathcal{H}$ is responsible for the contribution of the attenuation anisotropy. For the P-wave, $\mathcal{H} = 0$ results in $\mathcal{A}_P = \dfrac{1}{2Q_{33}}$, and the P-wave attenuation becomes isotropic. For the SV-wave, isotropic attenuation implies that $\mathcal{H} = \dfrac{Q_{33}-Q_{55}}{Q_{55}}$, which yields $\mathcal{A}_{SV} = \dfrac{1}{2Q_{55}}$.

Note that for P-waves at vertical incidence ($\theta = 0°$), $\mathcal{H} = 0$, and $\mathcal{A}_P = \dfrac{1}{2Q_{33}}$. In the horizontal direction ($\theta = 90°$), $\mathcal{H} = \dfrac{Q_{33}-Q_{11}}{Q_{11}}$ and $\mathcal{A}_P = \dfrac{1}{2Q_{11}}$. Hence, $\mathcal{H} = \dfrac{Q_{33}-Q_{11}}{Q_{11}}$ gives the fractional difference between the P-wave attenuation coefficients in the horizontal and the vertical directions and can be used to characterize the P-wave attenuation anisotropy (see the next section).

For SV-waves the value $\mathcal{H} = \dfrac{Q_{33}-Q_{55}}{Q_{55}}$ is the same for both the vertical and the horizontal directions, and the coefficient $\mathcal{A}_{SV} = \dfrac{1}{2Q_{55}}$ at both directions.

The high accuracy of the approximate solutions for $\mathcal{A}$ is confirmed by the example in Figure 2. The model is elliptical for the velocity anisotropy since $\epsilon = \delta$, but the shape of the attenuation coefficients is strongly nonel-

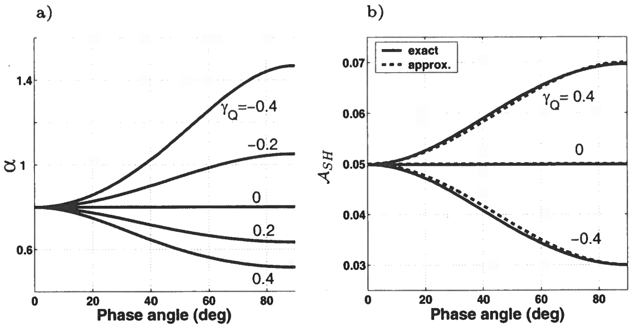

Figure 4. Factor α (a) and the attenuation coefficient $\mathcal{A}_{SH}$ (b) for the SH-wave in a TI medium with $\gamma = 0.1$, $Q_{55} = 10$, and γ_Q varying from -0.4 to 0.4. The exact $\mathcal{A}_{SH}$ is computed from equation (26), and the approximate $\mathcal{A}_{SH}$ from equation (34).

ter α yields

$$\alpha = \frac{(1+2\gamma)\sin^2\theta + \cos^2\theta}{(1+2\gamma)(1+\gamma_Q)\sin^2\theta + \cos^2\theta}\,. \tag{32}$$

When both γ and γ_Q are small ($|\gamma| \ll 1$, $|\gamma_Q| \ll 1$), α can be linearized in these parameters:

$$\alpha = 1 - \gamma_Q \sin^2\theta\,. \tag{33}$$

The attenuation coefficient from equation (27) then becomes

$$\mathcal{A}_{SH} = \frac{1}{2Q_{55}}(1 + \gamma_Q \sin^2\theta)\,. \tag{34}$$

Equation (34) has the same form as the SH-wave phase velocity linearized in the parameter γ (Thomsen, 1986).

It is clear from equation (34) that γ_Q determines the rate and sign of the variation of $\mathcal{A}_{SH}(\theta)$ away from the vertical (symmetry) direction. When $\gamma_Q > 0$, the factor α decreases with the phase angle θ, which causes an increase in the attenuation coefficient (Figure 4). In contrast, for negative γ_Q the coefficient $\mathcal{A}_{SH}(\theta)$ decreases with angle. If the magnitude of the velocity anisotropy is small (i.e., $|\gamma| \ll 1$), approximation (34) gives an accurate estimate of the attenuation coefficient even for relatively large absolute values of γ_Q reaching 0.4 (Figure 4b).

4.2 P-SV wave parameters ϵ_Q and δ_Q

The attenuation-anisotropy parameter ϵ_Q can be defined by analogy with the Thomsen parameter ϵ:

$$\epsilon_Q = \frac{1/Q_{11} - 1/Q_{33}}{1/Q_{33}} = \frac{Q_{33} - Q_{11}}{Q_{11}}\,, \tag{35}$$

ϵ_Q is equal to the fractional difference between the P-wave attenuation coefficients in the horizontal and vertical directions.

To complete the description of TI attenuation, we need to introduce a parameter similar to the Thomsen's δ that involves the quality-factor component Q_{13}. It seems that we can simply adapt the definition of δ by replacing the stiffnesses c_{ij} with $1/Q_{ij}$:

$$\hat{\delta}_Q \equiv \frac{(1/Q_{13} + 1/Q_{55})^2 - (1/Q_{33} - 1/Q_{55})^2}{2/Q_{13}(1/Q_{33} - 1/Q_{55})}\,. \tag{36}$$

The parameter $\hat{\delta}_Q$ from equation (36), however, is not physically meaningful. For example, when the attenuation is isotropic and $Q_{33} = Q_{55}$ (Gautam et al., 2003), the anisotropic parameters are supposed to vanish. Instead, $\hat{\delta}_Q$ for isotropic Q goes to infinity.

As discussed by Tsvankin [2001, see equation (1.49)], the parameter δ proved to be extremely useful in describing the signatures of reflected P-waves in VTI media because it determines the second derivative of the P-wave phase-velocity function in the vertical (symmetry) direction (the first derivative goes to zero). Therefore, although the expression for δ in terms of the stiffness coefficients cannot be directly adapted to attenuative media, a physically meaningful definition of δ_Q can be obtained from the second derivative of the P-wave attenuation coefficient $\mathcal{A}_P$ at $\theta = 0$:

$$\left.\frac{d^2\mathcal{A}_P}{d\theta^2}\right|_{\theta=0} = 2\mathcal{A}_P|_{\theta=0}\,\delta_Q\,. \tag{37}$$

In other words, the parameter δ_Q controls the curvature of the coefficient $\mathcal{A}_P$ in the vertical direction.

Assuming that both the attenuation and the attenuation anisotropy are weak, we find the following explicit expression for δ_Q (Appendix C):

$$\delta_Q \equiv \frac{\dfrac{Q_{33} - Q_{55}}{Q_{55}} c_{55} \dfrac{(c_{13} + c_{33})^2}{(c_{33} - c_{55})} + 2\dfrac{Q_{33} - Q_{13}}{Q_{13}} c_{13}(c_{13} + c_{55})}{c_{33}(c_{33} - c_{55})}\,. \tag{38}$$

The role of δ_Q in describing the P-wave attenuation anisotropy is similar to that of δ in the P-wave phase-velocity equation (Thomsen, 1986; Tsvankin, 2001). Since the first derivative of $\mathcal{A}_P$ for $\theta = 0$ is equal to zero, δ_Q is responsible for the angular variation of the P-wave attenuation coefficient near the vertical direction.

In the special case of a purely isotropic (i.e., angle-independent) velocity function, δ_Q reduces to a weighted summation of the fractional differences $(Q_{33} - Q_{55})/Q_{55}$ and $(Q_{33} - Q_{13})/Q_{13}$:

$$\delta_Q = \frac{Q_{33} - Q_{55}}{Q_{55}} \frac{4\mu}{\lambda + 2\mu} + \frac{Q_{33} - Q_{13}}{Q_{13}} \frac{2\lambda}{\lambda + 2\mu}\,, \tag{39}$$

where λ and μ are the Lame parameters.

Unless attenuation is uncommonly strong, the phase velocities of P-and SV-waves are close to those in the purely elastic medium and do not depend on the attenuation parameters ϵ_Q and δ_Q. Equation (38) for where g is defined in equation (40),

$$g_Q \equiv \frac{Q_{33}}{Q_{55}}, \tag{46}$$

and

$$\sigma \equiv \frac{V_{P0}^2}{V_{S0}^2}(\epsilon - \delta) = \frac{\epsilon - \delta}{g}. \tag{47}$$

If $|\sigma| \ll 1$, equation (45) can be further simplified to

$$\mathcal{A}_{SV} = \frac{1}{2Q_{55}}\left(1 + \sigma_Q \sin^2\theta \cos^2\theta\right), \tag{48}$$

where

$$\sigma_Q \equiv \frac{(1 - g - g_Q)(\epsilon - \delta) + (1 - g)(\epsilon_Q - \delta_Q)}{g g_Q}, \tag{49}$$

σ_Q determines the curvature of the SV-wave attenuation coefficient $\mathcal{A}_{SV}$ in the symmetry direction. According to equation (48), the attenuation for SV-waves becomes isotropic when

$$\epsilon_Q - \delta_Q = \left(\frac{g_Q}{1 - g} - 1\right)(\epsilon - \delta). \tag{50}$$

Note that the assumption $|\sigma| \ll 1$ may not be valid for many TI formations because σ typically has a substantial magnitude even when $|\epsilon - \delta|$ is small.

5.3 Numerical examples

The accuracy of the approximate solutions (43) and (48) is illustrated by numerical tests in Figures 6–8. The P-wave attenuation coefficient in Figure 6 has an extremum (a maximum) near 43° because ϵ_Q and δ_Q have different signs. Otherwise, $\mathcal{A}_P$ varies monotonically between the vertical and horizontal directions. Approximation (48) predicts a minimum of the SV-wave attenuation coefficient at $\theta = 45°$. The curve of $\mathcal{A}_{SV}$ has a concave shape because σ_Q in equation (48) is negative and large by absolute value. The extrema of the exact attenuation coefficients in Figure 6 (solid lines) are shifted toward the vertical axis with respect to their approximate positions.

The approximations for both attenuation coefficients give satisfactory results for near-vertical propagation directions with angles θ up to about 30°. The error becomes noticeable for intermediate angles $30° < \theta < 75°$ and then decreases again near the horizontal plane. Note that both the velocity and attenuation anisotropy for the model from Figure 6 is not weak (see Figure 7), and the values of $\sigma = 0.75$ and $\sigma_Q = -2.13$ are particularly large.

Figure 8 displays the attenuation coefficients for a TI medium with $\epsilon_Q = \delta_Q = 0$. In agreement with equation (43), the P-wave attenuation is almost isotropic, and $\mathcal{A}_P$ traces out a curve close to a circle. The attenuation coefficient of SV-waves, however, deviates from a circle because of the contribution of the velocity anisotropy in equation (48). Hence, isotropic Q in anisotropic media results in angle-dependent attenuation except for the special case of $Q_{ij} \equiv Q$.

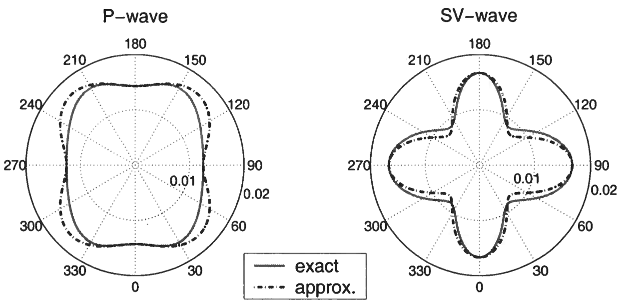

Figure 6. Attenuation coefficients of P-waves (left) and SV-waves (right) as functions of the phase angle. The solid curves are the exact values of $\mathcal{A}$ obtained by jointly solving equations (B3) and (B4); the dashed curves are the approximate coefficients from equations (43) and (48). The model parameters are V_{P0}=2.42 km/s, V_{S0}=1.4 km/s, $\epsilon = 0.4$, $\delta = 0.15$, $Q_{33} = 35$, $Q_{55} = 30$, $\epsilon_Q = -0.125$, and $\delta_Q = 0.94$.

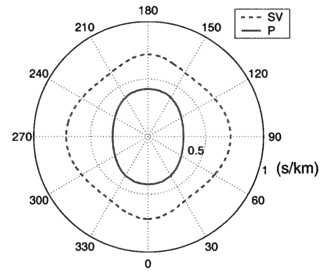

Figure 7. Slownesses of P- and SV-waves for the model from Figure 6.

If ϵ_Q and δ_Q satisfy condition (50), the attenuation coefficient of SV-waves is independent of direction (Figure 9). The curve of the P-wave coefficient $\mathcal{A}_P$ looks almost elliptical, but "elliptical attenuation anisotropy" for P-waves requires that $\epsilon_Q = \delta_Q$.

6 RADIATION PATTERNS IN ATTENUATIVE TI MEDIA

Here, we discuss the influence of attenuation on the radiation patterns of body waves excited by a point force in a homogeneous anisotropic medium. To obtain the Green's function, we apply the stationary-phase method to the Weyl-type integral for point-source radiation following the analytic results of Tsvankin and Chesnokov (1990).

code was written in Matlab for 2D TI models following the algorithm described in Carcione (2001). We discretize the model into 240×240 grid points, with a grid spacing of 5 m in both the vertical and horizontal directions. The SH-wave was excited by a point source at the center of the model. The central frequency of the wavelet is 21 Hz, the time step is 1 ms.

The SH-wave displacement for a model with $Q_{55} = 5$ and $Q_{66} = 10$ ($\gamma_Q = -0.5$) is displayed in Figure 10. The influence of attenuation is particularly convenient to study for SH-waves, because in purely elastic TI media the amplitude along the elliptical SH-wavefront is constant (Tsvankin, 2001), as illustrated by Figure 11. Since the quality factor increases away from the symmetry axis, the largest attenuation in Figure 10 is observed in the vertical direction.

The modeling results can be used to estimate the attenuation coefficient for a range of group angles ψ ($\psi = 0°, 30°, 45°, 60°$, and $90°$). The group attenuation coefficient k^I_G satisfies the equation

$$\frac{A_1}{A_0} = \exp(-k^I_G R)\,, \qquad (57)$$

where A_1 and A_0 are the spectral amplitudes at the central frequency obtained for the attenuative and associated purely elastic models, respectively. Hence,

$$k^I_G = \ln\left(\frac{A_0}{A_1}\right)/R\,. \qquad (58)$$

The coefficient k^I_G estimated using equation (58) as a function of the group angle is marked by crosses in Figure 12. To verify the relationship between the group and phase attenuation coefficients, we first compute the phase coefficient $k^I(\theta)$ (solid line) from equations (32) and (34). Then we calculate the group angle ψ from the phase angle θ and obtain the group coefficient $k^I_G(\psi)$ (dashed line) from equation (55). This analytic coefficient k^I_G is sufficiently close to the measured value, which corroborates the validity of equation (55).

The above results suggest that the attenuation-anisotropy parameter γ_Q can be estimated from the group attenuation coefficient k^I_G in the following way. After obtaining the anisotropy parameter γ using velocity or traveltime measurements, we can calculate the phase angles corresponding to the group angles at the receiver locations. The phase attenuation coefficient k^I is then computed from equation (55) for the available range of phase angles, and γ_Q can be found from equation (34).

Accurate measurements of attenuation from seismic data, however, are not easy to implement in practice. Even in the simple modeling example in Figure 12, the coefficient k^I_G at a group angle of 30° is found with a significant error because of the instability of attenuation estimates in the frequency domain.

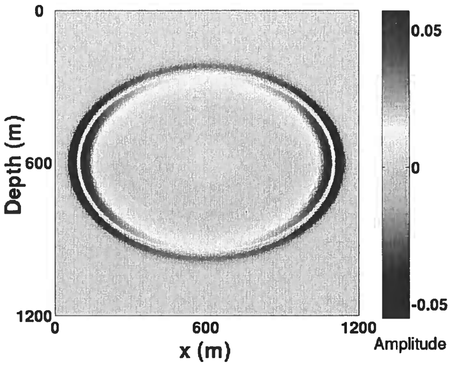

Figure 10. 2D snapshot of the SH-wavefront (particle displacement) propagating in a VTI medium with VTI Q. The model parameters are $V_{S0} = 1.83$ km/s, $\gamma = 0.44$, $Q_{55} = 5$, and $\gamma_Q = -0.5$; the time t=0.25 s.

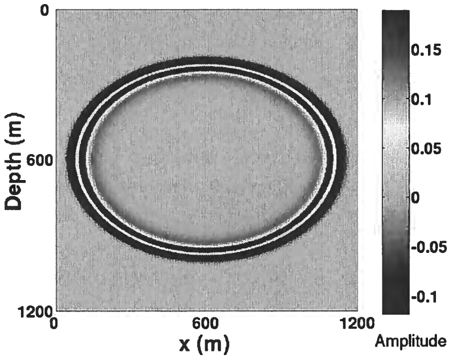

Figure 11. Same as Figure 10, but without attenuation ($Q_{55} = Q_{66} = \infty$).

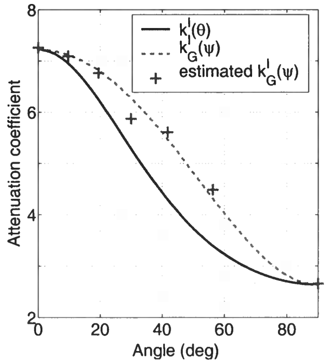

Figure 12. Comparison of the measured and computed group attenuation coefficients for the model from Figure 10. The solid curve is the phase attenuation coefficient k^I, the dashed curve is the group attenuation coefficient k^I_G computed from equation (55), and crosses are the values of k^I_G measured from the synthetic data using equation (58). The horizontal axis represents the phase angle for k^I and the group angle for k^I_G.

anisotropic rocks: 62nd Ann. Internat. Mtg., Soc Expl. Geophys., Expanded Abstracts, 640–643.

Blangy, J. P., 1994, AVO in transversely Isotropic media—An overview: Geophysics **49**, 775–781.

Carcione, J. M., 1997, Reflection and transmission of qP-qS plane waves at a plane boundary between viscoelastic transversely isotropic media: Geophys. J. Int. **129**, 669-680.

Carcione, J. M., 2000, A model for seismic velocity and attenuation in petroleum source rocks: Geophysics **65**, 1080–1092.

Carcione, J. M., 2001, Wave fields in real media: wave propagation in anisotropic, anelastic, and porous media: Pergamon.

Chichinina, T., Sabinin, V., and Ronquillo-Jarrillo, G., 2004, Azimuthal variation of P-wave attenuation for fracture characterization: Geophysics (submitted).

Gautam, K., Batzle, M., and Hofmann, R., 2003, Effect of fluids on attenuation of elastic waves: 73rd Ann. Internat. Mtg., Soc Expl. Geophys., Expanded Abstracts, 1592-1595.

Helbig, K., 1994, Foundations of anisotropy for exploration seismics: Pergamon.

Hosten, B., Deschamps, M., and Tittmann B. R., 1987, Inhomogeneous wave generation and propagation in lossy anisotropic solids: application to the characterization of viscoelastic composite materials: J. Acoust. Soc. Am., **82**, 1763–1770.

Johnston, D. H., and Toksöz, M. N., 1981, Definitions and terminology, *in* Seismic wave attenuation: Geophysics reprinted series, No. 2.

Lynn, H. B., Campagna, D., Simon, K. M., and Beckham, W. E., 1999, Relationship of P-wave seismic attributes, azimuthal anisotropy, and commercial gas pay in 3-D P-wave multiazimuth data, Rulison Field, Piceance Basin, Colorado: Geophysics, **64**, 1293–1311.

Prasad, M., and Nur, A., 2003, Velocity and attenuation anisotropy in reservoir rocks: 73rd Ann. Internat. Mtg., Soc Expl. Geophys., Expanded Abstracts, 1652-1655.

Rathore, J. S., Fjaer, E., Holt, R. M., and Renlie, L., 1995, Acoustic anisotropy of a synthetic sandstone with controlled crack geometry: Geophys. Prosp., **43**, 805–829.

Sayers, C. M., 1994, The elastic anisotropy of shales: J. Geophys. Res., **99**(B1), 767–774.

Thomsen , L., 1986, Weak elastic anisotropy: Geophysics, **51**, 1954–1966.

Tsvankin, I., and Chesnokov, E. M., 1990, Synthesis of body wave seismograms from point sources in anisotropic media: J. Geophys. Res., **95**(B7), 11317–11331.

Tsvankin, I., 1995, Seismic wavefields in layered isotropic media: Course Notes, Samizdat Press.

Tsvankin, I., 2001, Seismic signatures and analysis of reflection data in anisotropic media: Elsevier.

Ursin, B., and Stovas, A., 2002, Reflection and transmission responses of a layered isotropic viscoelastic medium: Geophysics, **67**, 307–323.

APPENDIX A: PLANE SH-WAVES IN ATTENUATIVE TI MEDIA

The Christoffel equation for a plane SH-wave propagating in an attenuative VTI medium yields

$$\tilde{c}_{66}\tilde{k}_1^2 + \tilde{c}_{55}\tilde{k}_3^2 - \rho\omega^2 = 0\,, \tag{A1}$$

where $\tilde{c}_{ij} = c_{ij} + ic^I_{ij}$ are the complex stiffness coefficients. The complex wavenumber is represented as $\tilde{k}_i = k_i - ik^I_i$, where $k^I = \sqrt{k_1^{I2} + k_2^{I2} + k_3^{I2}}$ is the attenuation coefficient. Hereafter, we limit the discussion to *homogeneous* wave propagation by assuming $\mathbf{k} \parallel \mathbf{k}^I$.

A1 VTI Q

For the general VTI form of the matrix $\mathbf{Q}$, equation (A1) becomes

$$[(c_{66} + ic^I_{66})n_1^2 + (c_{55} + ic^I_{55})n_3^2](k - ik^I)^2 - \rho\omega^2 = 0\,, \tag{A2}$$

which can be divided into the real part

$$(c_{66}n_1^2 + c_{55}n_3^2)[k^2 - (k^I)^2] + (c^I_{66}n_1^2 + c^I_{55}n_3^2)2kk^I \\ -\rho\omega^2 = 0\,, \tag{A3}$$

and the imaginary part

$$(c^I_{66}n_1^2 + c^I_{55}n_3^2)[k^2 - (k^I)^2] - (c_{66}n_1^2 + c_{55}n_3^2)2kk^I \\ = 0\,, \tag{A4}$$

where $n_1 = \sin\theta$ and $n_3 = \cos\theta$.

By expressing the complex stiffnesses through the Q_{ij} components and introducing $c_{66} = c_{55}(1+2\gamma)$, equation (A4) can be rewritten as

$$k^2 - (k^I)^2 - 2Q_{55}\alpha kk^I = 0\,, \tag{A5}$$

where

$$\alpha \equiv \frac{(1+2\gamma)n_1^2 + n_3^2}{(1+2\gamma)\dfrac{Q_{55}}{Q_{66}}n_1^2 + n_3^2}\,. \tag{A6}$$

The only physically meaningful solution k^I of equation (A5) is

$$k^I = k(\sqrt{1 + (Q_{55}\alpha)^2} - Q_{55}\alpha)\,. \tag{A7}$$

The real part, equation (A3), then reduces to

$$(c_{66}n_1^2 + c_{55}n_3^2)\left[k^2 - (k^I)^2 + \frac{2kk^I}{Q_{55}\alpha}\right] - \rho\omega^2 = 0\,, \tag{A8}$$

which gives the following expression for the phase velocity of the SH-wave:

$$V_{SH} = V_{SH}^{\text{elast}} \cdot \xi_Q\,; \tag{A9}$$

where ξ_Q is given in equation (A14), and $V^{\text{elast}}_{\{P,SV\}}$ is P- or SV-wave phase velocity in the reference purely-elastic VTI medium:

$$V^{\text{elast}}_{\{P,SV\}} = \frac{1}{2\rho} \cdot \Big\{(c_{11} + c_{55})n_1^2 + (c_{33} + c_{55})n_3^2 \pm \sqrt{[(c_{11} - c_{55})n_1^2 - (c_{33} - c_{55})n_3^2]^2 + 4(c_{13} + c_{55})^2 n_1^2 n_3^2}\Big\}^{\frac{1}{2}} . \tag{B13}$$

APPENDIX C: APPROXIMATE SOLUTIONS FOR WEAK ATTENUATION AND WEAK ATTENUATION ANISOTROPY

C1 Attenuation coefficient for P- and SV-waves

Here, we simplify the attenuation coefficient derived in Appendix B1 under the assumption of weak attenuation and weak attenuation anisotropy. If the attenuation is weak ($k^I \ll k$), the term $(k^I)^2$ in the difference $k^2 - (k^I)^2$ can be ignored. If the attenuation anisotropy is weak, then $|\frac{Q_{33} - Q_{11}}{Q_{11}}| \ll 1$, $|\frac{Q_{33} - Q_{55}}{Q_{55}}| \ll 1$, and $|\frac{Q_{33} - Q_{13}}{Q_{13}}| \ll 1$. The terms $\frac{\Delta^a}{Q_{33}} 2kk^I$, $\frac{\Delta^b}{Q_{33}} 2kk^I$, and $\frac{\Delta^c}{Q_{33}} 2kk^I$ in equations (B5) are of the second-order compared to k^2, and $\mathcal{K}_1^a \approx \mathcal{K}_1^b \approx \mathcal{K}_1^c \approx \mathcal{K}_1$. It can be further shown that for weak attenuation $\mathcal{K}_1 \approx k^2$, which allows us to represent equations (B10) as

$$\begin{aligned} A &= (c_{11} n_1^2 + c_{55} n_3^2)[(c_{55} n_1^2 + c_{33} n_3^2)k^2 - \rho\omega^2] , \\ B &= (c_{55} n_1^2 + c_{33} n_3^2)[(c_{11} n_1^2 + c_{55} n_3^2)k^2 - \rho\omega^2] , \\ C &= 2(c_{13} + c_{55})^2 n_1^2 n_3^2 k^2 . \end{aligned} \tag{C1}$$

In the limit of weak attenuation, equation (B9) takes the form

$$k^2 - (k^I)^2 - 2Q_{33} k k^I = -\frac{A\Delta^a + B\Delta^b - C\Delta^c}{A + B - C} k^2 , \tag{C2}$$

and

$$\mathcal{A} = \frac{k^I}{k} = \sqrt{1 + Q_{33}^2 + \mathcal{H}} - Q_{33} , \tag{C3}$$

where

$$\mathcal{H} = \frac{A\Delta^a + B\Delta^b - C\Delta^c}{A + B - C} . \tag{C4}$$

Further linearization of equation (C3) yields

$$\mathcal{A} = \frac{1}{2Q_{33}}(1 + \mathcal{H}) . \tag{C5}$$

C2 Parameter δ_Q

The attenuation-anisotropy parameter δ_Q is defined through the second derivative of $\mathcal{A}_P$ with respect to the phase angle θ at vertical incidence:

$$\left.\frac{d^2 \mathcal{A}_P}{d\theta^2}\right|_{\theta=0} = 2\, \mathcal{A}_P|_{\theta=0}\, \delta_Q . \tag{C6}$$

Substitution of $\mathcal{A}$ from equation (C5) leads to the following expression for δ_Q:

$$\delta_Q = \frac{1}{2} \left.\frac{d^2 \mathcal{H}}{d\theta^2}\right|_{\theta=0} \tag{C7}$$

for the case of weak attenuation. By evaluating $\left.\frac{d^2 \mathcal{H}}{d\theta^2}\right|_{\theta=0}$ and taking into account that for P-waves $\mathcal{H}|_{\theta=0} = 0$ and $\left.\frac{\partial \mathcal{H}}{\partial \theta}\right|_{\theta=0} = 0$, we obtain

$$\delta_Q = \frac{\frac{Q_{33} - Q_{55}}{Q_{55}} c_{55} \frac{(C_{13} + c_{33})^2}{(c_{33} - c_{55})} + 2\frac{Q_{33} - Q_{13}}{Q_{13}} c_{13}(c_{13} + c_{55})}{c_{33}(c_{33} - c_{55})} . \tag{C8}$$

APPENDIX D: POINT-SOURCE RADIATION IN ANISOTROPIC ATTENUATIVE MEDIA

The derivation in this section follows the methodology discussed by Tsvankin and Chesnokov (1990) and Tsvankin (1995) for purely elastic media. The wavefield from a point force (i.e., the Green's function) is decomposed into plane waves by applying Fourier transforms to the wave equation and then performing integration over one of the wavenumbers. The zero-order approximation of the stationary phase method (SPM) is used to evaluate the resulting integral and obtain the displacement in the far field.

D1 Models with $Q_{ij} \equiv Q$

The wave equation for a point force embedded in an arbitrarily anisotropic, attenuative, homogeneous medium can be written as

$$\rho \frac{\partial^2 u_i}{\partial t^2} - \tilde{c}_{ijkl} \frac{\partial^2 u_k}{\partial x_j \partial x_l} = h_i(t)\delta(\mathbf{x}) , \tag{D1}$$

where ρ is the density, $\mathbf{u}(t, \mathbf{x})$ is the displacement vector, $h_i(t)$ is the source signal, and $\delta(\mathbf{x})$ is the 3D δ function that indicates that the source is located at the origin of the Cartesian coordinate system. $\tilde{c}_{ijkl}$ is the fourth-rank tensor of the complex stiffnesses, $\tilde{c}_{ijkl} = c_{ijkl} + i c^I_{ijkl}$.

By representing the displacement vector through a 3D Fourier integral, Tsvankin and Chesnokov (1990) obtained a decomposition of point-source radiation into plane waves that can be adapted for attenuative media. We consider an arbitrarily anisotropic medium with $\frac{c_{ij}}{c^I_{ij}} \equiv Q$ for any $i, j = 1 \sim 6$ and assume homogeneous

Q, approximate expression for $\mathcal{A}^\nu$ are given in equation (43) for P-waves and (45) for SV-waves. The phase term of $\tilde{S}_i(\omega, \mathbf{x})$ from equation (D8) has the form

$$\Phi = -\frac{1}{V^\nu}(r \sin\theta + z \sin\theta) \,. \tag{D13}$$

Applying the stationary-phase condition $\frac{d\Phi}{d\theta} = 0$, we arrive at the following equation for the stationary-phase point θ:

$$\tan\theta = \frac{r}{z} + \frac{1}{z\cos\theta} V^\nu \frac{\partial p^\nu}{\partial\theta}(r\sin\theta + z\cos\theta) \,. \tag{D14}$$

Substitution of the stationary-phase angle θ from equation (D14) into the attenuation term $\exp\left[-i\frac{\omega\mathcal{A}^\nu}{V^\nu}(r\sin\theta + z\cos\theta)\right]$ yields the "group" attenuation in the source-receiver direction:

$$k_G^I = \frac{\omega}{V^\nu}\mathcal{A}^\nu \frac{r\sin\theta + z\cos\theta}{\sqrt{r^2 + z^2}} \,, \tag{D15}$$

and

$$k_G^I = k^I \cos(\psi - \theta) \,, \tag{D16}$$

where ψ is the group angle.

The far-field spectrum $\tilde{S}_i(\omega, \mathbf{x})$ then becomes

$$\tilde{S}_i^\nu(\omega, \mathbf{x}) = (1 - i\mathcal{A}^\nu)^2 \exp\left[-\frac{\omega(r\sin\theta + z\cos\theta)}{V^\nu}\mathcal{A}^\nu\right] \times \tilde{S}_i^{\nu,\mathrm{elast}}(\omega, \mathbf{x}) \,. \tag{D17}$$

CWP-473P

Joint P- and S-wave velocity reflection tomography using PP and PS data: An approach based on co-depthing and differential semblance in scattering angle optimization

Stig-Kyrre Foss†, Bjørn Ursin‡, and Maarten V. de Hoop*

† *Department of Mathematical Sciences, NTNU, N-7491 Trondheim, Norway*
‡ *Department of Petroleum Engineering and Applied Geophysics, NTNU, N-7491 Trondheim, Norway*
* *Center for Wave Phenomena, Colorado School of Mines, Golden CO, USA*

1st April 2004

ABSTRACT
The velocity-depth ambiguity in depth migration is a well known problem stemming from several factors, such as limited aperture, band-limitation of the source and the interplay between parameters of the background medium contributing to the non-uniqueness of the problem. In addition, the isotropic assumption can cause severe depth errors in the presence of anisotropy. These are severe issues when considering PP and PS images from depth migration where geologically equivalent horizons should be mapped to the same depths. The present method is based upon the differential semblance misfit function in angle to find fitting background models. This requires amplitude-compensated angle-domain common image-point gathers to be uniform. Depth consistency between the PP and PS depth image is enforced through a regularization approach penalizing mistie between key imaged reflectors in addition to the differential semblance misfit function. By migration/map demigration, time information is obtained on the key reflectors of the PP and PS image. This time information, which is independent of the velocity model, can be map-migrated to reconstruct the reflectors in depth for a given background model giving an automatic way to quantify the depth discrepancy in the tomographic approach. An approximative simplification uses the normal-incidence point rays in the map migration. The method is presented in a general 3-D framework allowing for the use of true depth information such as well markers and the inclusion of anisotropy. A strategy is presented to retrieve all parameters of a transversly isotropic medium with a known symmetry axis depending on the available information. This is employed on an ocean bottom seismic field data set from the North Sea.

Key words: Reflection tomography, generalized Radon transform, differential semblance in angle, anisotropy, converted waves.

1 INTRODUCTION

Here, we demonstrate the use of annihilator-based migration velocity analysis (MVA), related to the differential semblance (Symes and Carazzone, 1991) approach, on joint PP and PS reflectiondata. The misfit function associated with this approach is unique in that it depends smoothly on the velocity model. As is common in MVA we model the reflectiondata in the single scattering approximation, yielding a forward scattering operator that, given a velocity model, maps reflectorsto reflections. By a gradient-based search of the model space, the range of the forward scattering operator is adapted to contain the data. Data are in the range if they can be predicted by the operator.

Annihilators detect whether the data are in the range of the forward scattering operator (Stolk and de Hoop, 2002). They have their counterpart in the image domain: The data are in the range if the common image-point gathers (CIGs) obtained from the data – parametrized by scattering angle and azimuth – are *uniform*, i.e., flatand show angle-independent amplitude; annihilators emerge as derivatives with angle.

to time. Using map migration (Kleyn, 1977; Gjoystdal and Ursin, 1981) of the time horizons for every suggested velocity model we are able to quantify the depth mismatch in an automatic way. Notice that the time horizons need only be picked once. Map (de)migration can be used in complex media; see Douma and de Hoop (2003) for details and references. For the converted-wave events the ability to perform PS map migration is highly dependent on how close we are to the true model initially; hence we have opted for applying the 'PP+PS=SS' approach of Grechka and Tsvankin (2002b) to convert PS to SS for this purpose. In this paper we use a zero-offset restriction by map demigrating normal incidence point (NIP) rays (Hubral and Krey, 1980) as suggested by Whitcombe (1994) . For the mode converted waves we employ a simplified version of the 'PP+PS=SS' approach using NIP rays to compute approximate zero-offset SS traveltime data.

The outline of the paper is as follows. In following section, we introduce notation and show how to transform data to CIGs in scattering angle and azimuth for the purpose of velocity analysis. The formulation here is in 3-D and follows the presentation of Ursin (2003); the 2.5-D formulation and its subleties are presented in Foss *et al.* (2003a). Then we give a brief review of PP angle tomography (Brandsberg-Dahl *al.*, 2003b) and its extension to mode-converted waves. In the next section, we introduce our co-depthing methodology in the framework of the differential semblance in angle optimization by adding a penalizing term to the misfit function. Then we present a step-wise strategy using the aforementioned tomography tools to obtain values of a transversely isotropic (TI) medium with a known symmetry axis. Although the strategy is presented for a 3-D medium, we disregard the presence of azimuthal anisotropy. Such a medium is equivalent to a TI medium with a vertical symmetry axis through the Bond transformations (Carcione, 2001). It can be parameterized by v_{P0}, v_{S0}, ε, and δ. which are the vertical P- and S-wave velocities and the Thomsen (1986) parameters, respectively. The optimization strategy is split into the following steps:

(i) isotropic P-wave velocity analysis on PP CIGs using differential semblance in angle;
(ii) isotropic S-wave velocity analysis on PS CIGs using differential semblance in angle, making use of the P-wave velocity model obtained in (i);
(iii) seismic interpretation of the PP and PS images for key reflectors; map demigration of these reflectors yielding time horizons;
(iv) co-depthing of PP and PS images of key reflectors to obtain an optimal isotropic S-wave velocity model, using the differential semblance in angle of the PP and PS CIGs as regularizer;
(v) differential semblance in angle and semblance optimization of PP and PS CIGs jointly allowing the model to become anisotropic, enforcing the depth consistency.

Several authors have discussed the point that, in order to obtain information on the δ parameter, one either needs information of the true depth of a reflectorthrough well logs or traveltimes from rays that have traveled at an oblique angle, e.g., from strongly dipping reflectorsor from large-offset data (Audebert *et al.*, 2001; Iversen *et al.*, 2000). In the absence of such information, several approaches have been suggested (Alkhalifah and Tsvankin, 1995; Grechka and Tsvankin, 2002b). Here, we make the convenient choice of setting δ equal to zero considering a quasi-TIV medium. The remaining ε parameter is not the true anisotropy parameter, but an effective one.

Finally, we employ the above methodology on a North Sea ocean bottom seismic (OBS) field data set to obtain first a quasi-TIV velocity model and then all parameters of a TIV velocity model.

2 MIGRATION TO 'UNIFORM' ANGLE COMMON IMAGE-POINT GATHERS

Dip, scattering angle, and azimuth. We consider migration of seismic data in a 3-D heterogeneous anisotropic elastic medium. The geometry is shown in Figure 1 where the image point is denoted by $\mathbf{y} = (y_1, y_2, y_3)$. Source positions in the acquisition manifold are denoted by $\mathbf{x}^s$ and receiver positions by $\mathbf{x}^r$ (bold fonts indicate vectors). The superscripts s and r indicate association with a ray from a source and a receiver, respectively. The covector $\mathbf{p}^s(\mathbf{y})$ is the slowness vector of the ray connecting the source point $\mathbf{x}^s$ with the image point $\mathbf{y}$ evaluated at the latter point; $\mathbf{p}^s(\mathbf{x}^s)$ indicates the slowness along this ray evaluated at the source. It is the projection $\boldsymbol{\pi}^s(\mathbf{x}^s)$ of $\mathbf{p}^s(\mathbf{x}^s)$ on the acquisition manifold that is detected (via slope estimates) in the data. We furthermore introduce the phase direction $\boldsymbol{\alpha}^s = \mathbf{p}^s/|\mathbf{p}^s|$ and the phase velocity v^s according to $|\mathbf{p}^s| = 1/v^s$. A similar notation is employed for the slowness vector related quantities along the ray connecting the receiver with the image point, namely $\mathbf{p}^r(\mathbf{y})$, $\mathbf{p}^r(\mathbf{x}^r)$, and $\boldsymbol{\pi}^r(\mathbf{x}^r)$, as well as $\boldsymbol{\alpha}^r$ and v^r. The polarization vector, $\mathbf{h}$, is defined in the same manner as that for the slowness vector at the source, receiver and image point. The migration dip, $\boldsymbol{\nu}^m(\mathbf{y})$, is the direction $\boldsymbol{\nu}^m(\mathbf{y}) = \mathbf{p}^m(\mathbf{y})/|\mathbf{p}^m(\mathbf{y})|$ of the migration slowness vector, $\mathbf{p}^m(\mathbf{y}) = \mathbf{p}^s(\mathbf{y}) + \mathbf{p}^r(\mathbf{y})$.

The scattering angle, θ, between incoming and scattered rays, is defined by

$$\cos\theta = \boldsymbol{\alpha}^s \cdot \boldsymbol{\alpha}^r \quad \text{at } \mathbf{y}; \quad \theta = \theta(\mathbf{x}^r, \mathbf{y}, \mathbf{x}^s) \tag{1}$$

for a particular diffraction branch away from caustics at $\mathbf{x}^r$ or $\mathbf{x}^s$. The scattering azimuth, ψ, is the angular displacement of the vector $\boldsymbol{\psi}/|\boldsymbol{\psi}|$ with

$$\boldsymbol{\psi} = (\boldsymbol{\alpha}^s \times \boldsymbol{\alpha}^r) \times \boldsymbol{\nu}^m \quad \text{at } \mathbf{y}; \quad \psi = \psi(\mathbf{x}^r, \mathbf{y}, \mathbf{x}^s). \tag{2}$$

The two-way traveltime for a particular diffraction branch associated with a ray path connecting $\mathbf{x}^r$ with $\mathbf{x}^s$ via $\mathbf{y}$ is denoted by $T = T(\mathbf{x}^r, \mathbf{y}, \mathbf{x}^s)$.

Map (de)migration. Map migration describes how the geometry of a reflectionis mapped on the geometry of a reflector,

$$\Sigma : (\mathbf{x}^s, \mathbf{x}^r, t, \boldsymbol{\pi}^s, \boldsymbol{\pi}^r) \mapsto (\mathbf{y}, \mathbf{p}^m) \text{ at } t = T(\mathbf{x}^r, \mathbf{y}, \mathbf{x}^s) \tag{3}$$

such that the normal to the reflector is given by $\boldsymbol{\nu}^m$. For a given value of (θ, ψ) this process can be reversed to yield map

AVA compensation. The relative contrast in the medium parameters is formally defined by the 'vector'

$$\mathbf{c}^{(1)}(\mathbf{y}) = \left\{ \frac{\rho^{(1)}(\mathbf{y})}{\rho^{(0)}(\mathbf{y})}, \frac{c^{(1)}_{ijkl}(\mathbf{y})}{\rho^{(0)}(\mathbf{y}) v^s_\circ(\mathbf{y}) v^r_\circ(\mathbf{y})} \right\}^T . \tag{11}$$

Its dimension depends on the symmetry of the elastic medium. For the PP and PS reflectionproblem in a TIV medium, which will be treated in the field data example, it is of dimension 5. We have assumed that $\mathbf{c}^{(1)}(\mathbf{y}) = \widetilde{\mathbf{c}}^{(1)}(\mathbf{y}, \phi(\mathbf{y}))$ with $(\widetilde{\mathbf{c}}^{(1)})'(\mathbf{y}, \phi(\mathbf{y})) = \mathbf{C}(\mathbf{y})\, \delta(\phi(\mathbf{y}))$, where $'$ denotes the derivative with respect to the second argument, and $\mathbf{C}$ denotes the local magnitude of the jump across the zero level set of ϕ. Then (de Hoop and Bleistein, 1997, (38))

$$S^{(1)}(\mathbf{x}^\phi; \theta, \psi) = \mathbf{r}^T(\mathbf{x}^r(\mathbf{x}^\phi, \boldsymbol{\nu}_\phi, \theta, \psi), \mathbf{x}^\phi, \mathbf{x}^s(\mathbf{x}^\phi, \boldsymbol{\nu}_\phi, \theta, \psi))\mathbf{C}(\mathbf{x}^\phi), \tag{12}$$

where $\mathbf{r}$ denotes the 'vector' of radiation patterns

$$\mathbf{r}(\mathbf{x}^r, \mathbf{y}, \mathbf{x}^s) = \{h^s_m(\mathbf{y}) h^r_m(\mathbf{y}), [h^s_i(\mathbf{y}) p^s_j(\mathbf{y}) h^r_k(\mathbf{y}) p^r_l(\mathbf{y})] v^s_\circ(\mathbf{y}) v^r_\circ(\mathbf{y})\}^T . \tag{13}$$

Here, $v^s_\circ$ and $v^r_\circ$ are the phase velocities at $\mathbf{y}$ averaged over phase angles. We refer to $S^{(1)}$ as linearized scattering coefficients; $\hat{S}^{(1)}$ is a filtered realization of $S^{(1)}$, where the filter is determined by the illumination.

For the estimation of the smoothly varying parameters of the background medium (velocity model) we use a slight modification of transform (6), with

$$\mathcal{I}(\mathbf{y}; \theta, \psi) := \int_{E_{\nu^m}} \partial_t \tilde{u}(\mathbf{x}^r, \mathbf{y}, \mathbf{x}^s) \frac{|\mathbf{p}^m(\mathbf{y})|^3}{|\mathbf{r}(\mathbf{x}^r, \mathbf{y}, \mathbf{x}^s)|} d\boldsymbol{\nu}^m, \tag{14}$$

$|\mathbf{r}(\mathbf{x}^r, \mathbf{y}, \mathbf{x}^s)|$ is the Euclidean norm of the 'vector' of radiation patterns. At specular reflectionpoints, $S^{(1)}$ in (12) gets replaced by

$$\mathbf{e}(\mathbf{x}^\phi; \theta, \psi)^T \mathbf{C}(\mathbf{x}^\phi) \quad \text{with} \quad \mathbf{e}(\mathbf{x}^\phi; \theta, \psi) = \frac{\mathbf{r}(\mathbf{x}^r(\mathbf{x}^\phi, \boldsymbol{\nu}_\phi, \theta, \psi), \mathbf{x}^\phi, \mathbf{x}^s(\mathbf{x}^\phi, \boldsymbol{\nu}_\phi, \theta, \psi))}{|\mathbf{r}(\mathbf{x}^r(\mathbf{x}^\phi, \boldsymbol{\nu}_\phi, \theta, \psi), \mathbf{x}^\phi, \mathbf{x}^s(\mathbf{x}^\phi, \boldsymbol{\nu}_\phi, \theta, \psi))|}.$$

We anticipate that $\mathbf{e}$ is only weakly dependent on (θ, ψ); hence, Ursin (2003) refers to (14) as amplitude-compensated migration.

For interpretation and comparisons, we also use the structural image,

$$\mathcal{I}(\mathbf{y}) = \iint \mathcal{I}(\mathbf{y}; \theta, \psi)\, d\theta d\psi. \tag{15}$$

Subscripts are used to indicate whether a current common image-point gather (14) or structural image (15) is computed from PP or PS reflections:$\mathcal{I}_{PP}$ and $\mathcal{I}_{PS}$, respectively.

In the presence of caustics, $\mathcal{I}(\mathbf{y}; \theta, \psi)$ as defined in (14) commonly generates artifacts. A remedy for this is the use of the downward continuation approach from which an angle transform can be extracted that generates CIGs in angle without artifacts (Stolk and de Hoop, 2004). In the field case study in this paper, we believe that the formation of caustics plays a minor role; the complexity here arises from the elasticity.

3 ANGLE REFLECTION TOMOGRAPHY BY OPTIMIZATION

Tomography is performed to estimate the parameters describing the smooth part of the medium in equation (5) by kinematic and dynamic ray tracing, to compute the different quantities and factors in (7). The parameters are the density at the sources and receivers and the elastic stiffness tensor in the subsurface. For an isotropic background medium, only the P-wave velocity is required for a P-wave mode and only the S-wave velocity for an S-wave mode. Each parameter is given a representation with a finite number of coefficients, defining a finite-dimensional subspace of velocity models. If we assume that n coefficients, denoted by $\mathbf{m} = (m_1, \ldots, m_n)$, are sufficient to describe the background medium, the CIGs generated by (14) are denoted by $\mathcal{I}(\mathbf{y}, \mathbf{m}; \theta, \psi)$.

The differential semblance in angle misfit function Symes and Carazzone, 1991; Brandsberg-Dahl *et al.*, 2003b) for PP reflections is given by

$$\mathcal{J}_{PP}(\mathbf{m}) = \frac{1}{2} \iiint |\partial_{\theta,\psi} \mathcal{I}_{PP}(\mathbf{y}, \mathbf{m}; \theta, \psi)|^2\, d\theta d\psi d\mathbf{y}. \tag{16}$$

A minimum of this function is found for uniform gathers; uniform gathers guarantee optimal focusing of the structural image. The misfit function can be minimized by a gradient-based search of the model space such as a quasi-Newton method (Gill *et al.*, 1981).

In setting up the optimization, one has to decide which quantities are kept fixed under perturbation of the velocity model in between the reflectorand the acquisition manifold: $(\mathbf{y}, \mathbf{p}^m, \theta, \psi)$ or $(\mathbf{x}^s, \mathbf{x}^r, t, \boldsymbol{\pi}^s, \boldsymbol{\pi}^r)$. We will keep the first set of variables fixed in the present approach. A component of the gradient of the misfit function (16) is then given by (Brandsberg-Dahl *al.*, 2003b)

$$\frac{\partial \mathcal{J}_{PP}(\mathbf{m})}{\partial m_i} = \iiint (\partial_{\theta,\psi} \mathcal{I}_{PP}(\mathbf{y}, \mathbf{m}; \theta, \psi)) \frac{\partial \partial_{\theta,\psi} \mathcal{I}_{PP}(\mathbf{y}, \mathbf{m}; \theta, \psi)}{\partial m_i}\, d\theta d\psi d\mathbf{y}. \tag{17}$$

emerging points at the acquisition surface: Zero scattering angle does not necessarily imply zero offset.

In an *unacceptable* velocity model, let us assume that we have successfully identified an interface on both a PP image and a PS image that is geologically the same but is imaged at different depths. This situation is sketched in Figure 6, where both the PP and PS images of the key reflectorare indicated. The dotted lines indicate the S-wave rays while the solid lines indicate the P-wave rays. In the unacceptable model, the PS event is imaged at $\mathbf{y}'$, while the PP event is imaged at $\mathbf{y}$, assuming the same $\mathbf{x}$ position for the NIP-P ray through map demigration; the PS event tied to the PS image has two-way traveltime $\tau_{PS}(\mathbf{x}, \mathbf{x}'')$ ($\mathbf{x}' \neq \mathbf{x}''$ as the model is unacceptable). The zero-scattering-angle PP and PS two-way traveltimes are data obtained from map demigration, and are considered to be correct. If we assume that $\mathbf{x}'' \approx \mathbf{x}'$, we can use (20) to compute $\tau_{SS}(\mathbf{x}'')$,

$$\tau_{SS}(\mathbf{x}'') \approx 2\tau_{PS}(\mathbf{x}, \mathbf{x}'') - \tau_{PP}(\mathbf{x}). \tag{21}$$

We have obtained *pure S-wave* NIP two-way traveltimes that we will exploit as data from now on. The techniques of the previous subsection apply to these data; see Figure 5.

Misfit functional for co-depthing

The initial interpretations in (19) yield $(\mathbf{x}, \tau^j_{PP}(\mathbf{x}), \boldsymbol{\pi}^{x;j}_{PP}(\mathbf{x}))$ and $(\mathbf{x}, \tau^j_{SS}(\mathbf{x}), \boldsymbol{\pi}^{x;j}_{SS}(\mathbf{x}))$ by map demigration and the 'PP+PS=SS' approximation (21). We are then able to compute the imaged depth of the key reflectors,

$$(y_1, y_2, z^j_{PP}(y_1, y_2; \tau^j_{PP}, \boldsymbol{\pi}^{x;j}_{PP}, \mathbf{m})), \qquad (y_1, y_2, z^j_{SS}(y_1, y_2; \tau^j_{SS}, \boldsymbol{\pi}^{x;j}_{SS}, \mathbf{m})), \tag{22}$$

in an automatic way through map migration based on the medium parameters, $\mathbf{m}$, governing the P-wave and the S-wave propagation in a discriminate fashion. For example, we can define a misfit functional for co-depthing, penalizing the mistie between the picked PP reflectorin depth (19) and the map-migrated SS reflectorbased on the medium parameters governing the S-wave propagation, viz.,

$$\mathcal{J}_D(\mathbf{m}) = \frac{1}{2}\sum_j \iint \Big| z^j_{SS}(y_1, y_2; \tau^j_{SS}, \boldsymbol{\pi}^{x;j}_{SS}, \mathbf{m})) - z^j_{PP}(y_1, y_2)\Big|^2 dy_1 dy_2. \tag{23}$$

The reason to use the depths of interfaces picked on PP images as a reference is that they are usually much better determined in view of the PP versus PS ray coverage. Poorer ray coverage implies an increased ambiguity in reflectordepth (Bube, 1995). The misfit functional can also be formulated to penalize the mistie between PP and SS interfaces and well log markers $(y_1, y_2, z^j_w(y_1, y_2))$ at discrete (y_1, y_2) points.

A misfit functional like (23) allows for a gradient-based search in model space for an optimum model choice. The gradient of (23) involves the derivative of the depth of the reflectors with respect to the medium,

$$\frac{\partial \mathcal{J}_D}{\partial m_i}(\mathbf{m}) = \sum_j \iint \frac{\partial z^j_{SS}}{\partial m_i}(y_1, y_2; \tau^j_{SS}, \boldsymbol{\pi}^{x;j}_{SS}, \mathbf{m})) (z^j_{SS}(y_1, y_2; \tau^j_{SS}, \boldsymbol{\pi}^{x;j}_{SS}, \mathbf{m}) - z^j_{PP}(y_1, y_2)) dy_1 dy_2. \tag{24}$$

This derivative is defined in the framework of ray perturbation theory and coincides with a tangent to the velocity ray (Iversen, 2001).

We arrive at a joint angle tomography and co-depthing misfit functional,

$$\mathcal{J}(\mathbf{m}) = \lambda_1 \mathcal{J}_{PP}(\mathbf{m}) + \lambda_2 \mathcal{J}_{PS}(\mathbf{m}) + \mu \mathcal{J}_D(\mathbf{m}), \tag{25}$$

where λ_1, λ_2 and μ are regularization parameters governing the trade-off between uniform CIGs and depth consistency. By setting $\mu = 0$ the search aims at matching the range of the PP and PS forward scattering operators to the relevant data constituents. The co-depthing is accomplished by setting $\mu \gg \lambda_1, \lambda_2 > 0$ and aims at a search in model space without changing the range of the forward scattering operators.

5 STRATEGY FOR DEPTH-CONSISTENT PP AND PS ANGLE TOMOGRAPHY IN A TI MEDIUM

We consider a transversely isotropic (TI) medium with a known global direction of the symmetry axis in 3-D. The medium is equivalent to a TI medium with a vertical symmetry axis (TIV) through the Bond transformation (Carcione, 2001). Thus the medium is described by 4 parameters, for example the vertical P- and S-wave velocities v_{P0}, v_{S0} and Thomsen's (1986) δ and ε. We approach the problem of estimating a velocity model in the framework of TI media by performing the model updates in a bootstrapping manner, using the following steps reflecting a hierarchy of model complexity; the misfit functional is given in (25):

(i) We first carry out isotropic P-wave velocity analysis on PP CIGs using differential semblance in angle ($\lambda_1 = 1$, $\lambda_2 = 0$, $\mu = 0$).

(ii) Keeping the P-wave velocity model obtained in (i) fixed, we carry out isotropic S-wave velocity analysis on PS CIGs using differential semblance in angle ($\lambda_1 = 0$, $\lambda_2 = 1$, $\mu = 0$).

(iii) We carry out seismic interpretation of the PP and PS images for key reflectors, and pick them (including the dips). The reflectorpicked on the PP image will yield the 'reference' in the misfit functional $\mathcal{J}_D$. We map demigrate the results, making use of the P- and S-wave velocity models obtained in (i) and (ii) – we derive SS time horizons and slopes, which play the role of data.

(iv) We carry out co-depthing keeping the P-wave velocity model from (i) fixed, making use of map migration of the data obtained in (iii). The differential semblance in angle contribution to misfit plays the role of regularization ($\lambda_1 = 0$, $\mu \gg \lambda_2 > 0$).

(v) Finally, we carry out differential semblance in angle and semblance optimization of PP and PS CIGs jointly, allowing of dips (Grechka *et al.*, 2002), or other information concerning depths of reflectors,as discussed by Audebert *et al.* (2001). If well-log information is present, the true depth of the reflectors can be obtained where the wells penetrate them. The true depth of a reflector– in the absence of too strong lateral heterogeneity – is governed by the v_{P0} parameter, the vertical P-wave velocity, which can be obtained by matching the PP reflectors to well markers by map migration, similar to (23).

We assume weak anisotropy. We denote the estimate for the P-wave velocity function obtained in (i) by $\hat{v}_P$. In the absence of too strong lateral heterogeneity, the P-wave velocity obtained in (i) is approximately an interval NMO velocity,

$$\hat{v}_P \approx v_{PNMO}. \tag{34}$$

The δ parameter is the parameter that causes the tradeoff between v_{PNMO} and v_{P0} through equation (32). Based on (Grechka and Tsvankin, 2002a, (4)), the S-wave velocity obtained in (ii), denoted by $\hat{v}_S$, will approximately be an interval NMO velocity also,

$$\hat{v}_S \approx v_{SNMO}. \tag{35}$$

However, after co-depthing (step (iv)), the estimate, denoted by $\hat{v}_S$ again, may differ from v_{SNMO}.

To maintain the depth consistency obtained after (iv), while allowing anisotropy, the ratio of the vertical interval P- and S-wave velocities needs to be kept fixed. On the one hand, having assumed isotropy up to this stage, our estimate for this ratio would be $\hat{v}_P/\hat{v}_S$, which implies in the search for anisotropic parameters that

$$\frac{v_{P0}}{v_{S0}} = \frac{\hat{v}_P}{\hat{v}_S} = \frac{v_{P0}\sqrt{1+2\delta}}{\hat{v}_S} = \text{constant}. \tag{36}$$

In the presence of anisotropy, however, the ratio of interval NMO velocities and the ratio of vertical velocities can be very different. In the absence of too strong lateral heterogeneity, in the framework of a Dix-type formula, the v_{P0}/v_{S0} ratio can be estimated from the ratio of vertical PP and SS times obtained from NMO analysis for PP and PS reflections,and kept fixed.

PS angle tomography is now carried out to estimate ε (cf. (30)). In the absence of information needed to resolve the δ parameter, we simply set $\delta = 0$, thus allowing only a special case of a TIV medium for the velocity model. We then use the ratio in (36) to fix the interval vertical velocity v_{S0}. The outcome of the optimization provides an effective (a 'working') anisotropy parameter, not a true estimate of the local parameter ε itself. The effective parameter yields focused, depth-consistent PP and PS images yet with an uncertainty in abolute depth (due to $\delta = 0$).

6 FIELD DATA EXAMPLE

We tested our procedure on an ocean-bottom seismic (OBS) line from data over the Norwegian sector of the North Sea. Out of necessesity, we use a 2.5-D formalism developed by Foss *et al.* (2003a) and Foss and Ursin (2003), considering 3-D wave propagation in a 2-D model where all calculations are done in a properly chosen plane. The data have been subjected to standard processing such as static corrections, designature, p-z summation (multiple removal), and τ-p deconvolution Yilmaz, 1987).

(i) For isotropic PP angle tomography we use the P-wave parametrization in (26), but in 2-D. Thus the B-spline is 2-D and $\mathbf{x} = (x_1, x_3)$ in the following. The 2-D B-spline nodes are sampled every 250 m in the horizontal direction and every 100 m in depth. The image resulting from a simple 1-D optimization is used to identify the layering of the velocity model. In this initial optimization, a relatively dense sampling in depth was deemed necessary because of the observed rapid velocity increases. The time horizons of the interface geometry in (26) are found from map demigration as described in previous sections. These time horizons, a total of 14, are used in the subsequent velocity-estimation steps to control the interface geometry in (26). The starting values of constant velocity and velocity gradient within the layers are taken from well information from close to the 2-D slice in the medium under consideration here. The initial model and the corresponding PP image are given in Figures 7 (top left) and 9.

To construct a well-behaved misfit function (17) and guarantee a numerically stable computation of the gradient (17), we bandpass filter the data between 3 and 15 Hz. The derivatives in angle inside the misfit function are tapered at small and large angles to remove truncation effects. We normalize the misfit function (17) following Chauris and Noble (2001) to reduce the influenceof erroneous amplitude calculations and noise in the data (this could have been circumvented by making the GRT of the data to CIGs unitary). The gradient contributions are tapered as we approach the boundaries of the model or in places with low ray coverage. Before calculating both the gradient and the misfit function, we smooth the CIGS by a simple $\{1/4, 1/2, 1/4\}$ convolution filter in angle and depth; in addition, we apply a 2-D Fourier 'dip' filter (in depth and angle) to suppress imaging artifacts and noise. The filter is applied adaptively, allowing for events with smaller moveout as we approach uniform gathers. This is done in a conservative manner so as to avoid destroying the moveout behavior of the primary events. These considerations are taken into account in all subsequent calculations.

The 14 CIGs are sampled every 250 m from 1250 m onwards. Each CIG is sampled every 0.5 degrees up to 45 degrees in incoming P-wave reflectionangle. Figure 8 shows the a) starting, b) after 4 iterations and c) after 7 iterations (final) collection of CIGS in the optimization. The resulting velocity model and corresponding PP image are given in Figures 7 (top right) and 10, respectively. The optimization for the B-spline coefficients was carried out in the final couple of iterations, but this showed little improvement in the misfit function. Notice in particular the movement of the interface geometry in the final velocity model Figure 7 (top right) as compared with the initial one (top left).

(ii) The initial S-wave velocity model is chosen naively by a fixed v_S/v_P ratio for the entire model based on the final P-wave velocity, and is given in Figure 11 (left). The corresponding PS image is given in Figure 13. The P-wave velocity model is considered reliable up to 45 degrees incomsemblance-based misfit,

$$\mathcal{S}_{PS}(\mathbf{m}) = 1 - \frac{1}{2}\left(\frac{1}{N^{+}_{\theta,\psi}N^{+}_{y_1,y_2}}\iint \frac{\int\left|\iint \mathcal{I}^{+}_{PS}(\mathbf{y},\mathbf{m};\theta,\psi)d\theta d\psi\right|^2 dy_3}{\iiint\left|\mathcal{I}^{+}_{PS}(\mathbf{y},\mathbf{m};\theta,\psi)\right|^2 d\theta d\psi dy_3}dy_1dy_2. + \frac{1}{N^{-}_{\theta,\psi}N^{-}_{y_1,y_2}}\iint \frac{\int\left|\iint \mathcal{I}^{-}_{PS}(\mathbf{y},\mathbf{m};\theta,\psi)d\theta d\psi\right|^2 dy_3}{\iiint\left|\mathcal{I}^{-}_{PS}(\mathbf{y},\mathbf{m};\theta,\psi)\right|^2 d\theta d\psi dy_3}dy_1dy_2\right),$$

where $N^{+}_{\theta,\psi}$ and $N^{+}_{y_1,y_2}$ are defined as in (37) for the positive CIGS and $N^{-}_{\theta,\psi}$ and $N^{-}_{y_1,y_2}$ for the negative CIGS.

Figure 20 illustrates the shapes of the misfit for the five different layers in a layer-stripping approach as function of ε and δ. In the layer stripping approach, we use the optimal (ε, δ) values obtained in the layers above the layer in which the parameters are under investigation. Shown, by column, are the semblance misfits for PS, PP (equations (??) and (37)), their normalized sum, and our joint PP, PS differential semblance in angle misfit ($\lambda_1 = \lambda_2 = 1$, $\mu = 0$). The PP and PS semblance functions are plotted on the same scale. In the PS semblance plot, the apparent valley at a 45 degree angle is governed by $(\varepsilon - \delta)$ as in equation (33). This indicates the feasibility of detecting anisotropy in the PS CIGS, without discriminating between the two parameters. In the PP semblance plot we are unable to observe significant change in the value of the misfit function with changing anisotropy. This is expected as the data offsets are not sufficiently large for the shallow part of the model because of the aforementioned mute.

In the joint PP, PS semblance and joint PP, PS differential semblance in angle misfit plots, the lines $\delta = 0$ and

$$\varepsilon - \hat{\varepsilon} = \delta - \hat{\delta}, \tag{38}$$

are drawn, where $\hat{\varepsilon}$ and $\hat{\delta}$ are optimal values for ϵ and δ in each layer, and can be found in Table 1. In the first three layers the values are chosen using the PS semblance plot only, with $\delta = 0$, since there is not enough resolution in δ. In layers 4 and 5 we use the joint PP, PS semblance plots. In these layers values for ε and δ can be resolved by locating the semblance misfit minimum after analyzing the joint PP, PS differential semblance in angle misfit function first. In the deepest layer, a threshold on the differential semblance in angle misfit function limits the region where the semblance misfit minimum is to be found, and thus enables us to discriminate between the two apparent minima in the semblance misfit function.

In the calculations we use a fixed depth window of the CIGs. This implies, for example, that if δ becomes too negative, an event can move out of this depth window and hence no longer contributes to the misfit.

The final PP and PS CIGs for the $\hat{\varepsilon}$ and $\hat{\delta}$ values in Table 1 are shown in Figure 21. The corresponding images are given in Figures 22 and 23 in *depth* and in *two-way* PP *time* (obtained by depth-to-time conversion using the P-wave velocities from (i)) in Figures 24 and 25. The images in the latter two figures correlate very well. For comparison, the initial PP image obtained in (i) is also converted to two-way PP time in Figure 26.

layer	$\hat{\varepsilon}$	$\hat{\delta}$
1	0.035	0.0
2	0.0	0.0
3	0.02	0.0
4	0.09	-0.04
5	-0.02	-0.02

Table 1. Anisotropic parameter values resulting from layer stripping.

7 DISCUSSION AND CONCLUSION

We have presented a reflection tomographic or MVA approach to obtain depth-consistent PP and PS images by making use of a differential semblance in angle measures and map (de)migration, enabling automatic measurement of any mistie in depth. This involves an extension of differential semblance in angle to converted waves, as well as the development of a co-depthing measure. The co-depthing procedure is derived from the zero scattering angle case of Grechka and Tsvankin's 'PP+PS=SS' concept. When the velocity model is far from the true model, or when there is a significant inconsistency between the models governing the P-wave leg and the S-wave leg of the PS scattering event, the approximation we make in the 'PP+PS=SS' concept deteriorates. Also, the current co-depthing procedure, based on zero scattering angle, fails to apply in the presence of caustics. Then the co-depthing procedure can be refined by using the aforementioned 'PP+PS=SS' approach to compute *prestack* SS traveltimes and slopes, and making use of finite-offset map (de)migration.

Perhaps one would expect that by first estimating a P-wave velocity model from PP reflections and then an S-wave velocity model from PS reflections would guarantee consistency in depth between PP and PS images, since the mode-converted wave is tied to the P wave. The field data example illustrates that this is not the case: The difference in depths can be several hundred meters even if the differential semblance in angle measure, through uniform CIGS, indicate a model fitting both the PP and PS scattering events.

The tying of the PP and PS events forces us to take anisotropy into account; this has been observed by several authors, see for example Artola *et al.* (2003). We developed an approach derived from joint PP and PS angle tomography, consisting of five steps, for carrying out MVA. We estimated a compressional- and shear-wave velocity model based on a quasi-TIV medium (Thomsen's $\delta = 0$) assumption. We also succeeded in estimating δ separately from ε, with a degree of uncertainty, in part of the model; in this estimation we made additional use of a semblance measure applied to the PP and

residual prestack migration: Proceedings 67th Ann. Internat. Mtg. Soc. of Expl. Geophys., pages 1762–1765.

Foss, S. K., and Ursin, B., 2003, 2.5-D modeling, inversion and angle migration in anisotropic elastic media: Geophysical Prospecting, Accepted.

Foss, S. K., de Hoop, M., and Ursin, B., 2003a, Linearized 2.5-D parameter imaging-inversion in anisotropic elasic media: Geophys. J. Int., submitted.

——— 2003b, A practical approach to automated pp angle tomography: EAGE / SEG summer research workshop in Trieste.

Gill, P. E., Murray, W., and H., W. M., 1981, Practical optimization: , Academic Press.

Gjoystdal, H., and Ursin, B., 1981, Inversion of reflection times in three-dimensions: Geophysics, **46**, 972–983.

Grechka, V., and Tsvankin, I., 2002a, The joint nonhyperbolic moveout inversion of pp and ps data in vti media: Geophysics, **67**, 1929–1932.

——— 2002b, Pp + ps = ss: Geophysics, **67**, 1961–1971.

Grechka, V., Pech, A., and Tsvankin, I., 2002, Multicomponent stacking-velocity tomography for transversely isotropic media: Geophysics, **67**, 1564–1574.

Herrenschmidt, A., Granger, P.-Y., Audebert, F., Gerea, C., Etienne, G., Stopin, A., Alerini, M., Le Bégat, S., Lambaré, G., Berthet, P., Nebieridze, S., and Boelle, J.-L., 2001, Comparison of different strategies for velocity model building and imaging of pp and ps real data: The Leading Edge, **20**, 984–995.

Hubral, P., and Krey, T., 1980, Interval velocities from seismic reflectiontime measurements: , Soc. of Expl. Geophys.

Iversen, E., Gjøystdal, H., and Hansen, J. O., 2000, Prestack map migration an engine for parameter estimation in ti media: Proceedings 70th Ann. Internat. Mtg., Soc. Explor. Geophys., pages 1004–1007.

Iversen, E., 2001, First-order perturbation theory for seismic isochrones: Studia geophysica et geodaetica, **45**, 394–444.

Kleyn, A. H., 1977, On the migration of reflection-timecontour maps: Geophys. Prosp., **25**, 125–140.

Plessix, R.-E., ten Kroode, F., and Mulder, W., 2000, Automatic crosswell tomography by differential semblance optimization: theory and gradient computation: Geophysical Prospecting, **48**, 913–935.

Sayers, C. M., Smit, T. J. H., van Eden, C., Wervelman, R., Bachmann, B., Fitts, T., Bingham, J., McLachlan, K., Hooyman, P., Noeth, S., and Mandhiri, D., 2004, Use of reflectiontomography to predict pore pressure in overpressured reservoir sands: 74th Ann. Internat. Mtg., Soc. Explor. Geophys., Expanded Abstracts, –.

Sollid, A., 2000, Imaging of ocean bottom seismic data: Ph.D. thesis, Norwegian University of Science and Technology, Trondheim.

Stolk, C. C., and de Hoop, M. V., 2002, Microlocal analysis of seismic inverse scattering in anisotropic elastic media: Communications in Pure and Applied Mathematics, **55**, 261–301.

Stolk, C. C., and de Hoop, M. V., 2004, Seismic inverse scattering in the downward continuation approach: SIAM J. Appl. Math.

Stolk, C. C., 2002, Microlocal analysis of the scattering angle transform: Comm. PDE, **27**, 1879–1900.

Stopin, A., and Ehinger, A., 2001, Joint pp ps tomographic inversion of the mahogany 2-d-4-c obc seismic data: Proceedings 71th Ann. Internat. Mtg., Soc. Explor. Geophys., pages 837–840.

Stork, C., and Clayton, R. W., 1986, Analysis of the resolution between ambiguous velocity and reflectorposition for traveltime tomography: Proceedings 56th Ann. Internat. Mtg., Soc. Explor. Geophys., pages 545–550.

Symes, W., and Carazzone, J., 1991, Velocity inversion by differential semblance optimization: Geophysics, **56**, 654–663.

Symes, W., 1991, A differential semblance algorithm for the inverse problem of reflectionseismology: Computers Math. Applic., **22**, 147–178.

Symes, W., All stationary points of differential semblance are asymptotic global minimizers: layered acoustics:, Rice Inversion Project, Annual report, 2000.

Taner, M. T., and Koehler, F., 1969, Velocity spectra - Digital computer derivation and applications of velocity functions: Geophysics, **34**, 859–881.

Thomsen, L., 1986, Weak elastic anisotropy: Geophysics, **51**, 1954–1966.

Thomsen, L., 1999, Converted-wave reflection seismology over inhomogeneous, anisotropic media: Geophysics, **64**, 678–690.

Tsvankin, I., and Grechka, V., 2002, 3D description and inversion of reflection moveout of PS-waves in anisotropic media: Geoph. Prosp., **50**, 301–316.

Tygel, M., Schleicher, J., and Hubral, P., 1994, Pulse distortion in depth migration: Geophysics, **59**, 1561–1569.

Ursin, B., 2003, Parameter inversion and angle migration in anisotropic elastic media: Geophysics, Accepted.

Versteeg, R. J., 1993, Sensitivity of prestack depth migration to the velocity model: Geophysics, **58**, 873–882.

Whitcombe, D. N., 1994, Fast model building using demigration and single-step ray migration: Geophysics, **59**, 439–449.

Yilmaz, O., 1987, Seismic data processing: vol. 2 of *Investigations in Geophysics*, Society of Exploration Geophysicists, Tulsa.

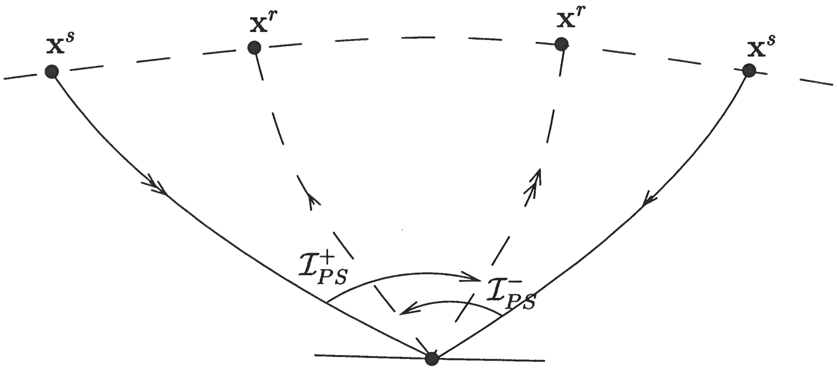

Figure 3. Positive and negative PS CIGS, $\mathcal{I}^+_{PS}$ and $\mathcal{I}^-_{PS}$. The arrows indicate the ray directions in the two reflectionevents. The solid and dashed curves are the P- and S-wave legs, respectively, of the different events.

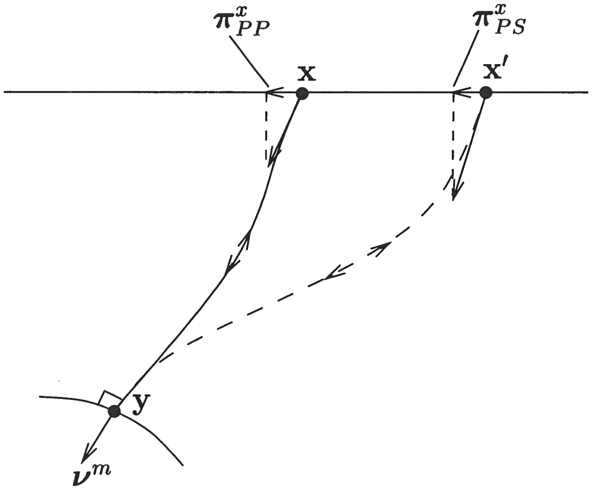

Figure 4. Two normal-incidence-point (NIP) rays for the P and S wave from the subsurface point $\mathbf{y}$.

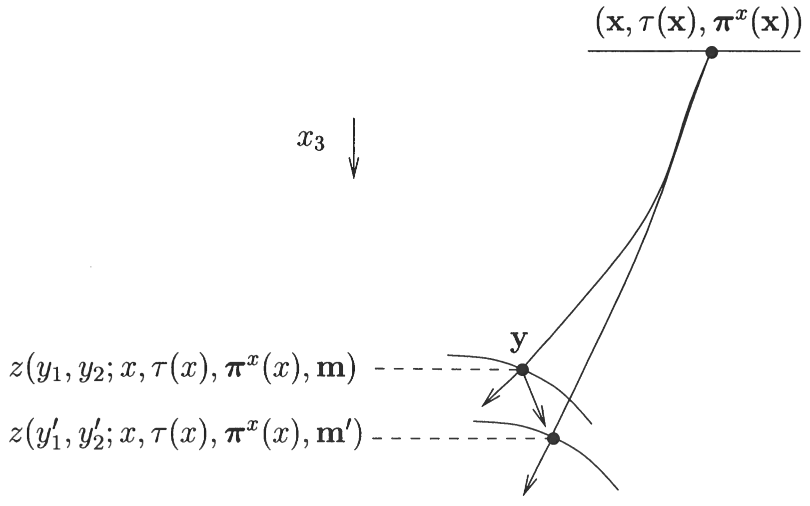

Figure 5. Mapping of the NIP reflectiontraveltime function and slopes to reflectordepths and dips, given a velocity model $\mathbf{m}$ and $\mathbf{m}\ '$.

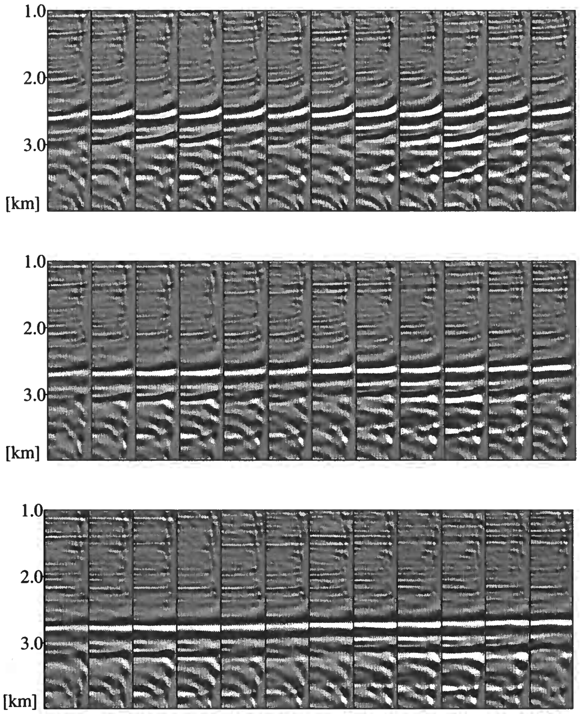

Figure 8. The common-image point gathers of the isotropic P-wave velocity optimization after 0, 4, and 7 iterations.

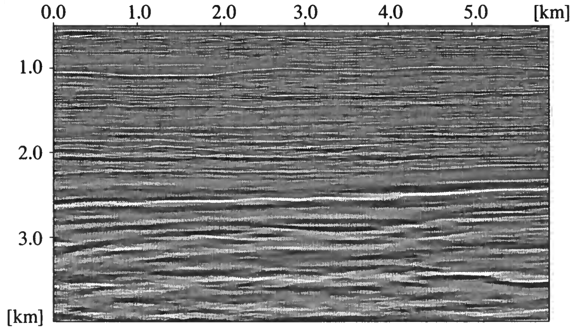

Figure 9. PS image using the initial S-wave velocity model in Figure 11 (left) and using the P-wave velocity model from the isotropic P-wave angle tomography.

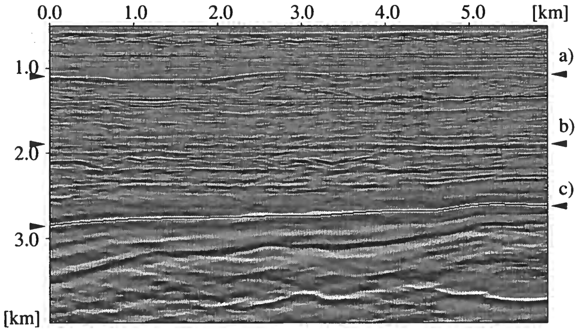

Figure 10. The PP image using the final isotropic P-wave velocity model in Figure 7 (top right). Indicated with arrows are a selection of interfaces of particular interest, denoted by a), b) and c).

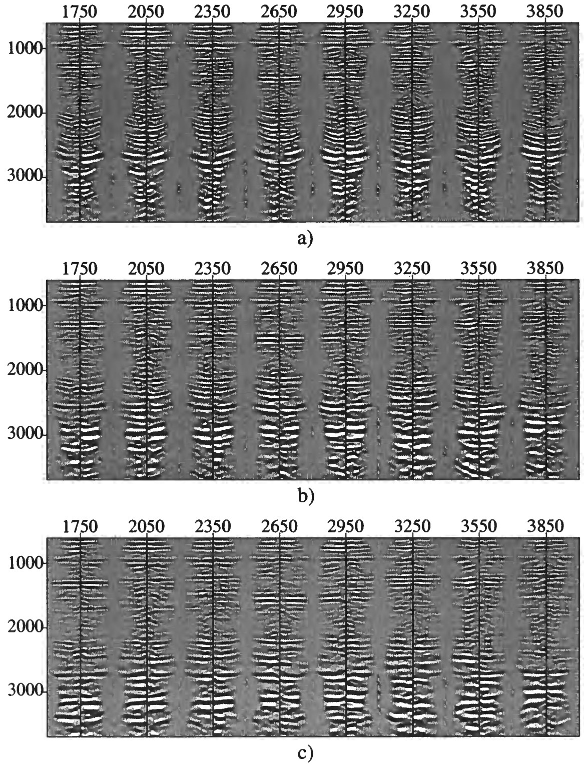

Figure 12. The common-image point gathers of the isotropic S-wave velocity optimization after 0, 2, and 5 iterations.

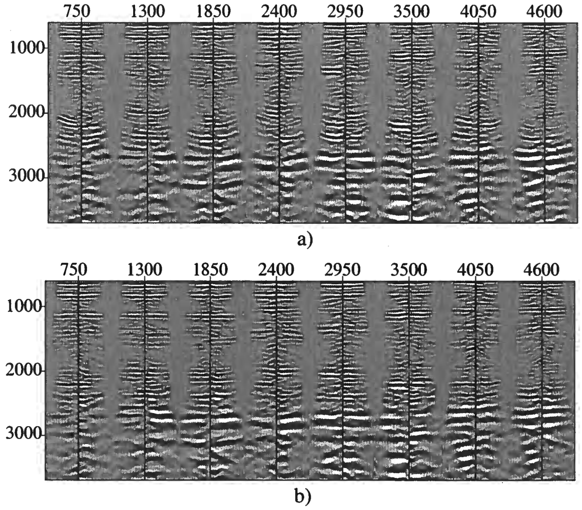

Figure 16. The common-image point gathers of the angle tomography in ε after a) 0 and b) 2 iterations.

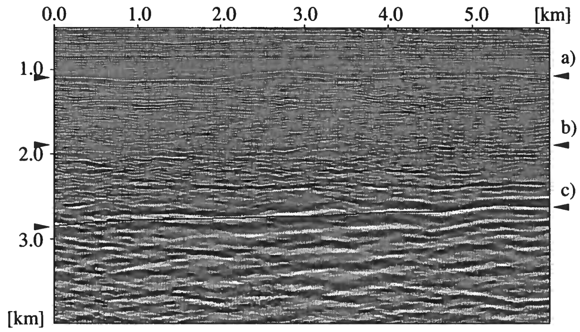

Figure 17. PS image after isotropic co-depthing.

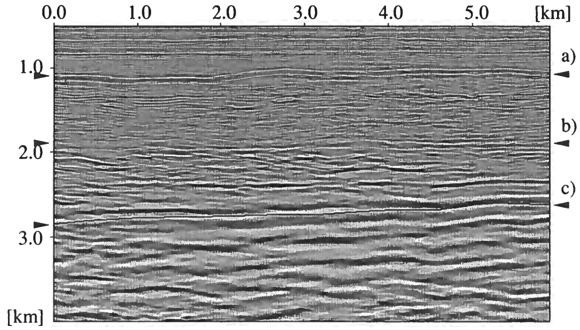

Figure 18. PS image after quasi-TIV parameter update ($\delta = 0$).

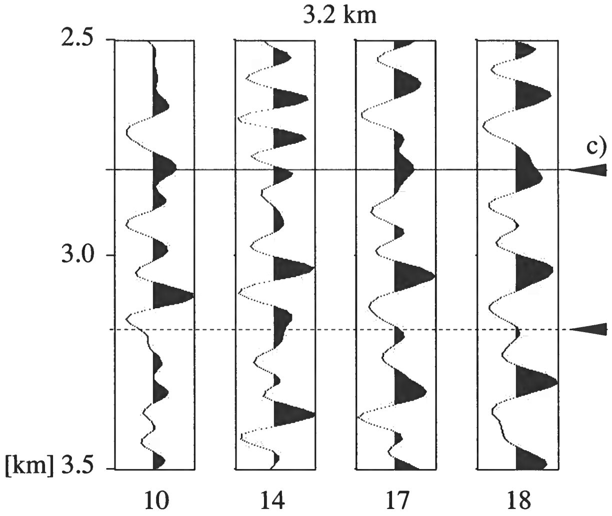

Figure 19. A single trace, at 3200 m horizontal distance, from the images in Figures 10 (step (i)), 14 (step (ii)), 17 (step (iv)) and 18 (step (v)).

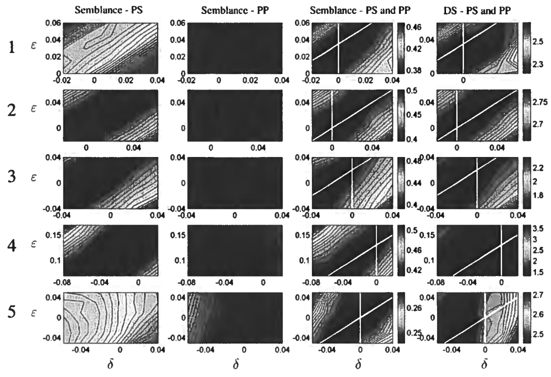

Figure 20. Contour plots for anisotropic layers 1-5 (vertical direction) and misfit plots for PS, PP and PP+PS semblance, and differential semblance in angle for PP+PS. The semblance plots are given by equations (37) and (**??**), formulated as minimization problems for comparison with the differential semblance misfit function.

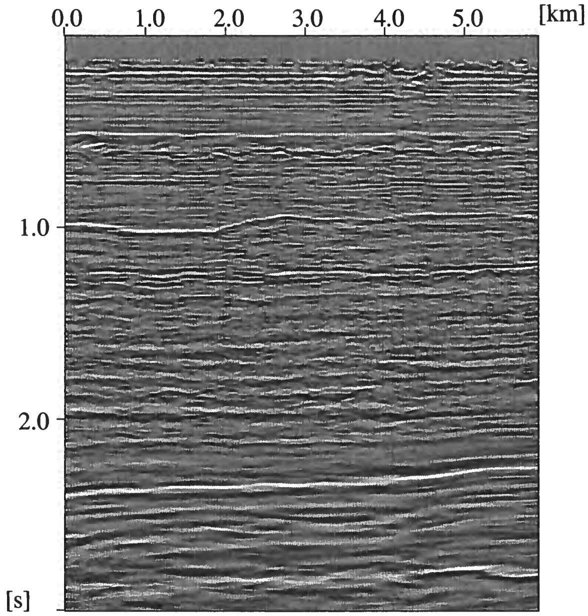

Figure 26. The initial PP image obtained in (i) (same as in Figure 9), in two-way PP time.

Data continuation in the presence of caustics: A synthetic data example

Alison E. Malcolm and Maarten V. de Hoop
Center for Wave Phenomena, Colorado School of Mines

ABSTRACT
In data continuation, the information present in the collected data is used to estimate data at new positions. We investigate two examples of data continuation: data healing and dip moveout. By composing a modeling operator with an imaging operator an operator to perform each of the tasks can be constructed. We review the theory and present an algorithm for data continuation specifically directed at these two examples. This algorithm is able to continue data in the presence of caustics. To demonstrate the performance of this algorithm, we use a synthetic example in which there are caustics.

Key words: data healing, DMO, data mapping, offset continuation, artifacts

1 INTRODUCTION

Often data collected in the field are not sufficient for processing. For example, it is not possible to collect zero-offset data but these data are important in attenuating surface-related multiples. Also, the data collected are sometimes incomplete; certain offsets may be missing, for example. Such gaps in the data can cause problems in imaging. Errors introduced in the computation of missing data will propagate into other procedures in which these data are used; thus, an accurate data continuation algorithm is important. A fundamental limitation to this type of data continuation is that it is not possible to compute missing data that scattered from a subsurface point not sampled in the available data.

To get around problems introduced by missing data, we propose a method of data continuation that allows missing data to be filled in from the available data (data healing) and the computation of different geometries than those collected originally, as in dip moveout (DMO) for example. The theory to do this involves the composition of an imaging/migration operator and a modeling/demigration operator to form a single operator that maps the initial data set to a second, computed, data set. This theory is discussed in detail in Malcolm *et al.* (2003). We are particularly interested in situations in which caustics occur. This puts our theory in a framework similar to that of depth migration, which goes beyond the time migration framework of Fomel (2003), Bleistein *et al.* (2000), and Stolt (2002).

We have developed an algorithm to test this theory and illustrate its capabilities using synthetic data. To accurately fill in missing data in the presence of caustics, knowledge of the smooth velocity model is required. Our algorithm relies on this knowledge and in turn, the missing data it fills in assists in the migration and velocity analysis portions of data processing. Thus, we see the three processes of data continuation, velocity analysis, and migration as interdependent steps in the imaging process.

2 THEORY AND ALGORITHM

As stated in the introduction, we construct an operator to calculate missing data from the available data by composing a modeling operator with an imaging operator. It is the exact form of the modeling operator used in the composition that determines the form of the output data. In this paper we discuss two forms of this operator: data healing, for which the output data are a more complete version of the input data set, and DMO, for which the output data are exploding-reflector-data computed from non-zero-offset-data. For data healing, the modeling operator is fairly general. It simply models data with source and receiver positions in the range missing in the original data set. For DMO, however, the modeling

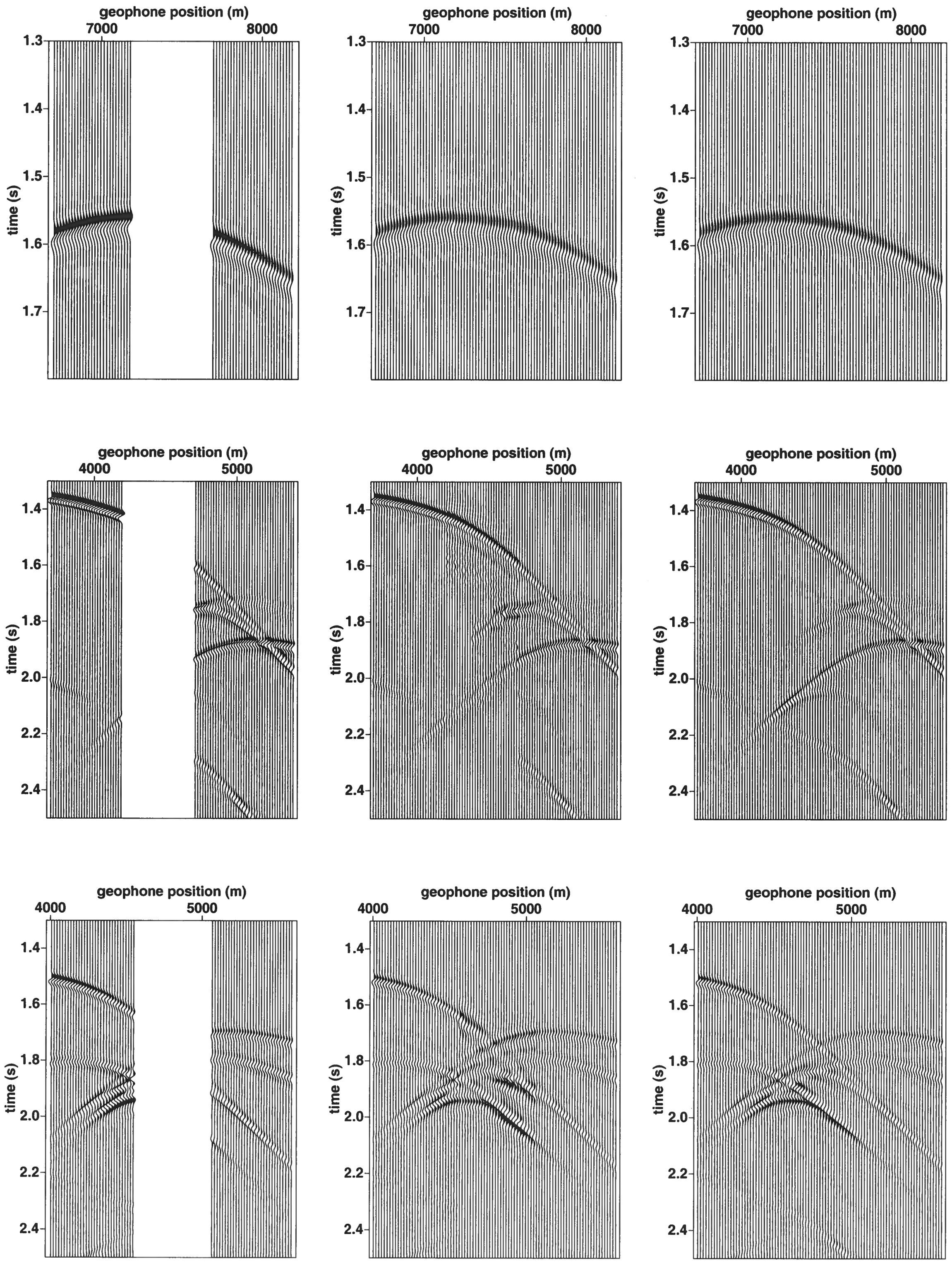

Figure 2. In each row of this figure a different shot record has a block of traces removed and then reconstructed. The left column shows the input data, the middle column is the reconstructed data, and the right column is the actual full synthetic shot record. The position of the first shot record is s = 7188 m, that of the second is s = 4200 m and the third is located at s = 4560. The locations of these shots are denoted with vertical lines in the velocity model, shown in Figure 1.

cost strongly dependent on the complexity of the velocity model. Because of this dependence and because of the varied applications for which this technique may be useful, evaluation of the cost-effectiveness of the method must be made on a case-by-case basis. Although the work presented here is in 2D, the theory remains valid in 3D although the implementation is somewhat more difficult. In addition, the extension to anisotropy is straightforward, provided the anisotropic velocity model is known.

ACKNOWLEDGMENTS

We acknowledge the contributions to the development of the underlying theory made by J. H. Le Rousseau, and the assistance with the algorithm from H. Calandra, S.-K. Foss and S. Brandsberg-Dahl. This work was supported by the sponsors of the Consortium Project on Seismic Inverse Methods for Complex Structures at the Center for Wave Phenomena and by Total.

REFERENCES

Bleistein, N., Cohen, J. K., & Stockwell, J. W. 2000. *Mathematics of Multidimensional Seismic Imaging, Migration and Inversion.* New York: Springer-Verlag.

Brandsberg-Dahl, S., de Hoop, M. V., & Ursin, B. 2003. Focusing in dip and AVA compensation on scattering-angle/azimuth gathers. *Geophysics*, **68**, 232–254.

Fomel, S. 2003. Theory of differential offset continuation. *Geophysics*, **68**, 718–732.

Malcolm, A. E., de Hoop, M. V., & Le Rousseau, J. H. 2003. The applicability of DMO/AMO in the presence of caustics. *submitted to Geophysics.* CWP-436P, 2003 project review book.

Stolt, R. H. 2002. Seismic data mapping and reconstruction. *Geophysics*, **67**, 890–908.

CWP-481

Geometrical-spreading correction for P-waves in layered azimuthally anisotropic media

Xiaoxia Xu and Ilya Tsvankin
Center for Wave Phenomena, Department of Geophysics, Colorado School of Mines, Golden, CO 80401.

ABSTRACT

Compensation for the geometrical spreading along the raypath is an essential step in AVO (amplitude variation with offset) analysis, in particular for wide-azimuth surveys. Here, we propose an efficient methodology to correct long-spread reflection data for the geometrical spreading in stratified azimuthally anisotropic media. The geometrical-spreading factor is expressed through the reflection traveltime described by the nonhyperbolic moveout equation that has the same form as that in VTI (transversely isotropic with a vertical symmetry axis) media.

For P-waves, the adapted VTI equation is parameterized by the normal-moveout (NMO) ellipse and the azimuthally varying anellipticity parameter η. If the vertical symmetry planes have uniform orientation in all layers, a close approximation to the exact traveltime can be obtained by using the expression for $\eta(\alpha)$ originally derived for a single orthorhombic layer. For models with misaligned symmetry planes, the azimuthal variation of η is described by an additional angle that controls the rotation of the "principal" axes of the function $\eta(\alpha)$ with respect to the NMO ellipse.

The moveout parameters are estimated from the 3D nonhyperbolic semblance algorithm of Vasconcelos and Tsvankin that operates simultaneously with traces at all offsets and azimuths. Numerical tests for models composed of orthorhombic layers with strong, depth-varying velocity anisotropy confirm the high accuracy of our travetime-fitting procedure and, therefore, of the geometrical-spreading correction. In the presence of azimuthal anisotropy above the reflector, the azimuthal variation of the geometrical-spreading factor is often comparable to that of the reflection coefficient.

The algorithm was applied to 3D data collected at Weyburn field (Canada) to evaluate the geometrical spreading for wide-azimuth P-wave reflections. The geometrical-spreading factor for the reflection from the top of the fractured reservoir is clearly influenced by the azimuthal anisotropy in the overburden, which should cause distortions in the azimuthal AVO attributes. Since our geometrical-spreading correction is entirely based on the kinematics of reflected arrivals, it can be readily incorporated into the processing flow of azimuthal AVO analysis.

Key words: geometrical-spreading correction, azimuthal anisotropy, wide-azimuth AVO

Introduction

Seismic signatures measured in wide-azimuth reflection surveys may be strongly influenced by azimuthal anisotropy associated with natural fracture systems or dipping transversely isotropic layers (e.g., shales). The inversion of azimuthally varying moveout velocities, polarization vectors, and amplitudes of reflected waves gives valuable information for characterization of frac-

Here, $V_{\mathrm{nmo}}^{(1)}$ and $V_{\mathrm{nmo}}^{(2)}$ are the semi-minor and semi-major axes of the NMO ellipse, respectively, and ϕ is the azimuth of the semi-major axis with respect to the acquisition frame. Explicit expressions for the coefficients $A_4(\alpha)$ and $A(\alpha)$ for an orthorhombic layer are given in Al-Dajani et al. (1998) and Paper I.

The nonhyperbolic (x^4) term in equation (2) can be simplified by using an approximate equivalence between the P-wave kinematics in the vertical symmetry planes of orthorhombic and VTI (transversely isotropic with a vertical symmetry axis) media. As shown in Paper I, the VTI moveout equation of Alkhalifah and Tsvankin (1995) can be adapted for an orthorhombic layer by introducing an azimuthally varying anellipticity coefficient $\eta(\alpha)$ (Pech and Tsvankin, 2003):

$$\begin{aligned} T^2(x,\alpha) = T_0^2 &+ \frac{x^2}{V_{\mathrm{nmo}}^2(\alpha)} \\ &- \frac{2\eta(\alpha)\, x^4}{V_{\mathrm{nmo}}^2(\alpha)\,[T_0^2\, V_{\mathrm{nmo}}^2(\alpha) + (1 + 2\eta(\alpha))\, x^2]}\,, \end{aligned} \tag{4}$$

$$\begin{aligned} \eta(\alpha) &= \eta^{(1)} \sin^2(\alpha - \phi) + \eta^{(2)} \cos^2(\alpha - \phi) \\ &- \eta^{(3)} \sin^2(\alpha - \phi) \cos^2(\alpha - \phi). \end{aligned} \tag{5}$$

The anellipticity parameters $\eta^{(1)}$, $\eta^{(1)}$, and $\eta^{(3)}$ are defined in the symmetry planes by analogy with the Alkhalifah-Tsvankin parameter η for VTI media (Grechka and Tsvankin, 1999b).

Numerical testing in Paper I proves that equation (4) provides a close approximation for P-wave moveout in a homogeneous orthorhombic layer. Below we apply equation (4) to more complicated, multilayered azimuthally anisotropic models.

Traveltime fitting for layered orthorhombic media

Models with uniform symmetry-plane orientation

Suppose the medium above the reflector is composed of horizontal layers with anisotropic symmetries no lower than orthorhombic, and the vertical symmetry planes in each layer have the same orientation. Note that in azimuthally isotropic (i.e., VTI or purely isotropic) layers any vertical plane is a plane of mirror symmetry. The uniform orientation of the symmetry planes in all layers implies that the model as a whole has two orthogonal vertical symmetry planes.

Because of the kinematic equivalence between the symmetry planes of orthorhombic and VTI media, P-wave nonhyperbolic moveout in the symmetry-plane directions is described by equation (4) with the effective parameter η computed from the VTI averaging equations (Tsvankin, 1997; 2001, Appendix 4B). Although for off-symmetry azimuthal directions the kinematic analogy with VTI media is valid only for weak anisotropy, the results of Paper I indicate that equation (4) parameterized by the best-fit values of V_{nmo} and η should still be sufficiently accurate. Therefore, the main issue in applying equation (4) to layered media with aligned symmetry planes is whether or not the azimuthal variation of the effective parameter $\eta(\alpha)$ can be described by the single-layer equation (5).

To estimate the effective moveout parameters in equation (4), we employ the 3D nonhyperbolic semblance algorithm of Vasconcelos and Tsvankin (2004). Wide-azimuth synthetic data are generated using ANRAY, the 3D anisotropic ray-tracing code developed by Gajewski and Pšenčík (1987). Vasconcelos and Tsvankin (2004) developed a three-step inversion procedure designed to make the multiparameter semblance search more efficient. First, conventional-spread data are used to reconstruct the NMO ellipse and evaluate the azimuth ϕ and the NMO velocities $V_{\mathrm{nmo}}^{(1)}$ and $V_{\mathrm{nmo}}^{(2)}$. Second, the anellipticity parameters $\eta^{(1)}$ and $\eta^{(2)}$, which are defined in the vertical symmetry planes, are estimated from the VTI nonhyperbolic semblance analysis in narrow sectors centered at the symmetry-plane directions. Third, the initial values of the parameters ϕ, $V_{\mathrm{nmo}}^{(1)}$, $V_{\mathrm{nmo}}^{(2)}$, $\eta^{(1)}$, and $\eta^{(2)}$ are used to specify the starting model for nonhyperbolic semblance search based on equations (4), (3), and (5).

Application of the algorithm to the four-layer model with the parameters listed in Table 1 confirms that equation (4) accurately describes long-spread moveout for the full range of azimuths. The model includes two orthorhombic layers with substantial magnitude of polar and azimuthal anisotropy sandwiched between two isotropic layers. As illustrated by Figure 1, the traveltimes computed from equation (4) with the inverted moveout parameters provide an excellent fit to the exact ray-traced traveltimes. The error of equation (4) does not exceed 0.3% of the zero-offset traveltime; similar results were obtained for a wide range of plausible orthorhombic models. The high accuracy of the traveltime fitting method, however, does not imply that the estimated parameters are close to the analytic values of the NMO velocities and the coefficient η because of the tradeoffs between various moveout coefficients (see Vasconcelos and Tsvankin, 2004). Nevertheless, as long as equation (4) is close to the exact traveltime, the moveout coefficients provide accurate input for the geometrical-spreading correction.

Models with misaligned symmetry planes

For media without throughgoing vertical symmetry planes, the azimuthal variation of the quartic moveout coefficient A_4 becomes more complicated and is described by five different trigonometric functions of the azimuth α (Al-Dajani et al., 1998). This implies that equation (5) for the azimuthally varying parameter η may no longer be accurate. However, extensive testing

α:

$$\eta(\alpha) = \frac{1}{8} \left\{ \frac{1}{V^4_{\mathrm{nmo}}(\alpha)\, t_0} \left[\sum_{i=1}^{N} (V^{(i)}_{\mathrm{nmo}}(\alpha))^4 \, (1 + 8\eta^{(i)}(\alpha))\, t_0^{(i)} \right] - 1 \right\}, \tag{6}$$

where $V^{(i)}_{\mathrm{nmo}}(\alpha)$ and $\eta^{(i)}(\alpha)$ are the interval parameters in layer i. Although equation (7) may become inaccurate for models with strong azimuthal anisotropy, it usually reproduces the shape of the azimuthal variation of the effective η (Al-Dajani et al., 1998).

Figure 3 shows a comparison between the parameter η computed from equation (7) (solid curve) and estimated by the moveout-inversion algorithm (dashed) for a two-layer orthorhombic model with misaligned symmetry planes. The shape of the two curves is quite similar, which explains the relatively low magnitude of the time residuals produced by equation (4). The misalignment of the symmetry planes, however, causes a rotation of the estimated η-curve with respect to the one calculated from equation (7).

The moveout-inversion algorithm cannot accommodate this rotation because the "principal axes" of the azimuthal variation of $\eta(\alpha)$ in equation (5) are parallel to the axes of the NMO ellipse [equation (3)]. Therefore, the traveltime fitting at far offsets can be improved by decoupling the nonhyperbolic moveout term from the NMO ellipse and introducing an additional angle ϕ_1 responsible for the azimuthal orientation of the effective parameter η:

$$\begin{aligned} \eta(\alpha) &= \eta^{(1)} \sin^2(\alpha - \phi_1) + \eta^{(2)} \cos^2(\alpha - \phi_1) \\ &- \eta^{(3)} \sin^2(\alpha - \phi_1) \cos^2(\alpha - \phi_1)\,. \end{aligned} \tag{7}$$

The first two steps of the modified moveout-inversion algorithm remain the same as those described above, but at last step we fix the orientation of the NMO ellipse (angle ϕ) and search for the angle ϕ_1 and the other parameters using the full range of offsets and azimuths. Application of this algorithm to the model in Figure 2 results in a greatly improved time fitting (Figure 4) and a 15% increase in the semblance value for the best-fit model.

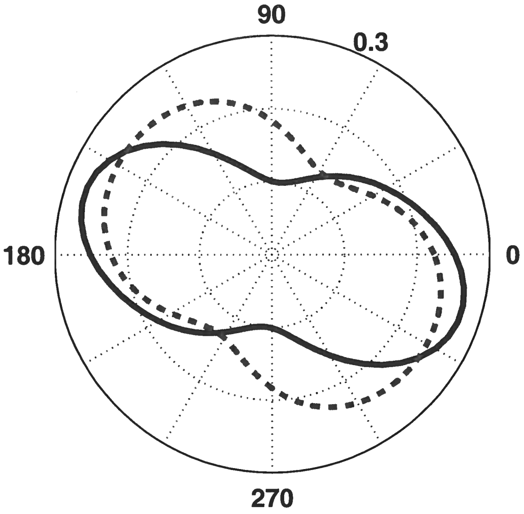

Figure 3. Comparison of the effective parameter $\eta(\alpha)$ computed from equation (7) (solid curve) and estimated by the inversion algorithm (dashed). The model is composed of two orthorhombic layers; for the top layer, $\phi = 15°$, $V_{P0} = 2.5$, $\epsilon^{(1)} = 0.2$, $\epsilon^{(2)} = 0.15$, $\delta^{(1)} = -0.1$, $\delta^{(2)} = 0.15$, and $\delta^{(3)} = 0.15$; for the bottom layer, $\phi = 0°$, $V_{P0} = 3.0$, $\epsilon^{(1)} = 0.15$, $\epsilon^{(2)} = 0.2$, $\delta^{(1)} = 0.15$, $\delta^{(2)} = -0.1$, $\delta^{(3)} = -0.15$.

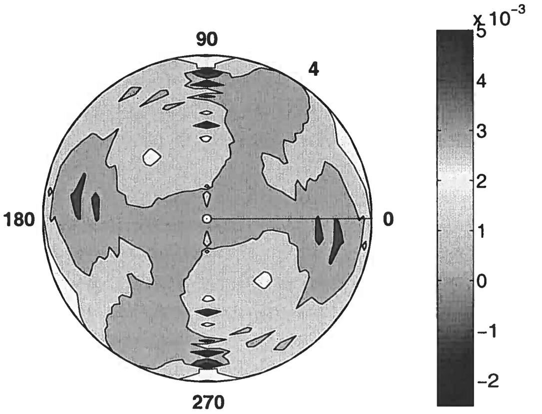

Figure 4. Same as Figure 2, but the traveltime fitting was performed using the modified inversion algorithm that allows for an independent orientation of the $\eta(\alpha)$-curve. The estimated parameters are $\phi = 81°$, $V^{(1)}_{\mathrm{nmo}} = 2.586$ km/s, $V^{(2)}_{\mathrm{nmo}} = 3.00$ km/s, $\eta^{(1)} = 0.594$, $\eta^{(2)} = 0.339$, $\eta^{(3)} = 0.161$, and $\phi_1 = 89°$.

Azimuth-dependent geometrical-spreading correction

The traveltime derivatives in the geometrical spreading equation (1) can be computed from the best-fit moveout parameters in equation (4). Explicit expressions for these derivatives are given in Paper I for the original form of the moveout equation with a single azimuthal angle ϕ. If the modified moveout equation provides a better fit to the traveltimes (e.g., a higher semblance value), the time derivatives can be easily rewritten using equation (7) for the parameter $\eta(\alpha)$.

The geometrical-spreading factor also depends on the group angles at the source (ϕ^s) and receiver (ϕ^r) locations, which are equal to each other for models with a horizontal symmetry plane. In most cases, the subsurface layer containing the source can be treated as isotropic and has a known P-wave velocity V. Then the angle ϕ^s can be computed using the ray parameter p estimated from the traveltime derivative dT/dx: $\sin\phi^s = p\,V$ (Ursin and Hokstad, 2003).

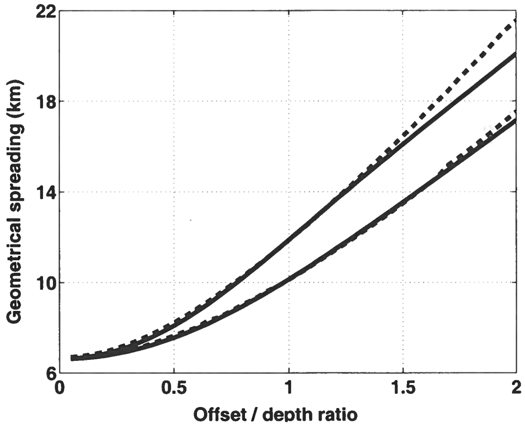

Figure 8. Accuracy of our method for the reflection from layer 3 in model 1; the azimuths are $\alpha = 0°$ and $90°$. The factor L is computed from dynamic ray tracing (dashed line) and our algorithm (solid).

Tsvankin (2004) are in good agreement with the analysis of shear-wave splitting by Cardona (2002) and of the azimuthal AVO response by Jenner (2001).

In particular, Jenner (2001) found that the P-wave AVO attributes at the reservoir level vary with azimuth. His amplitude processing, however, included only the conventional geometrical-spreading correction for isotropic media. To evaluate possible distortions of the AVO response caused by the influence of anisotropy on the geometrical spreading, we applied our algorithm to the reflection from the top of the reservoir (Figure 9). The moveout parameters were obtained by Vasconcelos and Tsvankin (2004) using the original equation (4) with a single azimuthal angle ϕ.

A plan view of the normalized geometrical-spreading factor in the overburden is displayed in Figure 9. The influence of anisotropy causes a dramatic 50% distortion in the geometrical spreading for offset-to-depth ratios close to two. The magnitude of the azimuthal variation of the factor L at far offsets reaches 10% (Figure 10). Such a difference between the geometrical spreading in the east-west and north-south directions is sufficiently large to cause distortions in the azimuthal variation of the AVO gradient studied by Jenner (2001).

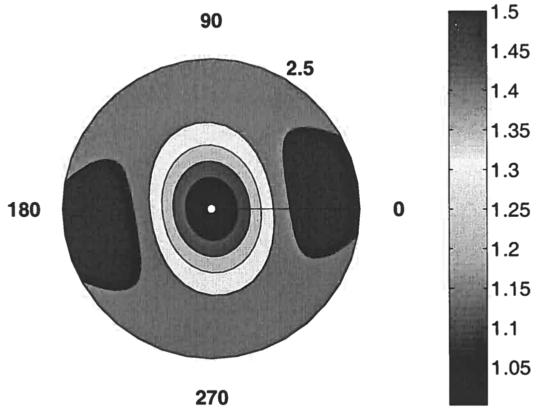

Figure 9. Plan view of the normalized geometrical spreading for the P-wave reflection from the Mississippian formation (the top of the reservoir) at Weyburn field computed for CMP 10829. The factor L is normalized by its value in the reference isotropic homogeneous medium with $V_{\rm nmo} = (V^{(1)}_{\rm nmo} + V^{(2)}_{\rm nmo})/2$. The moveout parameters are taken from Vasconcelos and Tsvankin (2004): $\phi = 99°$, $V^{(1)}_{\rm nmo} = 2.371$ km/s, $V^{(2)}_{\rm nmo} = 2.464$ km/s, $\eta^{(1)} = 0.255$, $\eta^{(2)} = 0.186$, and $\eta^{(3)} = -0.062$. The depth of the reflector is 1.4 km (the maximum offset-to-depth ratio is 2.5).

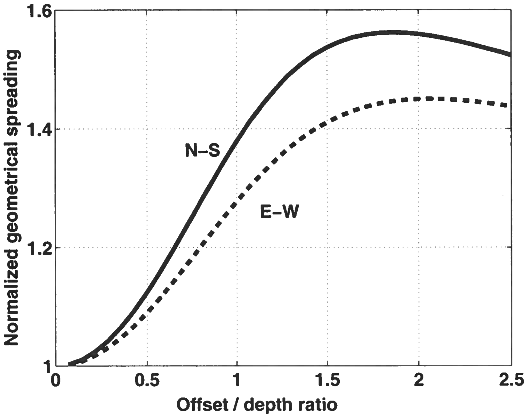

Figure 10. Normalized geometrical spreading for the reflection from the Mississippian formation computed in the east-west and north-south directions for CMP 10829.

Discussion and conclusions

The formalism suggested in Paper I (Xu et al., 2003) for describing the geometrical spreading of reflected waves is used here to develop a practical methodology for the P-wave geometrical-spreading correction in layered azimuthally anisotropic media. The correction, which involves the spatial derivatives of the reflection traveltime and the group-velocity vector at the source location, does not require knowledge of the velocity model. If the layer containing the source is isotropic, the group angle can be estimated in a straightforward way from the slope of the traveltime curve. Hence, the main issue in computing the geometrical-spreading factor from surface data is to find a sufficiently accurate, smooth approximation for wide-azimuth, long-offset reflection moveout in the presence of azimuthal anisotropy.

Numerical testing shows that even for models composed of strongly anisotropic orthorhombic layers, long-spread P-wave reflection traveltime can be accurately described by a nonhyperbolic moveout equation that has the same form as the widely used Alkhalifah-

Jenner, E., 2001, Azimuthal anisotropy of 3-D compressional wave seismic data, Weyburn field, Saskatchewan, Canada.: PhD theis, Colorado School of Mines.

Lynn, H.B., Campagna, D., Simon, K.M., and Beckham, W.E., 1999, Relationship pf P-wave seismic attributes, azimuthal anisotropy, and commercial gas pay in 3-D P-wave multiazimuth data, Rulison Field, Piceance Basin, Colorado: Geophysics, **64**, 1312–1328.

Mallick, S., Craft, K., and Meister, L., 1998, Determination of the principal directions of azimuthal anisotropy from P-wave seismic data: Geophysics, **63**, 692–706.

Maultzsch, S., Horne, S., Archer, S., and Burkhardt, H., 2003, Effects of an anisotropic overburden on azimuthal amplitude analysis in horizontal transverse isotropic media: Geophysics Prospecting, **51**, 61–74.

Pech, A., and Tsvankin, I., 2003, Quartic moveout coefficient for a dipping azimuthally anisotropic layer: CWP Annual Project Review (CWP-452), 133–142, (also Geophysics, in print).

Rüger, A., 2001, Reflection coefficients and azimuthal AVO analysis in anisotropic media: Society of Exploration Geophysics.

Schleicher, J., Tygel, M., Ursin, B., and Bleistein, N., 2001, The Kirchhoff-Helmholtz integral for anisotropic elastic media: Wave Motion, **34**, 353–364.

Tsvankin, I., and Thomsen, L., 1994, Nonhyperbolic reflection moveout in anisotropic media: Geophysics, **59**, 1290–1304.

Tsvankin, I., 1995, Body-wave radiation patterns and AVO in transversely isotropic media: Geophysics, **60**, 1409–1425.

Tsvankin, I., 1997, Anisotropic parameters and P-wave velocity for orthorhombic media: Geophysics, **62**, 1292–1309.

Tsvankin, I., 2001, Seismic signatures and analysis of reflection data in anisotropic media: Elsevier Science Publ. Co., Inc.

Ursin, B., and Hokstad, K., 2003, Geometrical spreading in a layered transversely isotropic medium with vertical symmetry axis: Geophysics, **68**, 2082–2091.

Vasconcelos, I., and Tsvankin, I., 2004, Nonhyperbolic moveout inversion of P-waves in azimuthally anisotropic media: Algorithm and application to field data: CWP Annual Project Review.

Xu, X., Tsvankin, I., and Pech, A., 2003, Geometrical spreading of reflected waves in azimuthally anisotropic media: CWP Annual Project Review (CWP-447), 37–47, (also submitted to Geophysics).

Seismic detection of a spatially-limited fluid pulse ascending a growth fault: Modeling and interpretation

Matthew Haney[1], Roel Snieder[1], and Jon Sheiman[2]
[1] *Center for Wave Phenomena, Colorado School of Mines, Golden, CO 80401*
[2] *Shell International Exploration and Production Inc., Houston, TX 77025*

ABSTRACT

We report on what is, to our knowledge, the first image of a fluid pulse inside a fault-zone that, based on geochemical evidence, is ascending the fault with time. The fluid pulse is confined to a growth fault (the B-fault) at the South Eugene Island 330 field, offshore Louisiana. Though the thickness of the fault-zone may only be tens of meters, or a fraction of a seismic wavelength, at the location of the fluid pulse, it is detectable because the fluid pulse is of high fluid pressure and, hence, low P-wave velocity. We extract the amplitude of the fault-plane reflection from the B-fault by applying a dip-filter to migrated 3D seismic data gathered by Shell in 1992. The reflectivity at the location of the fluid pulse is roughly three times greater than at an unremarkable part of the B-fault where a sonic log passed through the fault in 1993. We modify the sonic log by placing a 30 m low velocity zone at the fault-plane, representing a model of the fluid pulse. After generating synthetic seismograms from both the sonic log and the modified sonic log, we find that the low velocity zone produces high reflectivity similar to that observed at the fluid pulse. The ability to detect such a spatially-limited, high fluid pressure anomaly has implications for the understanding of hydrocarbon migration mechanisms and the time scale of reservoir-recharge in the Gulf of Mexico.

Key words: episodic fluid flow, faults, hydrocarbon migration

Introduction

Faults have long been characterized as zones of highly focused deformation and fluid flow in the subsurface; the exact mechanism of fluid flow and rate of flow along faults are, however, not well understood. For instance, Revil and Cathles (2002) claim that fluids may propagate as solitary waves along faults at the rate of kilometers per year. Since faults deform, or slip, in an episodic manner, it has been postulated that flow along faults should also be episodic and linked to the slip events (Sibson, 1990). Episodic flow along faults may be common in sedimentary basins worldwide. In the Gulf of Mexico, growth faults cutting through young, poorly consolidated sediments provide a means for hydrocarbons generated in deep source rocks to migrate into shallower, economically producible reservoirs.

We have previously established from 3D seismic data collected at the South Eugene Island field, offshore Louisiana, that fault-plane reflections from the main basin-bounding growth fault (the A-fault) indicate the portions over which the fault acts as a lateral seal (Haney *et al.*, 2004). In this brief paper, we extend our interpretation of the seismic data to examine the possibility that the faults at South Eugene Island also act as vertical conduits for fluid migration. Such behavior has been observed during the Global Basins Research Network (GBRN) drilling project at South Eugene Island (Anderson *et al.*, 1995) and highlights the dual nature of faults as both effective lateral seals and vertical fluid migration pathways.

We find that at one location, the intersection of the A10ST well with a fault synthetic to the A-fault, known as the B-fault, high fault-plane reflectivity occurs where a fluid pulse has been documented from drilling records

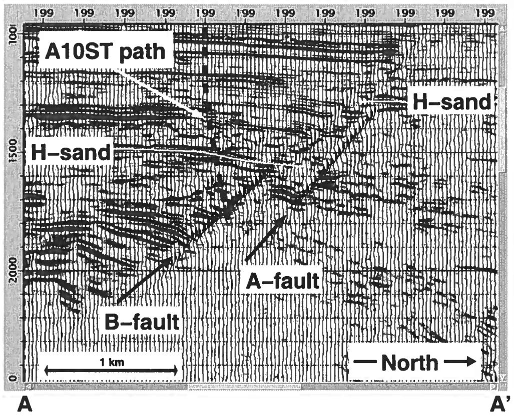

Figure 2. Overlay of the time-migrated seismic data (variable density) with a dip-filtered version (wiggle trace) of the same data along line A-A′. The dip-filtering is in the direction of fault dip to accentuate fault-plane reflections. The H-sand is highlighted to indicate the total throw across the A-fault and B-fault. The path of the A10ST well is projected into the A-A′ plane. The vertical axis is two-way-time in milliseconds and, taking the approximation that 1 ms two-way-time = 1 m depth, the vertical exaggeration of the plot is about 2×.

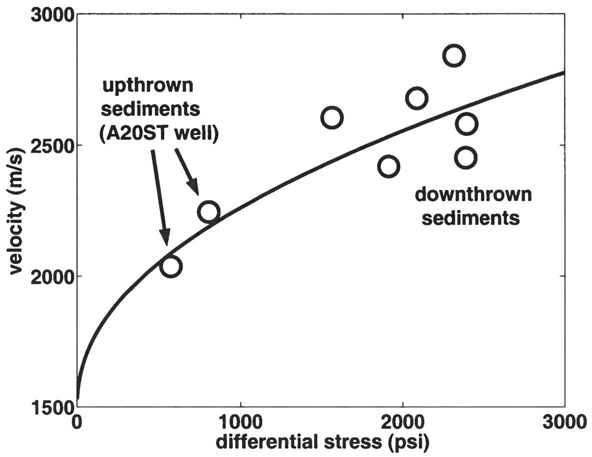

Figure 3. A plot of sonic velocity versus differential stress compiled from wells where both a fluid pressure measurement and a sonic log existed. Data points are shown as circles. The pressure data used to construct the plot comes from Losh *et al.* (1999) and the velocity data comes from sonic logs available at Shell. Data from both the upthrown and downthrown sediments have been included in this plot, with the measurements from the upthrown sediments coming exclusively from the A20ST well. The six data points from the downthrown sediments each represent a different well. The sonic velocity is seen to decrease as the differential stress decreases, or equivalently, as the fluid pressure rises. Also shown is a best-fit Bowers type relation as a solid line (Sayers *et al.*, 2003).

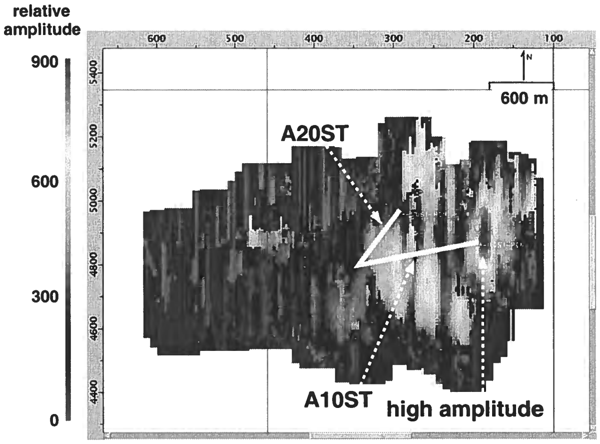

Figure 4. Reflection amplitude from the B-fault as a function of position on the fault-plane. The view is the same as in Fig. 1. Note the smearing of the reflection amplitudes in the up-down direction due to the dip-filter processing we employed to isolate the fault-plane reflection from the B-fault. The A20ST well, which intersected the B-fault in a "dead-zone", does not encounter an unusually high-amplitude anomaly on the fault-plane. In contrast, the A10ST well, which encountered a fluid pulse at the B-fault, terminates into the strongest reflecting portion of the fault. The reflectivity at the intersection of the A10ST well is approximately three times greater than at the A20ST well.

the A-fault. Other factors that are not plotted in Fig. 3, such as porosity and lithology, may also play a role in defining the overpressures at South Eugene Island.

After extracting the maximum amplitude of the fault-plane reflection from the B-fault, we obtain the reflectivity map shown in Fig. 4. Strong reflectivity, shown as brighter colors, come and go on the fault-plane due to the sharp lateral sealing of the B-fault. However, the strongest reflection amplitude occurs at the intersection of the A10ST well with the B-fault - where a fluid pulse has been reported by Losh *et al.* (1999). At this location, we hypothesize that the fault-plane reflection arises due to a combination of the sharp lateral seal and the spatially-limited fluid pulse in the fault zone. We test this hypothesis in the next section by constructing synthetic seismograms with a sonic log from the A20ST well that crosses the B-fault. Finally, we note that, from the reflectivity map in Fig. 4, the magnitude of the fault-plane reflection at the A10ST well is three times larger than the reflection at the A20ST well, where we have sonic velocity information.

Numerical modeling from A20ST sonic log

To better understand the variation of elastic properties that could give rise to the high reflectivity obfault, we have demonstrated that a low velocity zone at the fault-plane qualitatively agrees with the relative strength of reflected amplitudes in seismic data. The ability of reflected seismic waves to detect a fluid pulse could lead to a better understanding of hydrocarbon migration or an entirely new play concept based on drilling hydrocarbons in a fault zone. Future work will attempt to observe the fluid pulse move in different vintages of seismic data taken over a period of ten years. Other possible causes of the amplitude anomaly at A10ST, in addition to stacking errors and AVO effects, will also be explored.

Acknowledgments

The authors thank Steven Losh of Cornell for access to the A20ST well logs and for numerous discussions about South Eugene Island. Shell International Exploration and Production has provided funding for this research.

REFERENCES

Anderson, R. N., Billeaud, L. B., Flemings, P. B., Losh, S., and Whelan, J. K. 1995. *Results of the Pathfinder Drilling Program into a Major Growth Fault, Part of the GBRN/DOE Dynamic Enhanced Recovery Project in Eugene Island 330 Field, Gulf of Mexico*, Global Basins Research Network, Lamont-Doherty Earth Observatory.

Haney, M., Sheiman, J., Snieder, R., Naruk, S., Busch, J., and Wilkins, S. 2004. Fault-plane reflections as a diagnostic of pressure differences in reservoirs: South Eugene Island, offshore Louisiana, in: *Proceedings of EAGE Special Session on Fault and Top Seals*, Montpellier, France.

Losh, S., Eglinton, L., Schoell, M., and Wood, J. 1999. Vertical and Lateral Fluid Flow Related to a Large Growth Fault, South Eugene Island Block 330 Field, Offshore Louisiana. *AAPG Bulletin*, **83**, *244-276*.

Losh, S. and Cathles III, L. 2004. Fault Conduit/Fault Seal Behavior, South Eugene Island Block 330 Field, Offshore Louisiana, in: *Proceedings of EAGE Special Session on Fault and Top Seals*, Montpellier, France.

Revil, A. and Cathles III, L. M. 2002. Fluid transport by solitary waves along growing faults: A field example from the South Eugene Island Basin, Gulf of Mexico. *Earth and Planetary Science Letters*, **202**, *321-335*.

Sayers, C. M., Smit, T. J. H., van Eden, C., Wervelman, R., Bachmann, B., Fitts, T., Bingham, J., Mclachlan, K., Hooyman; P., Noeth, S., and Mandhiri, D. 2003. Use of reflection tomography to predict pore pressure in overpressured reservoir sands, 73rd Ann. Internat. Mtg. Soc. Expl. Geophys., Expanded Abstracts, 1362-1365.

Sibson, R. H. 1990. Conditions for fault-valve behavior, in: *Deformation Mechanisms, Rheology and Tectonics*, eds. R. J. Knipe and E. H. Rutter, Geological Society Special Publication No. 54, Alden Press, Oxford, 15-28.

Whelan, J. K., Eglinton, L., Kennicutt II, M. C., and Qian, Y. 2001. Short-time-scale (year) variations of petroleum fluids from the U. S. Gulf Coast, em Geochim. Cosmochim. Acta, **65**, *3529-3555*.

CWP-483

Time-lapse monitoring of rock properties with coda wave interferometry

Alexandre Grêt[†], Roel Snieder[†] and John Scales[‡]
[†] *Center for Wave Phenomena, Department of Geophysics, Colorado School of Mines, CO 80401, USA*
[‡] *Physical Acoustics Lab, Colorado School of Mines, CO 80401, USA*

ABSTRACT
The coda of a waveform consists of that part of the signal after the directly arriving phases. In a finite medium, or in one that is strongly heterogeneous, the late time coda is dominated by waves which have repeatedly sampled the medium. Small changes in a medium which might have no detectable influence on the first arrivals may be amplified by this repeated sampling and thus made visible in the coda. We refer to this use of multiple-sampling coda waveforms as *Coda Wave Interferometry.* We have exploited ultrasonic coda waves to monitor time-varying rock-properties in a laboratory environment. We have also studied the dependence of velocity on uni-axial stress in Berea sandstone, the non-linear temperature dependence of velocity in granite and the change in velocity due to an increase of water saturation in sandstone. There are many other possible applications of Coda Wave Interferometry in geophysics, including dam and volcano monitoring, time-lapse reservoir characterization, and rock physics.

Key words: velocity estimation, coda wave, multiple scattering, time-lapse, rock physics, acoustic emissions, fluid saturation

Introduction

Geophysicists investigate the structure of the subsurface by making indirect measurements on the surface and relating them to those predicted by theoretical Earth models. The Earth, however, is a highly complex system, and we almost always have to simplify our models in order to make them tractable. In many applications, this simplification means treating unmodeled physics as noise, with the result that information contained in the data is discarded. For seismic data, this typically means ignoring the coda waves that make up the tail of a seismogram. (In music the coda is the concluding passage of a movement or composition (Latin *cauda*, tail).) Geophysical applications based on use of the coda waves include earthquake prediction (Aki, 1985; Sato, 1988), volcano monitoring (Aki, 2000; Fehler *et al.*, 1998) or monitoring of temporal changes in the subsurface (Chouet, 1979; Revenaugh, 1995)(see also (Aki & Chouet, 1975).)

Consider the following examples: in monitoring a nuclear waste disposal site, one is not primarily interested in imaging the site. However, it is critical to monitor temporal changes in the site. In recent years, applied geophysicists have spent much effort on time-lapse seismology to monitor hydrocarbon reservoirs during recovery operations. Hydrocarbons move in the subsurface, reservoir rocks are artificially fractured, water-oil horizons move and steam propagates through the reservoir (Lumley, 1995; Wang, 1997). The high sensitivity of coda waves to small perturbations of the medium, makes them a powerful tool to monitor these kinds of changes.

We present four laboratory experiments in which we monitor the change in seismic velocity resulting from a change in uni-axial stress in a sample of Berea sandstone, from a temperature change in a sample of Elberton granite, a sample of aluminum and from a change in water saturation in a sample of Berea sandstone. We excite and record ultrasonic waves and extract the velocity change from the coda waves.

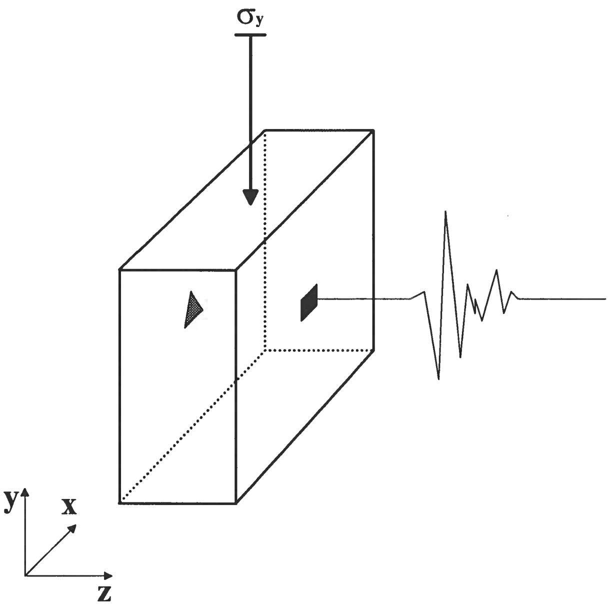

Figure 1. Experimental setup. The cuboid represents the Berea sandstone with orientation defined in the lower left corner of the figure. Sonic waves are transmitted in the z-direction and a uni-axial load is applied in the y-direction. A P-wave transceiver (triangle) and a P-wave receiver (rectangle) are used throughout the experiment. The cuboid has a size of 12,5 cm by 40 cm by 40 cm.

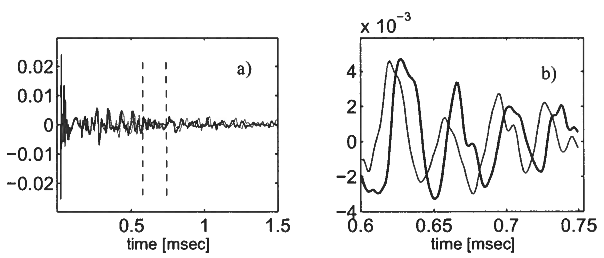

Figure 2. a) Two waveforms recorded at an applied uni-axial load level of 6 MPa (thick line) and 8 MPa (thin line) are shown in the same figure. b) The same two waveforms as Figure 3a, but only a small time window of the signal is shown; the time interval is marked by the two dashed lines in Figure 3a. The two coda waves are strongly correlated even. The sonic wave (in this time interval) has traveled through about 2.5 m of rock and bounced back and forth about 20 times.

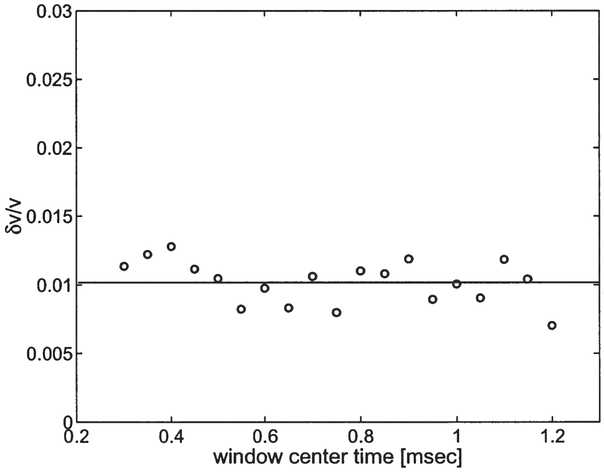

Figure 3. Velocity change estimates for 20 windows with different center times. The mean velocity change is 1.02 % and the standard deviation is 0.16 %

$$\frac{\delta v}{v} = \frac{-t_{max}}{t}. \tag{9}$$

In the following experiments we only consider the relative velocity change estimated from the coda of the ultrasonic measurements. However, other types of perturbations leave a different signature on the time shifted correlation coefficient (Snieder *et al.*, 2002) and could be used to monitor rock-properties not discussed here.

The laboratory experiments discussed in this paper are a combination of both, multiply scattering (from the cristals or grains in the rocks) and the repetitive sampling of the same area by reflections of the boundaries (bouncing ball and/or surface wave). However, the above formulation using the Feynman path summation includes both cases and we can use the same theory for all our measurements.

All the laboratory experiments discussed in this paper involve essentially the same measurement of ultrasonic waves, we measure the inpulse response of a rock sample with compressional ultrasonic transducers. The difference lays in the physics of the change introduced and the geometry of the rock sample.

Monitoring uni-axial stress in Berea sandstone

Time-varying stress fields are important in a number of areas of geophysics. Changes on plate boundaries are important in order to understand plate tectonics (Bokelmann & Silver, 2002). In earthquake prediction, the deformation field is important for understanding fault behavior and its relation to earthquake occurrence (Stein, 1999; Freed & Lin, 2001; Niu *et al.*, 2003). In hydrocarbon reservoirs, the stress field is changed by recovery operations. It is important to understand the temporal change for time-lapse reservoir monitoring (Teanby *et al.*, 2004). Or consider the "Room and Pillar" is a method of underground coal mining, in which approximately half of the coal is left in place to support the roof of the active mining area. Large pillars are left while rooms of coal are extracted. Monitoring the stress field in the pillars and roof is crucial in a safe mining procedure (Nikitin, 2003).

Wyllie et al. (1958) et al. measured ultrasonic P-wave velocity as a function of effective stress in water

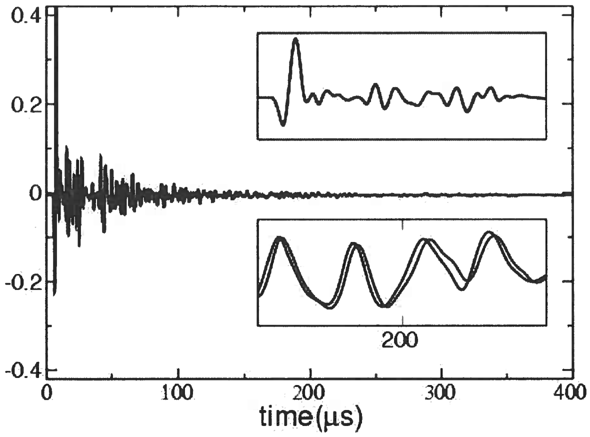

Figure 5. Wave-forms recorded in the berea sandstone sample for two different levels of water saturation (water infiltrated 2cm of the rock (thick line) and 3cm (thin line)). The insets show details of the wave-forms around the first arrival

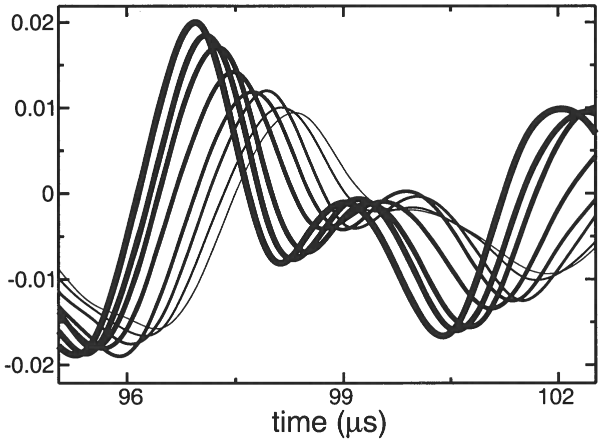

Figure 6. As the water rises in the rock sample the waves slow down accordingly. Eight waveforms are shown, each measured at a different hight of the water front. The fastest (thickest line) is measured on the dry sandstone and the slowest (thinest line) is measured at a water front hight of 7cm. It is important to note that the waveforms of the first arriving phases are identical for a water rise of 1cm.

with an approximate hight of 20 cm and an approximate diameter of 5 cm. The sample is equipped with a compressional source on one side and an identical receiver on the other (Figure 4). The room-dry sample is placed in a container holding 5mm of water. While the water is sucked into the pores of the sandstone by capillary pressure, the water-level in the container is kept constant at 5 mm. While the water-front is rising from 5mm to 10 cm, the ultrasonic impulse-response measurement is repeated for every 1cm increase in water-level. Again, for a 20 cm sample and a water-front rise of 1 cm there is no significant travel-time difference for the first arriving waves (see top inset of Figure 5). In a late time window (bottom inset of Figure5), however, we see a distinct time shift of the wave-forms. Figure 6 shows the consistent slowing of the sonic waves with increasing water-level.

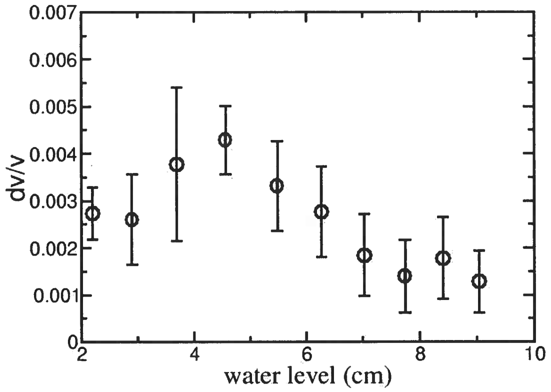

Figure 7. Absolute values of $\delta v/v$ in berea sandstone, for approximately 1cm water level intervals from room-dry to 9cm into the sample. Error bars are one standard deviation, calculated from multiple windows over the coda of the ultrasonic measurement

For each change of 1cm in water-level the relative change in velocity is estimated, with 12 different 0.1 ms time windows of the coda waves. The relative velocity change is of the order of 0.3% for a water-level rise of 1cm with an error of 0.05% (Figure 7). It is important to note that in many laboratory experiments, the change in the seismic velocity is measured for saturation changes of about 5% on small samples. With Coda Wave Interferometry we can monitor fluid saturation about 10 times more precisely.

Thus by using the coda waveforms, small changes in fluid saturation or migration, which have no effect on the first arriving phases of the data, can be readily seen in the coda. We believe that this technique can be used to monitor groundwater, DNAPL contamination sites and hydrocarbon reservoirs during enhanced recovery operations.

Monitoring Thermally Induced Velocity Changes in Aluminum

The dependence of ultrasonic velocity on temperature in metals and alloys is an important characteristic in itored by two thermocouples glued to the side of the sample and in the borehole (Figure 8).

While increasing the temperature from 25^oC to 90^oC, the ultrasonic measurement is repeated for every 5^oC increase in temperature. Then the aluminum sample is cooled to room-temperature and the experiment is repeated again for every 5^oC in temperature decrease. In addition, acoustic emissions are counted for every temperature interval.

In some published laboratory experiments, the change in the seismic velocity is measured for a temperature change of about 100^oC (Kern *et al.*, 2001; Timur, 1977; Peselnick & Stewart, 1975; Hughes & Maurette, 1956). For a 11 cm small sample and a temperature difference of only 5^oC, there is no significant travel-time difference for the first arriving waves (see top inset of Figure 9). Therefore, first arriving waves do not provide any information about velocity changes. In a late time window (bottom inset of Figure 9), we see a distinct time shift of the wave-forms. This information can be used to infer the change of sonic velocity with temperature.

For each change of 5^oC in temperature the relative change in velocity is estimated with 20 different 0.1ms time windows of the coda waves 10. The relative velocity change is of the order of 0.15% for a temperature change of 5^oC with an error of 0.025% (Figure 11). It is important to note that the relative velocity change with temperature does not depend on whether the sample is in the heating or the cooling phase. Furthermore, there is no measurable velocity difference at room temperature before and after the sample has gone through the heating cycle.

This laboratory experiment is important to test the presence of temperature effects on the measurement equipment, like piezoelectric transducer, cables, transducer couplant or mounting devices. Since we measure a linear velocity change with temperature in aluminum (Weaver & Lobkis, 2000), we conclude that these effects can be neglected.

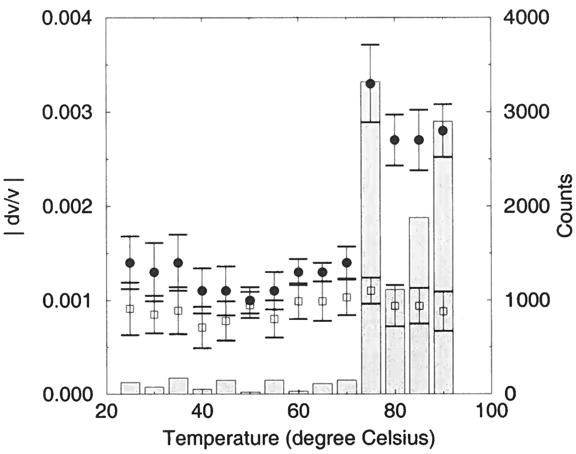

Figure 12. Absolute values of $\delta v/v$ in Elberton granite, for 5^oC temperature intervals from 25^oC to 90^oC. Circles correspond to the heating phase and rectangles to the cooling phase. The histograms show the count of acoustic emissions for a given temperature interval.

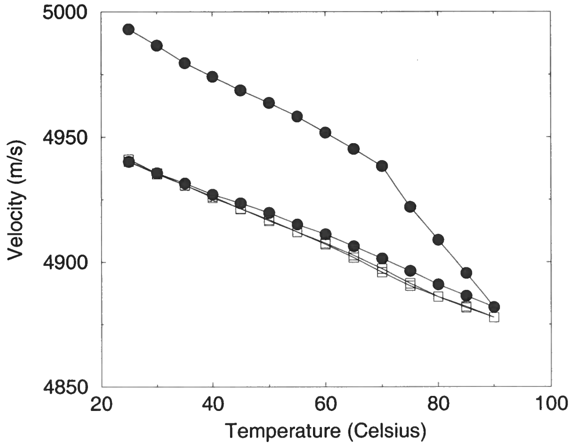

Figure 13. Absolute velocity versus temperature in Elberton granite, for two heating cycles. Filled circles represent the first heating cycle and rectangles the second. Note that on the second heating cycle the temperature dependent velocities during the heating and cooling phase are almost not distinguishable.

Monitoring Thermally Induced Velocity Change and Acoustic Emissions in Granite

With the same technique and same experimental setup described above, we measured the thermally induced velocity change in a granite sample. During the heating phase the velocity decrease is constant for each 5^oC increase in temperatures, below 70^oC, however for every 5^oC increase above that temperature, the velocity change is non-linear (Figure 12). A temperature of 70^oC corresponds to the critical fracture temperature for granite (Johnson *et al.*, 1978; Fredrich & Wong, 1986). Thermal cracking results from the internal stress concentration induced by thermal expansion anisotropy or thermal expansion mismatch between minerals or grains. Such micro-cracking is a similar effect as the thermal stresses induced by thermal gradients in homogeneous solids; for a high temperature gradient, cracking may occur even in a perfectly homogeneous solid (Boley & Weiner, 1960). Fredrich & Wong (1986) show that thermal cracking in rocks occurs principally along mineral or grain boundaries. The thermally induced cracks can influence significantly both the mechanical

Christensen, N.I., & Wang, H.F. 1985. The Influence of Pore Pressure and Confining Pressure on Dynamic Elastic Properties of Berea Sandstone. *Geophysics*, **50**, 207.

Fehler, M., Roberts, P., & Fairbanks, T. 1998. A temporal change in coda wave attenuation observed during an eruption of Mount St. Helens. *J. Geophys. Res.*, **93**, 4367–4373.

Fredrich, J.T., & Wong, T. 1986. Micromechanics of thermally induced cracking in three crustal rocks. *J. Geophys. Res.*, **91**, 12743–12764.

Freed, A.M., & Lin, J. 2001. Delayed triggering of the 1999 Hector Mine earthquake by viscoelastic stress transfer. *Nature*, **411**, 180–183.

Griffin, T.W., & Watson, K.W. 2002. A Comparison of Field Techniques for Confirming Dense Nonaqeuous Phase Liquids. *Ground Water Monitoring and Remediation*, **22**(2).

Hicks, W.G., & Berry, J.E. 1956. Application of Continuous Velocity logs to Determination of Fluid Saturation of Reservoir Rocks. *Geophysics*, **21**, 739.

Hughes, D.S., & Maurette, C. 1956. Variation of elastic wave velocities in granites with pressure and temperature. *Geophysics*, **21**, 277–284.

Ide, J.M. 1937. The velocity of sound in rocks and glasses as a function of temperature. *J. Geol.*, **45**, 689–716.

Johnson, B., Gangi, A.F., & Handin, J. 1978. Thermal cracking subjected to slow, uniform temperature changes. *paper presented at 19th U.S. Rock Mechanics Symposium, U.S. Nat. Comm. for Rock Mech., Univ. of Nevada, Reno.*

Kaiser, J. 1953. Erkenntnisse und Folgerungen aus der Messung von Gerüschen bei Zugbeanspruchung von metallischen Werkstoffen. *Archiv Eisenhüttenwesen*, **24**, 43–45.

Kern, H., Popp, T., Gorbatsevich, F., Zkarikov, A., Labanov, K.V., & Smirnov, Yu.P. 2001. Pressure and temperature dependence of V_P and V_S in rocks from the superdeep well and from surface analogues at Kola and the nature of velocity anisotropy. *Tectonophysics*, **338**, 113–134.

King, M.S. 1966. Wave Velocities in Rocks as a Functin of Changes in Overvurden Pressure and Pore Fluid Saturation. *Geophysics*, **31**, 50.

Kobori, O., & Iwashimizu, Y. 1990. *Effects of stress and temperature on ultrasonic velocity.* Elastic Waves and Ultrasonic Nondestructive Evaluation. Elsevier.

Kurita, K., & Fujii, N. 1979. Stress memory of crystalline rocks in acoustic emission. *Geophys. Res. Letters*, **6**, 9–12.

Lavrov, A. 2002. The Kaiser effect in rocks: principles and stress estimation technique. *International Journal of Rock Mechanics and Mining Sciences*, **40**, 151–171.

Lumley, D.E. 1995. *Seismic time-lapse monitoring of subsurface fluid flow.* Ph.D. thesis, Stanford Univ.

Nikitin, O. 2003. Mining block stability analysis for room-and-pillar mining with continuous miner in estonian oil shale mines. *Oil Shale*, **20**, 515–528.

Niu, F., Silver, P.G., Nadeau, R.M., & McEvilly, T.V. 2003. Migration of seismic scatterers associated with the 1993 Parkfield aseismic transient event. *Nature*, **426**, 544–548.

Nur, A., & Simmons, G. 1969. The Effect of Saturation on Velocity in Low Porosity Rocks. *Earth Planet. Sci. Lett*, **7**, 183.

Peselnick, L., & Stewart, R.M. 1975. A sample assembly for velocity measurements of rocks at elevated temperatures and pressures. *J. Geophys. Res.*, **80**, 3765–3768.

Revenaugh, J. 1995. The Contribution of Topographic Scattering to Teleseismic Coda in Southern California. *Geophys. Res. Lett.*, **22**, 543–546.

Salama, K., & Ling, C.K. 1980. The effect of stress on the temperature dependence of ultrasonic velocity. *J. Appld. Phys.*, **51**, 1505.

Sarkar, D., Bakulin, A., & Kranz, R. L. 2003. Anisotropic inversion of seismic data for stressed media: Theory and a physical modeling study on Berea Sandstone. *Geophysics*, **68**(2), 690–704.

Sato, H. 1988. Temporal change in scattering and attenuation associated with the earthquake occurence - a review of recent studies on coda waves. *Pure Appl. Geophy.*, **126**, 465–497.

Simmons, G., & Cooper, H.W. 1978. Thermal cycling cracks in three igneous rocks. *Int. J. Rock Mech.*, **15**, 145–148.

Snieder, R. 1999. Imaging and Averaging in Complex Media. *Pages 405–454 of:* Fouque, J.P. (ed), *Diffuse waves in complex media.* Dordrecht: Kluwer.

Snieder, R. 2002. Coda wave interferometry and the equilibration of energy in elastic media. *Phys. Rev. E*, **66**.

Snieder, R., Grêt, A., Douma, H., & Scales, J. 2002. Coda Wave Interferometry for Estimating Nonlinear Behavior in Seismic Velocity. *Science*, **295**, 2253–2255.

Stein, R.S. 1999. The role of stress transfer in earthquake occurrence. *Nature*, **402**, 605–609.

Teanby, N., Kendall, J.M., Jones, R.H., & Barkved, O. 2004. Stress-induced temporal variations in seismic anisotropy observed in microseismic data. *Geophys. Jour. Int.*, **156**, 459.

Thirumalai, K., & Demou, S.G. 1973. Thermal expansion behaviour of intact and thermal fractured mine rocks. *Am. Inst. Phys. Conf. Proc.*

Timur, A. 1977. Temperature dependence of compressional and shear wave velocities in rocks. *Geophysics*, **42**, 950–956.

Todd, T.P. 1973. Effects of cracks on elastic properties of low porosity rocks. *Thesis, Massachusetts Institute of Technology.*

Wang, Z. 1997. Feasibility of time-lapse seismic reservoir monitoring: The physical basis. *The Leading Edge*, **16**, 1327–1329.

Weaver, R.L., & Lobkis, O.I. 2000. Temperature Dependence of Diffuse Field Phase. *Ultrasonics*, **38**, 491–494.

Wyllie, M.R., Gregory, A.R., & Gardner, G.H.F. 1958. An Experimental Investigation of Fractors Affecting Elastic Wave Velocities in Porous Media. *Geophysics*, **23**, 459.

Time-lapse traveltime change of singly-scattered acoustic waves

Carlos Pacheco and Roel Snieder
Center for Wave Phenomena, Dept. of Geophysics, Colorado School of Mines, Golden, CO 80401

ABSTRACT

We present a technique based on the single scattering approximation that relates temporal changes in the acoustic velocity to changes in the traveltime of singly-scattered waves. We describe wave propagation in a random medium with homogeneous statistical properties as a single scattering process where the fluctuations of the velocity with respect to the background velocity are assumed to be weak. This corresponds to one of two end-member regimes of wave propagation in a random medium, the first being single scattering, and the second multiple scattering. We present a formulation that relates the change in the phase of the scattered wavefield to a localized slowness perturbation in a weakly scattering medium by means of the Born approximation for the scattered wavefield. We validate the methodology with synthetic seismograms calculated with finite-differences for 2D acoustic waves.

Key words: scattering, Born approximation, random media

1 INTRODUCTION

In the search for technically simple and computationally inexpensive methods for monitoring the time varying behavior of the subsurface, such as changes associated with a producing hydrocarbon reservoir, we consider coda wave methods to be promising because of their great sensitivity to small changes in the medium. Here we explore the time-lapse behavior of singly scattered acoustic waves under changes in the background velocity of the medium.

Coda waves are the result of the interaction of an incident wave with the heterogeneities of the medium that gives rise to scattered waves. Many studies have described these scattered waves as multiply scattered waves, and the diffusion approximation has been employed to characterize the energy transport in strongly scattering media (Aki & Chouet, 1975; Turner & Weaver, 1994; Page *et al.*, 1995; Schriemer *et al.*, 1997). In particular, multiply scattered waves have been used to monitor temporal changes in the medium due to high sensitivity of these waves to small changes in the medium (Weitz & Pine, 1993; Yodh, 1995; Snieder *et al.*, 2002; Jian *et al.*, 2003). Recently, Pacheco and Snieder (2003) used the diffusion approximation to model the traveltime change of multiply scattered waves due to a localized velocity perturbation.

There are many important practical applications where scattering is not sufficiently strong for the diffusion approximation to be used to model the energy propagation in the scattering medium. Seismic imaging techniques, as used in oil exploration (Claerbout, 1985), rely on the single scattering approximation to obtain an image of the subsurface.

In the single scattering model all scattered waves are assumed to have been scattered once on their way from the source to the receiver, this is usually called the first Born approximation. The application of this approximation to coda waves is valid for weakly scattering media; this means that the mean free path of the waves between the scatterers is greater than the path length. The Born approximation has been used in theoretical studies of the apparent attenuation of a scattering medium (Chernov, 1960; Wu, 1982) and in the analysis of the decay of the coda envelope for microearthquakes (Aki & Chouet, 1975; Sato, 1977). Kopnichev (1977) calculated the time dependence of the energy of the seismogram's coda by applying the Born approximation to scattering theory.

Here we consider the time-lapse variation of the

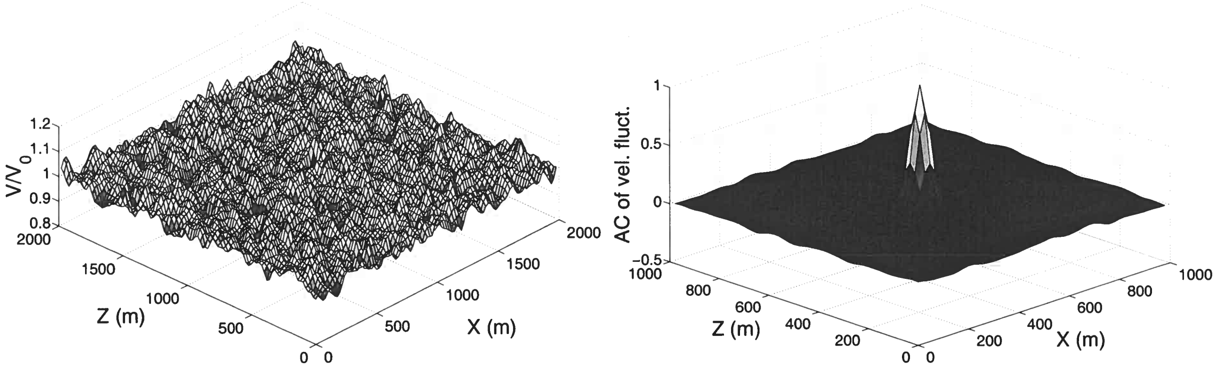

Figure 2. Left: Velocity field with random velocity fluctuations. Right: Autocorrelation of the velocity fluctuations.

unperturbed and perturbed paths that arrive at the receiver at time t.

When we introduce a small perturbation of the propagation slowness, the effect of this perturbation on the geometrical spreading and the scattering strength can be ignored, and the dominant effect on the waveform arises from the change in the traveltime of the wave that travels along each path:

$$u_p(t) = \sum_P A_P(t - \tau_P), \tag{2}$$

where τ_P is the traveltime perturbation for the propagation along trajectory P due to the slowness perturbation. Snieder (2002) characterized the change in the wavefield using the time-windowed cross-correlation function, defined as

$$C_{up}^{(t,t_w)}(t_s) = \int_{t-t_w}^{t+t_w} u_u(t')u_p(t'+t_s)dt', \tag{3}$$

where t denotes the center of a time window of length $2t_w$, and t_s the lag time for the correlation. When Eqs. (1) and (2) are inserted into Eq. (3), double sums $\sum_{PP'}$ appear. We assume that in these double sums, the cross terms related to different paths ($P \neq P'$) are incoherent and average out to zero when the mean of the source signal vanishes. The contribution of the cross-terms is estimated by Snieder (2004). A dimensionless measure of the change of the wavefield is given by the time-windowed correlation coefficient, which is given by

$$R^{(t,t_w)}(t_s) = \frac{\int_{t-t_w}^{t+t_w} u_u(t')u_p(t'+t_s)dt'}{\left(\int_{t-t_w}^{t+t_w} u_u^2(t')dt' \int_{t-t_w}^{t+t_w} u_p^2(t')dt'\right)^{1/2}}. \tag{4}$$

For time shifts t_s much smaller than the dominant period T of the wave, a second order Taylor expansion of the $A_P(t' + t_s - \tau_P)$ in τ_P gives (Snieder, 2002)

$$R^{(t,t_w)}(t_s) = 1 - \frac{1}{2}\bar{\omega}^2\langle(\tau - t_s)\rangle(t, t_w), \tag{5}$$

where $\bar{\omega}$ is the dominant frequency of the wave. In this expression $\langle ...\rangle(t, t_w)$ denotes the average over all trajectories that arrive in the time window $(t-t_w, t+t_w)$ with a weight factor that is given by the mean intensity of the waves on the time window (Snieder, 2002). Thus, averages are taken with a weight factor that is given by the intensity of each singly-scattered wave. This means that in this work, the average traveltime change $\langle\tau(t, t_w)\rangle$ is given by an average of the traveltime change of individual waves with different paths P arriving on the time window $(t - t_w, t + t_w)$, i.e.

$$\langle\tau(t, t_w)\rangle = \frac{\sum_P w_P(t, t_w)\tau_P(t, t_w)}{\sum_P w_P(t, t_w)}, \tag{6}$$

where the weighting factor $w_P(t, t_w)$ is given by the mean intensity for the singly scattered waves arriving on the time window $(t - t_w, t + t_w)$. Our task is to find an expression for intensity of each path P in the single scattering regime and substitute that into Eq. (6), and to relate τ_P to the time-lapse change in the slowness of the medium.

3 SINGLY-SCATTERED WAVES

A seismic wave propagating in a spatially heterogeneous medium is treated as a source pulse which remains unaltered in wave shape despite interactions with the heterogeneities plus scattered waves generated by the source pulse as it encounters heterogeneities in the medium. This is the basis of the single scattering model.

In our numerical implementation of this single scattering model we assume that the velocity field is a statistically homogeneous quasi-random medium where small scale velocity fluctuations with Gaussian autocorrelation function are added to a constant background velocity as pictured on Figure 2. The scale of the velocity fluctuations is given by the correlation length a of the velocity fluctuations. The relative magnitude of the velocity fluctuations with respect to the mean is given by the standard deviation σ of the fluctuations with re-

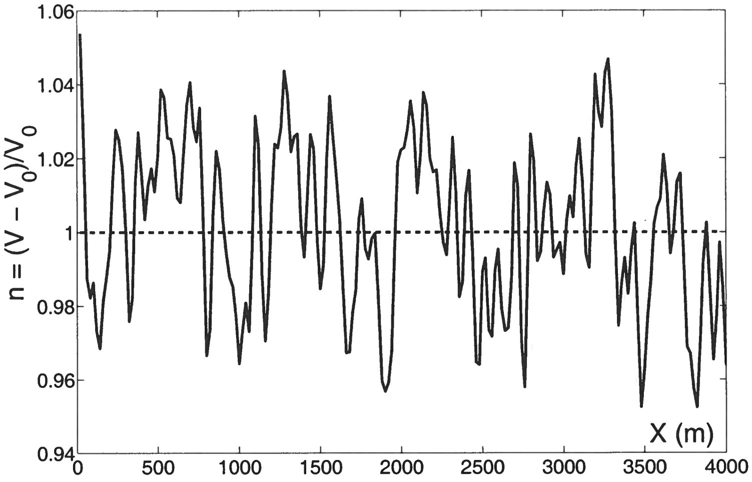

Figure 4. Plot of the relative fluctuations of the velocity field $n(x)$ along direction x.

4.1 Single Scattering Intensity

Sato (1977) derived the space-time dependence of the energy density of scattered waves in 3D assuming single isotropic scattering due to uniformly distributed scatterers. His model explains how scattered energy is homogeneously distributed as lapse time increases. In this approach, the scattered field is assumed to be linearly proportional to the perturbation in the constitutive parameters (in our case, the acoustic velocity). We use in this study this approach to describe the time-space evolution of the intensity of the scattered waves.

We derive the expression for the time-space dependent intensity for an isotropic source in a statistically homogeneous random medium in the single scattering regime. This gives the intensity $I_P(t)$ of single scattering waves with traveltime t and path P. The assumption here is that waves with different paths P (different scatterer location on the single-scattering ellipse) and the same traveltime may have different intensity $I_P(t)$. The derivation for scalar waves is shown in two dimensions (2D). Suppose that the wave velocity $v(\mathbf{x})$ can be represented as a perturbation from a constant background velocity v_0 (see Figure 4) such that

$$v(\mathbf{x}) = v_0\left(1 + n(\mathbf{x})\right). \tag{8}$$

For the present discussion, $n(\mathbf{x})$ is assumed to be small ($n(\mathbf{x}) \ll 1$) so that

$$\frac{1}{v^2(\mathbf{x})} = \frac{1}{{v_0}^2}(1 - 2n(\mathbf{x})). \tag{9}$$

In the last equation we have retained only the first order term of an expansion about powers of $n(\mathbf{x})$, this is consistent with the Born approximation. The Helmholtz equation is given by

$$\nabla^2 u + \frac{\omega^2}{{v_0}^2}[1 - 2n(\mathbf{x})]u = 0. \tag{10}$$

The solution of the Helmholtz equation in the Born approximation is, in the frequency domain, given by (Bleistein *et al.*, 2001)

$$u(\mathbf{x_g}, \mathbf{x_s}, \omega) = u_0(\mathbf{x_g}, \mathbf{x_s}, \omega) + 2\frac{\omega^2}{{v_0}^2}\int_A n(\mathbf{x})\ u_0(\mathbf{x}, \mathbf{x_s}, \omega)\ G_0(\mathbf{x_g}, \mathbf{x}, \omega)\ dA(\mathbf{x}), \tag{11}$$

where $u_0(\mathbf{x_g}, \mathbf{x_s})$ is the incident or unperturbed wavefield generated at source location $\mathbf{x_s}$. The term $G_0(\mathbf{x_g}, \mathbf{x})$ represents the free space Green's function that satisfies the Helmholtz equation for the homogeneous medium with velocity v_0:

$$\left[\nabla^2 + \frac{\omega^2}{{v_0}^2}\right] G_0(\mathbf{x_g}, \mathbf{x}, \omega) = \delta(\mathbf{x_g} - \mathbf{x}). \tag{12}$$

The free space Green's function in two dimension $G_0(\mathbf{x_g}, \mathbf{x}, \omega)$ is

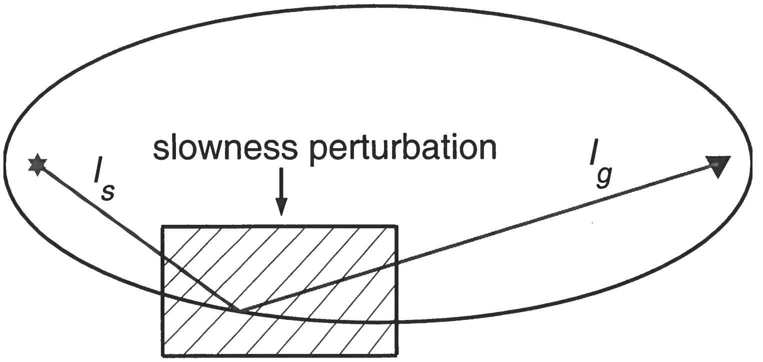

Figure 5. Geometry of a single scattering path P and a localized slowness perturbation $\delta s(\mathbf{x})$: l_s is the path from the source to the edge of the ellipse and l_g is the path from the edge of the ellipse to the receiver.

$$\langle n(\mathbf{x_1})\; n(\mathbf{x_2})\rangle = \langle n^2\rangle \delta(\mathbf{x_1} - \mathbf{x_2}). \tag{26}$$

Inserting this into Eq. (25) we obtain

$$\langle I(\mathbf{x_s}, \mathbf{x_g}, t)\rangle = \frac{1}{4{v_0}^2} \int_A \frac{\langle n^2(\mathbf{x})\rangle}{r_s r_g}\, W\left(t - \frac{r_s + r_g}{v_0}\right)\, dA(\mathbf{x}), \tag{27}$$

where

$$W\left(t - \frac{r_s + r_g}{v_0}\right) = \left[S^2\left(t - \frac{r_s + r_g}{v_0}\right) + S^{H\,2}\left(t - \frac{r_g + r_g}{v_0}\right)\right], \tag{28}$$

and where C is a constant. In the high frequency approximation (point source) we approximate this function as

$$W\left(t - \frac{r_s + r_g}{v_0}\right) \simeq \delta\left(t - \frac{r_s + r_g}{v_0}\right), \tag{29}$$

and the mean intensity becomes

$$\langle I(\mathbf{x_s}, \mathbf{x_g}, t)\rangle = C \int_A \frac{\langle n^2(\mathbf{x})\rangle}{r_s r_g}\, \delta\left(t - \frac{r_s + r_g}{v_0}\right)\, dA(\mathbf{x}). \tag{30}$$

where C is a constant. Eq. (30) represents the total average intensity at receiver $\mathbf{x_s}$ due to an impulse generated at the source location $\mathbf{x_s}$ and transmitted through the scattering medium. Let us look just at the contribution to the total intensity of an area element at location $\mathbf{x}$. The contribution to the total intensity of the wavefield will be

$$\langle dI(\mathbf{x_s}, \mathbf{x_g}, t)\rangle = C\frac{\langle n^2(\mathbf{x})\rangle}{r_s r_g}\, \delta\left(t - \frac{r_s + r_g}{v_0}\right)\, dA(\mathbf{x}). \tag{31}$$

Eq. (31) is the contribution to the total intensity from an area element dA located at point $\mathbf{x}$. But this can also be interpreted as the intensity of the singly-scattered waves with paths P visiting location $\mathbf{x}$. In other words, $\langle dI(\mathbf{x_s}, \mathbf{x_g}, t)\rangle$ represents the weight factor or intensity of the paths $w_P(\mathbf{x}, t)$ that enters Eq. (7). Since the constant C cancels out in Eq. (7), we have that the weight factor for the ensemble averaging over scattering paths is

$$w(\mathbf{x}, t) = \frac{\langle n^2(\mathbf{x})\rangle}{r_s r_g}\, \delta\left(t - \frac{r_s + r_g}{v_0}\right). \tag{32}$$

4.2 Integral Representation for the Mean Traveltime Change in the Single Scattering regime

We now turn our attention to the change that a wave with path P undergoes when we introduce a small change in the propagation velocity. Suppose that the background slowness in a certain region is perturbed by an amount $\delta s(\mathbf{x})$ small enough that the ray is essentially unchanged (see Figure 5). The traveltime of the scattered wave with trajectory P is given by

$$t_P = \int_{l_s} \frac{1}{v_0} dl + \int_{l_g} \frac{1}{v_0} dl = \frac{r_s + r_g}{v_0}, \tag{33}$$

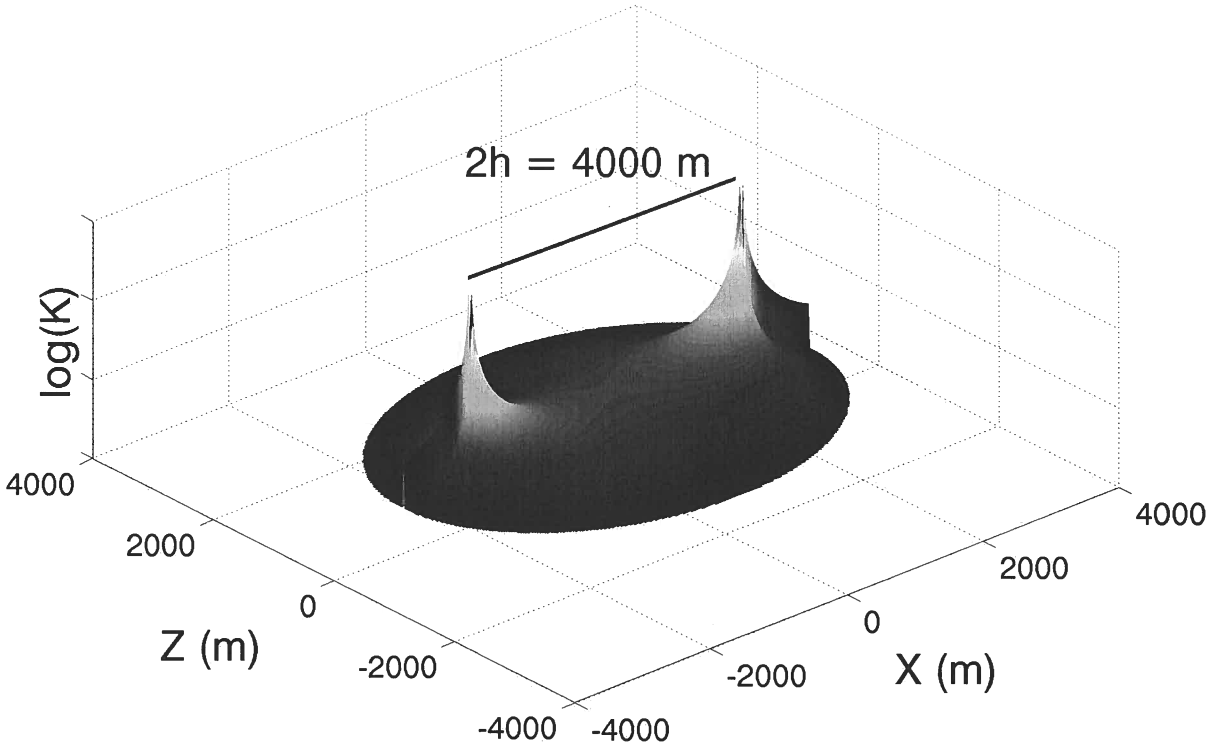

Figure 7. Logarithm of K as function of location for $h = 2000m$ and $t = 1s$.

where h is the half-distance between source and receiver and we have made use of the geometrical variables specified in Figure A4, explained in Appendix A. Eq. (38) accounts for the average change in the traveltime of singly-scattered waves due to a localized slowness perturbation $\delta s(\mathbf{x})$. This expression gives the linearized relationship between the mean traveltime change and the localized slowness perturbation $\delta s(\mathbf{x})$, i.e.

$$\langle \tau(t) \rangle = \int_A K(\mathbf{x}, t)\ \delta s(\mathbf{x})\ dA(\mathbf{x}), \tag{39}$$

where $K(\mathbf{x}, t)$ is the integration kernel that relates the mean traveltime change at traveltime t with a localized slowness perturbation at $\mathbf{x}$ for a given source and receiver configuration, and is given by

$$K(\mathbf{x}, t) = \frac{1}{2\pi h\sqrt{\left(\frac{v_0 t}{2h}\right)^2 - 1}} \left[\frac{r_s}{s} + \frac{r_g}{g}\right]. \tag{40}$$

The kernel $K(\mathbf{x}, t)$ is the sensitivity function of the mean traveltime change for the slowness perturbation. It has dimensions of 1/distance. Figure 7 shows a plot of the logarithm of K as a function of location for half source-receiver distance $h = 2000m$ and propagation time $t = 1s$. The distribution is peaked at the source and receiver location, and decreases rapidly from both locations until it vanishes outside the single scattering ellipse described by the traveltime t. In the next section we use Eq. (38) to calculate numerically the mean traveltime change for a localized perturbation for different source and receiver geometries.

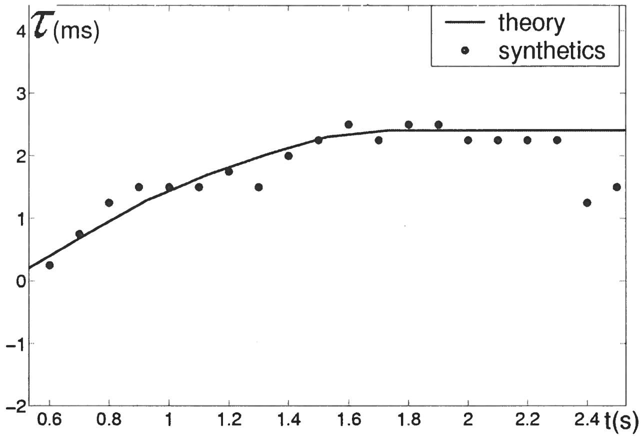

Figure 11. Theoretical versus measured mean traveltime change for receiver $R1$ located 500 m from the source. The window length in the cross-correlation is 500 ms (approximately 12 periods).

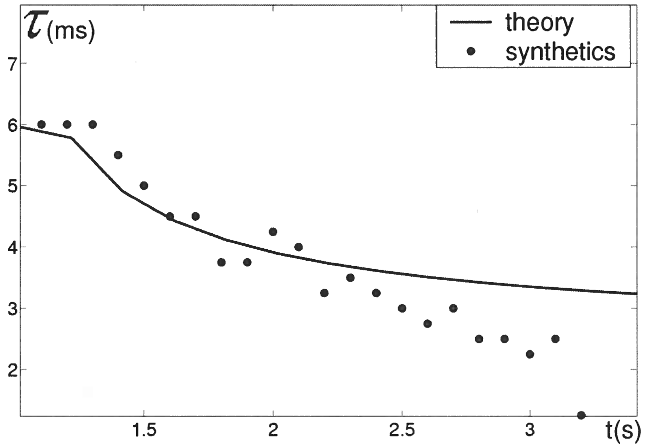

Figure 12. Theoretical versus measured mean traveltime change for receiver $R2$ located 5500 m away from the source. The window length in the cross-correlation is 500 ms (approximately 12 periods).

comparison is shown in Figures 11, 12, 13 and 14. The theoretical mean traveltime change $\langle \tau(t) \rangle$ was calculated using Eq.(38) for a range of traveltimes t. The mean traveltime of the synthetic seismograms was obtained using the time-windowed cross-correlation technique using a window length of 500 ms (approximately 12 periods at the dominant frequency).

Figure 11 shows the mean traveltime change for receiver $R1$ located 500 m away from the source and ahead of the localized slowness perturbation. Notice that the mean traveltime change starts increasing and then reaches a maximum. For receiver $R2$ the mean traveltime change decreases from a maximum at $t = 1.0s$. We also show the mean traveltime change for receivers $R3$ and $R4$ in Figures 13 and 14, respectively.

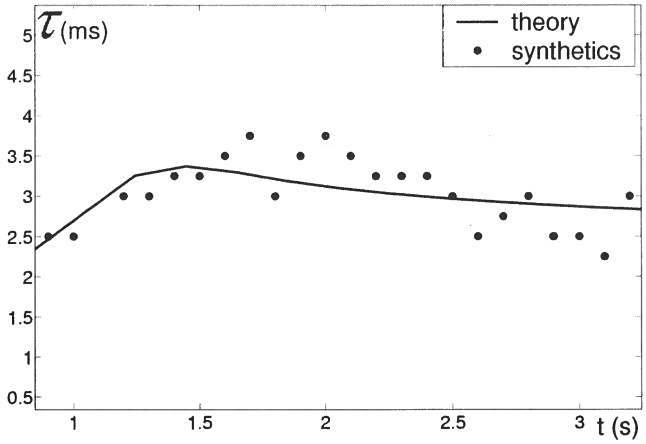

Figure 13. Theoretical versus measured mean traveltime change for receiver $R3$ located 4500 m away from the source. The window length in the cross-correlation is 500 ms (approximately 12 periods).

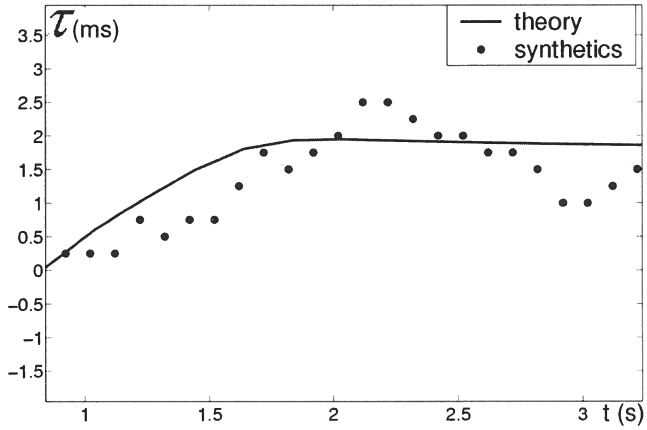

Figure 14. Theoretical versus measured mean traveltime change for receiver $R4$ located 4500 m away from the source. The window length in the cross-correlation is 500 ms (approximately 12 periods).

Despite fluctuations about the predicted mean traveltime change (because of the randomness of the model), there is a good agreement between the theoretical and the measured mean traveltime change $\langle \tau(t) \rangle$ for all cases shown here.

For different source and receiver pairs we obtain different values of the mean traveltime change as a function of time. The difference in the traveltime change for different source and receiver pairs can be exploited in a tomographic scheme to invert the mean traveltime change information to estimate the location and magnitude of the slowness perturbation in a linearized inverse formulation using Eq. (39).

We compare the mean traveltime change calculated for the single scattering regime with the mean traveltime change calculated for the multiple scattering regime for the forward problem and show some examples. Future work will involve obtaining the shape and magnitude of the slowness perturbation from the measured traveltime changes for different source-receiver pairs.

We obtained the expression for the mean traveltime change for 2D acoustic waves. The extension to 3D acoustic waves (not shown here) is left as future work. For 3D we will have to consider ellipsoid surfaces with the foci at the source and receiver location. Elastic waves present a more complicated problem, since we have to take into account conversions between different modes.

In developing the expression of the mean traveltime change $\langle \tau(t) \rangle$ as an average over different paths we assume that the paths before and after the perturbation are the same. Should this not be the case, the weight of each scattering path losses significance. This imposes some constraints on the magnitude of the slowness perturbations that we can solve using our approximation, since the perturbations have to be small enough in order that the paths are preserved after the perturbation. A perturbation that is too weak, tough, will make the traveltime changes to fall under the limit of detectability. Future work needs to specify the ranges in the values of the magnitude of the slowness or velocity perturbation for our theory to be valid and/or useful.

The most important result of this work is that we are able to predict the traveltime change of singly-scattered waves in a statistical way without any knowledge of the scattering properties of the medium (no diffusion constant, mean free path or standard deviation of the velocity fluctuations σ value is required for the calculation). As long as we can describe the wavefield by means of the single scattering approximation, the perturbation of the traveltime of the scattered waves depends linearly on the localized slowness perturbation. This technique has the potential of imaging time-lapse changes of the scattering medium. This technique can be used to detect temporal variations in the slowness of the medium for a random medium characterized by homogeneously distributed weak scatterers.

REFERENCES

Aki, K., & Chouet, B. 1975. Origin of coda waves: source, attenuation and scattering effects. *J. Geophys. Res.*, **80**(23), 3322–3341.

Aldridge, D. 1994. Linearization of the eikonal equation. *Geophysics*, **59**(10), 1631–1632.

Bleistein, N., Cohen, J., & Stockwell, J. 2001. *Mathematics of Multidimensional Seismic Imaging, Migration and Inversion.* Interdisciplinary Applied Mathematics, vol. 13. Springer.

Chernov, L.A. 1960. *Wave Propagation in a Random Medium.* McGraw-Hill, New York.

Claerbout, J. 1985. *Imaging the Earth's Interior.* Blackwell.

Jian, Z., Pearce, J., & Mittleman, D.M. 2003. Characterizing Individual Scattering Events by Measuring the Amplitude and Phase of the Electric Field Diffusing through a Random Medium. *Phys. Rev. Lett.*, **93**(3), 339031–339034.

Kopnichev, Y. 1977. The role of multiple scattering in the formation of a seismogram's tail. *Inveztiya Academy of Science USSR, Physics of the Solid Earth*, **13**, 394–398.

Leary, P. C. 2002. Numerical simulation of first-order backscattered P and S waves for time-lapse seismic imaging in heterogeneous reservoirs. *Geophys. J. Int.*, **148**, 402–425.

Morse, P., & Feshbach, H. 1953. *Methods of Theoretical Physics.* McGraw-Hill Book company, Inc.

Pacheco, C., & Snieder, R. 2003 (May). *Localizing change with Coda Wave Interferometry: Derivation and validation of the sensitivity kernel.* Tech. rept. Center for Wave Phenomena: Colorado School of Mines, Golden, CO, 80401.

Page, J.H., Schriemer, H.P., Bailey, A.E., & Weitz, D.A. 1995. Experimental test of the diffusion approximation for multiply scattered waves. *Phys Rev E*, **52**(3), 3106–3114.

Sato, H. 1977. Energy propagation icluding scattering effect: single isotropic scattering approximation. *J. Phys. Earth*, **25**, 27–41.

Schriemer, H., Cowan, M., Page, J., Liu, Zhengyou, & Weitz, D. 1997. Energy Velocity of Diffusing waves in strongly scattering media. *Phys Rev Lettters*, **79**(17), 3166–319.

Snieder, R. 1999. Imaging and averaging in complex media. *Pages 405–454 of:* Fouque, J.P. (ed), *Diffuse Waves in Complex Media.* Kluwer Academic Publishers.

Snieder, R. 2002. Coda wave interferometry and the equilibration of energy in elastic media. *Phys. Rev. E*, **66**, 1–8.

Snieder, R. 2003. Coda waves, a tail of correlations. *Phys. Rev. Lett.* In press.

Snieder, R., Gret, A., & Douma, H. 2002. Coda wave interferometry for estimating nonlinear behavoir in seismic velocity. *Science*, **295**(22), 2253–2255.

Turner, J., & Weaver, R. 1994. Radiative transfer of ultrasound. *J. Acoust. Soc. Am.*, **96**, 3654–3673.

Weitz, D.A., & Pine, D.J. 1993. Diffusing Wave Spectroscopy. *Pages 652–720 of:* Brown, W. (ed), *Dynamic light scattering, The method and some applications.* Oxford: Clarendon Press.

Wu, R. 1982. Attenuation of short period seismic waves due to scattering. *Geoph. Res. Lett.*, **9**(1), 9–12.

Yodh, A. 1995. Spectroscopy and imaging with diffusing light. *Physics Today*, March, 34–40.

Since the integrand does not depend on θ we obtain

$$I_D = \frac{\pi}{h}\int_1^{\infty} d\varepsilon \frac{1}{\sqrt{\varepsilon^2 - 1}}\,\delta\left(\varepsilon - \frac{v_0 t}{2h}\right). \tag{A8}$$

Using the sifting property of the delta function, and since $\varepsilon = v_0 t/2h$ lies within the interval of integration, we obtain

$$I_D = \frac{\pi}{h}\frac{1}{\sqrt{\left(\frac{v_o t}{2h}\right)^2 - 1}}, \tag{A9}$$

and we can write Eq. (A1) as follows

$$\langle \tau(t)\rangle = \frac{1}{I_D}\int_0^{2\pi} d\theta \int_1^{+\infty} \frac{d\varepsilon}{\sqrt{\varepsilon^2 - 1}}\left[\int_{l_s(\mathbf{x})} \frac{1}{2h}\delta\left(\varepsilon - \frac{v_0 t}{2h}\right)\,\delta s(\mathbf{x})\, dl(\mathbf{x}) + \int_{l_g(\mathbf{x})} \frac{1}{2h}\delta\left(\varepsilon - \frac{v_0 t}{2h}\right)\,\delta s(\mathbf{x})\, dl(\mathbf{x})\right]. \tag{A10}$$

For convenience, we can write the expression of the mean traveltime change as the sum of the mean traveltime change from the source location $\mathbf{x_s}$ to the edge of the ellipse plus the mean traveltime change from the edge of the ellipse to the receiver location $\mathbf{x_g}$. Thus,

$$\langle \tau(t)\rangle = I_s + I_g, \tag{A11}$$

where I_s and I_g are

$$I_s = \frac{1}{I_D}\int_0^{2\pi} d\theta \int_1^{+\infty} \frac{d\varepsilon}{\sqrt{\varepsilon^2 - 1}}\int_{l_s(\mathbf{x})} \frac{1}{2h}\delta\left(\varepsilon - \frac{v_0 t}{2h}\right)\,\delta s(\mathbf{x})\, dl(\mathbf{x}), \tag{A12}$$

$$I_g = \frac{1}{I_D}\int_0^{2\pi} d\theta \int_1^{+\infty} \frac{d\varepsilon}{\sqrt{\varepsilon^2 - 1}}\int_{l_g(\mathbf{x})} \frac{1}{2h}\delta\left(\varepsilon - \frac{v_0 t}{2h}\right)\,\delta s(\mathbf{x})\, dl(\mathbf{x}), \tag{A13}$$

Let us first analyze the contribution to the mean traveltime change of the paths that start at the source and finish at the edge of the ellipse. Substituting the value of I_D on Eq. (A12) and using again the shifting property of the delta function, we obtain

$$I_s = \frac{1}{2\pi}\int_0^{2\pi} d\theta \int_{l_s(\mathbf{x})} \delta s(\mathbf{x})\, dl(\mathbf{x}). \tag{A14}$$

Eq. (A14) states that the mean traveltime change of paths starting at the source and ending at the edge of the ellipse is an average of the traveltime change of the different paths l_s for each value of θ. This looks simple enough, but it is not yet useful, as we would like the expression for the mean traveltime change to take the form of an area integral over the Cartesian coordinates x and y. The key is to realize that the combination of the θ-integral and the dl-integral sweeps over the whole interior of the single-scattering ellipse. Thus, we want to obtain the value of $d\theta dl$ as a function of $dxdy$. The question is, then, what is the scaling factor if rewrite Eq. (A14) as an integral over the Cartesian coordinates x and y.

Let dl be an increment in length along the path l_s from the source location to the edge of the ellipse and de be an increment in length along the edge of the ellipse for an increment in angle $d\theta$. Then,

$$dA = \frac{s}{r_s}(\mathbf{dl} \times \mathbf{de}) = \frac{s}{r_s} dl\, de\, sin(\phi), \tag{A15}$$

where ϕ is the angle between the unit vector $\mathbf{n}$ pointing along the direction of the path l_s and and the vector $\mathbf{e}$ parallel to the edge of the ellipse on the point of intersection, as described in Figure A2. The term s/r_s corrects for the fact that the surface area shrinks as we approach the source.

Let us compute the length element de along the edge of the ellipse. We get this by differentiating x and y in elliptical coordinates with respect to angle θ, i.e.

$$de = \sqrt{dx^2 + dy^2}, \tag{A16}$$

where

$$dx = -h\ \varepsilon\ sin(\theta)\ d\theta, \tag{A17}$$

and

$$dy = h\ \sqrt{\varepsilon^2 - 1}\, cos(\theta)\ d\theta). \tag{A18}$$

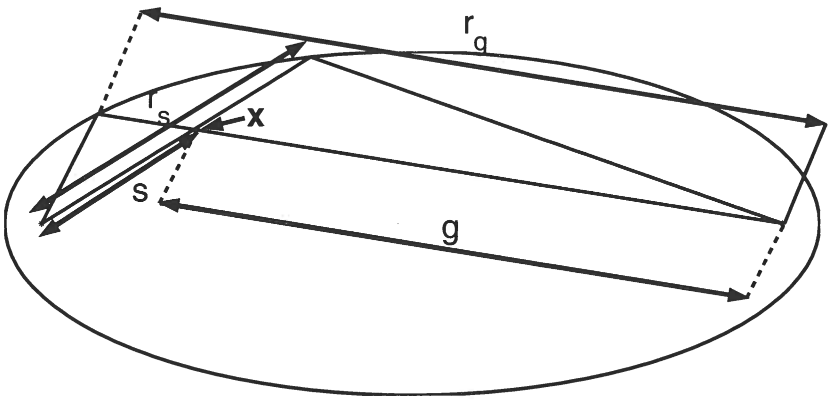

Figure A4. Geometry used in the derivation of Eq. 38. Distances are shown in dashed lines: s is the distance from $\mathbf{x_s}$ to $\mathbf{x}$; r_s is the distance from $\mathbf{x_s}$ to the scatterer on the single-scattering ellipse; g is the distance from $\mathbf{x_g}$ to $\mathbf{x}$ and r_g is the distance from $\mathbf{x_g}$ to the other scatterer on the ellipse.

so that,

$$\mathbf{e} = \frac{1}{\sqrt{\varepsilon^2 - cos^2(\theta)}} \begin{pmatrix} -\varepsilon sin(\theta) \\ \sqrt{\varepsilon^2 - 1} cos(\theta) \end{pmatrix} \tag{A23}$$

We now calculate the term $sin(\phi)$ from the magnitude of the cross-product between $\mathbf{n}$ and $\mathbf{e}$. Thus,

$$sin(\phi) = |\mathbf{n} \times \mathbf{e}| = \frac{\sqrt{\varepsilon^2 - 1}}{\sqrt{\varepsilon^2 - cos^2(\theta)}}. \tag{A24}$$

Using $\varepsilon = v_0 t/2h$ we get

$$sin(\phi) = \frac{\sqrt{\left(\frac{v_0 t}{2h}\right)^2 - 1}}{\sqrt{\left(\frac{v_0 t}{2h}\right)^2 - cos^2(\theta)}}. \tag{A25}$$

Insert this with Eq. (A22) into Eq. (A18) and we obtain

$$dA = dx\, dy = h \frac{s}{r_s} \sqrt{\left(\frac{v_0 t}{2h}\right)^2 - 1}\, dl\, d\theta. \tag{A26}$$

From Eq. (A26) we can obtain $dl\, d\theta$ as a function of dA. Therefore,

$$dl\, d\theta = \frac{r_s}{s} \frac{dA}{h\sqrt{\left(\frac{v_0 t}{2h}\right)^2 - 1}}, \tag{A27}$$

and we can substitute the integral over dl and $d\theta$ in Eq. (A14) with an integral over area, where the area to be integrated is the interior of the single-scattering ellipse at time t, i.e.

$$I_s = \frac{1}{2\pi h\sqrt{\left(\frac{v_0 t}{2h}\right)^2 - 1}} \int_A \frac{r_s}{s}(\mathbf{x})\, \delta s(\mathbf{x})\, dA(\mathbf{x}). \tag{A28}$$

By symmetry, the second integral I_g that accounts for the mean traveltime changes of the paths going from the edge of the ellipse to the receiver location $\mathbf{x}$ gives a similar contribution.

Taking the integral I_g into account and using the symmetry of source and receiver location, we get, using the notation of pictured in Fig. A4 the expression for the mean traveltime change for waves in the single-scattering regime with traveltime t

$$\langle \tau(t) \rangle = \frac{1}{2\pi h\sqrt{\left(\frac{v_0 t}{2h}\right)^2 - 1}} \int_A \left[\frac{r_s}{s} + \frac{r_g}{g}\right](\mathbf{x})\, \delta s(\mathbf{x})\, dA(\mathbf{x}). \tag{A29}$$

Extracting the Green's function from the correlation of coda waves, an alternative derivation based on stationary phase

Roel Snieder

Center for Wave Phenomena and Dept. of Geophysics, Colorado School of Mines, Golden CO 80401-1887

ABSTRACT

The Green's function of waves that propagate between two receivers can be found by cross-correlating multiply-scattered waves recorded at these receivers. This technique obviates the need for a source at one of these locations, and is therefore called *passive imaging.* This principle has been explained by assuming that the normal modes of the system are uncorrelated and that all carry the same amount of energy (equipartitioning). Here I present an alternative derivation of passive imaging of the ballistic wave that is not based on normal modes. The derivation is valid for scalar waves in three dimensions, and for elastic surface waves. Passive imaging of the ballistic wave is based on the destructive interference of waves radiated from scatterers away from the receiver line, and the constructive interference of waves radiated from secondary sources near the receiver line. The derivation presented here shows that the global requirement of the equipartitioning of normal modes can be relaxed to the local requirement that the scattered waves propagate on average isotropically near the receivers.

Key words: passive imaging, daylight imaging, correlation

1 INTRODUCTION

Passive imaging is a technique wherein waves recorded at two receiver locations are correlated to give the Green's function that describes the direct wave propagation between these receivers. The tail of multiply scattered waves is called the *coda*, after the Latin word for tail. Coda waves are effective for monitoring temporal changes in media (Snieder et al., 2002; Cowan et al., 2002). Using coda waves to determine the Green's function is useful because it provides information on wave propagation between two points in space without the need for a source at either of these two points. The Green's function thus obtained can be used to form an image of the medium. Passive imaging has been used in seismic exploration (Louie, 2001; Wapenaar et al., 2002), helioseismology (Rickett and Claerbout, 2000), and ultrasonics with either an active source (Lobkis and Weaver, 2001; Derode et al., 2003a; Malcolm et al., 2003) or thermal noise that excites the coda (Weaver and Lobkis, 2001; Weaver and Lobkis, 2003). Numerical experiments have shown that passive imaging can be used both in closed and in open systems (Roux and Fink, 2003; Derode et al., 2003b).

Campillo and Paul (2003) recently used passive imaging in crustal seismology by retrieving the surface wave Green's function between seismological stations within Mexico using coda waves generated by earthquakes along the west coast of Mexico. The theoretical explanation offered in their work is based on the assumption of equipartitioning of the Earth's modes (Lobkis and Weaver, 2001). These modes can either be the normal modes of the Earth, or the surface wave modes that describe the guided waves that propagate along the Earth's surface.

Suppose one invokes the Earth's normal modes. In the study of Campillo and Paul (2003), records of the ground motion with a duration of about 600 sec were used. It takes about 1100 sec for a P-wave to propagate to the other side of the earth (Stein and Wysession, 2003); for an S-wave it takes even longer, so, in their

Marion, 1991), and time reversed imaging (Derode et al., 1999).

The double sum $\sum_{s,s'}$ in expression (3) can be split into a sum over diagonal terms $\sum_{s=s'}$ and a sum $\sum_{s\neq s'}$ over cross terms. I show in the appendix that for a random medium, the ensemble average of the cross-terms vanishes provided the DC-component of the $S_s(t)$ is equal to zero. In a single realization of the medium, however, the cross-terms are nonzero. I also show in the appendix that for a single source event (e.g. an earthquake) the ratio of the cross terms to the diagonal terms is smaller than $\sqrt{2\Delta/T}$. When an average over N_{src} source events is carried out, this ratio is bounded by $\sqrt{2\Delta/N_{src}T}$. This means that by averaging over time, and possibly over different source events, the sum of the cross-terms can be made arbitrarily small by increasing the time interval T and the number of source events N_{src}. In the following I refer to this type of averaging as *time/event averaging.* Note that in several studies of passive imaging, time/event averaging as described here is the only type of averaging that is applied (Rickett and Claerbout, 2000; Lobkis and Weaver, 2001; Derode et al., 2003a; Weaver and Lobkis, 2001; Weaver and Lobkis, 2003; Campillo and Paul, 2003).

In the following I assume that sufficient time/event averaging is carried out so that the cross terms in the sum (3) can be ignored. With the definition (4) this reduces expression (3) to

$$C(\tau) = \sum_s C_s\left(\tau + \frac{r_1^{(s)} - r_2^{(s)}}{c}\right) / r_1^{(s)} r_2^{(s)} . \quad (5)$$

Since the Fourier transform of the cross correlation is equal to the power spectrum , Eq. (5) is given in the frequency domain by

$$C(\omega) = \sum_s |S_s(\omega)|^2 \frac{\exp\left(i\omega(r_2^{(s)} - r_1^{(s)})/c\right)}{r_1^{(s)} r_2^{(s)}} . \quad (6)$$

The power spectrum $|S_s(\omega)|^2$ does not depend on the phase fluctuations of the scattered waves, but is does depend on fluctuations in the amplitude. When the variations in the power spectrum are uncorrelated with the phase $\exp\left(i\omega(r_2^{(s)} - r_1^{(s)})/c\right)$, then

$$C(\omega) = \overline{|S(\omega)|^2} \sum_s \frac{\exp\left(i\omega(r_2^{(s)} - r_1^{(s)})/c\right)}{r_1^{(s)} r_2^{(s)}} , \quad (7)$$

with

$$\overline{|S(\omega)|^2} = \frac{1}{N} \sum_s |S_s(\omega)|^2 , \quad (8)$$

where N is the number of scatterers.

When there are many scatterers per wavelength, the summation over scatterers $\sum_s(\cdots)$ can be replaced by a volume integration $\int(\cdots)ndV$ that is weighted by the scatterer density n that is defined as the number of scatterers per unit volume. In this approximation equation (7) is given by

$$C(\omega) = \overline{|S(\omega)|^2} \int \frac{\exp\left(i\omega(r_2 - r_1)/c\right)}{r_1 r_2} ndxdydz , \quad (9)$$

with the distances r_1 and r_2 defined in Fig. 2.

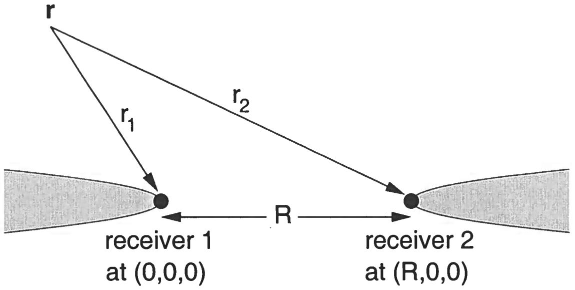

Figure 2. Definition of the geometric variables for the waves that travel from a scatterer at location **r** to two receivers. The region of constructive interference is indicated by the shaded regions.

The integration over the transverse coordinates x and y can be evaluated with the stationary phase approximation (Bender and Orszag, 1978; Bleistein, 1984). This technique leaves only the contribution of the points near the receiver line $y = z = 0$, for which the integrand is not oscillatory. In this approximation

$$C(\omega) = 2\pi\overline{|S(\omega)|^2} \frac{c}{-i\omega} \int_{-\infty}^{\infty} \frac{e^{ik(|R-x|-|x|)}}{||R-x|-|x||} ndx . \quad (10)$$

For scatterers to the left of the receivers ($x < 0$) the integrand is given by $\exp(ikR)/R$, for scatterers to the right of the receivers ($x > R$) the integrand is equal to $\exp(-ikR)/R$, and for scatterers between the receivers ($0 < x < R$) the integrand is given by $\exp(ik\,(R-2x))/\,|R-2x|$. Because the latter integrand is oscillatory, the region $0 < x < R$ gives a sub-dominant contribution to the integral of Eq. (10). Ignoring this contribution gives

$$\begin{aligned} C(\omega) = \quad & 8\pi^2\overline{|S(\omega)|^2}\left(\tfrac{c}{i\omega}\right) \\ & \times \left(-\tfrac{e^{ikR}}{4\pi R}\int_{-\infty}^{0} ndx - \tfrac{e^{-ikR}}{4\pi R}\int_{R}^{\infty} ndx\right) . \end{aligned} \quad (11)$$

The term $-\exp(ikR)/4\pi R$ is the Green's function that accounts for the waves that propagate between the receivers; this term comes from the integration over $x < 0$. The second term $-\exp(-ikR)/4\pi R$, which comes from the integration over $x > R$, is the advanced Green's function. The retarded Green's function comes from the waves that propagate from receiver 1 to receiver 2 and correlate for a positive lag time $\tau > 0$, as shown in the top panel of Fig. 3. The presence of the advanced Green's function is due to the waves that propagate from receiver 2 to receiver 1; these waves correlate for a negative lag time $\tau < 0$, as shown in the bottom

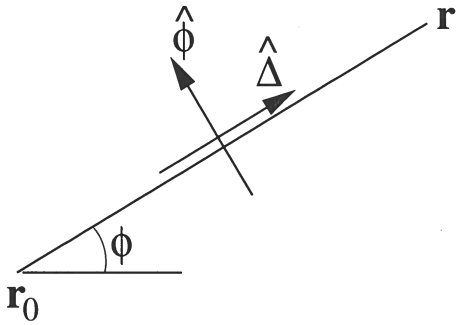

Figure 5. Definition of the unit vectors $\hat{\mathbf{\Delta}}$ and $\hat{\varphi}$ that define the radial and transverse polarizations, respectively.

give:

$$C(\omega) = 8\pi^2\overline{|S(\omega)|^2}\left(\tfrac{ncL}{i\omega}\right) \times \left(-\frac{e^{ikR}e^{-R/2L}}{4\pi R} - \frac{e^{-ikR}e^{-R/2L}}{4\pi R}\right) . \tag{12}$$

The x-integrals contribute a factor L to the correlation. The last two terms give the retarded and advanced Green's functions for the ballistic wave that propagates between the receivers.

The issue of the medium of propagation is also of relevance for the derivation of passive imaging based on normal modes (Lobkis and Weaver, 2001). That derivation has an open question: the normal modes of which system should be used? The normal modes of the true system, which includes the scatterers, are by definition uncoupled; equipartitioning among these modes therefore will not occur. The normal modes of a homogeneous system are coupled by the scatterers, which may result in equipartitioning of energy among the modes of the homogeneous model. However, this raises the question which homogeneous system to use? It is not clear from the derivation of Lobkis and Weaver (2001) from which system one obtains the Green's function. If this would be the Green's function of a medium that takes the scattering losses of the ballistic wave into account, then that medium is attenuating. In such a medium the normal modes are not orthogonal and the theory of Lobkis and Weaver (2001) must be generalized by using adjoint modes (Park and Gilbert, 1986).

4 SURFACE WAVES IN AN ELASTIC MEDIUM

Campillo and Paul (2003) obtained the full surface wave Green's tensor by correlating the direct product of the three components of the two receivers. In this section, I show that the treatment of the previous sections can be generalized to surface waves propagating in a layered elastic 3D medium with embedded scatterers. The surface-wave Green's tensor of a layered medium whose properties depend on the depth z only can be written in the frequency domain as

$$G_{ij}(\mathbf{r},\mathbf{r}_0) = \sum_m G_{ij}^m(\mathbf{r},\mathbf{r}_0) . \tag{13}$$

The total surface wave Green's tensor is expressed as a sum over surface-wave modes m that include both Rayleigh waves and Love waves. The surface wave Green's tensor of mode m in the far field is given by Snieder (1986a), and Snieder (2002)

$$G_{ij}^m(\mathbf{r},\mathbf{r}_0) = p_i^m(z,\varphi)p_j^{m*}(z_0,\varphi)\frac{e^{i(k_m R+\pi/4)}}{\sqrt{\frac{\pi}{2}k_m R}} , \tag{14}$$

where $R = \sqrt{(x-x_0)^2+(y-y_0)^2}$ is the distance between the points measured in the horizontal plane, and k_m is the horizontal wave-number of mode m. The polarization vectors $\mathbf{p}^m(z,\varphi)$ depend on the depth z and the azimuth φ of the path between points $\mathbf{r}_0$ and $\mathbf{r}$. The orientation of the polarization vectors can be expressed into the unit vectors $\hat{\mathbf{\Delta}}$ and $\hat{\varphi}$ that point in the radial and transverse direction, respectively, as defined in Fig. 5. For Love waves the polarization vector is related to the Love wave eigenfunction $l_1^m(z)$ (Snieder, 1986a; Aki and Richards, 2002) by

$$\mathbf{p}^m(z,\varphi) = l_1^m(z)\hat{\varphi} , \tag{15}$$

while for Rayleigh waves

$$\mathbf{p}^m(z,\varphi) = r_1^m(z)\hat{\mathbf{\Delta}} + ir_2^m(z)\hat{\mathbf{z}} , \tag{16}$$

with $r_1^m(z)$ and $r_2^m(z)$ the radial- and vertical-component modal functions of the Rayleigh waves (Snieder, 1986a; Aki and Richards, 2002). Following ref. Snieder (1986a), the surface-wave modes are assumed to be normalized according to the following convention

$$\begin{aligned} &4c_m U_m \textstyle\int_0^\infty \rho\ (l_1^m)^2\,dz = \\ &= 4c_m U_m \textstyle\int_0^\infty \rho\ \left((r_1^m)^2+(r_2^m)^2\right)dz = 1 , \end{aligned} \tag{17}$$

with c_m and U_m are the phase velocity and group velocity of mode m, respectively, and $\rho(z)$ the mass density.

When the two receivers record the three components of the ground motion, one can form the correlation tensor of all combinations of components:

$$C_{ij}(\tau) = \int u_{2i}(t+\tau)u_{1j}(t)dt , \tag{18}$$

where u_{2i}, for example, is the i-component of the displacement recorded at receiver 2. The recorded displacement can be written as a sum over the surface waves radiated by the different scatterers s. By analogy with Eq. (1) the displacement of the two receivers in the frequency domain is given by a double sum over scatterers s and surface wave modes m

where the dagger denotes the Hermitian conjugate. This expression contains infinite integrals. Incorporating the attenuative properties of the ballistic surface wave, as shown in section 3, gives

$$C_{ij}(\omega) = \pi \sum_{m} \overline{|S^m(\omega)|^2} n c_m L_m \left\{ \frac{G^m_{ij}(\mathbf{r}_2, \mathbf{r}_1)}{i\omega} + \left(\frac{G^m_{ij}(\mathbf{r}_1, \mathbf{r}_2)}{i\omega} \right)^{\dagger} \right\} , \quad (25)$$

where L_m is attenuation length of surface wave mode m, and where the Green's function of each mode is understood to contain an attenuation term $\exp(-R/2L_m)$.

This expression is similar to the corresponding result (12) for scalar waves in three dimensions. The correlation gives the superposition of the Green's function of the ballistic wave that propagates from receiver 1 to receiver 2 (the first term), and the ballistic wave Green's function that propagates in the opposite direction (the last term). Passive imaging with surface waves thus provides the superposition of the retarded and advanced surface wave Green's functions of the ballistic wave.

5 CONCLUSION

As shown in Eqs. (11) and (25), the ballistic wave Green's function can be obtained by a cross-correlation of the waveforms at two receivers. Two steps must be taken to extract this Green's function from the correlation. First, the correlation in the frequency domain must be multiplied by $i\omega/\overline{|S(\omega)|^2}$. The multiplication with $i\omega$ corresponds in the time domain to a differentiation that undoes the integration used in the cross-correlation. The division by the power spectrum $\overline{|S(\omega)|^2}$ corrects for frequency-dependent factors in the scattering coefficients, the source spectrum, and the receiver response. For the case of Eq. (11) for scalar waves in 3D, the power spectrum can be obtained from the waves recorded at the receivers. For the corresponding expression (25) for surface waves in an elastic medium, each mode must be corrected for the power spectrum of that mode. The scattering coefficients for surface wave modes strongly depend on the depth of the scatterers (Snieder, 1986a), and on topography (Snieder, 1986b). For this reason the average power spectrum $\overline{|S^m(\omega)|^2}$ of the scattered surface wave mode may depend strongly on the mode number m. It is not clear how $\overline{|S^m(\omega)|^2}$ can be extracted from the recorded waves. In applications in crustal seismology, the fundamental mode Love and Rayleigh waves usually dominate. The average power in the fundamental Rayleigh wave can be estimated from the vertical component. The power of the horizontal components can then be used to infer the power in the fundamental Love wave. Without correcting for the power spectrum, the cross-correlation may not give the correct frequency dependence of the Green's function.

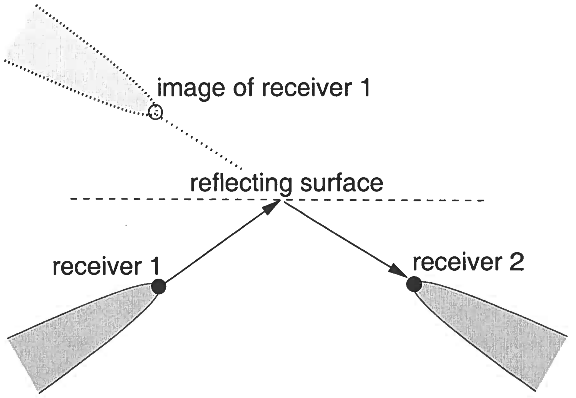

Figure 6. The wave path of a reflected wave. The receivers are shown by solid circles. The dark gray areas indicate the location of scatterers that give a stationary contribution to the integration over scatterers for the reflected wave. The open circle denotes the image of receiver 1 upon reflection in the free surface, and the light gray area is the image of the scatterers that contribute to the stationary phase solution for the reflected wave.

The second step that must be taken is due to the fact that the cross-correlation of the waves recorded at two receivers gives the superposition of the retarded and the advanced ballistic wave Green's functions. These two contributions can be unraveled in the time domain by restricting the signal to positive and negative time windows respectively (Lobkis and Weaver, 2001).

Physically, the derivation shown here implies that in general the scattered waves recorded at the two receivers are uncorrelated, except for the waves radiated from scatterers that are located near the receiver line. Passive imaging of the ballistic wave thus is based on constructive interference solely of those scattered waves that propagate along the receiver line.

Ultrasound experiments with a finite aluminum sample show that the ballistic wave as well as waves that are reflected from boundaries are reconstructed from passive imaging (Lobkis and Weaver, 2001; Weaver and Lobkis, 2001; Weaver and Lobkis, 2003). The theory presented here does not account for these reflected waves. When a wave reflects off a plane boundary, as shown in Fig. 6, the scattering paths from scatterers located in the dark gray areas interfere constructively. The theory presented here can be applied to this problem by invoking an image receiver and image scatterers as indicated by the open circle and light-gray area in Fig. 6. For a non-planar boundary or an inhomogeneous reference medium one needs to determine other stationary phase contributions to the integral over the scatterers. These contributions depend on the geometry of scattering path, and are not accounted for by the theory presented here.

The equilibration of normal modes (Lobkis and Weaver, 2001) provides a sufficient condition for con-

H. Takeuchi and M. Saito. Seismic surface waves. In B.A. Bolt, editor, *Seismology: surface waves and earth oscillations (Methods in Computational Physics, Vol. 11)*. Academic Press, New York, 1972.

T. Tanimoto. The three-dimensional shear wave structure in the mantle by overtone waveform inversion -I. radial seismogram inversion. *Geophys. J.R. Astron. Soc.*, 89:713–740, 1987.

K. Wapenaar, D. Draganov, J. Thorbecke, and J. Fokkema. Theory of acoustic daylight imaging revisited. In *Abstracts of the SEG 72nd Annual Meeting*, pages 2269–2272, 2002.

R. Weaver and O. Lobkis. On the emergence of the Green's function in the correlations of a diffuse filed: pulse-echo using thermal phonons. *Ultrasonics*, 40:435–439, 2003.

R.L. Weaver and O.I. Lobkis. Ultrasonics without a source: Thermal fluctuation correlations and MHz frequencies. *Phys. Rev. Lett.*, 87:134301–1/4, 2001.

the autocorrelation $C_s(t)$ is indicated by Δ. Each of the t'-integrals in (A8) then gives a contribution that is smaller than $C_{max}^2\Delta$. The remaining t-integral gives a contribution T. This implies that

$$\left\langle C_C^2(\tau)\right\rangle \leq 2N^2 C_{max}^2 T\Delta \; . \tag{A9}$$

In order to assess the importance of the cross terms, I compare this with the mean of the diagonal term. This mean is given by

$$\langle C_D(0)\rangle = \sum_s \int_0^T \langle S_s^2(t)\rangle \, dt = \sum_s \int_0^T \langle C_s(0)\rangle \, dt \; . \tag{A10}$$

Using the same estimates that led to (A9) then gives

$$\langle C_D(0)\rangle = \sum_s C_s(0)T \approx NC_{max}T \; , \tag{A11}$$

because the autocorrelation attains its maximum for a zero time lag. With the estimate (A9) this gives the following ratio of the standard deviation of the cross terms to the diagonal terms:

$$\frac{\left\langle C_C^2(\tau)\right\rangle^{1/2}}{\langle C_D(0)\rangle} \leq \sqrt{\frac{2\Delta}{T}} \; . \tag{A12}$$

Note that this ratio does not depend on the number of scatterers. When in addition to an averaging over time, N_{src} source events are used, and when the signals emitted by the scatterers for different source events are uncorrelated, the standard deviation of the cross terms increases with a factor $\sqrt{N_{src}}$ while the diagonal terms are proportional to N_{src}, so that

$$\frac{\left\langle C_C^2(\tau)\right\rangle^{1/2}}{\langle C_D(0)\rangle} \leq \sqrt{\frac{2\Delta}{N_{src}T}} \; . \tag{A13}$$

Volcano monitoring with a natural source: Application to Arenal Volcano, Costa Rica

Roel Snieder† and Mike Hagerty‡
†*Center for Wave Phenomena and Department of Geophysics, Colorado School of Mines, Golden, CO USA*
‡*Institute of Geological and Nuclear Sciences, 41 Bell Rd., South Gracefield, Lower Hutt, New Zealand*

ABSTRACT

Multiply scattered waves are a new tool for monitoring changes in the earth's subsurface. In this study we use the air pressure and displacement recorded at the Arenal Volcano for passive monitoring. The pressure pulses emitted by the volcano are associated with a complex displacement signal of overlapping coda waves. By deconvolving the ground motion with the air pressure for different time intervals we obtain a highly repeatable displacement signal that has the character of diffusive wave propagation. This deconvolved displacement signal slowly changes with the time interval analyzed in the employed data. This change can be explained by a shift in the point of excitation of the elastic waves over a distance of about 15 meters.

Key words: volcano monitoring, natural hazards, deconvolution

1 INTRODUCTION

The interior of volcanoes is highly heterogenous, leading to strong scattering of seismic waves. Wegler and Lühr (2001) showed that seismic waves generated by an airgun at Merapi are strongly scattered; the recorded coda waves have the signature of diffuse waves whose propagation is more like Brownian motion than ballistic propagation along rays. They inferred that the mean free path of the S-waves is only 100 m, much less than the size of the volcano.

Multiply scattered waves are sensitive to small changes in a medium since their propagation path is long in a limited region of space. This property forms the basis of Coda Wave Interferometry (Snieder, Grêt, Douma and Scales, 2002; Snieder, 2002). In this time-lapse technique, the change in multiply scattered waves for a given source-receiver pair is used to make inferences about the change in the medium or in the source position. The change in the coda waves is measured by computing the time-shifted cross-correlation before and after the change.

Coda wave interferometry requires a repeatable source. In active source experiments, such as the study of Wegler, Lühr and Ratdomopurbo (1999), who used an airgun in a water basin, this condition is satisfied. When passive sources are used, one needs to establish independently to what extent the source changes with time. Earthquake multiplets have been used for time-lapse measurements of the Earth's structure (Ratdomopurbo and Poupinet, 1995; Baisch and Bokelmann, 2001; Vidale and Li, 2003; Niu, Silver, Nadeau and McEvilly, 2003). In this work we study the feasibility of using the air pressure and displacement (Hagerty, Schwartz, Garcés and Protti, 2000) recorded on Arenal Volcano, Costa Rica, in order to monitor temporal changes in the structure of the volcano or the excitation mechanism of these waves.

2 THE EMPLOYED DATA

Arenal Volcano is a young (approximately 3,000 years old) stratovolcano located in northern Costa Rica. It was considered extinct prior to a violent Plinian eruption in 1968, and, since 1984 it has primarily exhibited strombolian activity characterized by small but frequent summit explosions. A broadband seismic and geodetic network was installed around the flanks of Arenal in 1995, and in 1997 a five-element linear array of seismometers and microphones was temporarily deployed on the western flank to record the seismic-acoustic wavefield (Hagerty, Schwartz, Garcés and Protti, 2000). In this paper we examine an approximately 16-min period

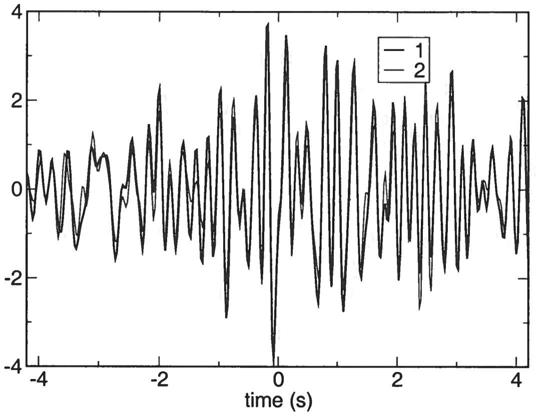

Figure 3. Enlargement of the deconvolved waveforms computed for ages 1 and 2.

For $t < -5$ s these deconvolved waveforms consist of uncorrelated random noise with a noise level that is significant compared to the coherent part of the wave field around $t = 0$ s. This is not surprising; the pressure signal in the top trace of figure 1 has a significant noise contamination between the pressure pulses. That noise contamination may be aggravated by any noise that is hidden on the displacement signal in the bottom trace of figure 1.

For times between -4 s and around 6 s the deconvolved waveforms are highly correlated. The only exception is the deconvolved signal for age 6, perhaps because of the lower signal level at that age. Because the deconvolved waves computed for the different ages are coherent after about -4 s, we judge that the impulse response in the deconvolved waves starts around that time. This does not mean, however, that the response of Arenal is acausal. The time difference between the arrival time of the pressure signal and the displacement is about 5 s. This agrees with the observed emergence of the signal in the deconvolved waveforms around $t = -4$ s.

The deconvolved waveforms have the character of diffusive waves; the coda slowly builds to a maximum at around $t = 0$ s, and then decays again. Superposed on these coda waves are distinct arrivals around $t = -3$ s and $t = 0$ s. The wave at $t = 0$ s may be due to the coupling of the air wave either to the ground motion or directly to the seismometer. Since the microphone and the seismometer are at the same location this wave arrives at $t = 0$ s. The waves arriving between -4 s and 6 s have a general character similar to the diffusive waves that have been reported for other volcanoes (Wegler and Lühr, 2001; Ratdomopurbo and Poupinet, 1995).

The deconvolved waveforms are most similar for adjacent ages. The early part of the deconvolved waveforms for the ages 1 and 2, shown in figure 3, exhibit large similarity of these waveforms. As can be seen in figure 2, this similarity decreases when the deconvolved wave from age 1 is compared with the deconvolved waves from progressively later ages.

4 THE CORRELATION OF THE DECONVOLVED SIGNALS

In this section we outline the theory of coda wave interferometry (Snieder, Grêt, Douma and Scales, 2002; Snieder, 2002). In this technique the time-shifted correlation coefficient of two signals $u_1(t)$ and $u_2(t)$ is used to quantify the degree of similarity of the signals. This coefficient is defined as

$$R(\tau) = \frac{\int_{t-T}^{t+T} u_1(t')u_2(t' + \tau)dt'}{\sqrt{\int_{t-T}^{t+T} u_1^2(t')dt' \int_{t-T}^{t+T} u_2^2(t')dt'}} \ . \tag{2}$$

The integration is over a time interval with duration $2T$ and center time t. By computing this correlation coefficient for windows with a different center time t one can infer the velocity change of the medium between the recording of the waveforms $u_1(t)$ and $u_2(t)$. Coda wave interferometry is based on path summation, wherein the signal is decomposed into a sum over all scattering paths, and all possible mode conversions (Snieder, 1999; Snieder, 2002). When the medium changes, the travel time of the wave along each path changes. The cross-correlation reaches its maximum at a time that is given by the mean travel time change over all paths. This mean is weighted by the energy of each arrival in the path summation. In the absence of noise, the value $R_{\max}$ of the correlation coefficient at its maximum is related to the variance of the travel time perturbation, σ_t^2, by

$$R_{\max} = 1 - \frac{1}{2}\overline{\omega^2}\sigma_t^2 \ , \tag{3}$$

where the variance is computed with the energy of each arrival as weight for each arrival. The frequency $\overline{\omega^2}$ is given by

$$\overline{\omega^2} = \frac{\int_{t-T}^{t+T} \dot{u}^2(t')dt'}{\int_{t-T}^{t+T} u^2(t')dt'} \ . \tag{4}$$

We computed the time-shifted cross-correlation between the deconvolved waves in figure 1 for different pairs of ages. The location of the maximum of the time-shifted cross-correlation does not depart significantly from the unshifted position $\tau = 0$. This is the case for both the early part ($-4 < t < 0$ s) as well as for the later part ($0 < t < 4$ s) of the coda. This means that the velocity of wave propagation did not change with age.

Visual inspection of figure 2 shows that the deconvolved waveforms themselves do change with age. The zero-lag cross-correlation computed for the time interval $-2.5 < t < 7.5$ s of the deconvolved wave from age 1 with the deconvolved waves from the other ages is shown in table 1. The cross-correlation generally decreases with of table 1. The change in the source location, which is of the order of 15 m between age 1 and the later ages, should be taken with a grain of salt. The model of an isotropic source is fairly arbitrary, and the value of the P-velocity is not based on any measurement. A change in the location of the source of the pressure pulses over a distance of about 15 m over 1000 s is not unrealistically large when compared to the size of the conduits and magma chambers in a volcano. This means that the decorrelation of the deconvolved waveforms can readily be explained by a change in the source location.

The averaged pressure pulses in figure 4 show a secondary phase (indicated by arrows) that moves to later times with age. It is not clear how this secondary phase is generated. It may be generated by a reflected wave or by a resonance in the fluids or gasses that generate the pressure pulses. A change in the position of the source of the pressure pulses could change the excitation of the resonating modes, which could result in a change of the secondary phase in the source signal.

6 CONCLUSIONS

The deconvolution of the displacement with the pressure for the employed six ages leads to highly reproducible deconvolved waveforms. The deconvolution used here is a simple process that can be carried out automatically in real-time. This opens the possibility to conduct volcano monitoring based on coda wave interferometry without using an active source.

The deconvolved waveforms slowly change with age. Assuming that this change is caused by a change in the source position, and assuming that the source is an isotropic point source, the changed waveforms can be explained by a displacement in the source position of about 15 m. Although his number is not particularly accurate, its order of magnitude is small compared to the size of the interior structure of the volcano. If the employed interpretation is correct, then coda wave interferometry can be used to infer small changes in the location of the pressure pulses that are generated at active volcanoes.

ACKNOWLEDGMENTS

We appreciate the comments of Ken Larner. This work was supported by the NSF (grant EAR-0106668).

REFERENCES

Baisch, S., and G. Bokelmann, Seismic waveform attributes before and after the Loma Prieta earthquake: Scattering change near the earhtquake and temporal recovery, *J. Geophys. Res.*, *106*, 16,323–16,337, 2001.

Garcés, M., M. Hagerty, and S. Schwartz, Magma acoustics and time-varying melt properties at Arenal Volcano, Costa Rica, *Geophys. Res. Lett.*, *25*, 293–2296, 1998.

Hagerty, M., S. Schwartz, M. Garcés, and M. Protti, Analysis of seismic and acoustic observations at Arenal Volcano, Costa Rica, 1995-1997, *J. Volcanol. Geotherm. Res.*, *101*, 27–65, 2000.

Murase, T., and A. McBirney, Properties of common igneous rocks and their melts at high temperatures, *Geol. Soc. Am. Bull.*, *84*, 3563–3592, 1973.

Niu, F., P. Silver, R. Nadeau, and T. McEvilly, Migration of seismic scatterers associated with the 1993 Parkfield aseismic transient event, *Nature*, *426*, 544–548, 2003.

Ratdomopurbo, A., and G. Poupinet, Monitoring a temporal change of seismic velocity in a volcano: Application to the 1992 eruption of Mt. Merapi (Indonesia), *Geophys. Res. Lett.*, *22*, 775–778, 1995.

Snieder, R., Imaging and averaging in complex media, in *Diffuse waves in complex media*, edited by J. Fouque, pp. 405–454, Kluwer, Dordrecht, 1999.

Snieder, R., Coda wave interferometry and the equilibration of energy in elastic media, *Phys. Rev. E*, *66*, 046,615–1,8, 2002.

Snieder, R., Constraining relative source locations with the seismic coda, *Project Review of the Consortium Project on Seismic Inverse Methods for Complex Structures*, pp. 207–216, 2003.

Snieder, R., A. Grêt, H. Douma, and J. Scales, Coda wave interferometry for estimating nonlinear behavior in seismic velocity, *Science*, *295*, 2253–2255, 2002.

Vidale, J., and Y. Li, Damage to the shallow Landers fault from the nearby Hector Mine earthquake, *Nature*, *421*, 524–526, 2003.

Wegler, U., and B. Lühr, Scattering behaviour at Merapi volcano (Java) revealed from an active seismic experiment, *Geophys. J. Int.*, *145*, 579–592, 2001.

Wegler, U., B. Luhr, and A. Ratdomopurbo, A repeatable seismic source for tomography at volcanoes, *Ann. di Geofisica*, *42*, 565–571, 1999.

Monitoring rapid temporal change in a volcano with Coda Wave Interferometry

Alexandre Grêt[†], Roel Snieder[†] and Rick Aster[‡]

[†] *Department of Geophysics and Center for Wave Phenomena, Colorado School of Mines, CO 80401, USA*
[‡] *Department of Earth and Environmental Science, New Mexico Tech, Socorro, NM, USA*

ABSTRACT

Multiply scattered waves dominate the late part of the seismic coda. Small changes in a medium, which would have no detectable influence on the first arrivals, are amplified by the multiple scattering and may be seen readily in the coda. We exploit this idea using *Coda Wave Interferometry* to monitor temporal changes in the subsurface of the Mt. Erebus Volcano, Antarctica. Mt. Erebus is one of the few volcanoes known to have a convecting lava lake. The convection provides a repeating seismic source producing seismic energy that propagates through the strongly scattering geology in the volcano. Over a time period of two month, the first arrivals of the seismic waves are highly reproducible. Up to one month this is also the case for the coda. After that however, the seismic coda decorrelates rapidly. This indicates a rapid change in the subsurface of the volcano, a change that could not be detected by means of single scattered seismic waves.

Key words: velocity estimation, coda wave, multiple scattering, time-lapse, volcano monitoring

Introduction

The coda of a waveform consists of that part of the signal after the directly arriving phases (Aki, 1969; Aki & Chouet, 1975). At late times the coda is dominated by multiply scattered waves. Geophysical applications based on coda waves include earthquake prediction (Aki, 1985; Sato, 1986), earthquake-magnitude estimation (Lee *et al.*, 1972), volcano monitoring (Aki & Ferrazzini, 2000; Fehler *et al.*, 1998) and monitoring of temporal changes in the subsurface (Robinson, 1987; Chouet, 1979; Revenaugh, 1995; Poupinet *et al.*, 1984). Laboratory applications include Diffusive Wave Spectroscopy (Cowan *et al.*, 2002), reversed time imaging (Fink, 1997), and medical imaging (Li *et al.*, 1997).

Small changes in a medium, which would have no detectable influence on the first arrivals, are amplified by the multiple scattering and may be seen readily in the coda. We have previously exploited ultrasonic coda waves to study non-linear temperature dependence of velocity in granite (Snieder *et al.*, 2002). This nonlinearity is related to acoustic emissions during thermal cracking (Fredrich & Wong, 1986). In contrast to other methods which use multiply scattered energy, the phase information of the coda is a central part of our analysis. There are many other possible applications of this *Coda Wave Interferometry* in geophysics, including dam monitoring, time-lapse reservoir characterization, and rock physics.

The subsurface in the regions of volcanoes is highly inhomogeneous. Such highly scattering media are attractive for the study of multiply scattering of seismic waves (Wegler & Luehr, 2001). In this paper we show the application of Coda Wave Interferometry for monitoring changes in the subsurface of Mt. Erebus, Antarctica.

Mount Erebus, it's Eruptions and the Seismic Network

Mt. Erebus, Ross Island, Antarctica, is currently the most active volcano in Antarctica. The summit of Mt. Erebus contains a persistent convecting lava lake

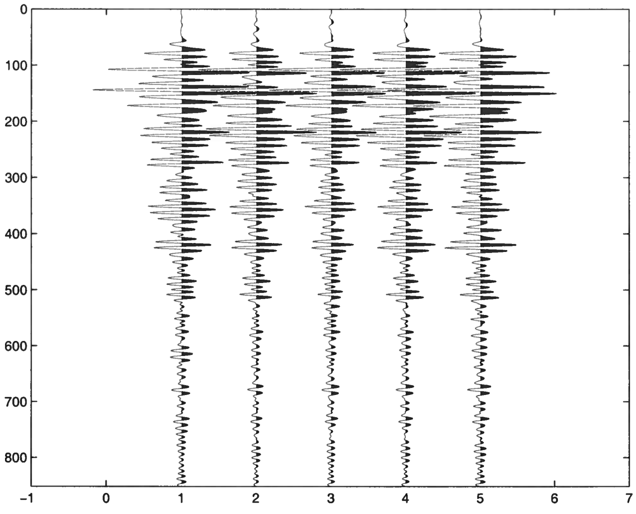

Figure 3. Five different events recorded at the broadband seismometer station E1S. Event one occurred on Dec. 12th, event two on Dec. 13th, event three on Dec. 14th and events four and five on Dec. 15th. Note how well the waveforms are reproducible over a time frame of days.

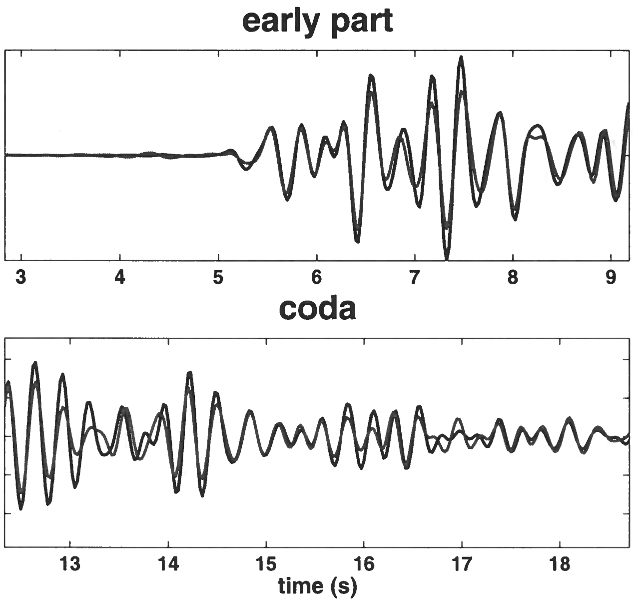

Figure 4. The top of the figure shows the early part of event one (red line) and event two (blue line), plotted on top of each other. The bottom of the figure shows the later part of the same events.

small to have an effect on the early part of the waveforms. In order to quantify the difference in waveforms, we compute maximum of the cross-correlation function for the early parts and the late parts respectively (Figure 6). In the top part of figure 6, the correlations for the early parts (source signature) stay high (around 0.9) over the whole two month period. For the later part of

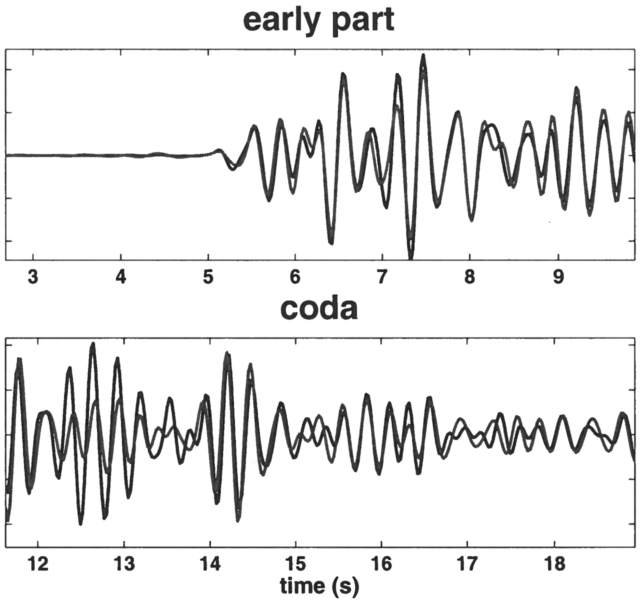

Figure 5. A plot similar to the previous one but the two events here occurred two weeks apart. The early parts still correlate extremely well but there is a larger difference in the late parts of the waveforms. We use this difference to monitor a change in the volcano. That change is too small to have an effect on the early part of the waveforms. In order to quantify the difference in waveforms, we compute the correlation coefficients for the early parts and the late parts respectively.

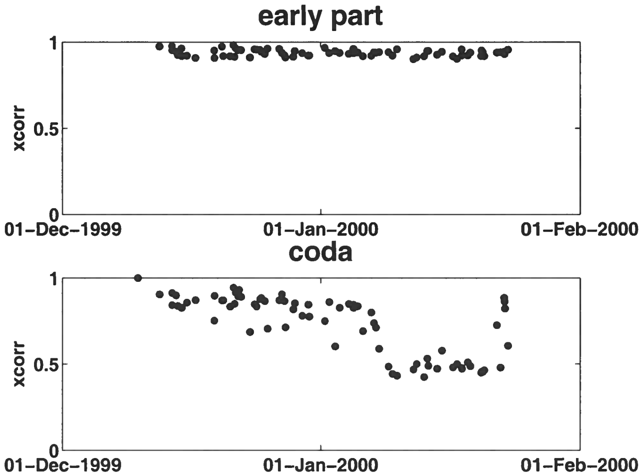

Figure 6. In the top of the figure the correlation coefficients for the early parts stay high (around 0.9) over the whole two month period. For the later part of the waveforms, however, the correlation coefficients have a sudden drop around the 8th of January 2000. This means, that around January 8 something has changed in the volcano that can't be seen in the early part of the waveforms.

REFERENCES

Aki, K. 1969. Analysis of seismic coda of local earthquakes as acattered waves. *J. Geophys. Res.*, **74**, 615–631.

Aki, K. 1985. Theory of earthquake prediction with special reference to monitoring of the quality factor of lithosphere by the coda method. *Earthquake Res. Bull.*, **3**, 219–230.

Aki, K., & Chouet, B. 1975. Origin of coda waves: Source, attenuation, and scattering effects. *J. Geophys. Res.*, **80**, 3322–3342.

Aki, K., & Ferrazzini, V. 2000. Seismic monitoring and modeling of an active volcano for prediction. *J. Geophys. Res*, **105**, 617–640.

Aster, R., Mah, S. Y., Kyle, P., McIntosh, W., Dunbar, N., Johnson, J., Ruiz, M., & McNamara, S. 2003. Very long period oscillations of Mount Erebus Volcano. *J. Geophys. Res.*, **108**.

Chouet, B. 1979. Temporal variation in the attenuation of earthquake coda near Stone Canyon, California. *Geophys. Res. Lett.*, **6**, 143–146.

Cowan, M. L., Jones, I. P., Page, J. H., & Weitz, D. A. 2002. Diffusing acoustic wave spectroscopy. *Physical Review E*, **65**, 066605–1–11.

Fehler, M., Roberts, P., & Fairbanks, T. 1998. A temporal change in coda wave attenuation observed during an eruption of Mount St. Helens. *J. Geophys. Res.*, **93**, 4367–4373.

Fink, M. 1997. Time reversed Acoustics. *Physics Today*, **20**, 34–40.

Fredrich, J.T., & Wong, T. 1986. Micromechanics of thermally induced cracking in three crustal rocks. *J. Geophys. Res.*, **91**, 12743–12764.

Lee, W. H. K., Bennett, R. E., & Meagher, K. L. 1972. A method of estimated magnitude of local earthquakes from signal duration. *U.S. Geol. Surv. Open File Report.*

Li, X., Durduran, T., Chance, B., Yodh, A.G., & Pattanayak, D. 1997. Diffraction Tomography for Biomedical Imaging with Diffuese-photon Density Waves. *Optic Letters*, **22**, 573–75.

Poupinet, G., Ellsworth, W.L., & Frechet, J. 1984. Monitoring Velocity Variations in the Crust Using Earthquake Doublets: an Application to the Calaveras Fault, California. *J. Geophys. Res.*, **89**, 5719–5731.

Revenaugh, J. 1995. The Contribution of Topographic Scattering to Teleseismic Coda in Southern California. *Geophys. Res. Lett.*, **22**, 543–546.

Robinson, R. 1987. Temporal variations in coda duration of local earthquakes in the Wellington region, New Zealand. *Pure Appl. Geophys.*, **125**.

Rowe, C., Aster, R., Schlue, R. Kyle P., & Dibble, J. 1998. Broadband recording of Strombolian explosions and associated very-long-period seismic signals on Mount Erebus volcano, Ross Island, Antarctica. *Geophys. Res. Lett.*, **25**, 2297–2300.

Sato, H. 1986. Temporal change in attenuation intensity before and after the eastern Yamanashi earthquake of 1983 in central Japan. *J. Geophys. Res.*, **91**, 2049–2061.

Snieder, R., Grêt, A., Douma, H., & Scales, J. 2002. Coda Wave Interferometry for Estimating Nonlinear Behavior in Seismic Velocity. *Science*, **295**, 2253–2255.

Wegler, U., & Luehr, B. 2001. Scattering behaviour at Merapi volcano (Java) revealed from an active seismic experiment. *Geophysical Journal International*, **147**, 579–592.

Inverse multiple scattering in the downward continuation approach: Preface

Alison E. Malcolm and Maarten V. De Hoop

Moses (1956) constructed a series to represent the quantum scattering potential in terms of measured reflection coefficents. Razavy (1975) extended this work to scalar wave scattering. These two papers show that it is formally possible to represent both the data as a series in the medium contrast (forward series) and the medium contrast as a series in the data (inverse series). In seismology the second series has been exploited by several authors to represent the medium contrast, or reflectors, as a series in the data. Taking only the first term of this series leads to the Born approximation. The analysis of the forward and inverse series in truly incomplete. For example, in general the series are not identifiable as Neumann series. Only for very simple obstacle scattering problems have properties of the forward series been proven. (There is a much better developed theory for the Schrödinger equation.) As a starting point for our approach we use the generalized Bremmer series as a forward series. De Hoop (1996) proved that this series is identifiable as a Neumann series. The first term of the generalized Bremmer series models seismic reflection data in the downward-continuation approach [with the double-square-root (DSR) equation]. Here, we develop a theory for inverse multiple scattering using the third term of a hybrid series derived from the generalized Bremmer series and the Lippmann-Schwinger series.

Fokkema and Van den Berg (1993) developed a rigorous theory for the suppression of surface-related-multiples. Their approach admits a series expansion in terms of the reflection data that is close to the inverse scattering series approach of Weglein (1997). Weglein (1997; 2003) has also used these ideas in an attempt to attenuate internal multiples in 1D along with a restricted class of 2D velocity models. Ten Kroode (2002) describes in more detail the theory underlying Weglein's approach and highlights some its fundamental limitations. One of the goals in our approach is to remove some of the limitations explained by Ten Kroode. For the sake of simplicity, we also focus on contributions from singly and triply scattered waves, though the extension to higher order is straightforward.

Weglein and ten Kroode use the Lippmann-Schwinger series to model triply scattered data. In that approach, ten Kroode makes the assumption that each scattering results in a change in direction between the incoming and outgoing waves. In other words, he enforces that the first scatter is strictly below the second scatter which is strictly above the third scatter. To encorporate this assumption naturally in the formulation of the problem, we construct a hybrid series between the Lippmann-Schwinger series and the Bremmer series. The Bremmer series has the advantage that it directly splits the wavefield into its up- and down-going constituents. In addition, the convergence properties on the Bremmer series (de Hoop, 1996) justify the truncation of the series after only a few terms. The Lippmann-Schwinger series alone is not even assymptotic (though for surface-related multiples it can be identified as a convergent series).

In his work, ten Kroode (2002) has to make two essential simplifying assumptions. The first is that there are no caustics in the wavefield. In our formulation we find it necessary to exclude only turning rays; this is necessary because the downward-continuation approach removes horizontally traveling waves. The second assumption is his so-called *traveltime monotonicity assumption*. This assumption requires, essentially, that the traveltime increase monotonically with depth. In other words, if primary energy arrives later in the data it must have come from a deeper reflector. As ten Kroode points out in his paper it is not difficult to violate this assumption.

In the absence of caustics and if the traveltime monotonicity assumption is valid, the work presented in the following paper reduces easily to the results of ten Kroode and thus Weglein. Our implementation is truly different, however, as we use the DSR equation explicitly. An advantage of using the DSR approach is that there are no artifacts in the image domain (de Hoop *et al.*, 2003b). When there are caustics and the traveltime monotonicity

CWP-486

Inverse multiple scattering in the downward continuation approach

Alison E. Malcolm and Maarten V. De Hoop
Center for Wave Phenomena, Colorado School of Mines

ABSTRACT
Imaging with seismic data is typically done in the single-scattering approximation. We move beyond this assumption to allow for triply scattered waves in the imaging process. We develop a scattering series that is a hybrid of the Lippmann-Schwinger scattering series and the Bremmer coupling series. From the third term of this hybrid series an approximation of data scattered three times is constructed. From the inverse hybrid series it is also evident that subtracting an image constructed from triply scattered data from an image constructed assuming singly scattered data results in an image that is third-order in the data. This is in contrast to the standard first-order approximation. We discuss both a standard inverse scattering operator and the wave equation angle transform as possible imaging techniques.

Key words: internal multiples, Bremmer series, Lippmann-Schwinger series

1 INTRODUCTION

In a seismic experiment, the source generates both compressional and shear waves that travel through the subsurface reflecting at discontinuities in the medium properties. These waves are then recorded at the surface. A collection of such experiments, recorded as a function of source position, receiver position, and time make up seismic data. It is generally assumed in seismic imaging that the recorded signals have reflected only once between the source and receiver. The goal of this paper is to move beyond this assumption to allow for waves which have scattered three times to be included in seismic imaging. Here, we consider only compressional waves and back scattering; i.e., sources and receivers are on the same surface. Although we discuss only the case of triple scattering, the extension to any finite odd-order scattering is straightforward. Constructing even-order scattered waves is fundamentally different, for a reflection experiment, because transmission in addition to reflection must be considered.

We use a series derived from the Lippmann-Schwinger-Dyson equation; this framework gives us both a forward and an inverse series representation. We also make use of the generalized Bremmer series (de Hoop, 1996), which is a forward series that splits the wavefield into its up- and down-going constituents. From these two series, we develop a hybrid between the Lippmann-Schwinger and Bremmer series. The hybrid series uses the directional decomposition of the Bremmer series along with the Lippmann-Schwinger medium decomposition into a known, smooth reference and unknown, singular perturbation. This allows us to trace waves through their up and down scatters while still preserving the contrast source formulation of the Lippmann-Schwinger construction. From the third term of the forward series, we model the triply scattered data. The third term of the inverse series describes the third-order (in the data) contribution to the image. We use the volume scattering framework as in Bremmer rather than the surface scattering model of Lippmann-Schwinger. We make this choice because de Hoop (2004) has shown that the downward continuation approach tended their work on surface-related multiples to suppress internal multiples generated at a single layer in the subsurface, given the medium parameters above the particular layer. Weglein and others (Weglein *et al.*, 1997; Weglein *et al.*, 2003) have used the Lippmann-Schwinger series to model and process seismic data, including the suppression of both surface-related and internal multiples. In ten Kroode (2002) the theory behind this approach is given in both one and two dimensions. He extends the work of Weglein *et al.* to a two-dimensional subsurface model satisfying two conditions: ten Kroode's traveltime monotonicity assumption, and the condition that the wavefield does not contain caustics. The work of Berkhout and Verschuur (1997) extends, via layer stripping, from the surface-related multiple case to that of internal multiples. Jakubowicz (1998) proposes a method for modeling internal multiples by correlating one primary reflection with the convolution of two other primary reflections. When the two assumptions of ten Kroode are satisfied, our method can be reduced to this construction with the addition of a time-windowing procedure; this is discussed further in remark 7.1. Kelamis *et al.* (2002) use an approach similar to Jakubowicz, in which the multiples are constructed from a combination of different data sets, both at the surface and in the subsurface. Van Borselen (2002), provides another extension of the surface-related multiple-attenuation algorithm proposed by Fokkema and van den Berg (1993) to the case of internal multiples. His method removes internal multiples by identifying either the shallowest layer involved in the multiple generation or a pseudo-boundary through which the multiples are assumed to have passed. The surface-related multiple attenuation method is then applied at the identified layer. In any method that predicts the internal multiples and subtracts them, an adaptive subtraction technique such as that suggested by Guitton (2004) must be used to compensate for illumination effects in the predicted multiples.

Many signal-processing methods are also available for suppressing multiples. The work of Buttkus (1979), which uses the different apparent stacking velocities for multiples and primaries, is an example of such filtering in the data domain. Sava and Guitton (2004) show how such techniques can be applied in the image domain. Symes (1999) provides a method of velocity analysis that also suppresses multiples through a data perturbation applied to remove events in the data that do not fit the assumptions used in generating a velocity model. Another approach, described by Essenreiter *et al.* (2001), uses computer learning to predict which events in the data are multiples given an initial set of identified primary and multiple events.

Although we are primarily concerned with the inverse problem, we discuss also the forward problem of modeling multiples. Since we are concerned here with the propagation of singularities, we construct only the most singular part of each term in the hybrid Lippmann-Schwinger-Bremmer series. From the third term of this series, we specifically construct distributions to model triply scattered data. These modeled data are used in the formulation of the inverse problem. The modeled data are needed in our approach since we construct the inverse problem through the prediction and subtraction of the triply scattered data in the image domain. The theory presented here does not account for multiple scattering from large numbers of fine layers. Instead, we assume a finite collection of scatterers with a separation large compared to the wavelength.

The work presented here is motivated by that of Razavy (1975) and Aminzadeh (1981). Razavy developed a method to estimate the wave velocity from reflection coefficients, with a series approach to the inverse problem. Aminzadeh used a Bremmer series approach to suppress surface-related multiples. In our hybrid series, we use the techniques from the generalized Bremmer series (de Hoop, 1996), although we remain in the framework of the Lippmann-Schwinger series as discussed by ten Kroode (2002). In this methodology we allow for lateral variation of the background velocity, as well as the presence of caustics. We require knowledge of the velocity model to the depth of the shallowest reflector involved in the triple scattering, and our approach to the suppression of multiples is applied in the image domain rather than the data domain. This is preferred as it allows for compensation of variations in illumination, which is different for triply scattered waves than for singly scattered waves. A by-product of the construction developed here is the prediction of internal multiples from subsets of the data.

In the next section we describe the techniques of the directional decomposition used in the Bremmer series. In the third section, we describe some of the details of the construction of one-way Green's functions. Following this we describe the contrast-source method used for the Lippmann-Schwinger series. In the fifth section, we construct the hybrid series. In the sixth section we use the hybrid series to model data, giving the first of our two main results in (89). Following this, we describe the methodology for the inverse series arriving at our second result, (113). In the final section we illustrate through isochrons how the propagation of integral form this is

$$u'_+ \quad = \int_{-\infty}^{z} G'_+(z,z_0) f_+(z_0)\, \mathrm{d}z_0 \qquad (11)$$

$$u'_- \quad = \int_{z}^{\infty} G'_-(z,z_0) f_-(z_0)\, \mathrm{d}z_0\,.$$

3 THE GREEN FUNCTION

In the previous section, we diagonalized the wave equation into two first-order equations. To do this, we implicitly assumed that the diagonal system is equivalent to the original equation. This is nearly the case, but the choice of a preferential direction alters the ability of the system to propagate singularities in directions orthogonal to the preferred direction. Here, we have chosen the vertical direction as the preferential direction and are thus unable to propagate singularities horizontally. To ensure that the diagonal system does not propagate singularities incorrectly, we need to attenuate the horizontally propagating singularities. The details of the method are given by Stolk and de Hoop (2004a); we give only a brief description here.

In order to identify horizontal propagation, we define the phase angle $\theta = \arcsin(c(z,x)\|\tau^{-1}\xi\|)$, where (ζ,ξ) is the cotangent vector associated with (z,x) and $c(z,x)$ is the velocity. Note that if the angle θ, is less than $\pi/2$ on a ray segment, the vertical velocity $\frac{\mathrm{d}z}{\mathrm{d}t}$ does not change sign, allowing the parameterization of the ray segment by z. Thus, for any ray segment and any given angle $\theta < \pi/2$, we can define a maximal interval,

$$(z_{\min,\pm}(z,x,\xi,\tau,\theta), z_{\max,\pm}(z,x,\xi,\tau,\theta))\,, \qquad (12)$$

for which the propagation away from a particular point (z,x,ξ,τ) can be parameterized by z. In Figure 1, the interval $(z_{\min,-}, z_{\max,-})$ is illustrated; it is the maximal interval containing the point (z,x) such that the angle of the ray with the vertical, θ, does not exceed a given value; in this case that value is θ_2.

The angle θ can be given physical meaning by looking at the ray picture, as is done in Figure 1. The wave equation is solved in all of phase space, however, which means that any restrictions we put on the wave operator must be done in all of phase space. To this end we introduce the set

$$I_\theta = \{(z,x,t,\zeta,\xi,\tau) \mid \arcsin(c(z,x)\|\tau^{-1}\xi\|) < \theta, |\zeta| < C|\tau|\}, \qquad (13)$$

illustrated in Figure 2, where C is some constant everywhere larger than $c(z,x)^{-1}$. Finally, we construct the sets

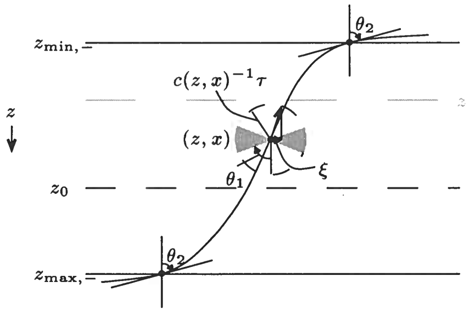

Figure 1. Removing horizontal propagations. The symbol of the cut-off operator ψ is one up to an angle of θ_1 and then tapers smoothly to zero at the angle θ_2. This removes all propagation at angles larger than θ_2.

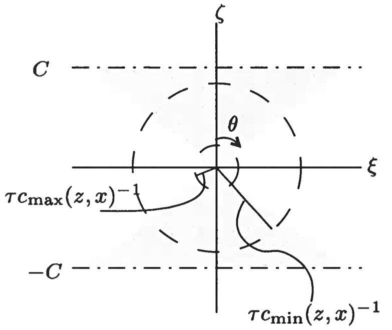

Figure 2. Illustration of I_θ. The shaded region represents the ray directions in the set. The minimum velocity in the region is c_{min} and the maximum is c_{max}.

$$J_-(z_0,\theta) \quad = \{(z,x,t,\zeta,\xi,\tau) \in I_\theta \mid \tau^{-1}\zeta < 0 \text{ and } z_{\max,-}(z,x,\xi,\tau,\theta) \geq z_0\}, \qquad (14)$$

and

$$J_+(z_0,\theta) \quad = \{(z,x,t,\zeta,\xi,\tau) \in I_\theta \mid \tau^{-1}\zeta > 0 \text{ and } z_{\max,+}(z,x,\xi,\tau,\theta) \geq z_0\}, \qquad (15)$$

which exclude all parts of phase space in which singularities propagate horizontally. Figure 1 illustrates the set $J_-(z_0,\theta_2)$, considering the shaded region as excluded from the set. The condition $z_{\max,-}(z,x,\xi,\tau,\theta) \geq z_0$, along with the implicit requirement that $z_{\min,-} < 0$ ensure that the two points between which one propagates the wavefield are within the allowed propagation interval $(z_{\min,-}, z_{\max,-})$.

The sets $J_\pm$ describe the portions of phase space that must be excluded to remove horizontally propagating singularities. To actually remove singularities from these regions, we define a pseudodifferential cutoff $\psi_{-,1} = \psi_{-,1}(z,z_0,x,D_x,D_t)$

In contrast, S_{+-} and S_{-+} are interpreted as reflection operators because they govern scatterings that result in a change of direction; from up-going to down-going and down-going to up-going respectively. (The the off-diagonal entries in the V operator matrix are true adjoints of one another whereas the diagonal entries are adjoints only to principal parts.)

To simplify the notation, we define

$$P_0 = \partial_z + \mathsf{B}_0\,, \tag{32}$$

its forward parametrix†,

$$\mathsf{L}_0 = \begin{pmatrix} G_+ & 0 \\ 0 & G_- \end{pmatrix} \tag{33}$$

recalling

$$V = \mathsf{Q}(z)\ \delta\mathsf{A}\ \mathsf{Q}^{-1}(z)\,. \tag{34}$$

In this notation, (29) reduces to

$$P_0\ \delta U = -VU\,, \tag{35}$$

or

$$\delta U = -\mathsf{L}_0(VU)\,. \tag{36}$$

The V operator is a multiplication along with a time derivative, whereas L_0 is the forward parametrix of a partial differential operator. Therefore the composition VU is a Volterra product. Writing $U = U_0 + \delta U$ gives

$$\delta U = -\mathsf{L}_0(VU_0) - \mathsf{L}_0(V\delta U)\,, \tag{37}$$

or equivalently,

$$(I + \mathsf{L}_0\ V)\ \delta U = -\mathsf{L}_0(VU_0)\,. \tag{38}$$

In analogy with (24), we introduce $\widehat{V}$, the matrix of $S_{\pm\pm}$ coefficients, viz,

$$V(z, x, D_t) = \widehat{V}(z, x)D_t^2, \tag{39}$$

which gives

$$(I + D_t^2 \mathsf{L}_0\ \widehat{V})\ \delta U = -D_t^2 \mathsf{L}_0(\widehat{V}U_0)\,, \tag{40}$$

where $\widehat{V}\delta U$ and $\widehat{V}U_0$ are products of distributions. This is the resolvent equation in our hybrid Lippmann-Schwinger-Bremmer formulation. (See (Yoshida, 1995) for details on resolvent equations.)

5 SCATTERING SERIES

5.1 Forward series

Having recognized (40) as a resolvent equation, we set up the recursion

$$\delta U = \sum_{m\in\mathbb{N}} (-1)^m \delta U_m(\widehat{V})\,, \tag{41}$$

where

$$\delta U_1(\widehat{V}) = D_t^2 \mathsf{L}_0(\widehat{V}U_0), \quad \text{and} \quad \delta U_m(\widehat{V}) = D_t^2 \mathsf{L}_0(\widehat{V}\delta U_{m-1}(\widehat{V})). \tag{42}$$

This recursion is motivated by the Neumann series. The expressions in (41) and (42) are not quite in the form of observables however; data are acquired only at the Earth's surface, but the L_0 operator models data arriving at all depth levels. We therefore define a restriction operator, R, which restricts the operator L_0 to the acquisition surface, $z = 0$. To avoid difficulties with the free boundary at the surface we will assume that the medium contrast, contained in V, has its support away from $z = 0$. In addition, (42) is in the diagonal system; to return to the 'true' coordinate system in which we make observations we must also apply the Q^{-1} operator to the expression for δU. We thus rewrite (41)

$$R\mathsf{Q}^{-1}\delta U = \sum_{m\in\mathbb{N}} (-1)^m R\mathsf{Q}^{-1}\delta U_m(\widehat{V})$$

where $R\mathsf{Q}^{-1}\delta U_1 = D_t^2 \mathsf{M}_0(\widehat{V}U_0)$, and

$$R\mathsf{Q}^{-1}\delta U = -D_t^2 \mathsf{M}_0(\widehat{V}(U_0 + \sum_{m\in\mathbb{N}} (-1)^m \delta U_m(\widehat{V})), \tag{43}$$

upon introducing the operator $\mathsf{M}_0 = R\mathsf{Q}^{-1}\mathsf{L}_0$. The composition $R\mathsf{L}_0$ is transversal provided there are no grazing rays (Stolk & de Hoop, 2000), which are already excluded by the ψ_1 cut-off. The composition with Q^{-1} also does not change the properties of the composite operator provided we satisfy the assumption in the generalized Bremmer series (de Hoop, 1996). Note that the recursion in (43) gives an expression for the data at the surface in terms of the unrestricted data from the previous term; the restriction is applied after the recursion is constructed.

For the leading-order, single scattering term we introduce the shorthand notation

$$d_1 = -R\mathsf{Q}^{-1}\delta U_1(\widehat{V}) = F(\widehat{V}) = -D_t^2 \mathsf{M}_0(\widehat{V}U_0). \tag{44}$$

Note that d_1 describes only the singly scattered part of the data. The operator F is the usual Born modeling operator. We can construct a left inverse to F, by $N^{-1}F^*$, where $N = F^*F$ is the normal operator, which is elliptic pseudodifferential under the DSR assumption of Stolk and de Hoop (2004a), and F^* is the adjoint of the modeling operator, i.e., the imaging/migration operator. This gives the estimate

$$\widehat{V}_1 = N^{-1}F^*(d_1), \tag{45}$$

---

† The parametrix of an operator is an asymptotic approximation to its inverse.

resentation is suggested for quantum mechanical problems by Moses (1956), where the analogue of (48) is his equation (3.12). It is also suggested by Razavy (1975) for wave problems, in which the analogue of (48) is his equation (33).

Substituting (48) into (41) yields a recursion for $\widehat{V}_m$ in terms of δU

$$\begin{aligned}
\delta U &= -D_t^2 \mathsf{L}_0(\widehat{V}_1 U_0) && (49)\\
0 &= -D_t^2 \mathsf{L}_0(\widehat{V}_2 U_0) + D_t^4 \mathsf{L}_0(\widehat{V}_1 \mathsf{L}_0(\widehat{V}_1 U_0)) && (50)\\
0 &= -D_t^2 \mathsf{L}_0(\widehat{V}_3 U_0) + D_t^4 \mathsf{L}_0(\widehat{V}_2 \mathsf{L}_0(\widehat{V}_1 U_0))\\
&\quad + D_t^4 \mathsf{L}_0(\widehat{V}_1 \mathsf{L}_0(\widehat{V}_2(U_0)))\\
&\quad - D_t^6 \mathsf{L}_0(\widehat{V}_1 \mathsf{L}_0(\widehat{V}_1 \mathsf{L}_0(\widehat{V}_1 U_0)))\,, && (51)
\end{aligned}$$

etc.

Substituting (48) into (43) yields a recursion for V_m in terms of the true data d

$$\begin{aligned}
d &= -D_t^2 \mathsf{M}_0(\widehat{V}_1 U_0) && (52)\\
0 &= -D_t^2 \mathsf{M}_0(\widehat{V}_2 U_0) + D_t^4 \mathsf{M}_0(\widehat{V}_1 \mathsf{L}_0(\widehat{V}_1 U_0)) && (53)\\
0 &= -D_t^2 \mathsf{M}_0(\widehat{V}_3 U_0) + D_t^4 \mathsf{M}_0(\widehat{V}_2 \mathsf{L}_0(\widehat{V}_1 U_0))\\
&\quad + D_t^4 \mathsf{M}_0(\widehat{V}_1 \mathsf{L}_0(\widehat{V}_2(U_0)))\\
&\quad - D_t^6 \mathsf{M}_0(\widehat{V}_1 \mathsf{L}_0(\widehat{V}_1 \mathsf{L}_0(\widehat{V}_1 U_0)))\,, && (54)
\end{aligned}$$

etc.

Equation (54) can be simplified using (50), since $D_t^2 \mathsf{M}_0(\widehat{V}_2 U_0)$ and $D_t^4 \mathsf{M}_0(\widehat{V}_1 \mathsf{L}_0(\widehat{V}_1 U_0))$ are identical distributions and $D_t^2 \mathsf{M}_0 \widehat{V}_1$ is a linear operator, to read

$$D_t^2 \mathsf{M}_0(\widehat{V}_3 U_0) = D_t^4 \mathsf{M}_0(\widehat{V}_2 \mathsf{L}_0(\widehat{V}_1 U_0))\,. \qquad (55)$$

Solving these recursions for $\widehat{V}$ gives a solution for the medium contrast. The first term in the series, given in (52), models singly scattered data. The third term, in (54), models first-order internal multiples as well as other primary events. (The second term, given in (53), models, among other things, primary events.) We have the following relation between the $\widehat{V}_j = \widehat{V}_j(d)$

$$\begin{aligned}
D_t^2 \mathsf{M}_0(\widehat{V}_2 U_0) &= D_t^4 \mathsf{M}_0(\widehat{V}_1 \mathsf{L}_0(\widehat{V}_1 U_0))\\
&= -D_t^2 \mathsf{M}_0(\widehat{V}_1 \delta U)\,, && (56)\\
D_t^2 \mathsf{M}_0(\widehat{V}_3 U_0) &= D_t^4 \mathsf{M}_0(\widehat{V}_2 \mathsf{L}_0(\widehat{V}_1 U_0))\\
&= -D_t^2 \mathsf{M}_0(\widehat{V}_2 \delta U) && (57)\\
D_t^2 \mathsf{M}_0(\widehat{V}_j U_0) &= -D_t^2 \mathsf{M}_0(\widehat{V}_{j-1} \delta U). && (58)
\end{aligned}$$

The general term in the recursion (58) follows because higher order terms are built from lower-order terms through the application of additional operators of the form $\mathsf{M}_0 \widehat{V}_i$ to the $(j-i)^{\text{th}}$-order terms to form terms of order j. Thus the sum of terms of order j will contain sub-series of the form

$D_t^2 \mathsf{M}_0 \widehat{V}_1$(sum of terms of order $j-1$ from (49-51)),

$D_t^2 \mathsf{M}_0 \widehat{V}_2$(sum of terms of order $j-2$ from (49-51)),

etc. For $j \geq 2$ the sub-series in brackets sum to zero because of the zero on the left-hand side of (50). Thus, the only terms of order j remaining in the series are of the form

$D_t^2 \mathsf{M}_0 \widehat{V_j} U_0$

and

$D_t^4 \mathsf{M}_0 \widehat{V}_{j-1} \mathsf{L}_0 \widehat{V}_1$,

from which the general term (58) follows. Note the similar structure between (58) and (42); (58) constructs the medium contrast in terms of the data, while (42) constructs the data in terms of the medium contrast.

From these relations, we deduce that the only inverse operator we need is $N^{-1}F^*$. Using this we can write the $\widehat{V}$-series as

$$\widehat{V} = N^{-1}F^* d - N^{-1}F^* \left(\sum_{m \in \mathbb{N}} \mathsf{M}_0(\widehat{V}_m \delta U) \right). \qquad (59)$$

We identify the series in the second term as a correction to the first term, which is the single scattering inverse. Additionally, $N^{-1}F^*$ can be replaced with A_{WE}, the wave equation angle transform (Stolk & de Hoop, 2004b), which computes an image $\Psi\widehat{V}(z,x,p)$, where $p = \tau^{-1}\xi$ is the horizontal slowness. An accurate reconstruction of $\Psi\widehat{V}(z,x,p)$ will be independent of p; this property can be exploited to improve the knowledge of the smooth background medium. The pseudodifferential operator Ψ corrects for illumination effects in the reconstruction of $\widehat{V}$; we cannot reconstruct a portion of the image, $\widehat{V}(z_0,x_0,p_0)$, for example, if the data do not scatter from the point (z_0,x_0) with slowness p_0.

Solving (56) for $\widehat{V}_2$ gives

$$\widehat{V}_2 = N^{-1}F^*(D_t^4 \mathsf{M}_0(\widehat{V}_1 \mathsf{L}_0(\widehat{V}_1 U_0))) = D_t^2 \widehat{V}_1 \mathsf{L}_0 \widehat{V}_1\,. \qquad (60)$$

This allows us to simplify (55) to

$$D_t^2 \mathsf{M}_0(V_3 U_0) = D_t^6 \mathsf{M}_0(V_1 \mathsf{L}_0(V_1 \mathsf{L}_0(V_1 U_0)))\,. \qquad (61)$$

In the above we have nowhere assumed the absence of caustics in the wavefield. In fact, thus far we have made only the DSR assumption (Stolk & de Hoop, 2004a) excluding horizontal propagation.

6 MODELING

6.1 Single scattering to double square-root

The first term in the forward scattering series given in (41) can be used to construct data in the

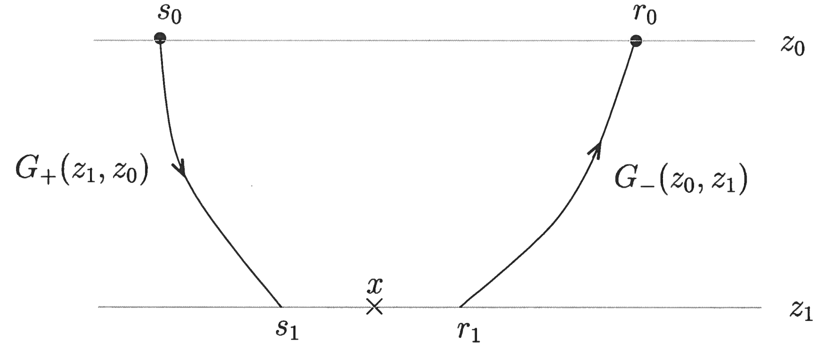

Figure 5. Notation and conventions.

To write (67) in terms of the Green function for the double-square-root equation, there must be integrations in (x_1, t_1) for each of the Green functions. To introduce these integrations we introduce two extension operators

$$E_1 : u(z, x) \mapsto \delta(r - s)u(z, \tfrac{r+s}{2}), \tag{68}$$

$$E_2 : u(z, r, s) \mapsto \delta(t)u(z, r, s). \tag{69}$$

These operators map the medium contrast, a, into data. They also apply the adjoint imaging condition, namely assuring that the two rays meet at the scattering point at time 0. The δ-functions allow the splitting of the single integration joining the two G_- operators into two integrals. This allows the two Green functions to both act on these data as we expect intuitively; each Green function continues the data from the subsurface to the surface. This condition is illustrated in Figure 5. With these operators, we re-write (67)

$$\begin{aligned}(F\widehat{V})(s_0, r_0, t_{r_0} - \tilde{t}_{s_0}) = \tfrac{1}{4}D^2_{t_{r_0}} \int_0^\infty \mathrm{d}z_1 \int \mathrm{d}s_1 \int \mathrm{d}r_1 \int_{\mathbb{R}_+} \mathrm{d}t_0 \int_{\mathbb{R}_+} \mathrm{d}t_1 Q^*_{-,r_0}(0) G_-(0, r_0, t_{r_0} - t_1 - t_0, z_1, r_1) Q_{-,r_1}(z_1) \\ Q^*_{-,\tilde{s}_0}(0) G_-(0, \tilde{s}_0, \underline{t_1 - \tilde{t}_{s_0}}, z_1, s_1, 0) Q_{-,s_1}(z_1)(E_1E_2a)(z_1, s_1, r_1, t_0) \,.\end{aligned} \tag{70}$$

We note that the two one-way Green's functions are connected through time convolution. To make this explicit we change integration variables from t_1 to $t' = t_1 - \tilde{t}_{s_0}$ (the underlined expression in (70)), giving

$$\begin{aligned}(F\widehat{V})(\tilde{s}_0, r_0, t_{r_0} - \tilde{t}_{s_0}) = \tfrac{1}{4}D^2_t \int_0^\infty \mathrm{d}z_1 \int \mathrm{d}s_1 \int \mathrm{d}r_1 \int_{\mathbb{R}_+} \mathrm{d}t_0 \int_{\mathbb{R}_+} \mathrm{d}t' Q^*_{-,r_0}(0) G_-(0, r_0, t_{r_0} - \tilde{t}_{s_0} - t' - t_0, z_1, r_1) Q_{-,r_1}(z_1) \\ Q^*_{-,\tilde{s}_0}(0) G_-(0, \tilde{s}_0, t', z_1, s_1) Q_{-,s_1}(0)(E_1E_2a)(z_1, s_1, r_1, t_0) \,.\end{aligned} \tag{71}$$

To write (71) in terms of the Green function for the double square-root operator, we first re-arrange terms giving

$$\begin{aligned}(F\widehat{V})(\tilde{s}_0, r_0, t_{r_0} - \tilde{t}_{s_0}) = \tfrac{1}{4}D^2_t Q_{-,r_0}(0) Q^*_{-,\tilde{s}_0}(0) \int_0^\infty \mathrm{d}z_1 \int \mathrm{d}s_1 \int \mathrm{d}r_1 \int_{\mathbb{R}_+} \mathrm{d}t_0 \\ \left\{\int_{\mathbb{R}_+} \mathrm{d}t' G_-(0, r_0, t_{r_0} - \tilde{t}_{s_0} - t' - t_0, z_1, r_1) G_-(0, \tilde{s}_0, t', z_1, s_1)\right\} \\ Q_{-,r_1}(z_1) Q_{-,s_1}(z_1)(E_1E_2a)(z_1, s_1, r_1, t_0) \,.\end{aligned} \tag{72}$$

We then introduce the operator $H(z_0, z_1)$, for $z_1 > z_0$, as

$$(H(z_0, z_1))(s_0, r_0, t - t_0, s_1, r_1) = \int_{\mathbb{R}_+} (G_-(z_0, z_1))(r_0, t - t' - t_0, r_1)(G_-(z, z_0))(s_0, t', s_1) \,\mathrm{d}t' \,. \tag{73}$$

Following the diagram in Figure 6, we see that the first scattering of the internal multiple, from s_0 through s_2, r_2 to m_r is nearly identical to the single scattering case. We cannot use the H operator however, since the second leg (from r_2 to m_r) does not reach the surface. Thus, we define

$$\delta u_{-,1}(z_1, m, t_a, 0, s_0, t_{s0}) = \tfrac{1}{4} D_{t_a}^2 \int \mathrm{d}\tilde{s}_0 \int_{\mathbb{R}_+} \mathrm{d}\tilde{t}_{s0} \int_{z_1}^{\infty} \mathrm{d}z_2 \int \mathrm{d}s_2 \int \mathrm{d}r_2 \int_{\mathbb{R}_+} \mathrm{d}t_0 \int_{\mathbb{R}_+} \mathrm{d}t' G_-(z_1, m, t_a - \tilde{t}_{s0} - t' - t_0, z_2, r_2)$$
$$G_-(0, \tilde{s}_0, t', z_2, s_2) Q_{-,r_2}(z_2) Q_{-,s_2}(z_2)\ (E_1 E_2 a)(z_2, s_2, r_2, t_0) Q^*_{-,\tilde{s}_0}(0) f(0, \tilde{s}_0, \tilde{t}_{s0}, 0, s_0, t_{s0}), \quad (75)$$

where $t' = t_1 - \tilde{t}_{s0}$ and t_a is the total time traveled along the ray (see Figure 7). In (75), we have applied the R operator to restrict the source to $z_0 = 0$, but have not returned to observables as the second leg, $G_-(z_1, m, t_a - \tilde{t}_{s0} - t' - t_0, z_2, r_2)$, does not reach the surface. The field, δu_1 acts as the source of waves for propagation from m_s to s_3, through the contrast source formulation used in the single-scattering case. This gives,

$$\delta u_{+,2}(z_3, x_3, t_3, 0, s_0, t_{s0}) = \tfrac{\mathrm{i}}{2} D_{t_3}^2 \int_{z_0}^{z_3} \mathrm{d}z_1 \int \mathrm{d}m \int_{\mathbb{R}_+} \mathrm{d}t_a$$
$$G_+(z_3, x_3, t_3 - t_a, z_1, m) Q_{+,m}(z_1) a(z_1) Q^*_{-,m}(z_1) \delta u_{-,1}(z_1, m, t_a, 0, s_0, t_{s0}), \quad (76)$$

which acts as a contrast source for the final ray, connecting r_3 with r_0,

$$d_3(s_0, r_0, t_4 - t_{s0}) = -\tfrac{\mathrm{i}}{2} D_{t_4}^2 Q^*_{-,r_0}(0) \int_0^{\infty} \mathrm{d}z_3 \int \mathrm{d}x_3 \int_{\mathbb{R}_+} \mathrm{d}t_4$$
$$G_-(0, r_0, t_4 - t_3, z_3, x_3) Q_{-,x_3}(z_3) a(z_3) Q^*_{+,x_3}(z_3) \delta u_{+,2}(z_3, x_3, t_3, 0, s_0, t_{s0}), \quad (77)$$

where we have returned to observables through the operator RQ^{-1}, introduced in (43). For the above construction to be valid, it is necessary that the three scattering positions are sufficiently far apart. This ensures that the wavefront sets of the $G_\pm$ distribution kernels do not align, making their product well-defined (Friedlander & Joshi, 1998 proposition 11.2.3).

We can now apply reciprocity to the G_+ of (76). We do this by substituting the expression for $\delta u_{+,2}$ in (76) into (77), which allows us to use the Q_+ operators from both expressions. This gives

$$d_3(s_0, r_0, t_4 - t_{s0}) = -\tfrac{1}{16} D_{t_4}^4 \int_0^{\infty} \mathrm{d}z_3 \int \mathrm{d}s_3 \int \mathrm{d}r_3 \int_{\mathbb{R}_+} \mathrm{d}t_3 \int_0^{z_3} \mathrm{d}z_1 \int \mathrm{d}m_s \int \mathrm{d}m_r \int_{\mathbb{R}_+} \mathrm{d}t_a$$
$$Q^*_{-,r_0}(0) G_-(0, r_0, t_4 - t_3, z_3, r_3) Q_{-,r_3}(z_3) \boxed{Q^*_{-,m_s}(z_1) G_-(z_1, m_s, \underline{t_3 - t_a}, z_3, s_3) Q_{-,s_3}(z_3)}$$
$$(E_1 a)(z_3, s_3, r_3) Q^*_{-,m_r}(z_1) (E_1 a)(z_1, m_s, m_r) \delta u_{-,1}(z_1, m_r, t_a, 0, s_0, t_{s0}); \quad (78)$$

we have also introduced the extension operator E_1, to split each of the m and x_3 integrations into two. The portion of the expression that has changed through reciprocity is in the box.

The insertion of the relation $G(z_a, x_a, t, z_b, x_b) = Q_{-,x_a}(z_a) G_-(z_a, x_a, t, z_b, x_b) Q_{-,z_b}(z_b)$ into (78), where G is the Green's function for the double square-root equation, shows the correspondence of (78) with expression (8) in (ten Kroode, 2002).

Noting that t_3 is independent of t_a, we can interchange their order of integration, which allows us to change integration variables from t_3 to $t'_3 = t_3 - t_a$ and introduce the E_2 operator at the third scatter. This results in

$$d_3(s_0, r_0, t_4 - t_{s0}) = -\tfrac{1}{16} D_t^4 \int_0^{\infty} \mathrm{d}z_3 \int \mathrm{d}s_3 \int \mathrm{d}r_3 \int_{\mathbb{R}_+} \mathrm{d}t_{30} \int_{\mathbb{R}_+} \mathrm{d}t_a \int_0^{z_3} \mathrm{d}z_1 \int \mathrm{d}m_s \int \mathrm{d}m_r \int_{\mathbb{R}_+} \mathrm{d}t'_3$$
$$Q^*_{-,r_0}(0) G_-(0, r_0, t_4 - t_a - t'_3 - t_{30}, z_3, r_3) Q_{-,r_3}(z_3) Q^*_{-,m_s}(z_1) G_-(z_1, m_s, t'_3, z_3, s_3) Q_{-,s_3}(z_3)$$
$$Q^*_{-,m_r}(z_1) (E_1 E_2 a)(z_3, s_3, r_3, t_{30}) (E_1 a)(z_1, m_s, m_r) \delta u_{-,1}(z_1, m_r, t_a, 0, s_0, t_{s0}), \quad (79)$$

which is a modeling operator for triply scattered waves. We have not yet introduced the E_2 operator at the m_s, m_r scattering point as it is not clear in which G the time t_{m0} should be placed. It will become necessary in what follows. In ten Kroode (2002), equation (8) is the Lippmann-Schwinger equivalent of (79); ten Kroode's equation is valid for wave propagation in a medium of up to 2 dimensions without caustics.

Thus far, we have constructed an operator (79) that is tri-linear in the medium contrast a. From a practical viewpoint, however, it is advantageous to construct an operator that acts on the data, as this is known, rather than the medium contrast. To this end, we reformulate (79) so that all the G operators interchanging the t'_3 and $t_{m'_s}$ integrations giving

$$\begin{aligned} d_3(s_0, r_0, t_4 - t_{s0}) = -\tfrac{1}{4} D_t^4 \int_0^\infty \mathrm{d}z_3 \int \mathrm{d}s_3 \int \mathrm{d}r_3 \int_{\mathbb{R}_+} \mathrm{d}t_{30} \int_0^{z_3} \mathrm{d}z_1 \int \mathrm{d}m_s \int \mathrm{d}m_r \int_{\mathbb{R}_+} \mathrm{d}t_a \int \mathrm{d}m'_s \int_{\mathbb{R}_+} \mathrm{d}t_{m'_s} \int_{\mathbb{R}_+} \mathrm{d}t''_3 \\ Q^*_{-,r_0}(0) G^*_-(z_1, m_s, t_{m'_s}, 0, m'_s) G_-(0, r_0, t_4 - t_a - t''_3 + t_{m'_s} - t_{30}, z_3, r_3) Q_{-,r_3}(z_3) Q^*_{-,m_s}(z_1) G_-(0, m'_s, t''_3, z_3, s_3) \\ Q_{-,s_3}(z_3) Q^*_{-,m_r}(z_1) (E_1 E_2 a)(z_3, s_3, r_3, t_{30}) (E_1 a)(z_1, m_s, m_r) \delta u_{-,1}(z_1, m_r, t_a, 0, s_0, t_{s0}) \,. \end{aligned} \tag{83}$$

We now substitute the H operator for the two G_- operators, interchanging the order of integration to obtain

$$\begin{aligned} d_3(s_0, r_0, t_4 - t_{s0}) = -\tfrac{1}{4} D_{t_4}^4 Q^*_{-,r_0}(0) \int_0^\infty \mathrm{d}z_3 \int_0^{z_3} \mathrm{d}z_1 \int \mathrm{d}m_s \int \mathrm{d}m_r \int_{\mathbb{R}_+} \mathrm{d}t_a \int \mathrm{d}m'_s \int_{\mathbb{R}_+} \mathrm{d}t_{m'_s} \\ Q^*_{-,m_s}(z_1) Q^*_{-,m_r}(z_1) G^*_-(z_1, m_s, 0, 0, m'_s, t_{m'_s}) \\ \int \mathrm{d}s_3 \int \mathrm{d}r_3 \int_{\mathbb{R}_+} \mathrm{d}t_{30} H(0, m'_s, r_0, t_4 - t_a + t_{m'_s} - t_{30}, z_3, s_3, r_3) Q_{-,s_3}(z_3) Q_{-,r_3}(z_3) \\ (E_1 a)(z_1, m_s, m_r) (E_1 E_2 a)(z_3, s_3, r_3, t_{30}) \delta u_{-,1}(z_1, m_r, t_a - t_{s0}, 0, s_0) \,. \end{aligned} \tag{84}$$

In (84), the G^*_- term in $\delta u_{-,1}$ does not depend on any of the variables in the operators preceding it. Thus, we may interchange operators to combine the two G^*_- terms. We do this, as well as changing the order of integration to move the t_a integral inside the $t_{m'_s}$ one and also introduce E_2, giving

$$\begin{aligned} d_3(s_0, r_0, t_4 - t_{s0}) = \tfrac{1}{16} D_t^6 Q^*_{-,r_0}(0) \int \mathrm{d}\tilde{s}_0 \int_{\mathbb{R}_+} \mathrm{d}\tilde{t}_{s0} \int_0^\infty \mathrm{d}z_3 \int_0^{z_3} \mathrm{d}z_1 \int_{z_1}^\infty \mathrm{d}z_2 \\ \int \mathrm{d}m_s \int \mathrm{d}m_r \int_{\mathbb{R}_+} \mathrm{d}t_{m0} \int \mathrm{d}m'_s \int \mathrm{d}m'_r \int_{\mathbb{R}_+} \mathrm{d}t_{m'_s} \int_{\mathbb{R}_+} \mathrm{d}t_{m'_r} (E_1 E_2 a)(z_1, m_s, m_r, t_{m0}) \\ Q^*_{-,m_s}(z_1) Q^*_{-,m_r}(z_1) G^*_-(z_1, m_s, t_{m'_s} - t_{m0}, 0, m'_s) G^*_-(z_1, m_r, t_{m'_r}, 0, m'_r) \Bigg\{ \int_{\mathbb{R}_+} \mathrm{d}t_a \\ \int \mathrm{d}s_3 \int \mathrm{d}r_3 \int_{\mathbb{R}_+} \mathrm{d}t_{30} H(0, m'_s, r_0, t_4 - t_a + t_{m'_s} - t_{30}, z_3, s_3, r_3) Q_{-,s_3}(z_3) Q_{-,r_3}(z_3) \\ (E_1 E_2 a)(z_3, s_3, r_3, t_{30}) \int \mathrm{d}s_2 \int \mathrm{d}r_2 \int_{\mathbb{R}_+} \mathrm{d}t_0 H(0, \tilde{s}_0, m'_r, t_a + t_{m'_r} - \tilde{t}_{s0} - t_0, z_2, s_2, r_2) \\ Q_{-,r_2}(z_2) Q_{-,s_2}(z_2) (E_1 E_2 a)(z_2, s_2, r_2, t_0) \Bigg\} Q^*_{-,\tilde{s}_0}(0) f(0, \tilde{s}_0, \tilde{t}_{s0}, 0, s_0, t_{s0}) \,. \end{aligned} \tag{85}$$

In (85), the expression in braces is a convolution in time. Because of this, we may shift time variables between the two H operators. To do this we change time variables from t_a to $t_b = t_a + t_{m'_r} - \tilde{t}_{s0}$. We then introduce the distribution w,

$$\begin{aligned} w(\tilde{s}_0, m'_r, t, m'_s, r_0; z_2, z_3) = \int_{\mathbb{R}_+} \mathrm{d}t_b \int \mathrm{d}r_3 \int \mathrm{d}s_3 \int_{\mathbb{R}_+} \mathrm{d}t_{30} H(0, m'_s, r_0, t - t_b - t_{30}, z_3, s_3, r_3) \\ Q_{-,s_3}(z_3) Q_{-,r_3}(z_3) (E_1 E_2 a)(z_3, s_3, r_3, t_{30}) \int \mathrm{d}s_2 \int \mathrm{d}r_2 \int_{\mathbb{R}_+} \mathrm{d}t_0 H(0, \tilde{s}_0, m'_r, t_b - t_0, z_2, s_2, r_2) \\ Q_{-,r_2}(z_2) Q_{-,s_2}(z_2) (E_1 E_2 a)(z_2, s_2, r_2, t_0), \end{aligned} \tag{86}$$

where we may allow the lower bound on the t_b integral to extend to 0, rather than $t_{m'_r}$ because $t_b > t_{m'_r}$ by definition. To overlay the operator w with the expression in braces in (85) we need only make the identification $t = t_4 + t_{m'_r} + t_{m'_s} - \tilde{t}_{s0}$. By changing the lower bound of the z_3 integral in (85) to z_1 and the upper bound of the z_1 integral to ∞ we may define

$$W(z_1; \tilde{s}_0, m'_r, t, m'_s, r_0) = \int_{z_1}^\infty \mathrm{d}z_3 \int_{z_1}^\infty \mathrm{d}z_2 \; w(\tilde{s}_0, m'_r, t, m'_s, r_0; z_2, z_3) \,. \tag{87}$$

In the definition of w, we now see the emergence of a new time variable $t_{m'} = t_{m'_r} + t_{m'_s}$ in the expression

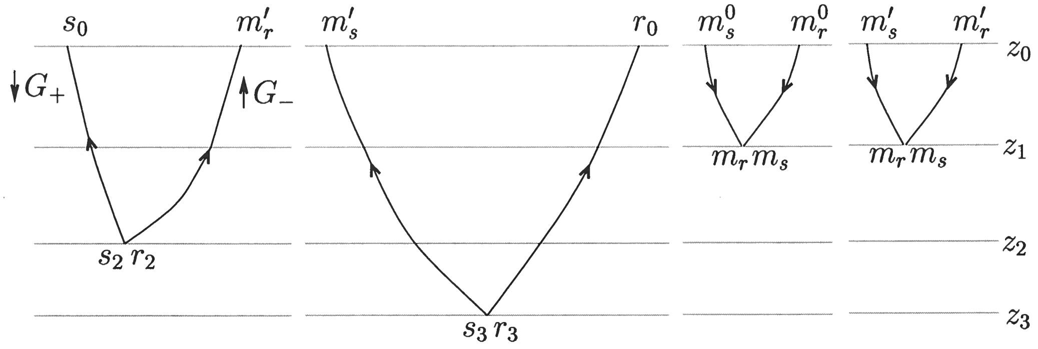

Figure 9. Illustration of the four operators used to construct the final modeling operator. Notice that R and H act at different surface points.

The operator $\Phi(z, x, D_z, D_x)$, which is also a pseudodifferential operator, corrects for illumination effects. Its symbol is 1 where there is illumination and zero elsewhere. In fact, the analysis requires that we replace the data, d_1, with $\psi_Y d_1$, where ψ_Y is a cut-off function which is zero near the boundary of the acquisition surface, Y. Further details of these cut-off operators can be found in (Stolk & de Hoop, 2004b).

In the single scattering approximation, the data in (74) are used as an approximation of the data d, in (52). To reconstruct V_1 we must apply the above inverse to these model data. This gives an estimate for the a distribution,

$$\langle a_1 \rangle(z, x) = \Phi(z, x, D_z, D_x)a, \tag{95}$$

which is, as expected, simply an amplitude change, or 'non-stationary' filter applied to the original medium contrast. We use the $\langle\cdot\rangle$ notation to indicate that this is an estimate of a rather than its true value, the subscript 1 indicates that this estimate is obtained through the single scattering approximation. From this estimate of a, we obtain an estimate of the matrix V_1 using (31).

7.2 triple scattering

In the framework of the series expansion in (59), we require only the single scattering inverse to estimate the third order contribution to V: we write the first and third terms of (59) as

$$\langle a_1 \rangle + \langle a_3 \rangle = N^{-1}F^* d - N^{-1}F^*(D_t^4 \mathsf{M}_0(\widehat{V}_1 \mathsf{L}_0(\widehat{V}_1 \delta U)))\,. \tag{96}$$

We will use the operator, J, on the right hand side in (94) in place of $N^{-1}F^*$ to estimate this inverse. The inverse series, (59) is a sum of terms of different order in the data, with the first term being first-order in the data and the third term third-order in the data. In the modeling formula, (89), the data are written as a trilinear operator on the medium contrast, a, as in the forward series (43). To estimate a_3 we need to write $D_t^4 \mathsf{M}_0(\widehat{V}_1 \mathsf{L}_0(\widehat{V}_1 \delta U))$, for which an expression was constructed in section 6.2, as a trilinear operator acting on the data. We then apply the single scattering inverse to this expression to estimate a_3, from which we can compute $\widehat{V}_3$.

To write d_3 in terms of the data, we insert the instantaneous point source into (89) as in the single scattering case. This gives

$$d_3(s_0, r_0, t_4 - t_{s_0}) = \tfrac{1}{16} D_t^6 Q^*_{-,r_0}(0) Q^*_{-,s_0}(0) \int_0^\infty \mathrm{d}z_1 \int \mathrm{d}m_s \int \mathrm{d}m_r \int_{\mathbb{R}_+} \mathrm{d}t_{m0} (E_1 E_2 a)(z_1, m_s, m_r, t_{m0}) \int \mathrm{d}m_s' \int \mathrm{d}m_r'$$
$$\int_{\mathbb{R}_+} \mathrm{d}t_{m'} Q^*_{-,m_s}(z_1) Q^*_{-,m_r}(z_1) H^*(z_1, m_s, m_r, t_{m'} - t_{m0}, 0, m_s', m_r') W(z_1; s_0, m_r', t_4 + t_{m'} - t_{s_0}, m_s', r_0)\,. \tag{97}$$

There are three equivalent ways in which one could proceed to write (89) in terms of the data only. First, one could replace each of the a terms with J applied to the data, giving a trilinear operator acting on the data. Second, one can re-arrange terms to introduce d directly in place of the a term at both z_2 and z_3, and use J to write the a term at z_1 in terms of the data. Third, one can rearrange terms to write all three a directly in terms of d. We will go through the second method in detail.

use of this fact and the notion of adjoint to rewrite (102) as

$$\begin{aligned}\langle d_3\rangle(s_0,r_0,t_4-t_{s_0}) ={}& \int \mathrm{d}m_s' \int \mathrm{d}m_r' \int_{\mathbb{R}_+} \mathrm{d}t_{m'} \int_0^\infty \mathrm{d}z_1 \int \mathrm{d}m_s \int \mathrm{d}m_r \int_{\mathbb{R}_+} \mathrm{d}t_{m^0} H(0,m_s',m_r',t_{m'}-t_{m^0},z_1,m_s,m_r)E_2 \\ & Q_{-,m_s}(z_1)Q_{-,m_r}(z_1)Q_{-,m_s}(z_1)^{-1}Q_{-,m_r}(z_1)^{-1} \left\{ \Xi^{-1}R_{2,t'} \int \mathrm{d}m_s^0 \int \mathrm{d}m_r^0 \int_{\mathbb{R}_+} \mathrm{d}t_{m^0} \right. \\ & \left. H^*(z_1,m_s,m_r,t_{m^0}-\overset{t'}{\cdot},0,m_s^0,m_r^0)Q_{-,m_s^0}^*(0)^{-1}Q_{-,m_r^0}^*(0)^{-1}d(m_s^0,m_r^0,t_{m^0}) \right\} \\ & Q_{-,m_s'}^*(0)^{-1}Q_{-,m_r'}^*(0)^{-1} \int_{\mathbb{R}_+} \mathrm{d}t_b\ \mathbf{d}(z_1;m_s',r_0,t_4+t_{m'}-t_b-t_{s_0})\mathbf{d}(z_1;s_0,m_r',t_b)\,, \qquad (103)\end{aligned}$$

which simplifies to

$$\begin{aligned}\langle d_3\rangle(s_0,r_0,t_4-t_{s_0}) ={}& \int \mathrm{d}m_s' \int \mathrm{d}m_r' \int_{\mathbb{R}_+} \mathrm{d}t_{m'} \int_0^\infty \mathrm{d}z_1 \int \mathrm{d}m_s \int \mathrm{d}m_r \int_{\mathbb{R}_+} \mathrm{d}t_{m^0} H(0,m_s',m_r',t_{m'}-t_{m^0},z_1,m_s,m_r)E_2\Xi^{-1}R_{2,t'} \\ & \int \mathrm{d}m_s^0 \int \mathrm{d}m_r^0 \int_{\mathbb{R}_+} \mathrm{d}t_{m^0} H^*(z_1,m_s,m_r,t_{m^0}-\overset{t'}{\cdot},0,m_s^0,m_r^0)Q_{-,m_s^0}^*(0)^{-1}Q_{-,m_r^0}^*(0)^{-1}d(m_s^0,m_r^0,t_{m^0}) \\ & Q_{-,m_s'}^*(0)^{-1}Q_{-,m_r'}^*(0)^{-1} \int_{\mathbb{R}_+} \mathrm{d}t_b\ \mathbf{d}(z_1;m_s',r_0,t_4+t_{m'}-t_b-t_{s_0})\mathbf{d}(z_1;s_0,m_r',t_b)\,. \qquad (104)\end{aligned}$$

We define

$$\begin{aligned}d_1'(z_1,s,r,t) ={}& D_t^2 Q_{-,s}^*(0)Q_{-,r}^*(0) \int \mathrm{d}s_1 \int \mathrm{d}r_1 \int_{\mathbb{R}_+} \mathrm{d}t_0 \\ & H(0,s,r,t-t_0,z_1,s_1,r_1)Q_{-,s_1}(z_1)Q_{-,r_1}(z_1)(E_1E_2a)(z_1,s_1,r_1,t_0)\,; \qquad (105)\end{aligned}$$

we use the notation d' because it is close to the derivative with respect to z_1 of d. The quantity d' is not one that can be measured, because one cannot tell directly from which depth the data come. To compute d', the expression in (94) must be substituted for a to write it in terms of what can be measured, d. Because of this, we can write (102) in terms of this d' 'data' set

$$\begin{aligned}d_3(s_0,r_0,t_4-t_{s_0}) ={}& \int_0^\infty \mathrm{d}z_1 \int \mathrm{d}m_s' \int \mathrm{d}m_r' \int_{\mathbb{R}_+} \mathrm{d}t_{m'} Q_{-,m_s'}^*(0)^{-1}Q_{-,m_r'}^*(0)^{-1}d_1'(z_1,m_s',m_r',t_{m'}) \\ & Q_{-,m_s'}^*(0)^{-1}Q_{-,m_r'}^*(0)^{-1} \int_{\mathbb{R}_+} \mathrm{d}t_b\ \mathbf{d}_1(z_1;m_s',r_0,t_4+t_{m'}-t_b-t_{s_0})\mathbf{d}_1(z_1;s_0,m_r',t_b)\,. \qquad (106)\end{aligned}$$

We have nearly succeeded in writing $D_t^4\mathsf{M}_0(\widehat{V}_1\mathsf{L}_0(\widehat{V}_1\delta U))$ in terms of the data d. We find, however that we cannot write (106) in terms of the actual data because of the z_1 dependence of each of the three 'data' sets.

Remark 7.1. If we ignore the z_1 dependence of $\mathbf{d}$ in (104), the composition

$$\int_0^\infty \mathrm{d}z_1 \int \mathrm{d}m_s \int \mathrm{d}m_r \int_{\mathbb{R}_+} \mathrm{d}t_{m^0} H(0,m_s',m_r',t_{m'}-t_{m^0},z_1,m_s,m_r)E_2\Xi^{-1}R_2H^*(z_1,m_s,m_r,t_{m^0},0,m_s^0,m_r^0)\,,$$

gives microlocally,

$$\delta(m_s'-m_s^0)\delta(m_r'-m_r^0)\delta(t_{m'}-t_{m^0})\,.$$

Then, (104) can be written as

$$\begin{aligned}\langle d_3\rangle(s_0,r_0,t_4-t_{s_0}) \sim{}& \int \mathrm{d}m_s' \int \mathrm{d}m_r' \int_{\mathbb{R}_+} \mathrm{d}t_{m'} Q_{-,m_s'}^*(0)^{-1}Q_{-,m_r'}^*(0)^{-1}d(m_s',m_r',t_{m'}) \\ & Q_{-,m_s'}^*(0)^{-1}Q_{-,m_r'}^*(0)^{-1} \int_{\mathbb{R}_+} \mathrm{d}t_b\ d(m_s',r_0,t_4+t_{m'}-t_b-t_{s_0})d(s_0,m_r',t_b)\,, \qquad (107)\end{aligned}$$

with the approximation $d \approx d_1$.

scattering is assumed (see Figure 10). The application of J to $\langle d_3 \rangle$ gives

$$\langle a_3 \rangle (z_4, x_4) = -R_1 Q_{-,s_4}(z_4)^{-1} Q_{-,r_4}(z_4)^{-1} \Xi^{-1} H^*(0, s_0, r_0, t_4 - t_{s_0}, z_4, s_4, r_4)$$
$$Q^*_{-,s_0}(0)^{-1} Q^*_{-,r_0}(0)^{-1} D_t^{-2} \langle d_3 \rangle (\overset{s_0}{\cdot}, \overset{r_0}{\cdot}, \overset{t_4 - t_{s_0}}{\cdot}). \quad (108)$$

As can be expected, this expression is not close to the true medium contrast at (z_4, x_4) since J is the single scattering inverse and thus will not correctly treat multiply scattered waves. Returning to (96) we see that the term $\widehat{V}_3$ has the opposite sign to $\widehat{V}_1$. Equation (108) is meant to remove the erroneous contribution to $\langle a \rangle$ made by imaging all the data as though they had scattered only once as is done in the construction of $\langle a_1 \rangle$.

7.3 Inverse series in angle gathers

The J operator discussed above computes an image of the subsurface given seismic data at the surface. There is more information available in seismic data than it exploits, however. For example, studying amplitude variations with scattering angle (the angle between the incoming and outgoing rays at the scattering point) an image, which is averaged over angle, is not sufficient. In addition, the imaging operator depends on the background velocity model, which is not in general known. One way of estimating this model is to look at the data as a function of angle at the scattering point, called an angle gather. With the correct velocity model, these angle gathers are independent of angle.

To construct these angle gathers, we use the wave-equation angle transform, $\tilde{A}_{\mathrm{WE}}$, as described by Stolk and de Hoop (2004b). Here, in place of $\tilde{A}_{\mathrm{WE}}$ we use the notation A_{WE}, where

$$(A_{\mathrm{WE}} d)(z, x, p) = \jmath^{-1} R_3 \Xi^{-1} Q_{-,s}(z)^{-1} Q_{-,r}(z)^{-1} H(0, z)^* Q^*_{-,s_0}(0)^{-1} Q^*_{-,r_0}(0)^{-1} D_t^{-2} d, \quad (109)$$

with p the slowness vector. We define $\jmath$, as the pseudodifferential operator compensating for amplitude effects. Its symbol is derived in Proposition 3.2 of (Stolk & de Hoop, 2004b). We also introduce R_3, through

$$R_3 \ : \ g(z, s, r, t) \mapsto (R_3 g)(z, x, p) = \int_{\mathbb{R}^{n-1}} g(z, x - \tfrac{h}{2}, x + \tfrac{h}{2}, ph) \chi(z, x, h) \, \mathrm{d}h, \quad (110)$$

where $h = \frac{s-r}{2}$ and χ is a pseudodifferential cutoff with compact support containing the point $h = 0$. Note that R_3 is a restriction operator, its properties are described by Stolk and de Hoop (2004b); it takes the place of R_1 and R_2 used previously. Applying the A_{WE} operator to data results in a family of images, parameterized by p. In this construction, the data $(A_{\mathrm{WE}} d)(z, x, p)$ are independent of the parameter p under a number of assumptions. One of these assumptions is that the data consist of only primary events. First-order internal multiples will violate these assumptions and thus will give contributions to $(A_{\mathrm{WE}} d)(z, x, p)$ that do depend on the parameter p.

In the series solution for $\widehat{V}$, we can use the angle transform to construct a series of solution families, dependent on the parameter p. From the singly scattered term (74), we get the reconstruction for a_1

$$\langle\!\langle a_1 \rangle\!\rangle (z, x, p) = (A_{\mathrm{WE}} \ d)(z, x, p), \quad (111)$$

where we use the notation $\langle\!\langle \cdot \rangle\!\rangle$ to denote an estimate obtained through the angle transform. We know that this can be written as

$$\Psi_{\mathrm{WE}}(z, x, p, D_z, D_x, 0)(a) = A_{\mathrm{WE}} d, \quad (112)$$

(Stolk & de Hoop, 2004b) where Ψ_{WE} is the composition of all of the pseudodifferential operators in (94), transformed via pullback into the angle coordinates.

The third-order contribution comes from $\langle d_3 \rangle$. Applying the wave-equation angle transform in place of the inverse from (94), we arrive at the following analogue of (108)

$$\langle\!\langle a_3 \rangle\!\rangle (z, x, p) = (A_{\mathrm{WE}} \ \langle d_3 \rangle)(z, x, p) \quad (113)$$

Again, $\langle\!\langle a_3 \rangle\!\rangle (z, x, p)$ should not be interpreted as a true medium contrast, but rather as a correction term to $\langle\!\langle a_1 \rangle\!\rangle$. Recalling from (48) that $\widehat{V}_1$ and $\widehat{V}_3$ have opposite sign, our best estimate of a comes from

$$\langle\!\langle a \rangle\!\rangle = \langle\!\langle a_1 \rangle\!\rangle - \langle\!\langle a_3 \rangle\!\rangle \, . \quad (114)$$

Although it is possible to subtract the two angle gathers, $\langle\!\langle a_1 \rangle\!\rangle$ and $\langle\!\langle a_3 \rangle\!\rangle$, (114) does not necessarily give a good estimate of a. This is because, although (112) assures us that $\langle\!\langle a_1 \rangle\!\rangle$ is a pseudodifferential operator

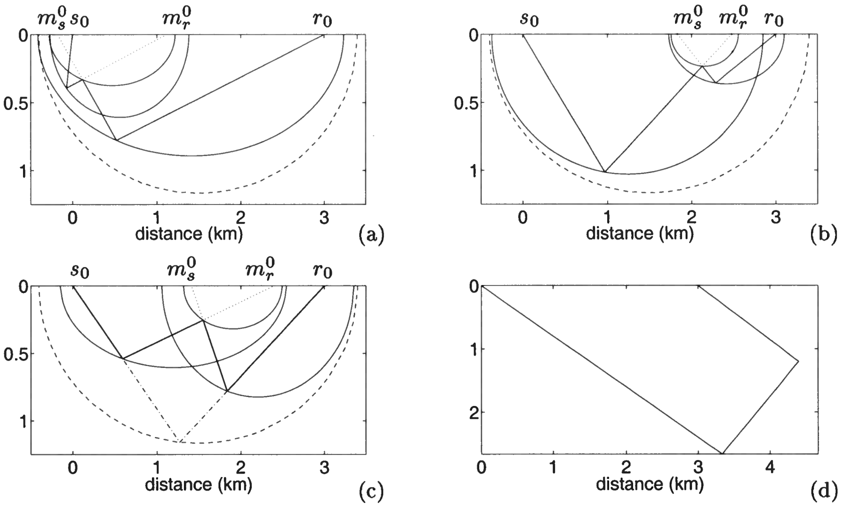

Figure 11. Two different situations contributing to the third-order term are shown in (a) and (b). The three solid curves are isochrons corresponding to the three singly scattered data points contributing to a third-order scattering event. The dashed curve is the corresponding single-scattering isochron (i.e. the same source and receiver positions and travel time as the triply scattered event assuming single scattering). The solid ray is the true travel path and the dashed rays illustrate the additional travel used to write the triply scattered data in terms of three single scatters. In (c) we show a triple scattering contribution difficult to distinguish from a singly scattered event (dash-dot ray), in data space, since the surface positions and initial slopes are the same. In (d), a contribution that violates our assumptions is shown; this is a doubly scattered event that would be recorded at the surface.

analogous contributions (Hron, 1972) will not pose a problem; the subtraction, $\langle\!\langle a_3 \rangle\!\rangle - \langle\!\langle a_1 \rangle\!\rangle$ will result in an amplitude correction. The event shown in (d), is not accounted for by our theory. The event shown is a doubly scattered event, and thus will contribute to a_2, which is not estimated here. Events like this make an important contribution to seismic data, especially near salt. However, the contribution from the majority of doubly scattered events is lost to the interior of the Earth. Such contributions are therefore more important for transmission experiments than reflection experiments like those studied here.

In Figure 12, the triple scattering isochron is shown. This isochron represents all points in the subsurface which could contribute to a particular point in the triply scattered data. In (a), points from the first scattering point at (z_2, s_2, r_2) are shown; the points in (b) are from the third scatter at (z_3, s_3, r_3). These two plots are mirror images of one another as expected from reciprocity. The points shown in (c), mark the position of the central scattering event at (z_1, m_s, m_r). In (c), the points do not cluster on lines like those in (a) and (b). This scattered distribution of points fills the interior of the corresponding single scattering isochron (dashed line). Thus we observe that while singly scattered data at a single source, receiver, and time sample the subsurface along an ellipse, triply scattered data at the same source, receiver, and time sample the entire interior of the same ellipse.

The algorithm described above requires knowledge of the velocity model to the depth z_1 of the up-to-down scatter. This knowledge is necessary to compute $\mathbf{d}$, when the traveltime monotonicity assumption is not valid. In addition, an adaptive subtraction technique is required to compensate for differences in illumintation between the singly and triply scattered data. In other words, a technique must be developed to subtract $\langle\!\langle a_3 \rangle\!\rangle$ from $\langle\!\langle a_1 \rangle\!\rangle$ in a way that is robust to differences in the subsurface sampling between the singly and triply scattered waves.

Am., 1507–1529.

Park, J., & Levin, V. 2001. Receiver functions from regional P waves. *Geophys. J. Int.*, **147**, 1–11.

Razavy, M. 1975. Determination of the wave velocity in an inhomogeneous medium from reflection data. *J. Acoust. Soc. Am.*, **58**, 956–963.

Revenaugh, J., & Jordan, T. H. 1987. Observations of first-order mantle reverberations. *Bull. Seism. Soc. Am.*, **77**, 1704–1717.

Revenaugh, J., & Jordan, T. H. 1989. A study of mantle layering beneath the western pacific. *Jour. Geoph. Res.*, **94**, 5787–5813.

Sava, P., & Guitton, A. 2004. Multiple attenuation in the image space. *submitted, Geophysics.*

Sjöstrand, J., & Grigis, A. 1994. *Microlocal Analysis for Differential Operators : An Introduction.* Cambridge: Cambridge University Press.

Stolk, C. C., & de Hoop, M. V. 2000. Modeling and inversion of seismic data in anisotropic elastic media. *Comm. Pure Appl. Math.* submitted.

Stolk, C. C., & de Hoop, M. V. 2004a. Modeling of seismic data in the downward continuation approach. *SIAM J. Appl. Math.* CWP468P.

Stolk, C. C., & de Hoop, M. V. 2004b. Seismic inverse scattering in the downward continuation approach. *SIAM J. Appl. Math.* CWP469P.

Symes, W., & Gockenbach, M. 1999. *Coherent noise suppression in velocity inversion.* Soc. of Expl. Geophys. Pages 1719–1722.

ten Kroode, A. P. E. 2002. Prediction of internal multiples. *Wave Motion*, **35**, 315–338.

van Borselen, R. 2002. Data-driven interbed multiple removal: Strategies and examples. *In: Expanded Abstracts.* Society of Exploration Geophysicists.

Verschuur, D. J., & Berkhout, A. 1997. Estimation of multiple scattering by iterative inversion, Part II: Practical aspects and examples. *Geophysics*, **62**(5), 1596–1611.

Weglein, A., Gasparotto, F. A., Carcalho, P. M., & Stolt, R. H. 1997. An inverse-scattering series method for attenuating multiples in seismic reflection data. *Geophysics*, **62**, 1975–1989.

Weglein, A., Araújo, F. B., Carvalho, P. M., Stolt, R. H., Matson, K. H., Coates, R. T., Corrigan, D., Foster, D. J., Shaw, S. A., & Zhang, H. 2003. Inverse scattering series and seismic exploration. *Inverse Problems*, **19**, R27–R83.

Yoshida, K. 1995. *Functional Analysis.* Berlin: Springer.

symbol	in or near	meaning
C	(19)	dissipative term
$\mathsf{L}, G_\pm, P$	(19)	same as above with dissipatitive term excluding horizontal propagation
$\cdot_0$		operator in the background medium
$\delta\cdot$		difference between operator in true and background media
$a = 2c_0^{-3}\delta c$	(24)	medium contrast
V	(34)	contrast source
$S_{\pm,\pm}$	(34)	reflection/transmission operators; elements of the V matrix
$\widehat{V}$	(38)	V without the D_t^2
R	(43)	restriction operator
$\mathsf{M}_0 = R\mathsf{Q}^{-1}\mathsf{L}_0$	(43)	parametrix of one-way equation restricted to acquisition surface and returned to the original second order system
d_1	(44)	single-scattered data
F	(44)	single scattering modeling operator
$V_m \quad (V = \delta P)$	(48)	contrast operator of order m in the data
N	(45)	normal operator
d	(48)	data
$\delta u_{\pm,j}$	(62)	wavefield after j scatters going in the ± direction
t_{s_0}	(62)	source time
$\tilde{\cdot}$	(62)	variables of integration over source parameters
z_j	(62)	j^{th} datum (see Figure 6)
s_j, r_j	(62)	j^{th} source/receiver (see Figure 6)
x_j	(62)	lateral position at j^{th} datum, generally $x_j = s_j = r_j$
$c_\pm$	(64)	components of contrast source
t_{r_0}	(65)	total single scattering traveltime
t_1	(65)	start time of single-scattering receiver ray
E_1, E_2	(69)	wave coupling operators
t_0	(70)	zero time at contrast for single scattering, at z_2 in triple scattering
t'	(71)	convolution variable
H	(73)	Green's function convolution operator
t_a	(75) Figure 7	time from s_0 through s_2, r_2 to m_r
m_s, m_r	(76)	lateral position of upward scatter (see Figure 6)
t_3	(76) Figure 7	t_a plus time from m_r, m_s to s_3, r_3
t_4	(77) Figure 7	total time on triple-scattered ray
t_3'	(79)	convolutional variable, equal to time from m_s, m_r to s_3, r_3
t_{30}	(79)	zero time at contrast at z_3
t_{m0}	(79),(88)	zero time at contrast at z_1
$t_{m_r'}$	(80) Figure 7	time from m_r' to m_r
$t_{m_s'}$	(82) Figure 7	time from m_s' to m_s
t_3''	(83)	convolutional variable, time from m_s' to s_3, r_3
$t_b = t_a + t_{m_r'}$	(85) Figure 7	time from s_0 through s_2, r_2 to m_r'
w	(86)	convolution of two 'data' sets
W	(87)	integral of w with respect to z_2 and z_3
$t_{m'} = t_{m_s'} + t_{m_r'}$	(88) Figure 7	time from m_s' through m_s, m_r to m_r'
K	(90)	downward continuation forward modelling operator
$R_{1,2}$	(91)	restriction operator, inverse of $E_{1,2}$
$\bar{\Xi}$, ψ_Y and $\bar{\Phi}(z, x, D_z, D_x)$	(94)	pseudodifferntial operators to correct for amplitude affects
$\langle\cdot\rangle$	(95)	estimate of quantity, for a using traditional inverse
$\mathbf{d}_1(z_1; s, r, t)$	(99)	single-scattered data with scatters only below the z_1 level
$(\mathbf{D}\langle a\rangle)(z_1, s, r, t)$	(99)	data with scatters only above the z_1 level
$R_{2,t'}$	(102)	R_2 operator acting in the t' variable
m_s^0, m_r^0	(102)	surface points for imaging at z_1
t_{m^0}	(102)	time from m_s^0 through m_s, m_r to m_r^0
d_1'	(104)	single scattered data without integration over z_1
A_{WE}	(109)	wave equation angle transform
$\jmath$	(110)	jacobian
R_3	(110)	operator to map (z, s, r, t) to (z, x, p)
h	(110)	half-offset
χ	(110)	pseudodifferential cutoff about $h = 0$
$\langle\!\langle\cdot\rangle\!\rangle$	(111)	estimate of medium contrast using angle transform
Ψ_{WE}	(112)	composition of pseudodifferential operators
p	(112)	slowness vector

A formalism for the suppression of multiple diffractions

Roel Snieder

Center for Wave Phenomena and Department of Geophysics, Colorado School of Mines, Golden CO 80401-1887

ABSTRACT

Diffracted multiples can be a problem in marine surveys since these waves appear in seismic data as a curtain of noise that obscures primaries. In this work I present a theory to suppress diffracted multiples that is based on a two-step process. The first step consists of the estimation of the scatterers near the sea-bottom. In the second step the reflections from the free surface are removed. There are reasons to believe that theoretical advances in the field of multiple suppression, as presented here, are of limited value unless limitations in the data acquisition can be overcome.

Key words: volcano monitoring, natural hazards, deconvolution

1 INTRODUCTION

Diffracted multiples are a major problem in areas with a rough sea-bottom, such as the Orme-Lange field, because the diffracted multiples obscure primaries that are the main target of the survey. The travel time curves of the diffracted multiples are steeper that those of the diffracted primaries, often to the extent that the diffracted multiples are aliased and show up in seismic data as a curtain of noise. Standard multiple elimination techniques cannot cope with these incoherent multiple diffractions, especially when the multiple elimination is carried out in the wavenumber domain, e.g. Verschuur et al. (1992).

In this paper the theory for the suppression of diffracted multiples is formulated as a two-step process. In the first step the scatterers near the sea-bottom are estimated, in the second step the reflections from the free water surface is removed (Noah's deconvolution (Riley & Claerbout, 1976)). The first step is based on a data-fitting procedure of the diffraction integral using a time window of the data that primarily contains the primary water-bottom diffractions. The removal of the free surface is formulated using the technique of Wapenaar et al. (1996).

It is questionable, though, if theoretical advances are sufficient to achieve a satisfactory suppression of multiple diffractions. These waves are likely to have bounce points at the free surface that may be far removed from the employed recorders, and the data that are needed to solve the integral equation for the multiple suppression may not have been recorded.

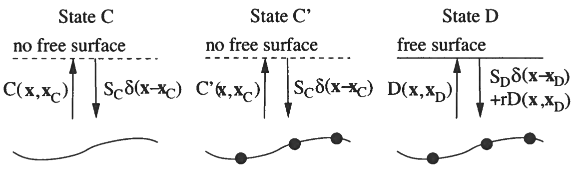

Figure 1. Definition of the corrected state C (without free surface and without scatterers), the intermediate state C' (without free surface but with scatterers), and the data state D (with a free surface and with scatterers). The scatterers are indicated by black circles.

2 COMPARING THREE DIFFERENT WAVE STATES

The basis for the suppression of diffracted and specular multiples forms the comparison of three different wavefields as shown in Figure 1. In this paper I follow Wapenaar et al. (1996), and decompose the wavefield in upcoming and downgoing waves. The pressure field in the water can be written as

$$\mathbf{p} = \begin{pmatrix} p_+ \\ p_- \end{pmatrix} , \tag{1}$$

where p_+ denotes the downgoing waves and p_- the upcoming waves.

developed for this problem (Kennett, 1979; Riley & Claerbout, 1976; Verschuur *et al.*, 1992; Weglein *et al.*, 1998; Wapenaar *et al.*, 2002). In this section I reformulate the theory of Wapenaar et al. (Wapenaar & Grimbergen, 1996; Wapenaar *et al.*, 2002) adapted to the wave states shown in Figure 1. The subsurface medium is the same in the D-state and the C'-state. Following equation (31) of ref. Wapenaar et al. (1996), these states are related by the following representation theorem:

$$\int_{\partial V} \mathbf{p}_{C'}^{T}\mathbf{N}\mathbf{p}_{D} n_z d^2 x_H = \int_{V} \left(\mathbf{p}_{C'}^{T}\mathbf{N}\mathbf{S}_D + \mathbf{S}_{C'}^{T}\mathbf{N}\mathbf{p}_D\right) dV \ , \tag{6}$$

where the vector $\mathbf{S}$ contains the upgoing and downgoing wave components of the source, and where the superscript T denotes the transpose. The matrix $\mathbf{N}$ is given by

$$\mathbf{N} = \begin{pmatrix} 0 & 1 \\ -1 & 0 \end{pmatrix} . \tag{7}$$

The bounds ∂V of the volume V in expression (6) are horizontal. For this reason, only the z-component of the outward pointing unit vector appears in the left hand side (6).

In the following I take the upper boundary of the surface just below the sources that excite the wavefield. At that boundary $n_z = -1$. Since the boundary is placed just below the sources, the sources are outside the volume and the right-hand side of (6) vanishes. The lower boundary is placed at infinite depth, so that it does not contribute. Inserting definition (7) and using the representations (2) for the state $C'$and (3) for the state D gives (after division by the source spectrum S_C),

$$\begin{aligned} D(\mathbf{x}_C, \mathbf{x}_D) \quad & - S_D C'(\mathbf{x}_D, \mathbf{x}_C) \\ & - r S_D \textstyle\int C'(\mathbf{x}, \mathbf{x}_C) D(\mathbf{x}, \mathbf{x}_D) d^2\mathbf{x} = 0 \ . \end{aligned} \tag{8}$$

By reciprocity, $C'(\mathbf{x}_1, \mathbf{x}_2) = C'(\mathbf{x}_2, \mathbf{x}_1)$. Only the source spectrum S_D appears in this expression, the subscript D in the source spectrum is suppressed in the following. Using this gives, with equation (4),

$$\begin{aligned} & D(\mathbf{x}_C, \mathbf{x}_D) - S\left\{C(\mathbf{x}_C, \mathbf{x}_D) + H(\mathbf{x}_C, \mathbf{x}_D)\right\} \\ & - r S \textstyle\int \left\{C(\mathbf{x}_C, \mathbf{x}) + H(\mathbf{x}_C, \mathbf{x})\right\} D(\mathbf{x}, \mathbf{x}_D) d^2\mathbf{x} = 0 \ . \end{aligned} \tag{9}$$

Before analyzing how this expression can be used to suppress diffracted multiples, let us first interpret this expression in terms of scattering diagrams. In a shorthand notation, the previous expression can be written as

$$D = S(C + H) + r S\,(C + H)\,D \ . \tag{10}$$

The products in this expression should be interpreted according to the notation of equation (9); hence the products entail an integration over the free surface. Iterating equation (10) gives the following expansion:

$$\begin{aligned} D \ & = S(C + H) + r S^2\,(C + H)\,(C + H) \\ & \quad + r^2 S^3\,(C + H)\,(C + H)\,(C + H) + \cdots \\ & = SC + SH + r S^2 CC \\ & \quad + r S^2 CH + r S^2 HC + r S^2 HH + \cdots \end{aligned} \tag{11}$$

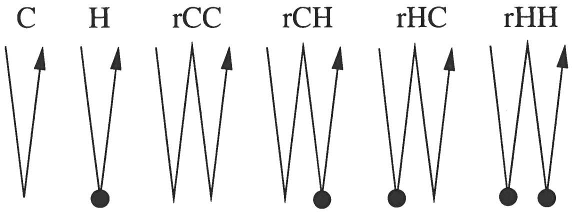

Figure 2. All first- and second-order scattering events in the expansion (11). The scatterers are indicated by black circles.

The different terms in the last line are depicted in the scattering diagrams of Figure 2. Each free-surface reflection is associated with a factor r. Each diffraction H is depicted by the scattering by a black circle. The reflections from the subsurface and the specular reflections of the sea bottom that are accounted for by the response C are denoted by a scattering event without a black circle. It follows from Figure 2 that all multiple scattering events where waves are reflected upward by the scatterers are accounted for. Multiple diffractions as well as peg-leg multiple reflections are contained in the series (11). This means that the integral equation (9) accounts for these multiple scattering paths as well.

3 SUPPRESSING THE DIFFRACTED MULTIPLES

In the integral equation (9), the data D have been measured and are thus given, whereas, the source spectrum S and the diffracted waves H are unknown. The goal of the procedure is to obtain the cleaned wavefield C. A parameter count shows that it is impossible to determine S, H, and C from this single equation. By using different time windows, however, these different unknowns can be unraveled.

The estimation of the source spectrum S is exactly the same as in existing procedures for multiple elimination (Verschuur *et al.*, 1992; Ikelle *et al.*, 1998). These references show how the source spectrum can be estimated and how this estimate can be iteratively improved while eliminating successive orders of multiples.

The estimation of C and H can be unraveled by applying a time window to the data that starts after the first water-bottom reflection and ends before the first water-bottom multiple, as shown in Figure 3. In the figure the window is indicated by dashed straight moval of diffracted multiples than for the removal of multiples from near-horizontal reflectors. In the latter case, and for small reflector dips, the wave paths of multiples don't move far from the vertical recording plane. This means that the surface bounce point of the multiples often lies within, or close to, the streamer array. If needed, an interpolation between the streamers can then be used to carry out the surface integration needed in the multiple elimination. For diffracted multiples the multiples are likely often associated with wave propagation some distance away from the recording plane, and an acquisition geometry based on streamers fails to collect the data necessary to carry out the surface integral needed for the elimination of diffracted multiples. Thus, the elimination of diffracted multiples cannot be achieved with theoretical advancements alone, but rather requires changes in the acquisition geometry in marine surveys.

ACKNOWLEDGEMENTS

I appreciate the discussions with Ray Abma, Bill Dragoset, Ken Larner, and Greg Wimpey.

REFERENCES

Berkhout, A.J., & Verschuur, D.J. 1997. Estimation of multiple scattering by iterative inversion, Part I: Theorerical considerations. *Geophysics*, **62**, 1586–1595.

Blonk, B., & Herman, G.C. 1996. Removal of scattered surface waves using multicomponent seismic data. *Geophysics*, **61**, 1483–1488.

Ernst, F, Herman, G.C., & Blonk, B. 1998. Reduction of near-surface scattering effects in seismic data. *The Leading Edge*, **17**, 759–764.

Ikelle, L.T., Roberts, G., & Weglein, A.B. 1998. Source Signature Estimation Based on the Removal of First Order Multiples. *Geophysics*, **62**, 1904–1920.

Kennett, B.L.N. 1979. The suppression of surface multiples on seismic records. *Geophys. Prosp.*, **27**, 584–600.

Riley, D.C., & Claerbout, J.F. 1976. 2-D multiple reflections. *Geophysics*, **41**, 592–620.

Verschuur, D.J., & Berkhout, A.J. 1997. Estimation of multiple scattering by iterative inversion, Part II: Practical aspects and examples. *Geophysics*, **62**, 1596–1611.

Verschuur, D.J., Berkhout, A.J., & Wapenaar, C.P.A. 1992. Adaptive surface-related multiple elimination. *Geophysics*, **57**, 1166–1177.

Wapenaar, C.P.A., & Grimbergen, J.L.T. 1996. Reciprocity theorems for one-way wavefields. *Geophys. J. Int.*, **127**, 169–177.

Wapenaar, K., Draganov, D., Thorbecke, J., & Fokkema, J. 2002. Theory of acoustic daylight imaging revisited. *Pages 2269–2272 of: Abstracts of the SEG 72nd Annual Meeting.*

Weglein, A.B., Gasparotto, F.A., Carvalho, P.M., & Stolt, R.H. 1998. An Inverse Scattering Series Method for Attenuating Multiples in Seismic Reflection Data. *Geophysics*, **62**, 1975–1989.

Weglein, A.B., Araújo, F.V., Carvalho, P.M., Stolt, R.H., Matson, K.H., Coates, R.T., Corrigan, D., Foster, D.J., Shaw, S.A., & Zhang, H. 2003. Inverse scattering series and seismic exploration. *Inverse Problems*, **19**, R27–R83.